

The present and future state of the Antarctic firn layer

Stefan Ligtenberg

Copyright © 2014, S. R. M. Ligtenberg, Utrecht, The Netherlands

Author: Stefan Ligtenberg

ISBN: 978-90-8891-834-6

Printing: proefschriftmaken.nl || Uitgeverij BOXPress, 's-Hertogenbosch

Institute for Marine and Atmospheric research Utrecht (IMAU)

Department of Physics and Astronomy

Faculty of Science

Utrecht University

Financial support was provided by the EU Framework 7 Programme ice2sea, grant number 226375, and the Netherlands Polar Programme (NPP) of the Netherlands Organisation for Scientific Research (NWO).

Cover: Graphical representation of the temporal evolution of an Antarctic firm depth-density profile from the contemporary climate (green line) till the future climate around 2200 (red line).

The present and future state of the Antarctic firn layer

De huidige en toekomstige staat van
de Antarctische firnlaag

(met een samenvatting in het Nederlands)

PROEFSCHRIFT

ter verkrijging van de graad van doctor aan de Universiteit Utrecht
op gezag van de rector magnificus, prof. dr. G. J. van der Zwaan,
ingevolge het besluit van het college voor promoties
in het openbaar te verdedigen op
woensdag 23 april 2014 des middags te 12.45 uur

door

Stefan Roderick Martijn Ligtenberg

geboren op 20 september 1986 te Apeldoorn

Promotor: Prof. dr. M. R. van den Broeke

Contents

Samenvatting	v
1 Introduction	1
1.1 Antarctic ice sheet	2
1.2 Ice sheet mass balance	3
1.2.1 Measuring ice sheet mass balance	4
1.2.2 Recent mass balance changes	6
1.3 Firn	8
1.4 Firn layer modeling	10
1.5 This thesis	12
2 Firn densification model	15
2.1 Introduction	16
2.2 Methods	18
2.2.1 Atmospheric forcing	18
2.2.2 Firn densification model	18
2.2.3 Model performance and tuning	21
2.3 Applications	24
2.3.1 Steady-state Antarctic firn density profiles	24
2.3.2 Time-dependent firn density and surface elevation	27
2.4 Conclusion	29
3 'Breathing' of the Antarctic ice sheet	31
3.1 Introduction	32
3.2 Methods	33
3.3 Results	33
3.4 Discussion	38
3.5 Summary and conclusions	39

4	Case study: Byrd Glacier blue ice area	41
4.1	Introduction	42
4.2	Methods	44
4.2.1	Atmospheric forcing	44
4.2.2	Firn densification model	45
4.2.3	Ice velocity	47
4.2.4	Blue ice area	47
4.3	Results	49
4.3.1	BIA feedback mechanisms	51
4.3.2	Sensitivity experiments	52
4.3.3	Combination of feedbacks	54
4.4	Discussion	57
4.5	Summary	57
5	Case study: the Antarctic Peninsula firn layer	59
5.1	Introduction	60
5.2	Methods	62
5.2.1	Firn densification model	62
5.2.2	Atmospheric forcing	62
5.2.3	Firn layer construction	65
5.3	Results	68
5.4	Discussion	72
6	Future climate and surface mass balance of Antarctica	75
6.1	Introduction	76
6.2	Methods	77
6.2.1	Surface mass balance	77
6.2.2	Regional atmospheric climate model RACMO2	78
6.2.3	GCM forcing	79
6.3	Results: current climate	81
6.3.1	Temperature	81
6.3.2	Surface mass balance (SMB)	82
6.3.3	RACMO2 - GCM comparison	84
6.4	Results: future climate	87
6.4.1	Evolution of T_{2m}	87

6.4.2	Evolution of the SMB	89
6.4.3	Influence on future sea level	93
6.5	Conclusion	96
7	Present and future variations in Antarctic firn air content	99
7.1	Introduction	100
7.2	Methods	102
7.2.1	Firn densification model	102
7.2.2	Atmospheric forcing	102
7.3	Results	104
7.3.1	Present day variations	104
7.3.2	Future variations	109
7.4	Discussion	114
7.5	Conclusion	115
8	Summary and outlook	117
8.1	Summary and conclusions	118
8.1.1	Firn densification model	118
8.1.2	Current state of the Antarctic firn layer	118
8.1.3	Future state of the Antarctic firn layer	120
8.2	Outlook	121
8.2.1	Firn modeling in Antarctica	121
8.2.2	Firn modeling in Greenland	123
8.2.3	Firn modeling on glaciers and ice caps	124
	Bibliography	125
	Bedankt! / Thanks!	133
	Publications	137
	Curriculum vitae	139

Samenvatting

Op plaatsen waar jaarlijks meer sneeuw valt dan er smelt, vormen zich gletsjers of ijskappen. De sneeuw die boven op dit landijs valt is een mengsel van ijskristallen en lucht en transformeert zich langzaam tot gletsjerijs met daarin kleine luchtbelletjes. Het overgangproduct van verse sneeuw naar gletsjerijs wordt firn genoemd. Bijna alle koude delen van een gletsjer of ijskap zijn bedekt met een firnlaag, zo ook de Antarctische ijskap. De Antarctische ijskap bevat bijna 90% van het landijs op Aarde en als dit allemaal zou smelten stijgt de zeespiegel wereldwijd met meer dan 58 meter. Dit zal in de komende eeuwen zeker niet gebeuren, maar dit getal geeft wel aan dat een relatief kleine verandering in de Antarctische ijsmassa al een relatief groot effect op de zeespiegel kan hebben. Het is daarom van belang om deze veranderingen zo precies mogelijk te meten, zodat bekend is hoeveel de Antarctische ijskap op dit moment bijdraagt aan zeespiegelverandering, maar ook om te kunnen voorspellen hoe groot de bijdrage in de toekomst kan zijn. Omdat het ijs van Antarctica voor 99% wordt bedekt met een dikke firnlaag, is kennis over deze firnlaag van essentieel belang voor een correcte berekening van de massabalans van het onderliggende ijs. In dit proefschrift worden de kenmerken van de huidige Antarctische firnlaag beschreven, alsook de toekomstige veranderingen onder invloed van een warmer en natter klimaat.

De dikte van een firnlaag hangt af van de snelheid waarmee de sneeuw compacteert. Verse sneeuw bestaat uit relatief grote sneeuw kristallen en daartussen poriën met lucht. Op Antarctica heeft verse sneeuw een dichtheid van ongeveer 350 kg m^{-3} . Mettertijd zullen de sneeuw kristallen zich herorganiseren, onder andere door langs elkaar te schuiven of samen te klonteren tot grotere kristallen. Hierdoor neemt de hoeveelheid lucht tussen de kristallen af en krijgt de sneeuw/firn een hogere dichtheid. Dit proces wordt firncompactie genoemd en gaat door totdat de dichtheid van gletsjerijs (ongeveer 917 kg m^{-3}) wordt bereikt. De snelheid waarmee firn compacteert wordt bepaald door de bovenliggende firnmassa en de temperatuur van de firnlaag. Nieuw gevallen sneeuw oefent extra druk uit op de onderliggende ijskristallen waardoor het compactieproces wordt versneld en er meer lucht uit de firnlaag verdwijnt. Bij een lagere temperatuur van de firn gaat de verdichting langzamer dan bij een hogere temperatuur.

Wanneer de oppervlaktetemperatuur boven het vriespunt komt zal de sneeuw aan het oppervlak smelten en gaan andere processen een rol spelen. Het smeltwater kan door de luchtporiën in de firnlaag naar beneden sijpelen, totdat het in firn terecht komt waar de temperatuur onder het vriespunt ligt. Daar zal het bevriezen als ijs, mits er genoeg energie en porieruimte

beschikbaar is. Doordat dit bevroren smeltwater in een relatief kort tijdsbestek alle lucht kan vervangen, wordt dit proces beschouwd als een zeer efficiënt 'compactie'-proces.

Om de kenmerken van de Antarctische firnlaag te bestuderen zou men idealiter een groot aantal firnkernen boren, maar dit is zowel een kostbare als logistiek ingewikkelde onderneming. Daarom wordt in dit proefschrift een computermodel gebruikt om de bovengenoemde processen in de firnlaag te beschrijven en uit te rekenen. Hierdoor is het mogelijk om een beeld te krijgen van de temporele en ruimtelijke verschillen van verschillende firnlaagkenmerken. Het in dit proefschrift gebruikte firnmodel is een verbetering ten opzichte van voorgaande modellen: voor het eerst wordt ook het smelten en herbevrozen van smeltwater gesimuleerd. Daardoor kan ook de firnlaag op relatief warme locaties aan de rand van de ijskap worden nagebootst. Daarnaast zijn de meest recente natuurkundige vergelijkingen voor firncompactie in het model opgenomen en geïkt met puntwaarnemingen van Antarctische firnlaagkenmerken.

Uit de resultaten van het verbeterde firnmodel blijkt dat de huidige firnlaag in Antarctica gemiddeld 100 meter dik is, maar dat dit van plaats tot plaats sterk verschilt. De dikte en dichtheid van de firnlaag op een bepaalde locatie worden bepaald door het klimaat aan het oppervlak. Op een relatief warme locatie zal de firn snel verdichten, waardoor de dichtheid van ijs al op een geringe diepte wordt bereikt en vice versa voor koude locaties. Waar veel sneeuw valt wordt firn sneller begraven, waardoor het weinig tijd heeft om te compacteren en de ijsdichtheid soms pas op een diepte van meer dan 150 meter wordt bereikt. In afwezigheid van smelt worden de dikste firnlagen dus gevonden in koudere gebieden met veel sneeuwval, terwijl de dunste firnlagen worden gevormd in een relatief warm en droog klimaat. Smelt zorgt in het algemeen voor snellere compactie en dus voor een minder dikke firnlaag. Op locaties waar de jaarlijkse smelt en/of sublimatie (faseovergang van sneeuw naar waterdamp) groter is dan de jaarlijkse sneeuwval zal zich helemaal geen firnlaag vormen. Dit is op 1 à 2 % van de Antarctische ijskap het geval.

Een manier om de dikte van de firnlaag uit te drukken is aan de hand van de hoeveelheid lucht die zich in de poriën van de firnlaag bevindt. In het binnenland wordt de meeste lucht in de firn gevonden; tussen de 30 en 45 meter lucht (in 100 tot 150 meter firn). Op locaties langs de kust, waar het warmer is en er smelt voorkomt, bevat de firnlaag gemiddeld tussen de 5 en 15 meter lucht. De hoeveelheid lucht in de firnlaag wordt onder andere gebruikt om waarnemingen van de dikte van de ijskap te corrigeren zodat alleen de werkelijke ijsdikte wordt gebruikt om de massa te berekenen. De resultaten in dit proefschrift laten zien dat het huidige ijsverlies van Antarctica mogelijk met 23.5% wordt onderschat doordat tot nu toe een versimpelde schatting voor de hoeveelheid lucht in de firnlaag werd gebruikt.

Doordat het klimaat boven de Antarctische ijskap niet constant is, variëren de dikte, dichtheid en luchthoeveelheid van de firnlaag niet alleen van plaats tot plaats maar ook in de tijd. Een warme of droge periode kan zorgen voor een dunnere firnlaag met minder ruimte voor lucht tussen de ijskristallen, terwijl een koude periode of hevige sneeuwval kan zorgen voor het tegenovergestelde. Naast veranderingen in de firnlaag zelf heeft dit ook consequenties voor

de hoogte van het sneeuwoppervlak van de ijskap. Als er veel sneeuw valt, zal het oppervlak omhoog komen, terwijl smelt zorgt voor oppervlakte daling. Ook de temperatuurafhankelijkheid van de compactiesnelheid zorgt ervoor dat de hoogte van het oppervlak reageert op koude en warme periodes. De op Antarctica aanwezige seizoenscyclus in zowel temperatuur als sneeuwval (minder in de zomer, meer in de winter) heeft dan ook tot gevolg dat het oppervlak van de ijskap jaarlijks gemiddeld 5.2 cm omhoog en omlaag beweegt. Deze seizoensfrequentie komt ook tot uitdrukking in de luchthoeveelheid van de firnlaag, waardoor dit proces ook wel 'het ademen van de Antarctische ijskap' wordt genoemd. De invloed van firnprocessen op de oppervlaktehoogte is vooral relevant voor de interpretatie van de, door satellieten gemeten, oppervlaktehoogteveranderingen welke worden gebruikt om de massabalans van de ijskap te berekenen. Deze variaties in oppervlaktehoogte kunnen zowel het gevolg zijn van veranderingen in ijsmassa als in luchtvolume; waar veranderingen in het eerste bijdragen aan de massabalans van de ijskap, is daar bij het tweede geen sprake van. Met een juiste verhouding tussen ijsmassa en luchtvolume kan worden voorkomen dat de massabalans van de ijskap verkeerd wordt berekend.

Op enkele plaatsen op de Antarctische ijskap is geen firnlaag aanwezig en bevindt zich gletsjerijs aan het oppervlak, zogenaamde blauwijsgebieden. Deze locaties worden gekenmerkt door jaarlijks meer ablatie (smelt en/of sublimatie) dan accumulatie (sneeuwval) van sneeuw aan het oppervlak. Doordat de gletsjer langzaam van boven naar beneden stroomt onder invloed van zwaartekracht, wordt een gevormde firnlaag meegevoerd met het ijs. Als deze een ablatiezone bereikt begint de afbraak van de aanwezige firnlaag. In dit proefschrift worden drie hoofdoorzaken gevonden voor de vorming van een blauwijsgebied; 1) stroomsnelheid van het ijs, 2) jaarlijkse ablatie en 3) dikte van de stroomopwaartse firnlaag. Slechts bij specifieke combinaties van deze factoren kan de gehele firnlaag verdwijnen en het gletsjerijs aan het oppervlak verschijnen.

Ongeveer de helft van de blauwijsgebieden worden veroorzaakt door verhoogde sublimatie als gevolg van hoge windsnelheden, vooral in het binnenland van Antarctica. Bij de andere helft is smelt de belangrijkste oorzaak, wanneer gedurende het zomerseizoen de gehele wintersneeuwval wegsmelt, wat vooral voorkomt op de drijvende ijsplaten van het Antarctische Schiereiland. Met het firnmodel zijn locaties aan te wijzen waar op dit moment een dunne firnlaag (met minder dan 3 meter lucht) aanwezig is of waar dit in de toekomst mogelijk zal gebeuren. In zo'n dunne firnlaag kan smeltwater niet altijd herbevrozen, waardoor een deel afstroomt naar zee en dus bijdraagt aan stijging van de zeespiegel. Het firnmodel laat zien dat in het huidige klimaat deze omstandigheden alleen voorkomen op de Larsen B en George VI Ijsplaten, wat overeenkomt met satellietwaarnemingen van smeltmeren op dezelfde locaties. In de toekomst zullen waarschijnlijk de andere drijvende ijsplaten op het Antarctische Schiereiland ook last krijgen van het afbreken van de firnlaag en met mogelijke vorming van smeltmeren.

Na deze beschrijving van de huidige staat van de Antarctische firnlaag kan vervolgens de vraag worden gesteld hoe deze zal reageren op toekomstige veranderingen in het klimaat.

Zal de firnlaag groeien doordat er meer sneeuw gaat vallen, of wordt de firnlaag juist dunner doordat het warmer wordt, wat leidt tot een snellere compactiesnelheid en meer smelt? Om deze vraag te kunnen beantwoorden is er allereerst een realistische verwachting voor het toekomstige klimaat van Antarctica nodig.

In dit proefschrift is het regionaal klimaatmodel RACMO2 gebruikt om verschillende mogelijkheden voor het toekomstig klimaat te simuleren. RACMO2 is door twee verschillende mondiale klimaatmodellen (HadCM3 en ECHAM5) en twee verschillende scenario's voor de uitstoot van broeikasgassen (A1B en E1) aangestuurd om zo de onzekerheid in het toekomstige klimaat na te bootsen. De simulaties laten zien dat de temperatuur boven de Antarctische ijskap stijgt met 1.8–3.0 °C tot aan het jaar 2100 en met 2.4–5.3 °C tot aan het jaar 2200. De warmere lucht zorgt enerzijds voor meer neerslag (warmere lucht kan immers meer waterdamp bevatten) en anderzijds voor meer ablatie door toenemende sublimatie en smelt. Gemiddeld over de ijskap wordt de toename in ablatie echter ruim overtroffen door de accumulatie-toename. Dit betekent dus dat er jaarlijks extra massa vanuit de oceaan aan het oppervlak van de Antarctische ijskap wordt toegevoegd: 98 miljard ton per jaar per iedere graad temperatuurstijging. Gecombineerd met de gesimuleerde temperatuurstijging leidt dit tot een zeespiegeldaling van 73–163 mm in de komende twee eeuwen. Hierbij moet wel worden opgemerkt dat een eventuele toename in stroomsnelheid van de ijskap, door zowel de extra massa als het versneld smelten aan de rand van de ijskap door warmer oceaanwater, niet is meegenomen. Zo'n versnelling zorgt voor een grotere ijsafvoer naar de oceaan en zal deze zeespiegeldaling zeer waarschijnlijk deels opheffen of zelfs overtreffen.

Met deze verwachting van het toekomstige klimaat is het mogelijk om de reactie van de huidige firnlaag op een toename in temperatuur, sneeuwval en smelt te simuleren. Meer sneeuwval leidt logischerwijs tot een dikkere firnlaag met een grotere luchthoeveelheid. In gebieden zonder smelt zijn er twee processen die dit effect voor ongeveer de helft compenseren; een snellere verdichting, als gevolg van hogere firntemperaturen, en een snellere transitie van firn naar ijs aan de onderkant van de firnlaag, doordat de totale firnlaagmassa toeneemt. In de komende 200 jaar neemt de luchthoeveelheid in deze 'droge' firngebieden toe met 4 tot 14%. In de kustgebieden zal de smelt toenemen, waardoor er meer smeltwater herbeviert in de firnlaag. Hier neemt de luchthoeveelheid in de firnlaag tot aan het jaar 2200 af met 50 tot 70%. Op de gehele ijskap zijn er procentueel echter veel meer gebieden met een volumetoename door sneeuwval dan met een volumeafname door smelt, waardoor er de komende jaren 120–150 km³ lucht per jaar bijkomt in de Antarctische firnlaag. Als deze toename in lucht zou worden geïnterpreteerd als een toename in massa leidt dit tot een verkeerde berekening van de massabalans.

Dit proefschrift beschrijft de temporele en ruimtelijke verschillen in de Antarctische firnlaag, in zowel het huidige als toekomstige klimaat. De resultaten laten zien dat deze verschillen dusdanig groot zijn dat kennis van firnlaagvariaties van cruciaal belang is voor een juiste interpretatie van massaveranderingen van de Antarctische ijskap.

1

Introduction

The Antarctic ice sheet is covered by a ~ 100 meter thick firn layer, consisting of fresh snow that slowly transforms to glacier ice under its own weight. The firn layer thus represents a boundary layer between the atmosphere and the underlying ice. Recently, interest in this underlying ice has increased due to observed changes in its mass and subsequent sea level rise. To correctly assess these changes, variations in firn layer density, thickness and depth need to be taken into account. This thesis describes variations in the present Antarctic firn layer and possible future changes due to a warming climate.

This thesis is a compilation of research articles that are presented in Chapters 2–7 and can also be read independently. Chapter 2 introduces the firn densification model that is used throughout this thesis. Hereafter, the present state of the Antarctic firn layer is examined in Chapters 3–5, followed by a discussion of future changes in the Antarctic climate and subsequent firn layer response (Chapters 6–7). Finally, Chapter 8 provides a summary of the main conclusions of this thesis, along with an outlook for future research in firn modeling.

This first chapter introduces the main topics of this thesis and provides some background information on the study area. First, the characteristics of the Antarctic ice sheet and its climate are presented. Next, the term ice-sheet mass balance is introduced, together with the main methods to measure mass balance. This section will be concluded by an overview of the present state of ice-sheet mass balance research. Hereafter, the main focus will be on firn. Characteristics of a typical firn layer and processes that determine temporal and spatial variations are discussed, as well as the concept of firn layer modeling. The chapter is concluded with an overview of this thesis.

1.1 Antarctic ice sheet

The Antarctic ice sheet (AIS) covers the complete Antarctic continent, apart from some isolated rock outcrops, and is the largest of the two major ice sheets on Earth, the other one being the Greenland ice sheet. Surrounded by the ocean on all sides, the continent and its ice sheet experience a unique climate. It is on average the coldest, windiest, driest and highest continent on Earth. The interior of the AIS consists of up to 4 kilometers thick ice [Fretwell *et al.*, 2013] that flows towards the coast, driven by internal deformation and sliding [Bamber *et al.*, 2000]. Along 75 % of the coast, the ice flows into the ocean to form large floating ice shelves, that buttress their feeding ice streams [Scambos *et al.*, 2004; Rignot *et al.*, 2004]. Figure 1.1 shows the surface elevation of the AIS and indicates locations used throughout this thesis. The average surface elevation of the AIS is ~ 1950 m above sea level (a.s.l.) and more than 83 % of its surface is higher than 1000 m a.s.l., with only the coastal regions and the ice shelves lying below this level.

The average annual 2-m temperature on Antarctica is -37 °C [Lenaerts, 2013] and the major part of the AIS never experiences temperatures above freezing at any time of the year. Only on the fringing ice shelves and in the Antarctic Peninsula, surface melt occurs regularly in austral summer (red line in Figure 1.1). As a result of these low temperatures, the air above the AIS contains little water vapor and therefore generates little precipitation. Especially the ice sheet interior is very dry, receiving only ~ 10 cm snow annually [Scambos *et al.*, 2012; Lenaerts *et al.*, 2012a]. The steep coastal areas, where orographic precipitation is more abundant, are wetter, although these are relatively small compared to the ice sheet interior. From the high interior of the AIS the surface gently slopes towards the coast and due to buoyant effects, cold air from high elevations flows downwards along these slopes, so-called katabatic winds. On steeper slopes and in confluence areas, wind speeds are higher, with the highest annual average near-surface wind speeds on Earth (>20 m s^{-1}) occurring in the coastal areas of Adélie Land, East Antarctica [Mawson, 1915; Wendler *et al.*, 1997; Lenaerts *et al.*, 2012b].

The AIS contains approximately 26.5 million km^3 of ice [Fretwell *et al.*, 2013], which is equivalent to 58.3 m of eustatic sea level rise (SLR) and represents almost 90 % of all land ice present on Earth. The remainder of frozen freshwater is found in Greenland (7.4 m) [Bamber *et al.*, 2013] and in smaller ice fields and glaciers (0.31–0.53 m), such as Alaska, Svalbard, Patagonia, the Himalaya and the Canadian Archipelago [Huss and Farinotti, 2012; Grinsted, 2013; Radić *et al.*, 2014; IPCC, 2013]. The AIS can be subdivided into the West Antarctic ice sheet (WAIS) and the larger East Antarctic ice sheet (EAIS), which are divided by the Transantarctic Mountains, running west of the Ross Ice Shelf, up to the Antarctic Peninsula (Figure 1.1). The ice shelves that fringe the AIS (grey areas in Figure 1.1) are typically a kilometer to a few hundred meters thick [Pritchard *et al.*, 2012], although only ~ 10 % of their mass is above sea level due to the $\sim 9/10$ relation between the density of glacier ice (~ 917 kg m^{-3}) and sea water (~ 1032 kg m^{-3}). Many ice shelves along the Antarctic coast are relatively similar in size ($\sim 10^4$ km^2), although two large ice shelves stand out in

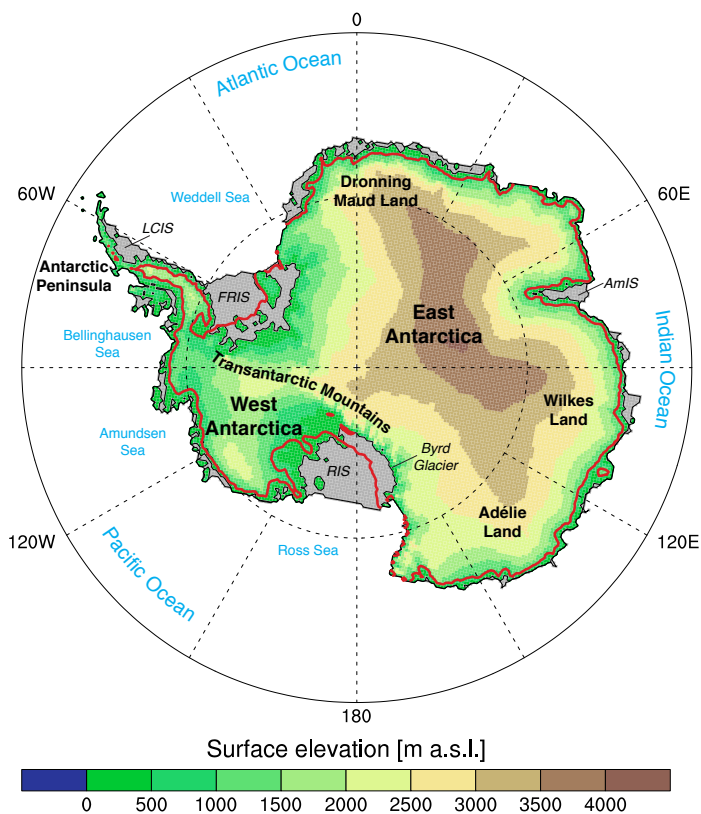


Figure 1.1: Map of Antarctica; shaded colors show the surface elevation of the grounded ice sheet, in meters above sea level (m a.s.l.). Grey indicates floating ice shelves and the thin black line shows the grounding line that marks the boundary between grounded and floating ice. Names indicate major regions of the ice sheet (bold black), oceanic subareas (blue) and other notable features (oblique black), such as Larsen C Ice Shelf (LCIS), Filchner-Ronne Ice Shelf (FRIS), Amery Ice Shelf (AmIS) and Ross Ice Shelf (RIS). The solid red line represents the upper boundary of the region where annual surface melt occurs (>2 mm water equivalent (w.e.) yr^{-1} melt over the 1979–2011 period [Lenaerts et al., 2012a]).

Figure 1.1; the Ross Ice Shelf (RIS) and Filchner-Ronne Ice Shelf (FRIS), each approximately $5.0 \cdot 10^5 \text{ km}^2$ [Rignot et al., 2013]. Along the EAIS coast between $40\text{--}170^\circ\text{E}$, less ice shelves are present.

1.2 Ice sheet mass balance

The vast amount of ice contained in the AIS makes that even a small relative change in its mass can have a significant effect on global sea level. Measuring or calculating the mass bal-

ance of an ice sheet is used to determine if it is gaining or losing mass, and hence contributes negatively and positively to SLR. The mass balance (MB) of an ice sheet is determined by mass input at its surface and mass output at its edges, surface mass balance (SMB) and ice discharge (D), respectively, i.e. $MB = SMB - D$.

The net mass input of an ice sheet is governed by the surface mass balance:

$$SMB = P - SU_s - SU_{ds} - ER_{ds} - RU \quad (1.1)$$

where P equals precipitation (solid and liquid), SU_s and SU_{ds} sublimation of surface snow and drifting snow, respectively, ER_{ds} erosion of drifting snow and RU runoff of meltwater [Lenaerts *et al.*, 2012a]. Precipitation is the largest component of the Antarctic SMB and mainly falls as snow on the ice sheet. Sublimation of surface and drifting snow, as well as drifting snow erosion, removes part of the accumulated snow. When snow melts at the surface, meltwater will percolate into the snow where it can refreeze as ice. If enough snow melts, the pore space gets saturated and meltwater can eventually run off into the ocean. In Antarctica, surface runoff is small as almost all meltwater refreezes locally; in Greenland however, it accounts for roughly half of the mass output [Ettema *et al.*, 2009; Van Angelen *et al.*, 2013].

Mass output of the AIS is governed by the discharge of solid ice into the ocean. The boundary between grounded and floating ice is called the grounding line and is often used as 'gate' where the discharge of grounded ice is calculated [Rignot *et al.*, 2011a]. When the ice passes the grounding line, it forms floating ice shelves. These ice shelves lose their mass to the ocean by two processes that are more or less equal in magnitude; i) iceberg calving at the front of the ice shelf and ii) basal melting at the bottom of the ice shelf that is in contact with the relatively warm ocean water [Depoorter *et al.*, 2013; Rignot *et al.*, 2013].

1.2.1 Measuring ice sheet mass balance

Due to the remoteness and sheer size of the AIS, measuring its mass balance is very challenging. Moreover, both the mass in- and output are large quantities with large uncertainties, making it difficult to accurately determine the much smaller difference between the two. Most techniques to assess mass balance directly involve satellite measurements that sample the complete ice sheet from space. Currently, there are three widely used methods: i) the mass budget method [e.g. Rignot *et al.*, 2008], ii) the volumetric method [e.g. Davis *et al.*, 2005] and iii) the gravimetric method [e.g. Velicogna and Wahr, 2006].

In the mass budget method, both the in- and output of mass to/from the ice sheet are calculated separately and the difference gives the mass balance of the ice sheet. The mass input is given by the SMB, which is either simulated with a climate model [Van de Berg *et al.*, 2006;

Lenaerts et al., 2012a] or estimated from in-situ observations interpolated with a satellite-derived background field [*Vaughan et al.*, 1999; *Arthern et al.*, 2006]. In Antarctica, the SMB is mainly determined by precipitation (snowfall). The other SMB components (rainfall, sublimation, drifting snow erosion and runoff) are all at least one order of magnitude smaller. Currently, the SMB of the grounded AIS is estimated at $1983 \pm 122 \text{ Gt yr}^{-1}$ [*Lenaerts et al.*, 2012a]. Mass output is calculated as the amount of ice that flows over the grounding line, given by the vertically averaged ice velocity multiplied by the ice thickness. Ice velocities are obtained from differencing radar satellite images (SAR Interferometry) [*Rignot et al.*, 2011b], while ice thickness is deduced from either the flotation criterium at the grounding line [*Rignot et al.*, 2011c] or direct observations using ice penetrating radar from airplanes [*Li et al.*, 2013; *Rignot et al.*, 2013].

The volumetric and gravimetric methods are based on measuring changes in volume and mass, rather than calculating the absolute values of the mass balance components. The volumetric method uses satellite altimetry (radar and laser) to measure surface elevation changes with time [*Davis et al.*, 2005; *Wingham et al.*, 2006; *Pritchard et al.*, 2009]. These changes in surface elevation provide a change in volume, which can be converted into an ice mass change if the density at which the elevation change occurs is known. Surface elevation changes can also be caused by other processes, such as bedrock movement due to changes in ice loading (glacial isostatic adjustment) [*Peltier*, 2004; *Spada et al.*, 2011; *Whitehouse et al.*, 2012], SMB changes [*Horwath et al.*, 2012], firn densification changes (*Helsen et al.* [2008] and this thesis) and sea level changes (only on ice shelves, *Pritchard et al.* [2012]). Therefore, to extract ice sheet mass balance from surface elevation measurements, multiple corrections have to be applied.

The gravimetric method directly measures the mass changes by observing the changes in the Earth's gravity field with the GRACE tandem satellites. GRACE consists of two identical satellites that measure their inter-satellite distance while orbiting the Earth. They are located approximately 220 km apart and therefore experience different, and constantly varying, gravitational pull from the Earth's gravity field. Differences in the inter-satellite distance can be converted into spatial and temporal variations in Earth's mass [*Tapley et al.*, 2004]. To extract ice sheet mass balance from GRACE measurements, all other mass changes have to be taken into account, such as glacial isostatic adjustment and ocean tides. It is important to explicitly distinguish the different processes, as their densities vary between $\sim 3500 \text{ kg m}^{-3}$ (bedrock), $\sim 1032 \text{ kg m}^{-3}$ (ocean water), $\sim 917 \text{ kg m}^{-3}$ (ice) and $\sim 350 \text{ kg m}^{-3}$ (surface snow) [*Riva et al.*, 2009]. In principle, the gravimetric method is the most direct method to measure mass balance changes; however, the spatial resolution of the GRACE satellite is currently relatively coarse ($\sim 250 \text{ km}$) compared to the other two methods, and no information is obtained about partitioning of the mass loss.

Although the three methods described above mainly rely on satellite observations to determine ice sheet mass balance (changes), they require corrections for surface processes for a correct interpretation. For example, the SMB is, apart from being a major component of the

mass-budget method, also used for corrections in the volumetric and gravimetric methods. For the volumetric method, mass changes in firn layer depth and density invoke up to three times more elevation change than the same mass change in ice. Also, the ice thickness at the grounding line, which is used in the mass-budget method, has to be corrected for the amount of air present in the firn layer, to prevent an overestimation of the ice discharge. In this thesis, the main focus will be on these surface processes and their importance in the determination of ice sheet mass balance.

1.2.2 Recent mass balance changes

During the last decades, the interest in ice sheet mass balance has increased tremendously, mainly because of the enhanced greenhouse effect and related global mean temperature rise, and its effect on the melting of land ice and subsequent contribution to SLR. Recent atmospheric warming has likely caused the most northerly ice shelves (IS) in the Antarctic Peninsula to disintegrate: Wordie IS in 1988, Larsen A IS in 1995, Larsen B IS in 2002 and Wilkins IS in 2008 [Doake and Vaughan, 1991; Doake *et al.*, 1998; Rack and Rott, 2004; Cook and Vaughan, 2010]. Although the break-up of an ice shelf does not influence sea level directly, the acceleration of the glaciers that feed into them does: when an ice shelf that buttresses these glaciers is (partly) removed, ice flow velocity will increase and more ice will drain into the ocean [Scambos *et al.*, 2004; Rignot *et al.*, 2004].

Elsewhere in Antarctica, progressive thinning of ice shelves [Pritchard *et al.*, 2012] has also led to increased ice velocities [Rignot *et al.*, 2011a]. This thinning is likely caused by oceanic forcing; relatively warm ocean water is directed into the sub-shelf cavities, where it can melt the ice shelf from beneath. In West Antarctica, the continental shelf has a favorable topography, with deep troughs that lead warm ocean water directly to the bottom of the ice shelves [Hellmer *et al.*, 2012; Pritchard *et al.*, 2012]. On a few East-Antarctic ice shelves (Moscow University IS and Totten IS), a different mechanism is found; here, a decrease in polynya extent (open water in sea ice) is causing less cold-polynya water to enter the sub-shelf cavity, leading to increased bottom melt rates [Khazendar *et al.*, 2013]. Although the mechanism is different, the result is similar: the ice shelf thins from below, diminishing the buttressing effect on inland glaciers, resulting in an increase of grounded ice velocities and enhanced ice discharge into the ocean.

Since the SMB of Antarctica has shown no clear trends over roughly the last half century [Monaghan *et al.*, 2006; Lenaerts *et al.*, 2012a], the increase in ice discharge means that the AIS mass balance has, on average, been negative over the last 20 years [Rignot *et al.*, 2011a]. The other two mass balance estimation techniques (volumetric and gravimetric) confirm this recent mass loss [Davis *et al.*, 2005; Zwally *et al.*, 2005; Ramilien *et al.*, 2006; Velicogna, 2009; Lee *et al.*, 2012]. Recently, a study reconciled the three above mentioned techniques and showed that the AIS has lost $71 \pm 53 \text{ Gt yr}^{-1}$ over the period 1992–2010 [Shepherd *et al.*,

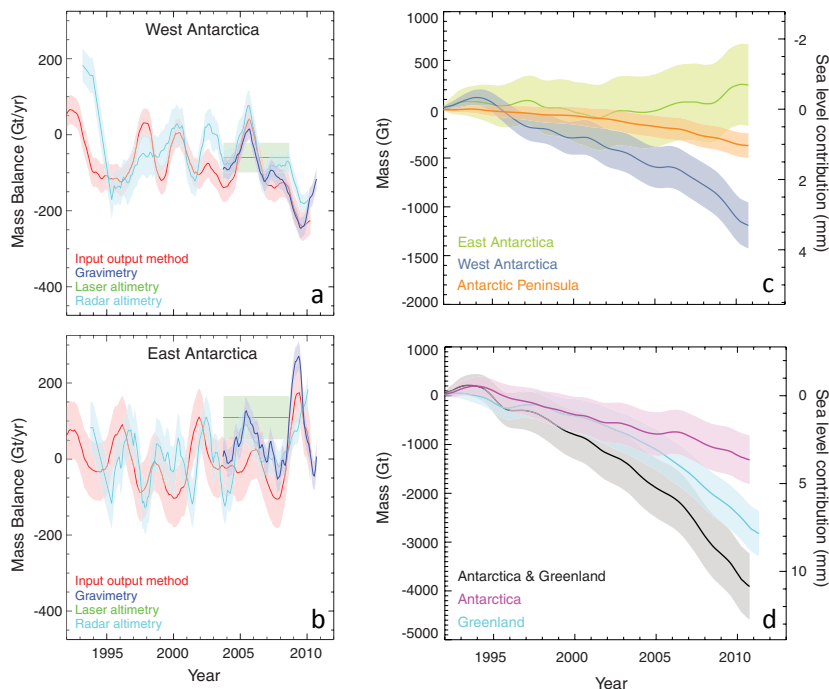


Figure 1.2: Rate of mass change (mass balance) of West Antarctica (a) and East Antarctica (b), as derived by the three mass balance techniques: mass-budget method (red), volumetric method (light blue and green) and gravimetric method (dark blue). The respective uncertainties are given by the light shading. Cumulative mass changes for the three main Antarctic regions (c) and for Greenland, Antarctica and a combination of both (d). The right axis in (c) and (d) represents the corresponding sea level changes (with 360 Gt yr^{-1} approximately equal to 1 mm global SLR). From Shepherd *et al.* [2012].

2012]. Figure 1.2 shows that the main mass loss has occurred in West Antarctica, while East Antarctica is close to mass balance or slightly gaining mass.

The AIS mass loss over 1992–2010 gives a total global SLR of 3.7 mm . Over the same period, the Greenland ice sheet (GrIS) has also been losing mass at a pace that is double that of the AIS ($142 \pm 49 \text{ Gt yr}^{-1}$, Figure 1.2d). Combined with its smaller annual mass turnover ($\sim 500 \text{ Gt yr}^{-1}$, [Rignot *et al.*, 2011a]), this indicates that the GrIS reacts more strongly to recent climate change than the AIS. Mass loss from the GrIS is equally divided between an increase in ice discharge and an increase in surface meltwater runoff [Van den Broeke *et al.*, 2009]. Over the past decades, the surface area of the GrIS where significant surface melt occurs has almost doubled [Fettweis *et al.*, 2011], with 2012 holding the current record with

~98 % of the GrIS surface experiencing melt on 12 July [Nghiem *et al.*, 2012; Tedesco *et al.*, 2013].

In the recent 5th Assessment Report (AR5) of the Intergovernmental Panel on Climate Change (IPCC), an extensive summary of the current knowledge on recent and future climate change and its effects is given [IPCC, 2013]. This includes the role of land ice in the climate system, its reaction to rising temperatures and the subsequent effect on sea level change. It is very likely that the ice loss of the GrIS and AIS has significantly increased over the last 20 years; from 34 and 30 Gt yr⁻¹ in 1992–2001 to 215 and 147 Gt yr⁻¹ in 2002–2011, respectively. Combined, the GrIS and AIS contributed 0.6 ± 0.2 mm yr⁻¹ to global mean SLR over the last 20 years, about 21 % of the total observed SLR over this period. Thermal expansion of ocean water (~39 %), melting of smaller ice caps and glaciers (~27 %) and land water storage (~13 %) are the other major components that contribute to total global mean SLR (2.3–3.4 mm yr⁻¹) over the period 1993–2010.

1.3 Firn

Firn is the transitional product between snow and ice. In mid-latitude regions, such as the Alps, firn is often used to describe snow that lasts through the summer and does not yet have the characteristics of glacier ice. The word 'firn' comes from the German language and literally means 'last year's snow'. In off-piste skiing, firn is usually used to indicate snow that has a denser and harder surface than fresh snow, mostly due to melting during daytime and refreezing of the meltwater during nighttime. In Antarctica, the word firn is used to indicate the layer of snow that covers the ice sheet and does not have the characteristics and density (~917 kg m⁻³) of glacier ice. The Antarctic firn layer is typically 50–150 m thick and the thickness is directly related to the local climate (Chapter 2). Generally, the thickest firn layers are found in relatively cold and/or high accumulation rate regions and thinner firn layers in warm and/or relatively dry regions. A firn layer can only exist if the long-term SMB is positive, i.e. more accumulation than ablation on an annual basis. Where this is not the case (i.e. in an ablation area), a firn layer is absent and glacier ice is exposed at the surface; a so-called blue ice area (Chapter 4). Blue ice areas cover 1–2 % of the Antarctic surface and are regions where annual sublimation and/or melt is larger than the annual accumulation of snow [Winther *et al.*, 2001].

In Antarctica, fresh snow typically consists for 1/3 of ice crystals and 2/3 of air, and has a density of ~350 kg m⁻³ [Kaspers *et al.*, 2004]. Over time, snow particles re-arrange, link, merge or shift under their own weight, thereby reducing the amount of air in the air-ice mixture [Herron and Langway, 1980]. When additional snow falls on top of this layer, pressure is added and more air will be removed from the firn. This process is called firn densification and continues until the density of glacier ice is reached: 917 kg m⁻³, i.e. when only ~8 % of air is left between the ice crystals. Firn densification does not only depend on the overburden

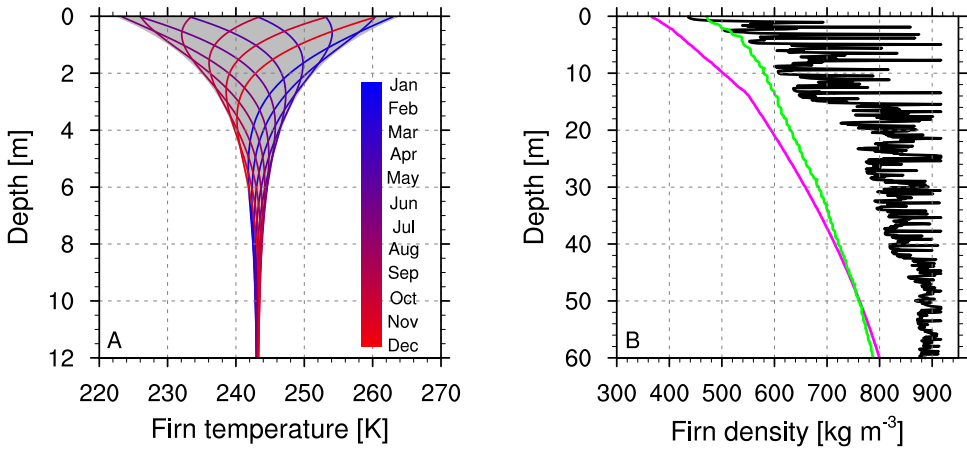


Figure 1.3: Typical firn temperature (A) and firn density (B) profiles for the Antarctic ice sheet. The temperature profiles are obtained from an idealized climate with a sine-like annual temperature cycle (average temperature of $T = -30^{\circ}\text{C}$ and annual amplitude of $T_{amp} = 20^{\circ}\text{C}$) and represent a temperature profile every month, from January (blue) to December (red). Note that January is the austral summer. Grey indicates the annual temperature spread at depth. Density profiles represent different Antarctic climates; cold and wet (magenta), warm and dry (green) and with substantial summer melt (black), respectively. Note the different depth scale between (A) and (B).

pressure, but also on temperature, density and snow crystal size and shape. Therefore, firn densification is difficult to study and model explicitly, which will be discussed in the next section and Chapter 2.

When surface temperatures are above freezing, the snow at the surface will melt and transform into liquid water. This water can percolate down through the air pores in the firn layer, where part of the meltwater will stay attached to the crystals due to capillary forces [Pfeffer *et al.*, 1990]. The meltwater will continue to move down through the firn column until it reaches a layer of sub-zero temperature, where it will refreeze [Illangasekare *et al.*, 1990]. When meltwater refreezes, it replaces part of the air space by ice, making the melting-refreezing cycle a very efficient 'densification' process. Only when there is no pore space left or when it cannot be reached, the excess meltwater will run off.

Figure 1.3 shows a selection of firn temperature and density profiles that are typical for the Antarctic firn layer. The temperature in the upper part of the firn layer is determined by the air temperature above the firn layer and therefore follows the seasonal cycle in atmospheric temperature. The surface temperature signal penetrates the firn pack with a certain time lag, which depends on the depth and density of the firn. For example, at 4 m depth, the annual maximum temperature is reached around April, while the maximum temperature at the surface is reached in January (austral summer). At 10–15 m depth, the seasonal temperature

signal is almost absent due to thermal diffusivity of the signal, and the local temperature is equal to the long-term average surface temperature.

Typical Antarctic firn density profiles show a slow and steady increase of density with depth, and the ice density (917 kg m^{-3}) is often reached at 100–150 m (not shown). The speed of firn densification depends on temperature and overburden pressure, as will be discussed in the next section and throughout this thesis. When melt occurs (black line in Figure 1.3b), firn layers with higher densities will form due to the relative high density of refrozen meltwater. When sufficient melt occurs, a part of the firn layer will turn into glacier ice, i.e. ice lens formation.

1.4 Firn layer modeling

In 1980, a seminal paper about semi-empirical firn modeling was published by *Herron and Langway* [1980], and their ideas are still used in many current firn densification models (FDM, e.g. *Zwally and Li* [2002]; *Arthern et al.* [2010]). These models are based on the idea that three stages can be defined in the firn densification process. During the first stage, for firn with a density less than 550 kg m^{-3} , the densification process is the most rapid due to packing of fresh snow and grain settling. If the density exceeds 550 kg m^{-3} , the speed of densification is roughly halved and firn densification is mainly caused by sublimation, diffusion and deformation of ice crystals ("sintering"). In Figure 1.3b, this distinction is especially visible in the magenta profile, which shows a more rapid density increase with depth for firn density $<550 \text{ kg m}^{-3}$. When the density reaches 830 kg m^{-3} , the so-called 'pore close-off depth', the air bubbles get trapped in the ice and further densification occurs through compression of these air bubbles.

The speed of firn densification depends exponentially on the local temperature, with higher temperatures causing quicker densification [*Herron and Langway*, 1980]. In the green density profile in Figure 1.3b, the small oscillations of firn density with depth are caused by the large local temperature difference between summer and winter (Figure 1.3a) that cause differences in seasonal densification speeds. However, the main driver of firn densification is the weight of the above-lying firn column that presses on the firn. In the previously mentioned FDMs, the average annual accumulation is used as a measure for this pressure, and the factors in these models are tuned to match observed firn profiles (i.e. 'semi-empirical' models). Other FDMs use the effective overburden pressure above a model firn layer to calculate the firn densification speed [e.g. *Barnola et al.*, 1991; *Spencer et al.*, 2001]. However, there is currently no clear evidence that one type of model is performing better than the other [*Lundin et al.*, in preparation]. In this thesis, a semi-empirical approach is used, and to make the FDM applicable to Antarctica some adaptations were made to the original model of *Helsen et al.* [2008], which are described in Chapter 2.

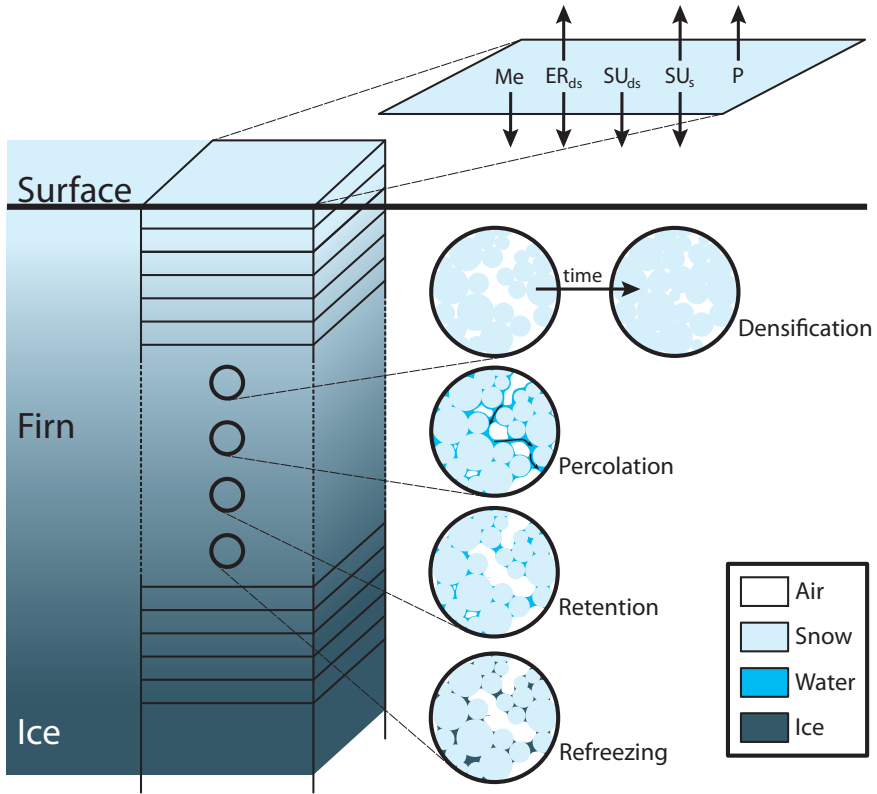


Figure 1.4: Schematic representation of the firm densification model (FDM) used in this thesis. At the surface the mass adding (arrow up) and mass removing (arrow down) SMB components are shown: precipitation (P), surface sublimation (SU_s), drifting snow sublimation (SU_{ds}) and erosion/deposition (ER_{ds}) and surface melt (Me). The four enlarged circles illustrate schematically the processes that are calculated within the model firn layer: firm densification and percolation, retention and refreezing of meltwater.

Besides modeling the densification rate, a FDM also describes other processes in the firn layer, such as temperature evolution, meltwater transport and refreezing, as well as mass fluxes at the surface of the firn layer (e.g. snowfall and sublimation). Figure 1.4 shows a schematic representation of the FDM used in this thesis. The model firn layer consists of a column that is discretized in model layers with a certain thickness, usually in the order of centimeters. At every model time step, the mass of the top layer is re-calculated using the mass addition (+) and removal (-) processes governed by the local SMB: precipitation (+), surface sublimation (+/-), drifting snow sublimation (-) /erosion (+/-) and surface melt (-). For every model layer, the firm densification and percolation, retention, refreezing or runoff of meltwater is calculated. In each model time step, the temperature, density, mass and liquid water content of the firn layers are calculated and stored.

We distinguish two applications of the FDM: i) steady-state firn profiles and ii) the time-dependent evolution of firn depth, density and temperature. The first application generates an average firn density profile, based on the local average climate conditions. These profiles are often used to calculate the average firn air thickness of the firn layer, i.e. the hypothetical thinning of the firn layer (in meters) when it would be compressed to the density of ice. This quantity can for example be used to correct the ice thickness at the grounding line in the mass-budget method (see Section 1.2.1). Also, spatial differences in firn layer characteristics can be quickly examined, as will be described in Chapter 2. The time-dependent mode of the FDM is used to simulate changes in the mass and depth of the firn layer with time. In this way, the temporal differences in firn density and temperature, but also the effect of all processes on the elevation of the surface, can be assessed. The latter is mainly used to convert satellite measured elevation changes to ice sheet mass changes.

1.5 This thesis

In this thesis, the present and future state of the Antarctic firn layer is examined using a combination of a regional atmospheric climate model (RACMO2) and a firn densification model (FDM). The FDM is forced at the surface with climate output from RACMO2 and evaluated with firn core observations. The following applications of the FDM are analyzed and discussed:

In **Chapter 2**, the FDM used in this theses is introduced; it simulates both the steady-state and the time evolution of firn depth and density. An existing model was updated using improved densification equations and extended with a snowmelt module that calculates the percolation, retention, refreezing and runoff of meltwater in the firn layer. The present average state of the Antarctic firn layer is discussed, as well as the resulting modeled firn air content.

Chapter 3 describes the seasonal cycle in firn depth, and hence surface elevation, that is found on the AIS. The seasonality is forced by the difference in precipitation between the (wet) winter and (drier) summer. As a result, the surface height of the AIS oscillates on an annual basis. Model simulations from the FDM are compared with satellite surface elevation measurements from the ENVISAT radar altimeter.

In the two following chapters, two different regional applications of the FDM are discussed; i) blue ice formation and ii) the Antarctic Peninsula firn layer. In **Chapter 4**, the blue ice area on Byrd Glacier is examined by simulating the firn layer evolution along an ice flow trajectory. Using multiple sensitivity simulations, the importance of blue ice feedback mechanisms on its own formation and existence are studied. **Chapter 5** discusses the steady-state firn layer in the Antarctic Peninsula. A high-resolution (5.5 km) RACMO2 simulation of the Antarctic Peninsula requires a realistic firn layer initialization to correctly simulate surface melt and runoff. Using a combination of steady-state and time-dependent FDM simulations

and firn air radar measurements, a realistic Antarctic Peninsula firn layer is constructed that is also used to identify regions that are likely to produce runoff at present or in the near-future.

Next, the focus is on the future state of the Antarctic climate and firn layer. In **Chapter 6**, a suite of RACMO2 future simulations is used to assess the impact of climate change and warming temperatures on the Antarctic climate and SMB. RACMO2 is forced at its boundaries with global climate model (GCM) output for different future emission scenarios. Late 20th century simulations are performed to analyze the climate bias in these GCM-forced simulations. In **Chapter 7**, these RACMO2 simulations are used to force the FDM in order to simulate the response of the firn layer across Antarctica on rising temperatures and increasing precipitation and melt in a future climate.

Finally, a summary of the main conclusions from this thesis will be given in **Chapter 8**, together with recommendations for future work on firn modeling.

Firn densification model

Summary

A firn densification model is presented that simulates steady-state Antarctic firn density profiles, as well as the temporal evolution of firn density and surface height. The model uses an improved firn densification expression that is tuned to fit depth-density observations. Liquid water processes (melt-water percolation, retention and refreezing) are also included. Two applications are presented. First, the steady-state model version is used to simulate the strong spatial variability in firn layer thickness across the Antarctic ice sheet. Second, the time-dependent model is run for 3 Antarctic locations with different climate conditions. Surface height changes are caused by a combination of accumulation, melting and firn densification processes. On all 3 locations, an upward trend of the surface during autumn, winter and spring is present, while during summer there is a more rapid lowering of the surface. Accumulation and (if present) melt introduce large inter-annual variability in surface height trends, possibly hiding ice dynamical thickening and thinning.

This chapter is published as: Ligtenberg S. R. M., M. M. Helsen, and M. R. van den Broeke (2011), An improved semi-empirical model for the densification of Antarctic firn. *The Cryosphere*, **5**, 809–819, doi:10.5194/tc-5-809-2011.

2.1 Introduction

The Antarctic ice sheet (AIS) is almost entirely covered by a layer of firn, the intermediate product in the transition from snow to ice. In Antarctica, fresh snow has a typical density of 350 kg m^{-3} , while glacier ice has a density of more than 900 kg m^{-3} . At low temperatures and accumulation rates, densification of firn is a slow process and the transition can take up to centuries or millennia. The large range of surface climate conditions in Antarctica introduces widely varying characteristics of the firn layer in space and time [Zwally and Li, 2002; Van den Broeke, 2008; Helsen et al., 2008]. For instance, the firn layer thickness can vary between a few tens of meters in the relatively warm coastal areas to $>100 \text{ m}$ in the cold interior of East Antarctica. In ablation areas, where sublimation, drifting snow erosion and/or melt exceed snowfall, the firn layer can even be completely absent, resulting in formation of blue ice areas [Winther et al., 2001].

The steady and transient states of the firn layer provide important information on firn air content and surface elevation changes. These are crucial parameters needed to estimate the contemporary mass balance of the AIS using remote-sensing techniques [Rignot et al., 2008; Helsen et al., 2008; Van den Broeke et al., 2008]. Figure 2.1, adjusted from Zwally and Li [2002], shows the various components of the vertical displacement of the ice sheet surface. A change in surface height with time (dH/dt) is given as the sum of these velocity components:

$$\frac{dH}{dt} = v_{\text{acc}} + v_{\text{me}} + v_{\text{fc}} + v_{\text{ice}} + v_{\text{b}} \quad (2.1)$$

where v_{acc} , v_{me} , v_{fc} , v_{ice} and v_{b} are the velocity components that represent accumulation, melt, firn compaction, ice flow and bedrock movement, respectively. Since we focus on relative short timescales, v_{b} is negligible and v_{ice} is assumed proportional to the average annual accumulation. The effect of sublimation is included in the accumulation velocity, v_{acc} . These velocity components can be combined in time-dependent firn densification models to calculate temporal changes in firn depth and density and surface height changes, by forcing them with time series of surface temperature, snowfall, sublimation and melt. These results can be used to convert satellite elevation change measurements to mass changes [Davis et al., 2005; Wingham et al., 2009, among others]. It has been demonstrated that variability in firn densification rate and accumulation strongly influences the observed surface height changes [McConnell et al., 2000; Helsen et al., 2008].

Several models have been proposed to describe firn densification. Some are based on physical principles [e.g. Wilkinson, 1988], while others use semi-empirical parameterizations [Herron and Langway, 1980; Barnola et al., 1991; Helsen et al., 2008; Arthern et al., 2010]. A distinction can also be made between models that describe the steady-state density profile, and models that simulate changes in the firn layer over time. Steady-state firn profiles can be used to estimate the amount of air in the firn column, which is used to convert ice thicknesses to total mass of an ice column. Van den Broeke [2008] showed that the steady-state solution of

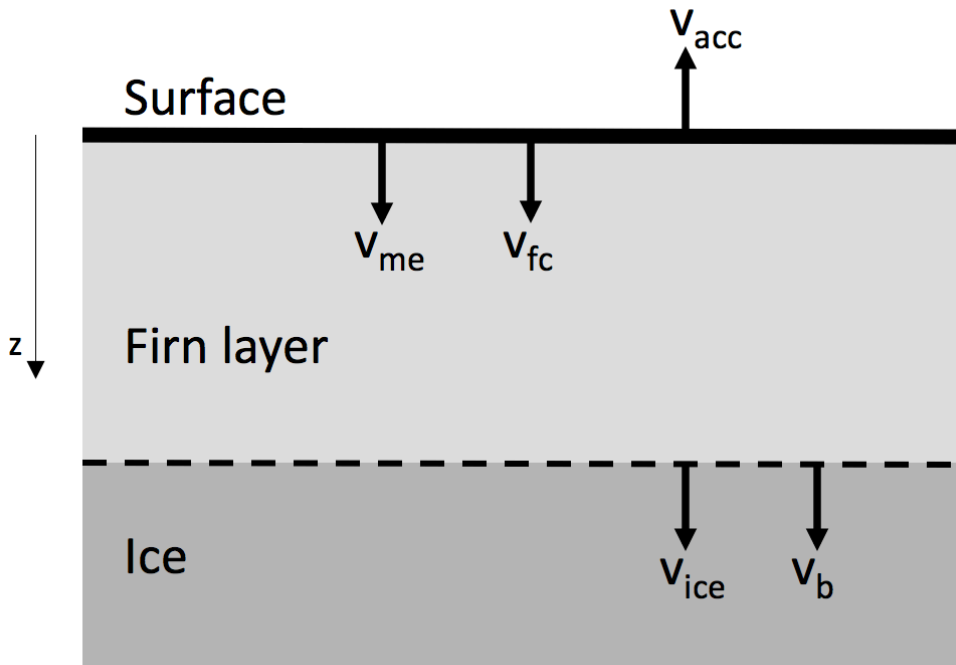


Figure 2.1: Schematic representation of the firn layer (including surface snow) and the velocity components contributing to surface elevation changes: accumulation (v_{acc}), melt (v_{me}), firn compaction (v_{fc}), downward ice flow (v_{ice}) and bedrock movement (v_b), adjusted from Zwally and Li [2002].

Barnola *et al.* [1991], forced with regional atmospheric climate model output from Van de Berg *et al.* [2006], is in good agreement with observations from firn cores. For the upper layers, this model uses the semi-empirical steady-state solution of Herron and Langway [1980], while for the lower part the equations of Pimienta and Duval [1987] are used. Recent expressions for time-dependent firn densification and depth are those of Helsen *et al.* [2008] and Arthern *et al.* [2010], which are both based on the model of Herron and Langway [1980]. The latter assumes that firn compaction has an Arrhenius-type temperature sensitivity and was tuned to fit steady-state density profiles from Greenland and Antarctica. A different temperature sensitivity was added by Zwally and Li [2002], which was later modified by Helsen *et al.* [2008] to make it suitable for Antarctica. None of these models included snowmelt and refreezing, while it is well known that the higher density of refrozen meltwater can have a significant effect on the density of the firn column and its densification rate.

In this paper we present a firn densification model (FDM) that calculates steady-state as well as time-dependent firn density profiles for Antarctica. The advantage of this model is that it uses the same densification expression for both purposes, tuned to optimally fit observations.

Also snowmelt and percolation, retention and refreezing of meltwater is implemented. In Section 2.2, we describe the model and its forcing. In Section 2.3, two applications are presented; first, we present an update of the characteristics and spatial variability of the steady-state Antarctic firn layer. Next, we present time series of surface height changes at various locations across Antarctica. For both applications, the FDM is forced with output of the regional atmospheric climate model RACMO2 [Lenaerts *et al.*, 2012a].

2.2 Methods

2.2.1 Atmospheric forcing

The FDM is forced at the surface by the surface mass balance, surface temperature and near-surface wind speed from the regional atmospheric climate model RACMO2. Model data is available for the period 1979–2009 at a temporal resolution of 6 h and a horizontal resolution of 27 km. RACMO2 is forced at the lateral boundaries with ERA-Interim re-analysis data, which also provides the sea ice cover and sea surface temperatures. The average annual accumulation, as used in this paper, is the sum of solid and liquid precipitation minus sublimation. The climate and surface mass balance of RACMO2 has been validated by *Kuipers Munneke et al.* [2011], *Lenaerts et al.* [2012c] and *Lenaerts and Van den Broeke* [2012] and is shown to provide a good representation of the Antarctic near-surface climate.

2.2.2 Firn densification model

Our FDM is a time-dependent one-dimensional model that keeps track of the density and temperature in a vertical firn column. New added surface snow is instantly treated as the upper layer of the vertical firn column. The fresh snow density for each grid point is determined by a parameterization of *Kaspers et al.* [2004], based on average annual accumulation (\bar{b} in mm w.e. yr⁻¹), 10 m wind speed (\bar{V}_{10} in m s⁻¹) and surface temperature (\bar{T}_s in K), with a slope correction for Antarctica by *Helsen et al.* [2008]:

$$\rho_s = -151.94 + 1.4266(73.6 + 1.06 \bar{T}_s + 0.0669 \bar{b} + 4.77 \bar{V}_{10}) \quad (2.2)$$

The previous time-dependent model version [*Helsen et al.*, 2008] did not consider processes associated with liquid water: rain, snowmelt, percolation and refreezing. In the new model, these processes are implemented by allowing liquid water from rain and/or snowmelt, as prescribed by RACMO2 output, to exist in – and move through – the firn column. The amount of snowmelt is removed from the top layer, and percolates down into the firn column. It refreezes when it reaches a firn layer with sufficient cold content ($T < 0$ °C) and pore space. To mimic capillary forces, a part of the liquid water remains in a layer that is at 0 °C. The

maximum amount of pore space used to store liquid water (W_{mi} in %) is taken as a function of the snow porosity P [Coléou and Lesaffre, 1998]:

$$W_{mi} = 1.7 + 5.7 \left(\frac{P}{1-P} \right) \quad (2.3)$$

Typical values for W_{mi} are 9–13 % close to the surface ($\rho = 300\text{--}400 \text{ kg m}^{-3}$) and 4 % lower in the firn column ($\rho \cong 650 \text{ kg m}^{-3}$). This retained water refreezes when the layer cools. By allowing water and therefore mass and heat to move through the firn column, the heat transport cannot be solved using an implicit numerical scheme, as in *Helsen et al.* [2008], but has to be solved explicitly, making the model computationally more expensive. The subsurface heat transport is simulated by using a one-dimensional time-dependent heat-transfer model [Paterson, 1994]:

$$\frac{\delta T}{\delta t} = k \frac{\delta^2 T}{\delta z^2} \quad (2.4)$$

where k is the thermal diffusivity. This heat-transfer equation only contains a heat conduction term, where formally also heat advection and internal heating by deformation of ice should be included. However, the latter is small in the firn zone and therefore neglected, heat advection is implicitly taken into account by the downward motion of the firn layers at the speed of v_{ice} [Helsen et al., 2008].

The initial density profile of the time-dependent simulation is obtained by spinning up the model as long as needed to refresh the entire firn layer. As the average annual accumulation and depth of the firn layer vary widely in space, the spin-up period is determined uniquely for every grid point. To obtain the input for the spin-up period, the 1979–2009 period is repeated into a time series long enough to refresh the entire firn layer. Hence, we assume this 31-year period is representative for the past 100–1000 years and the firn layer to be in steady state.

The previous model version used a densification expression adapted from *Zwally and Li* [2002], with a single densification expression for the complete density range. Various studies [Herron and Langway, 1980; Barnola et al., 1991] suggest one ($\rho \cong 550 \text{ kg m}^{-3}$) or even two ($\rho \cong 550 \text{ kg m}^{-3}$ and $\rho \cong 830 \text{ kg m}^{-3}$) critical values to separate different densification processes that occur in the firn column. In the upper part ($\rho \leq 550 \text{ kg m}^{-3}$), the dominant densification processes are grain settling and packing of snow grains [Herron and Langway, 1980]. Thereafter, densification is slower and mainly due to sublimation, diffusion and deformation processes until the density reaches the pore close-off depth ($\rho \cong 830 \text{ kg m}^{-3}$), where the remaining air bubbles get trapped in the ice. Further densification takes place by compression of these bubbles, until the density of glacier ice ($\rho \cong 917 \text{ kg m}^{-3}$) is reached. Obviously, outside the dry snow zone refreezing of meltwater and/or liquid precipitation also cause firn to densify.

Our FDM uses the dry snow densification expression proposed by *Arthern et al.* [2010] (Ar10 from now on) (Equation 2.5). Ar10 use different densification expressions above and below

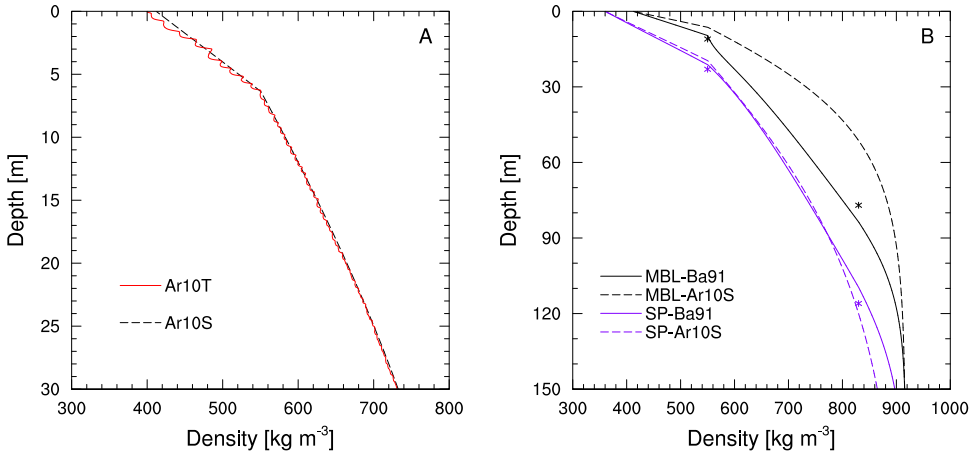


Figure 2.2: Firm density profiles of the steady-state Ar10S and time-dependent Ar10T densification expressions for a location in Marie Byrd Land (**A**) and steady-state density profiles of Ar10S and Ba91, with the observed z_{550} and z_{830} (**B**) for South Pole (purple) and the MBL location as in Figure A (black). Climatic characteristics of both points are listed in Table 2.1.

the critical density value ($\rho = 550 \text{ kg m}^{-3}$) and therefore are better able to capture the faster densification near the surface.

$$\text{Ar10T: } \frac{d\rho}{dt} = C \dot{b} g (\rho_i - \rho) e^{\left(\frac{-E_c}{RT_s} + \frac{E_g}{RT_s}\right)} \quad (2.5)$$

where E_c , E_g and C are constants, \dot{b} is the average annual accumulation, g the gravitational acceleration, ρ_i the ice density (917 kg m^{-3}) and R the gas constant and “T” in Ar10T refers to the time-dependent model version. Note that C has different values above (0.03) and below (0.07) the critical density level $\rho = 550 \text{ kg m}^{-3}$. To convert Ar10T to a steady-state solution (Ar10S), the vertical displacement of a firm layer has to equal the average annual accumulation rate divided by the ice density. Also the local temperature (T_s) in the exponential term is replaced by the annual average surface temperature (\bar{T}_s):

$$\text{Ar10S: } \frac{d\rho}{dz} = C dz \rho g (\rho_i - \rho) e^{\left(\frac{-E_c}{RT_s} + \frac{E_g}{RT_s}\right)} \quad (2.6)$$

where dz is the thickness of a firm layer in metres. Figure 2.2a compares firm density profiles from Equations 2.5 and 2.6 for a point in Marie Byrd Land (MBL), for which the climate characteristics are listed in Table 2.1. The oscillations in Ar10T are related to the strong non-linear dependence of densification rate on temperature. This effect is only present in the top few meters of the firm column, where the seasonal temperature cycle is significant. To compensate for this systematic bias and to enable a comparison with other steady-state

models, an offset is applied to the surface density in the steady-state model, so that the critical $\rho = 550 \text{ kg m}^{-3}$ level occurs at the same depth in both solutions.

2.2.3 Model performance and tuning

We compared the modeled depths of the critical density values $\rho = 550 \text{ kg m}^{-3}$ (z_{550}) and $\rho = 830 \text{ kg m}^{-3}$ (z_{830}) with observations from 48 ice core drilling sites in Antarctica (Figure 2.3) [Van den Broeke, 2008]. We also compare the results of the steady-state model to Van den Broeke [2008], who used the steady-state expressions of Barnola *et al.* [1991]:

$$\text{Ba91} : \begin{cases} \frac{d\rho}{dz} = 11 dz \rho (\rho_i - \rho) e^{\frac{-E}{RT_s}} & \text{for } \rho < 550 \text{ kg m}^{-3} \\ \frac{d\rho}{dz} = A_0 dz \rho^{\frac{t_{\text{yr}}}{b}} f_e(\rho) \Delta P^3 e^{\frac{-E}{RT_s}} & \text{for } \rho > 550 \text{ kg m}^{-3} \end{cases} \quad (2.7)$$

where E and A_0 are constants, t_{yr} is the number of seconds in a year and ΔP the overburden pressure. Figure 2.2b compares the density profiles of Equations 2.6 and 2.7 with the observed z_{550} and z_{830} at South Pole and MBL (climate characteristics are listed in Table 2.1). Although the densification expressions are quite different, the results for South Pole are similar and both correspond rather well with the observed depths. For the MBL point, Ba91 again shows good agreement with the observed depths, while Ar10S densifies too quickly and simulates too shallow critical depths. Around 15 m in the Ba91 simulation a numerical artifact is visible, caused by the overburden pressure ΔP in Equation 2.7. The densification rate is underestimated at these low depths since there is not enough overburden pressure in the above layers. However, Ba91 simulates the depths of the critical levels quite well.

Figure 2.4 compares observed and modeled z_{550} and z_{830} for all 48 observation locations. In order to isolate z_{830} from processes above z_{550} , we used $z_{830}^* = z_{830} - z_{550}$. Almost everywhere, Ar10S causes the firn to densify too quickly in the upper part of the firn column and therefore under-predicts z_{550} . The same pattern is observed for the points with a relatively small z_{830} , with deviations up to 50%. However, for points with larger z_{830} the pattern is reversed. The Ba91 results are very similar to those of Van den Broeke [2008], in which a previous RACMO2 dataset [Van de Berg *et al.*, 2006] was used.

Table 2.1: RACMO2 climate characteristics of a point in Marie Byrd Land (MBL) and South Pole (SP): latitude, longitude, height above sea level, average annual temperature, accumulation, 10 m wind speed and melt over the 1979–2009 period.

	Lat ($^{\circ}\text{N}$)	Lon ($^{\circ}\text{E}$)	h_s (m)	\bar{T}_s (K)	\bar{b} (mm yr $^{-1}$)	\bar{V}_{10} (m s $^{-1}$)	\bar{M} (mm yr $^{-1}$)
MBL	-79.6	-105.0	1912	241.0	306.0	6.64	0.0
SP	-90.0	0.0	2797	220.3	56.0	5.55	0.0

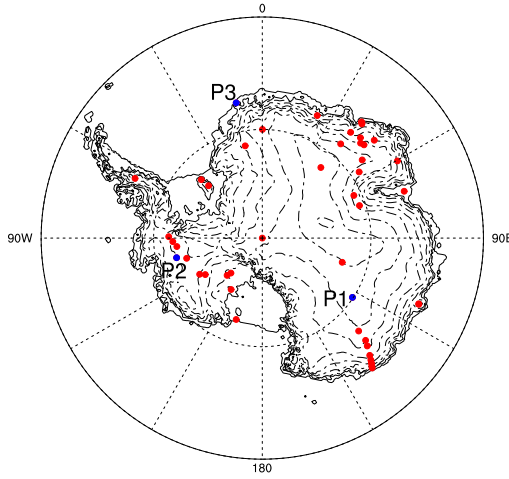


Figure 2.3: Locations of 48 firn cores used in the model comparison in Section 2.2 (red and blue) and the locations of P1, P2 and P3, used in the analysis in Section 2.3.2 (blue).

The ratio of modeled to observed depths (MO) in Ar10S is found to be highly correlated with average annual accumulation at the 48 core sites, both for z_{550} and z_{830} (Figure 2.5). The correlation is such that the effect of the average annual accumulation \dot{b} on the densification rate is too large. This also explains the agreement of Ar10S with observations in Figure 2.2b at South Pole, where low average annual accumulation leads to a MO-ratio close to 1. The higher average annual accumulation at MBL in Figure 2.2b on the other hand, leads to a MO-ratio < 1 and thereby shows an overestimated densification rate in Ar10S. Previously, *Herron and Langway* [1980] proposed the exponent α in \dot{b}^α to be chosen between 0.5 and 1.1. However, *Zwally and Li* [2002] and *Helsen et al.* [2008] later assumed $\alpha = 1$. To introduce the correct accumulation dependence, we multiply the densification expressions of Ar10S with the relations of the regressions in Figure 2.5, being:

$$\text{MO}_{550} = 1.435 - 0.151 \ln(\dot{b}) \quad \text{for } \rho < 550 \text{ kg m}^{-3} \quad (2.8)$$

$$\text{MO}_{830} = 2.366 - 0.293 \ln(\dot{b}) \quad \text{for } \rho > 550 \text{ kg m}^{-3} \quad (2.9)$$

For extreme average annual accumulation values ($\dot{b} > 3213 \text{ mm yr}^{-1}$), MO_{830} becomes negative, which occurs on a few points in the Antarctic Peninsula. $\text{MO}_{550} = 0$ is not reached for realistic values of \dot{b} . We impose a minimum value of 0.25 on MO_{550} and MO_{830} , corresponding roughly to areas where the average annual accumulation exceeds 1400 mm yr^{-1} . Figure 2.6 compares the observed to the updated model values of z_{550} and z_{830} . For both critical depths, the agreement of the steady-state FDM with the observations is now comparable to Ba91, but the great advantage of the new expression is that it can also be used in a time-dependent fashion.

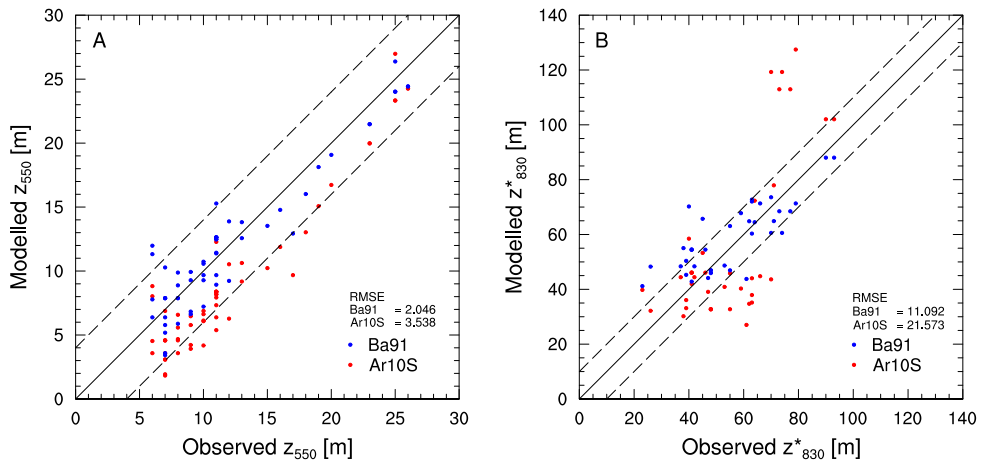


Figure 2.4: Modelled vs observed depth of the $\rho = 550 \text{ kg m}^{-3}$ (A) and $\rho = 830 \text{ kg m}^{-3}$ (B) levels, for the densification expressions of Ar10S and Ba91.

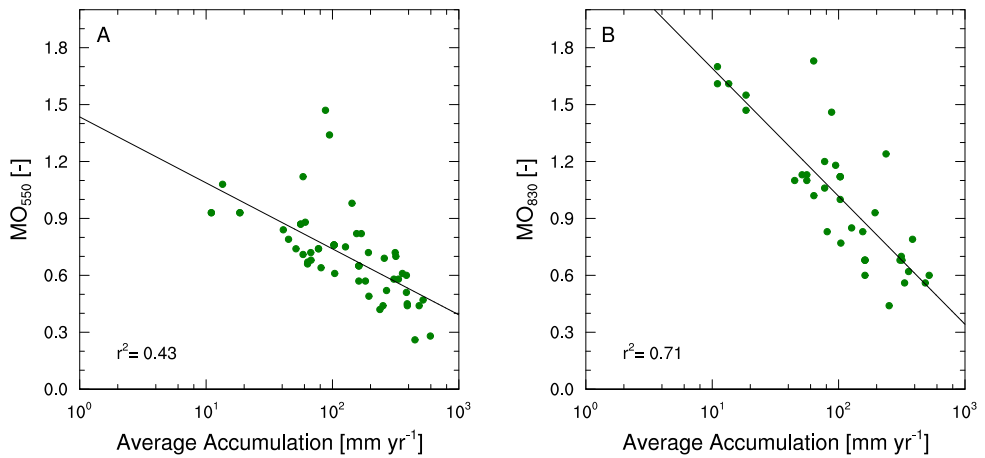


Figure 2.5: MO-ratio of Ar10S for z_{550} (A) and z_{830}^* (B) vs. the average annual accumulation, the regression line equations are listed in Equations 2.8 and 2.9.

2.3 Applications

2.3.1 Steady-state Antarctic firn density profiles

The steady-state expression forced by average RACMO2 climate fields of average annual accumulation, surface temperature and wind speed, enables us to look at the spatial variability of the characteristics of the Antarctic firn column (Figures 2.7 and 2.8). Since the resolution of RACMO2 output has increased from 55 to 27 km, we see much more detail than in *Van den Broeke* [2008]. The modeled density of the surface snow is shown in Figure 2.7a and shows a typical distribution of relatively low density surface snow in the East Antarctic interior ($300\text{--}340\text{ kg m}^{-3}$), and high densities along the ice sheet margin ($420\text{--}460\text{ kg m}^{-3}$), where temperature, precipitation and wind speeds are high. The two large ice shelves have a slightly lower surface density than other coastal regions because, in absence of orographic forcing, the average annual accumulation is relatively small. Along the West Antarctic coast and in the Antarctic Peninsula, the highest surface density values occur, forced by a combination of high temperatures, wind speeds and precipitation rates.

The points without values in Figs. 2.7 and 2.8 are regions where, according to RACMO2, no stable firn layer can exist as average annual accumulation (1979–2009) is exceeded by either sublimation or melt. The location of these so-called blue ice areas correspond reasonably well to the areas presented in *Winther et al.* [2001]. Wind-induced blue ice areas occur in the vicinity of the Lambert Glacier and along the eastern border of the Transantarctic Mountains. On Larsen C Ice Shelf, snowmelt exceeds precipitation in RACMO2, so no long-term firn layer can build up. As Larsen C is currently covered by a significant layer of firn [*Holland*

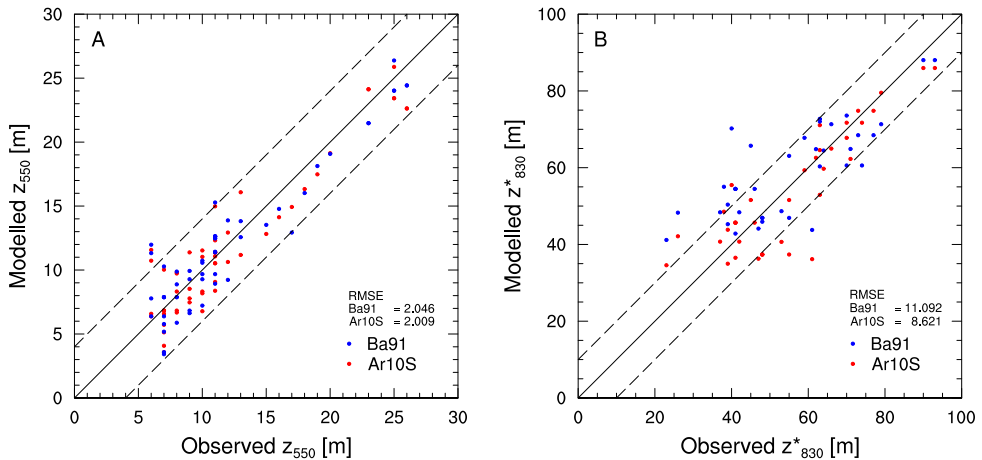


Figure 2.6: Modelled vs observed depth of the $\rho = 550\text{ kg m}^{-3}$ (A) and $\rho = 830\text{ kg m}^{-3}$ (B) levels, for the updated densification expressions of Ar10S and Ba91.

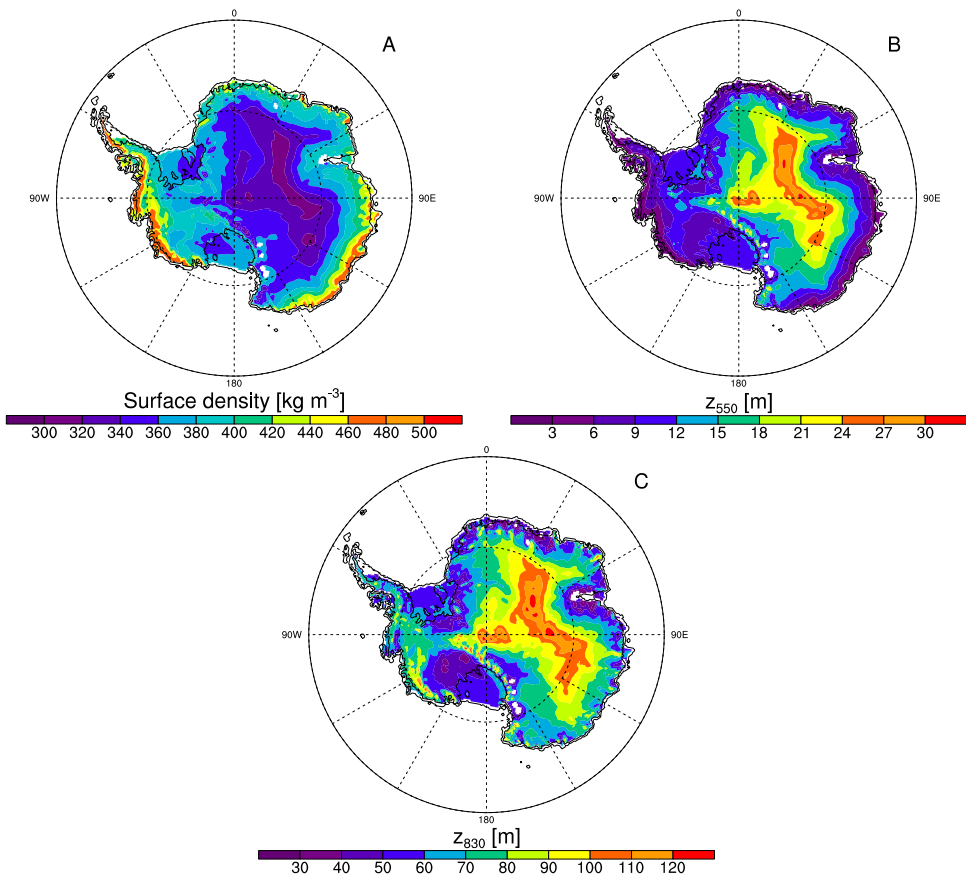


Figure 2.7: Modelled surface density (A) and depths of the critical density levels $\rho = 550 \text{ kg m}^{-3}$ (B) and $\rho = 830 \text{ kg m}^{-3}$ (C).

et al., 2011], it is likely that the present firn layer was formed before the recent warming of the Antarctic Peninsula [Vaughan *et al.*, 2003] and is now slowly degrading.

Figures 2.7b-c show the spatial distribution of two critical depths in the firn column; z_{550} and z_{830} . These fields show roughly the inverse pattern of surface density. This is especially valid for z_{550} as the surface density (ranging from 300 kg m^{-3} to 450 kg m^{-3}) determines the start of the density-depth profile. The highest values of z_{550} and z_{830} are found in the interior of East Antarctica with smaller values in the coastal regions. In West Antarctica and the Antarctic Peninsula the pattern is somewhat different; while z_{550} is small, z_{830} shows relatively high values. This is caused by the high average annual accumulation values in these regions; the fast burial of fresh snow leads to a slow densification with depth. The thickness of the firn column in Antarctica, taken as z_{830} , is only 40–50 m around and on the

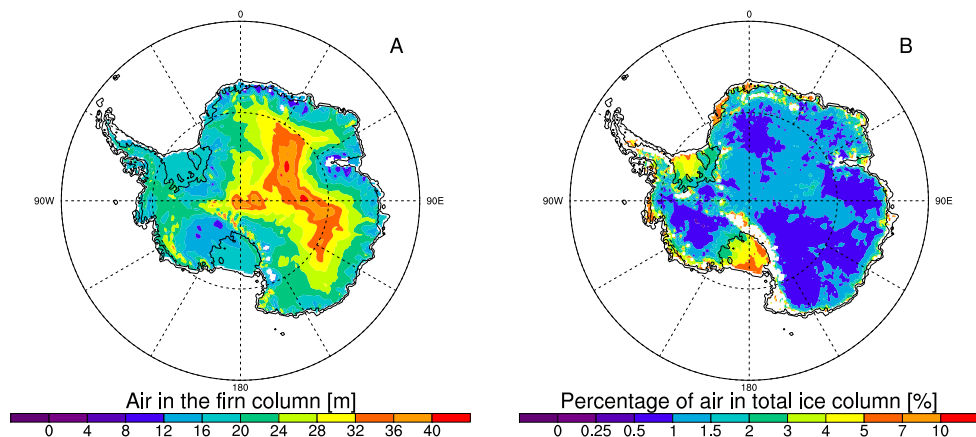


Figure 2.8: The modeled amount of air in the firn column, expressed as the firn correction in m (A) and as a fraction of the total thickness of the ice in % (B)

big ice shelves (Ross Ice Shelf, Filchner-Ronne Ice Shelf and the Amery Ice Shelf). Here, a combination of relatively high temperatures and relatively low precipitation amounts cause a rapid densification of firn with depth. The highest values are found on top of the East Antarctic plateau with values just reaching 120 m.

An important quantity is the amount of air in the firn column. The thickness change resulting from compressing the whole firn column until it has ice density gives the length of the firn air column. Figure 2.8a shows the spatial distribution of the length of this firn air column. It resembles the depth of the firn layer in Figure 2.7c, indicating that deeper firn columns generally contain more air than shallow columns. This is supported by the average density of the firn column, which shows little variability; values range between 650 kg m^{-3} on the East Antarctic plateau and 690 kg m^{-3} along the edges of the ice sheet (not shown). In other words, a deeper firn column is not necessarily denser, and will contain more air. On average there is 22.6 m air in the firn column (Fig 2.8a), but the modeled range of values is large (10–40 m) due to the previously mentioned climatic differences between the coastal regions and the interior. The average thickness of the Antarctic ice sheet is 2.06 km [Lythe *et al.*, 2001], so on average a correction of just over 1 % has to be applied to get the total mass of the ice sheet. However, ice thicknesses are smaller near the coast; here, the firn air correction can be significant, especially when it is used to derive ice thickness of floating glacier tongues, using surface elevation in combination with a flotation criterium [Van den Broeke *et al.*, 2008; Rignot *et al.*, 2008]. Figure 2.8b expresses the air thickness as a percentage of the total ice column. On the ice shelves and in coastal and mountainous areas, values of 7–9 % are found. White areas indicate ice thicknesses [Lythe *et al.*, 2001] that are shallower than the modeled firn-ice transition depths.

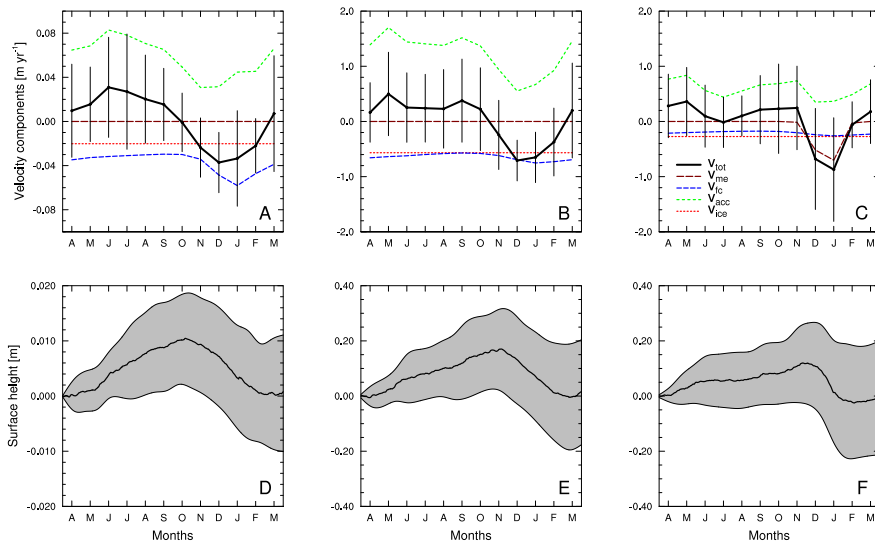


Figure 2.9: The monthly averaged (1979–2009) velocity components that determine the vertical displacement of the surface: v_{acc} , v_{me} , v_{fc} , v_{ice} and v_{tot} (**A**, **B**, **C**) and the daily averaged (1979–2009) surface height and standard deviation (**D**, **E**, **F**) for P1, P2 and P3 (see Figure 2.3). Note the different scales.

2.3.2 Time-dependent firn density and surface elevation

The new densification expressions can also be used in the time-dependent FDM. By forcing the time-dependent FDM with climate model time series, we obtain the evolution of the surface height with time and are able to study the individual processes that contribute to the vertical movement of the surface. Figures 2.9a–c show the seasonal cycle of the surface velocity components and Figures 2.9d–f the resulting surface elevation evolution, i.e. the integrated signal of v_{tot} in Figures 2.9a–c, for three locations on the AIS (Figure 2.3): P1 is located in the cold and dry East Antarctic interior, P2 is in wetter and warmer West Antarctica and P3 in coastal Dronning Maud Land where melt occurs annually. The climate characteristics of these points are shown in Table 2.2.

Table 2.2: RACMO2 climate characteristics of points P1, P2 and P3: latitude, longitude, height above sea level, average annual temperature, accumulation, 10 m wind speed and melt over the 1979–2009 period.

	Lat (°N)	Lon (°E)	h_s (m)	\bar{T}_s (K)	\bar{b} (mm yr ⁻¹)	\bar{V}_{10} (m s ⁻¹)	\bar{M} (mm yr ⁻¹)
P1	-75.1	123.4	3262	218.0	18.5	5.14	0.0
P2	-77.8	-102.9	1392	245.6	520.4	7.14	0.0
P3	-71.1	-10.9	40	255.7	251.0	8.26	53.2

The average seasonal cycle is similar for the three locations, with upward motion of the surface (positive v_{tot}) in autumn, winter and spring and a relatively strong downward motion (negative v_{tot}) in summer. At all three locations, v_{ice} is constant throughout the year, as it is assumed proportional to the average annual accumulation. At P1 and P2, no melt occurs ($v_{\text{melt}} = 0$), hence the seasonal variations are determined by accumulation and firn densification. The strong non-linear temperature dependence of the latter causes a densification peak in summer. In combination with a summer minimum in v_{acc} , this causes the summer lowering of the surface. The contribution of firn densification to the vertical movement of the surface is relatively constant from year to year, as only the upper few meters of the firn layer experience significant annual temperature changes. So, at P1 and P2, the variations in v_{total} are mainly caused by variability in snowfall.

At P3, melt mainly occurs in December and January, which lowers the surface significantly. In combination with the variability in accumulation, this leads to a relatively large inter-annual variability for the summer months. Interestingly, the contribution to surface lowering by firn densification is almost three times smaller at P3 than at P2. One reason is the presence of refrozen meltwater in the firn column at P3, which causes higher average firn densities and therefore limits the potential total firn densification. Also, the firn layer at P2 is much deeper than at P3, due to the higher average annual accumulation amounts.

Figure 2.10 shows the surface height evolution for the entire 31-year period (1979–2009) at P2 and P3. The evolution of the surface height in P1 shows small inter-annual variability and is therefore not included. For P2 and P3, the inter-annual variability as discussed above is

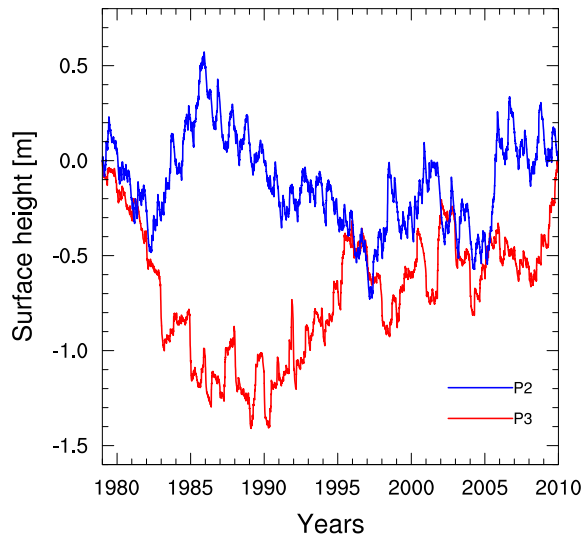


Figure 2.10: Surface height evolution (1979–2009) for P2 and P3 (see Figure 2.3).

visible as decadal trends. At P2, inter-annual variability is almost completely caused by accumulation variability where wetter (e.g. 2005–2006) and dryer (e.g. 1988–1991) than average periods cause upward or downward trends in surface height. An interesting asymmetry is visible: the lowering at P2 is more gentle than in P3, as firn densification is a slow, but steady process compared to melt. At P3, the more rapid lowering of the surface is often caused by strong melt seasons in combination with less than average precipitation (e.g. 1981–1983), while upward motions are associated with wetter periods in combination with a weak melt season (e.g. 2008–2009).

2.4 Conclusion

After introducing an accumulation dependence into the Ar10 densification expression, good agreement is found with 48 steady-state firn profiles from the Antarctic ice sheet. The steady-state version of the new densification expression produces results comparable to the steady-state solution of *Barnola et al.* [1991]. A great advantage of the updated expression is that it can also be used in time-dependent mode. Moreover, by introducing liquid water into the model, it can now be applied to the entire Antarctic ice sheet including its floating ice shelves, as long as the surface mass balance is positive and a firn layer can build up.

Several improvements to the model can be made. The accumulation dependence that has been introduced in the densification expression of *Arthern et al.* [2010] is tuned and validated with the same dataset of 48 Antarctic firn cores. Ideally, a part of the dataset should be used for tuning and another part for validation. However, the Antarctic climate is very diverse and some climate zones are only represented by a few points, so splitting the dataset of only 48 firn cores is no option at present. The time-dependent model can at present not be validated with observations, as long-term reliable surface height measurements at high temporal resolution are scarce. Satellite height measurements do not have the right time resolution and are often very noisy, while in-situ observations typically span less than a year. Moreover, to perform a thorough comparison with in-situ observations, the height measuring instrument should be fixed at a reference level outside the firn layer, which is virtually impossible.

This is also the reason for choosing to improve a semi-empirical model instead of using a more physically-based firn densification model. The physics of firn densification are still not fully understood and mainly observed in laboratories. This explains our choice for an empirical model that describes firn densification in relation to temperature and accumulation.

The fresh snow density parameterization of *Kaspers et al.* [2004] is now used in both the steady state and the time-dependent firn densification model. As the density of fresh snow is most likely not constant in time, this could be a point of improvement in future research of the time-dependent model. However, almost no observations on Antarctic fresh snow density are available: most observations are averaged over the first 0.5–1 m.

In steady-state mode, the FDM is used to assess the spatially variable characteristics of the Antarctic firn layer. On the cold and dry East Antarctic plateau, the lowest surface snow density and deepest firn-ice transitions are found. Moving towards the coastal areas the climate gets warmer, wetter and windier, causing the surface density to increase and the firn layer depth to decrease. Some regions do not obey this general pattern, e.g. the coast of West Antarctica shows high surface densities and small values of the depth of the $\rho = 550 \text{ kg m}^{-3}$ level (z_{550}), but deep firn-ice transition depths (z_{830}), reaching 120 m. The high average annual accumulation rate induces a fast burial of firn, which leads to small gradients in firn density with depth. The same effect occurs along the Antarctic mountain ranges, but is less evident and only present in some isolated spots.

Steady-state profiles can be used to quantify the amount of air in the firn column, a quantity needed to convert ice thickness to total ice mass. The firn correction averaged over the entire ice sheet is small (1 %), but along mountain ranges and especially on ice shelves, the values go up to 9 %. This constitutes a significant correction for ice flux calculations at the grounding line [e.g. *Rignot et al.*, 2008]. The spatial variability of firn layer characteristics resembles that presented by *Van den Broeke* [2008], but with much improved horizontal resolution.

The effect of melt is not included in the steady-state profiles: if melt occurs, meltwater re-freezes deeper in the firn column resulting in layers with higher density and/or complete ice lenses. In a steady-state profile these features cannot be modeled, as they move to greater depths with time. On average, the density will be higher due to this refrozen water. As heat is released upon refreezing, the local firn temperature will increase, further accelerating the densification. On the other hand, ice layers lead to a higher average density, which in turn decreases the potential densification rate.

The time-dependent version of the FDM is used to study the evolution of the surface height and firn density in time and depth. It shows that within three different climatic zones in Antarctica, the surface elevation has a clear annual cycle with upward motion in austral autumn, winter and spring due to accumulation and relatively slow firn compaction, and a lowering in summer when accumulation is lower and firn densification is more rapid in response to higher temperatures. If melt is present, the lowering of the surface in summer is even more pronounced. In the interior of Antarctica, the year-to-year surface elevation variability is almost completely caused by the variability in accumulation, while in melt areas the strength of the melt season is also important. Firn densification rate shows less year-to-year variability.

'Breathing' of the Antarctic ice sheet

Summary

One way to estimate the mass balance of an ice sheet is to convert satellite observed surface elevation changes into mass changes. In order to do so, elevation and mass changes due to firn processes must be taken into account. Here, we use a firn densification model to simulate seasonal variations in depth and mass of the Antarctic firn layer, and assess their influence on surface elevation. Forced by the seasonal cycle in temperature and accumulation, a clear seasonal cycle in average firn depth of the Antarctic ice sheet (AIS) is found with an amplitude of 0.026 m, representing a volume oscillation of 340 km³. The phase of this oscillation is rather constant across the AIS: the ice sheet volume increases in austral autumn, winter and spring and quickly decreases in austral summer. Seasonal accumulation differences are the major driver of this annual 'breathing', with temperature fluctuations playing a secondary role. The modeled seasonal elevation signal explains ~31 % of the seasonal elevation signal derived from ENVISAT radar altimetry, with both signals having similar phase.

This chapter is published as: Ligtenberg S. R. M., M. Horwath, M. R. van den Broeke, and B. Legrésy (2012), Quantifying the seasonal 'breathing' of the Antarctic ice sheet. *Geophysical Research Letters*, **39**, L23501, doi:10.1029/2012GL053628.

3.1 Introduction

The Antarctic ice sheet (AIS) is the largest reservoir of frozen water on Earth, containing the equivalent ice volume of 57 m global sea level rise [Lythe *et al.*, 2001]. With an annual mass turnover of ~ 2500 Gt [Lenaerts *et al.*, 2012a], even a relatively small change in the mass balance of the AIS has a significant effect on global sea level [IPCC, 2007; Van den Broeke *et al.*, 2011]. Estimating the mass balance of the AIS is difficult, because of its size, remoteness and the fact that it has only been studied intensively during the last half century. Currently, three methods are used for estimating the mass balance of the AIS: i) the mass budget method [Rignot *et al.*, 2011a], ii) the gravimetry method [Velicogna, 2009] and iii) the volumetric method [Davis *et al.*, 2005]. In the latter method, remotely sensed surface elevation (volume) changes are converted into mass changes. This conversion requires a correction for depth and mass changes of the firn layer, the mantle of compressed snow that covers the AIS.

Neglecting basal melt, the vertical movement of the ice sheet surface (dH/dt) is forced by snow accumulation (v_{acc}), sublimation (included in v_{acc}), snowmelt (v_{me}), firn compaction (v_{fc}), ice flow beneath the firn layer (v_{ice}), and buoyancy effects on floating ice shelves (v_{by}) [Ligtenberg *et al.*, 2011]:

$$\frac{dH}{dt} = v_{acc} + v_{me} + v_{fc} + v_{ice} + v_{by} \quad (3.1)$$

Following the seasonal cycle in temperature and accumulation, that affects v_{acc} , v_{me} and v_{fc} , the firn layer covering the ice sheets of Antarctica and Greenland 'breathes', i.e. it expands in winter and contracts in summer. Although this phenomenon is often mentioned in literature [e.g. Thomas *et al.*, 2008; Lee *et al.*, 2012], it has not yet been robustly quantified. For the Greenland firn layer, Braithwaite *et al.* [1994] suggested seasonal oscillations in surface elevation of 0.1–0.2 m, while Zwally and Li [2002] observed (0.25 m) and modeled (0.18 m) similar seasonal variations at Summit, Greenland. The only Antarctic observation suggests seasonal variations up to 0.6 m based on radar satellite altimetry [Yi *et al.*, 1997]. All studies report surface elevation minima in mid- or late summer and maxima in late-winter. These regular oscillations in surface elevation can be important when deriving surface elevation trends from satellite altimetry, especially in the case of short time series over just a few years with sparse sub-annual sampling [Gunter *et al.*, 2009]. In this study we combine output of a regional atmospheric climate model at relatively high horizontal resolution (~ 27 km) with a firn densification model to quantify this effect for the AIS. We compare apparent volume changes inferred from ENVISAT satellite radar altimetry (RA) to modeled volume changes.

3.2 Methods

We use a 1D, time-dependent firn densification model (FDM) that calculates temperature, density and liquid water content in a vertical firn column with a typical layer thickness of 5 cm [Ligtenberg *et al.*, 2011]. At the surface, the FDM is forced by 6 hour cumulated surface mass balance components (snowfall, rain, sublimation and snowmelt) and 6 hour average surface temperature (T_s) and 10 m windspeed from a regional atmospheric climate model (RACMO2) at ~ 27 km horizontal resolution [Lenaerts *et al.*, 2012a]. To obtain initial vertical firn profiles a spin-up procedure is used: sufficient iterations of the 1979–2011 climate are used to build up a complete firn layer, before the final run is performed [Ligtenberg *et al.*, 2011]. This approach assumes a stable climate for the past 100–200 years, i.e. no significant long-term (centennial) trends in temperature or accumulation. The final FDM simulation covers the 1979–2011 period with a time step of 15 minutes and output is stored every 2 days. In this paper we present i) changes in monthly surface elevation, e.g. a dH/dt value for January represents the change in surface elevation between the 31st of December and the 31st of January and ii) the amplitude and phase of a sine function fitted to the seasonal surface elevation oscillations.

We compare FDM results to ENVISAT radar altimetry data for the period October 2002 through October 2010, derived from the along-track repeat satellite RA approach [Legrésy *et al.*, 2006]. This approach analyses time series of altimetric observations at every along-track position along the 35-day repeat orbit. The effect of non-exact repeat positions in conjunction with local topography is corrected empirically. Time variable relative contributions of surface and volume echos are corrected using the echo shape corrections [Legrésy *et al.*, 2006]. Horwath *et al.* [2012] showed that having time series of RA corrected from the echo shape time variations makes them qualitatively consistent to GRACE observations at interannual and longer terms. The polar gap (south of 81.5°S), steep terrain areas and floating ice shelves are excluded from the RA dataset.

3.3 Results

Figure 3.1 shows the modeled surface elevation evolution averaged over the AIS, including its floating ice shelves, for the period 1979–2011. The seasonal cycle explains 30 % of the total temporal variability, but significant inter-annual variability also exists. For instance, the surface of the AIS rose on average by ~ 7 cm between 1979 and 1989, and fell by ~ 5 cm in each of the periods 1994–2000 and 2006–2009. These inter-annual variations are mainly associated with snowfall variability, as was also shown by Davis *et al.* [2005], Helsen *et al.* [2008] and Horwath *et al.* [2012]. Part of these variations is also explained by the steady state assumption that is made in the FDM (see, Section 3.2 and Ligtenberg *et al.* [2011]), forcing the surface elevation to start and end at zero. Long-term accumulation variability could add up

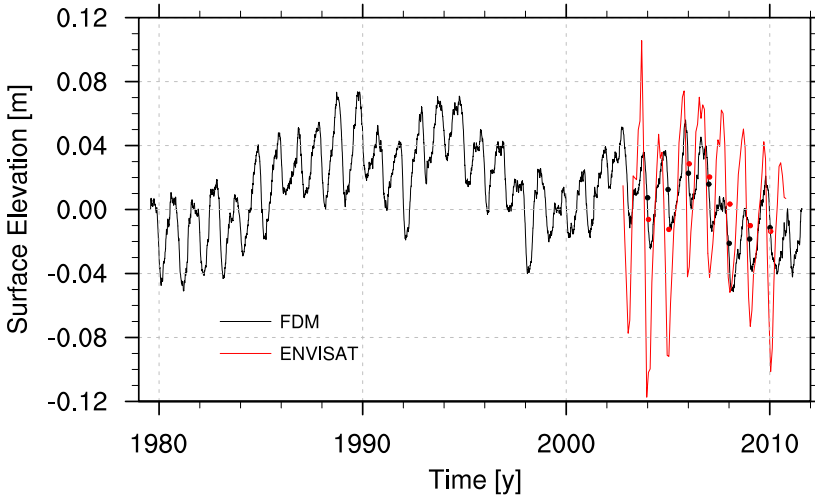


Figure 3.1: Ice sheet averaged surface elevation time series as simulated by the firn densification model (FDM, black) and as observed by the ENVISAT radar altimeter (ENVISAT, red). Dots indicate one-year surface elevation averages for the FDM (black) and ENVISAT (red). A 0.01 m surface elevation change is equal to a 131 km^3 (FDM) or 98 km^3 (RA) firn volume anomaly, because of the different areas of coverage (see Figure 3.4a-c).

to 8 % uncertainty in long-term surface elevation trends, while long-term snowmelt variability can increase the uncertainty by up to 30 % [Pritchard *et al.*, 2012].

In Figure 3.2, the average seasonal cycle of the surface elevation and its separate components from Equation 3.1 are shown. By definition, v_{ice} is constant throughout the year, and its magnitude equals the average annual accumulation rate divided by the ice density. The buoyancy effect (v_{by}) of the floating parts of the ice sheet, the coastal ice shelves, is small when averaged over the full AIS, and only locally important [Pritchard *et al.*, 2012]. Melting of snow (v_{me}) is only significant in summer and in the coastal regions of the AIS, where it forces a downward surface velocity mainly in December and January. Sublimation, which is incorporated in v_{acc} , has two components: surface sublimation, which peaks in summer, and drifting snow sublimation, which peaks in winter [Lenaerts and Van den Broeke, 2012]. However, the seasonal cycle in v_{acc} is dominated by the winter maximum in snowfall [Lenaerts *et al.*, 2012a]. Firn compaction (v_{fc}) shows only a relatively weak seasonal cycle, driven by enhanced compaction in summer and early winter, when the summer heat wave penetrates the firn pack. All processes combined result in a strongly negative dH/dt in December and January, when surface temperature, densification rate, snowmelt and surface sublimation peak. In combination with low accumulation this leads to rapid lowering of the surface. In autumn, winter and spring, the surface steadily rises under influence of enhanced winter snow accumulation and reduced densification rates, snowmelt and surface sublimation. In contrast to summer, there is no clear peak in winter surface rise.

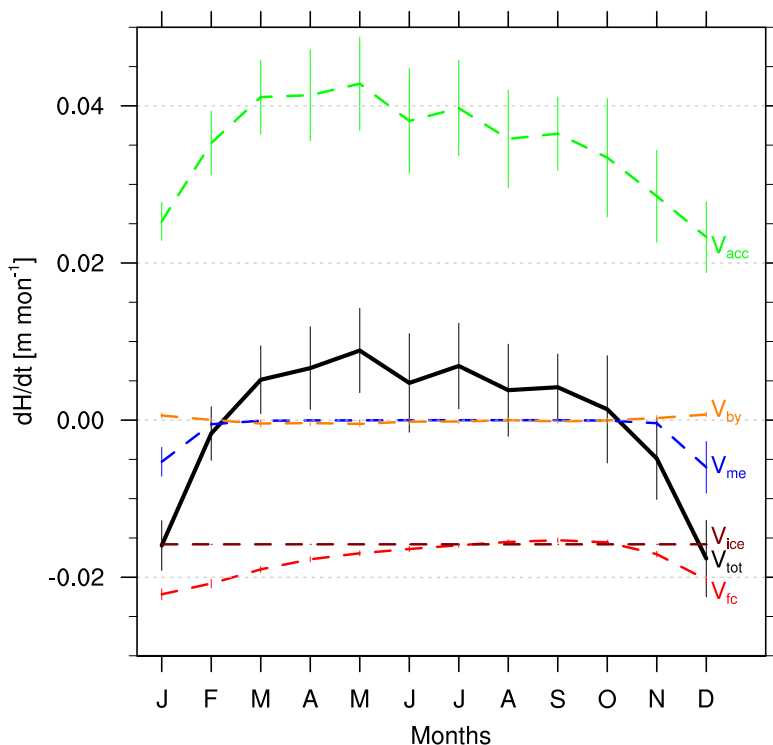


Figure 3.2: Monthly surface elevation changes (v_{tot} , black) and its components; accumulation (v_{acc} , green), firn compaction (v_{fc} , red), snowmelt (v_{me} , blue), vertical downward movement of ice (v_{ice} , brown) and buoyancy effects (v_{by} , orange) as simulated by the firn densification model.

Figure 3.3a-b shows that this seasonal cycle in surface elevation is spatially consistent across the AIS. In January, dH/dt is negative over most of the AIS. In winter, the signal is reversed and dH/dt is positive, however it is spatially less uniform (i.e. the areas with a reversed signal are more extensive) than the summer signal. The largest signals occur along the margins of the AIS, where temperature and accumulation rates are relatively high. A notable feature is the anomalous pattern along the Weddell Sea coast, i.e. the Antarctic Peninsula (AP) and Coats Land (78°S , 30°W). The driving force of this anomalous pattern is accumulation: for instance on the eastern AP, summer accumulation is three times higher than in winter, while on the western side it is the opposite. These accumulation characteristics are probably caused by the seasonally shifting direction of flow towards the mountain range of the AP.

The amplitude of the seasonal elevation oscillation is defined as half the peak-to-peak value of a sine function fitted to the seasonal cycle in surface elevation. The average over all local amplitudes of the AIS is 0.026 m, but spatially there are large differences (Figure 3.4a). Amplitudes of less than 0.005 m are found on the interior East Antarctic plateau, an area

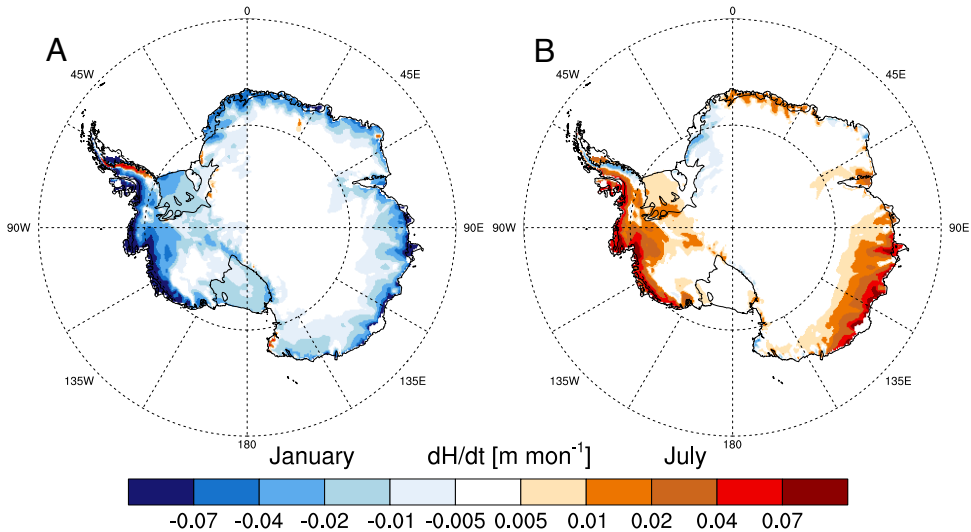


Figure 3.3: Spatial distribution of average monthly surface elevation changes (dH/dt) in summer (January, A) and winter (July, B).

with annual snowfall of 20–50 mm w.e. and very low T_s year round [Lenaerts *et al.*, 2012a]. Along the margins of the AIS, higher temperatures and accumulation rates result in larger surface elevation oscillations (0.1–0.3 m). The largest amplitude (0.35 m) is simulated just inland of Getz ice shelf (75°S, 130°W) in West Antarctica. The FDM cannot be applied to ablation regions where sublimation and/or snowmelt exceed accumulation, i.e. where a firn layer cannot develop (white areas in Figure 3.4a).

Figure 3.4b shows the phase of the elevation maximum, which generally occurs in late winter, spring or even early summer depending on the timing of the maximum in accumulation. Along the Weddell Sea coast, the anomalous pattern again emerges, with an elevation maximum in late summer.

Summed over the AIS, the average seasonal amplitude translates to a seasonal volume change of 340 km³. If we account for the air-ice ratio in near-surface firn this equals the ~ 100 Gt average seasonal mass change as reported by Lenaerts *et al.* [2012a], which corresponds to ~ 0.3 mm of global sea level equivalent and 4% of the total seasonal variation in ocean mass (6.8–8.5 mm) [Chambers *et al.*, 2004; Willis *et al.*, 2008].

Few observations exist to verify the modeled seasonal oscillations. At Summit, Greenland, surface elevation oscillations of 0.125 m have been measured [Zwally and Li, 2002], which compares well with values found in Antarctic regions with similar climate conditions (~ 250 mm w.e. annual accumulation, $\bar{T}_s \cong 244$ K and no snowmelt), such as coastal West-Antarctica.

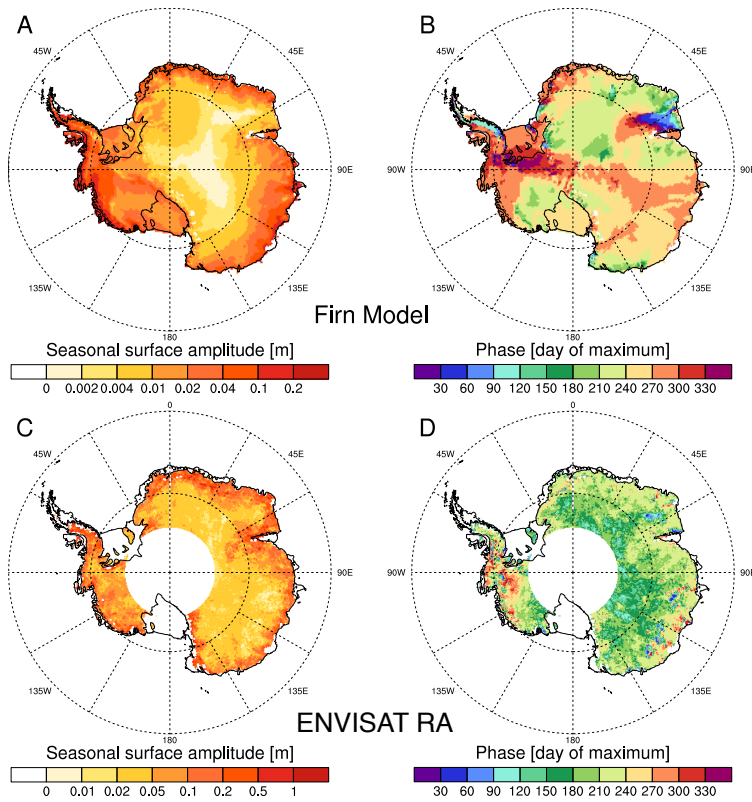


Figure 3.4: Average amplitude (A and C, note the different scale) and timing of phase maximum (B and D) of the seasonal surface elevation oscillation, from the firn densification model (1979–2011, A-B) and observed by ENVISAT radar altimetry (2002–2010, C-D). In A and B, white areas indicate locations where no firn layer is simulated, i.e. regions where annual snowmelt and/or sublimation are larger than accumulation. In C and D, white areas indicate regions where no observations are available (e.g. the polar gap south of 81.5°S and regions with steep terrain), or where observations are excluded from the analysis (e.g. ice shelves).

Time series of volume changes derived from ENVISAT RA over its region of coverage (red line in Figure 3.1; see Figure 3.4 for region of coverage) also show seasonal variations in surface elevation over the AIS. The seasonal amplitude from RA is considerably larger than the respective amplitude from FDM. The spatial distribution of the amplitude of RA and the FDM qualitatively agree (Figure 3.4a-c, note the different scale), with the lowest values in the East Antarctic interior and higher values along the margins. The average of the local seasonal amplitudes from the FDM, taken over the overlapping area, (0.029 m) represents 31 % of the RA amplitude (0.093 m). While the seasonal variations in the RA time series are significantly larger than those simulated by the FDM, the phase is similar. The phase

maximum in both methods occurs in the same season, although the RA surface elevation maximum is reached in late winter for most locations, which is on average 1–2 months earlier than in the FDM (Figure 3.4b,d and Figure 3.1). Interannual variations in both methods also show some similarities with a peak in surface elevation around 2006 and lowering thereafter (dots in Figure 3.1).

3.4 Discussion

When comparing results of FDM and RA on the seasonal time scale, we consider their differences as an upper bound on errors of either approach. In fact, there is no evident alternative method to assess RA or FDM seasonal errors on a regional or ice sheet scale, and no prior quantification of those errors. However, it is likely that most of the RA-FDM differences can be assigned to remaining systematic RA errors. An exaggeration of RA amplitudes is obvious in regions where RA amplitudes are on the order of, or larger than, the amount of annual snow accumulation. This is the case, for example, in Victoria Land (west of the Ross Ice Shelf) and around Lambert Glacier (74 °S, 65 °E) where RA amplitudes (Figure 3.4c) are significantly larger than the RACMO2 simulated accumulation [Lenaerts *et al.*, 2012a].

One crucial error source are time-variable relative contributions of surface and volume echos affecting the re-tracked heights [Legrésy and Rémy, 1998; Arthern *et al.*, 2001]. As mentioned in Section 3.2, here, we use the linear relation between the radar echo shape parameters and the re-tracked height, proposed by Legrésy *et al.* [2006], to build an empirical height correction at each point on the ice sheet. Lacroix *et al.* [2009] showed the effectiveness of this correction for variations following strong wind events. A limitation of the empirical time-variable echo shape correction lies in the assumption of just a single relation existing between the echo shape parameters and the height correction, while there may be various modes of echo shape changes depending on i) the underlying physical process (wind, snow accumulation, densification) and ii) the time scale. The seasonal compaction implies that changes in the density of snow layers impact their dielectric response to radar waves. It is therefore possible that part of the seasonal echo shape change is not well represented in the empirical correction. These seasonal radar penetration effects may amount to up to several centimeters in amplitude and are therefore the first candidate to explain the RA contribution to the RA-FDM differences. Future studies may involve using the FDM to infer a density profile, to model the dielectric variations of the medium (alike Lacroix *et al.* [2008]) and to relate it to the RA variations.

Orbital and reference frame issues [Yi *et al.*, 1997; Dong *et al.*, 2003] might also contribute to systematic seasonal effects in the RA measurements. They would show large-scale patterns independent of ice sheet geography, so an upper bound for such effects is given by the 2 cm level found in the Antarctic interior (Figure 3.4).

Some differences between the two datasets also arise from variations in ice flow observed by RA but not included in the FDM, where v_{ice} is assumed constant in time. Seasonal variations in ice flow may amount to the order of 10–20 % in Greenland (e.g. *Zwally et al.* [2002]; *Joughin et al.* [2008]; *Rosenau et al.* [2012]). In Antarctica, however, such variations are rare due to the limited supply of meltwater that could induce them [*Scambos et al.*, 2004]. Concerning flow variations on the interannual to decadal scale, *Rignot et al.* [2011a] report a 9 Gt yr^{-1} annual change of Antarctic discharge (corresponding to $8 \text{ km}^3 \text{ yr}^{-1}$ of volume discharge). This is a minor contribution to the interannual variations of $50\text{--}500 \text{ km}^3$ that can be deduced from Figure 3.1.

3.5 Summary and conclusions

Using a combination of a firn densification model and a regional atmospheric climate model, we quantify the component of the seasonal volume change, or 'breathing', of the AIS, forced by the seasonal cycle in accumulation and temperature. High temperatures and low accumulation cause the surface to lower rapidly in austral summer, while in autumn, winter and spring the surface steadily rises, mainly due to higher accumulation rates. During the 32-year period under consideration (1979–2011), a clear annual cycle in surface elevation is found with an amplitude of 0.026 m averaged over the AIS, equivalent to a 340 km^3 volume oscillation. Across the ice sheet, amplitude values range from $<0.002 \text{ m}$ (high East Antarctic plateau) to $>0.3 \text{ m}$ in the coastal regions of West Antarctica. The phase of the seasonal cycle, with surface rising in winter and lowering in summer, is spatially consistent across the AIS, except for the Weddell Sea coast; here the phase of the seasonal cycle in accumulation and hence surface elevation is reversed. The modeled seasonal variations in surface elevation explain $\sim 31 \%$ of the seasonal signal in ENVISAT radar altimetry data with a phase that is similar (maximum in late winter or early spring). These results can be used to correct surface elevation changes derived from altimetric records over short time intervals or with sparse temporal sampling.

Case study: Byrd Glacier blue ice area

Summary

Blue-ice areas (BIAs) cover $\sim 1\%$ of the East Antarctic ice sheet and are visual evidence of persistent ablation. In these regions, more snow is sublimated and/or eroded than is accumulated. The physical processes driving the formation of BIAs are poorly understood. Here we combine a firn densification model with high-resolution (5.5 km) maps of surface mass balance and ice velocity to simulate the build-up and removal of a firn layer along an ice flowline passing Byrd Glacier. A BIA is formed once the complete firn layer is removed. Feedback processes, which enhance blue-ice formation through the difference in surface characteristics of snow and ice, are examined using sensitivity simulations. The presence of blue ice on Byrd Glacier is found to be mainly determined by i) ice velocity, ii) surface mass balance and iii) the characteristics (thickness, mass) of the firn layer prior to entering the ablation area. With a moderate decrease of the surface mass balance, the location and extent of the simulated BIA on Byrd Glacier is found to be in good qualitative agreement with MODIS optical imagery.

This chapter is published as: Ligtenberg S. R. M., J. T. M. Lenaerts, M. R. van den Broeke, and T. A. Scambos (2014), On the formation of blue ice on Byrd Glacier, *Antarctica Journal of Glaciology*, **60**, 219, 41–50, doi:10.3189/2014JoG13J116

4.1 Introduction

The Antarctic ice sheet (AIS) is almost completely covered by a 50–150 m thick layer of firn, the transitional phase of snow to ice [Ligtenberg *et al.*, 2011]. In blue-ice areas (BIAs), however, no firn layer exists and glacier ice is exposed at the surface [Bintanja, 1999; Sinisalo and Moore, 2010]. Various observational and model studies show that 0.8–1.6 % of the AIS surface can be classified as a BIA [e.g. Winther *et al.*, 2001; Van den Broeke *et al.*, 2006a]. BIAs experience net ablation, caused by a combination of low precipitation, strong sublimation of drifting and surface snow, erosion of surface snow, and/or melt [Takahashi *et al.*, 1988; Bintanja and Van den Broeke, 1995; Van den Broeke *et al.*, 2006a]. To some extent, BIAs are self-sustaining; blue ice has a lower surface albedo (0.5–0.6) than snow (0.8–0.9) [Bintanja and Van den Broeke, 1995], leading to more absorbed radiation and higher surface temperatures in summer, enhancing sublimation rates. Also, blue ice is smoother than snow, making it harder to form a continuous snow cover on the surface [Van den Broeke and Bintanja, 1995a].

BIAs were first observed and studied in the 1950s during the Norwegian-British-Swedish Antarctica Expedition in Dronning Maud Land (DML) [e.g. Schytt, 1961]. During the following half-century, the main focus of BIA research was geological and paleoclimatological, as the ice at the surface of a BIA can be very old and therefore provides relatively easy access to climate archives. The discovery of numerous meteorites on BIAs further enhanced this interest [Yoshida *et al.*, 1971; Cassidy *et al.*, 1992]. Their smooth and hard surfaces also make them potential runways for wheeled aircraft [Swithinbank, 1991]. Later, the focus of research shifted more towards the physical properties of BIAs and their surface energy balance [e.g. Bintanja and Van den Broeke, 1995; Van den Broeke and Bintanja, 1995a,b].

BIAs can be mapped using spectral radiation data from satellites, typically by comparing visible bands with a near-or middle-infrared channel [e.g. Winther *et al.*, 2001; Brown and Scambos, 2004; Scambos *et al.*, 2007], or from climate models that simulate the surface mass balance (SMB) [Van den Broeke, 1997; Van den Broeke *et al.*, 2006a; Lenaerts *et al.*, 2012a]. A larger part of the East Antarctic plateau (~17 %) is classified as 'wind-glaze' or 'wind-scour' areas [Scambos *et al.*, 2012; Das *et al.*, 2013], which are characterized by a windswept, smooth surface. The SMB of wind-glaze areas is near zero (-20 to +20 kg m⁻² yr⁻¹), and slightly negative for wind-scour regions. However their surfaces still consist of firn instead of glacier ice, which can be explained by the finite residence time in ablation areas, owing to ice flow.

The formation of BIAs can be divided into two main processes: roughly half is classified as wind-induced BIA, while the other half is melt-induced [Winther *et al.*, 2001; Van den Broeke *et al.*, 2006a]. A wind-induced BIA is characterized by a smooth, rippled surface where wind divergence leads to snow erosion. In combination with ongoing sublimation, this causes a negative SMB. This BIA type is often observed on the leeward side of a nunatak in the ice sheet [Takahashi *et al.*, 1992; Bintanja, 1999]. Firstly, the nunatak blocks or redirects

precipitating and drifting snow, so snow does not deposit on the leeward side. Secondly, the rock causes turbulence and wind divergence on its leeward side, leading to more enhanced erosion and sublimation. Thirdly, ice velocity is low around a nunatak, giving the ablation processes time to remove the full firn layer. The horizontal length scale of a wind-induced BIA is related to the height of the nunatak [Takahashi *et al.*, 1992]. In DML and other mountainous areas (e.g. the Transantarctic Mountains), numerous wind-induced BIAs are present. In contrast, a melt-induced BIA shows a more irregular surface with depressions and hollows. When meltwater refreezes near the surface, or runs off to lower-lying areas, it can form lakes in surface depressions [Winther *et al.*, 2001]. Melt-induced BIAs are often found near the Antarctic coast, where temperatures are high enough to produce significant melt. The largest known area is located on Lambert Glacier and the Amery Ice Shelf, East Antarctica [Yu *et al.*, 2012].

Another BIA classification that can be used is whether the BIA occurs on flowing or near-stagnant ice ('open' and 'closed' types of BIA; Sinisalo and Moore [2010]). The latter occurs in the vicinity of nunataks that block the ice flow, so the ice becomes stagnant [Bintanja, 1999]. If the local SMB is negative, an equilibrium between ice inflow and surface ablation will be reached. BIAs also occur on fast-flowing ice. Their development depends on the ratio of surface mass removal and ice-flow velocity. When we consider an ice-flow trajectory from the ice divide to the ice shelf, the firn column that is carried by the ice grows or shrinks, depending on the local SMB (Figure 4.1). The firn layer mass balance (FMB) can be viewed as the difference between the SMB and the transition rate from firn to ice at the bottom of the

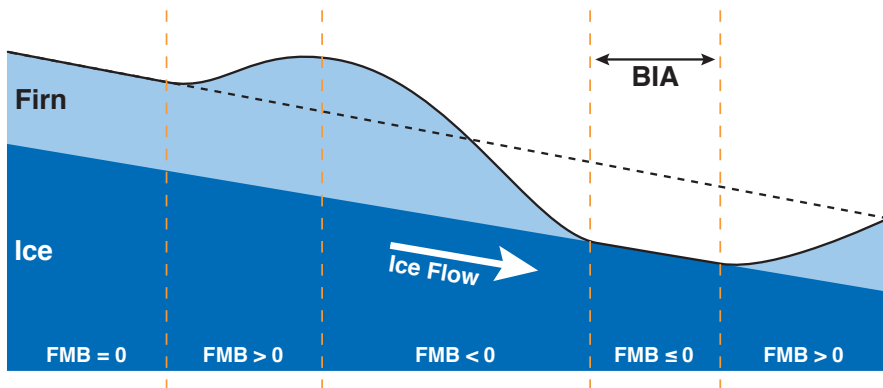


Figure 4.1: Schematic representation of an ice column, including a firn layer, along a flowline that flows from the ice divide (left) towards the glacier terminus (right). Orange lines separate regions with different regimes of firn mass balance (FMB), including the blue ice area (BIA).

firm layer. Near the ice divide (left in Figure 4.1), ice flow is slow and the firm layer is usually in equilibrium with the SMB, making the FMB equal to zero and the firm layer thickness constant in time. When the ice column flows into a region with higher SMB, the firm layer will grow. Likewise, the firm layer will shrink if an area of smaller SMB is encountered. In ablation areas, the entire firm layer can be removed, exposing the glacier ice at the surface, and thereby creating a BIA. When the ice column subsequently flows into a region with positive SMB, snow will start to accumulate at the surface, forming a new firm column. These types of BIAs are often found along the coastal margins of East Antarctica or on valley glaciers in mountainous areas (e.g. Byrd and Beardmore Glaciers; *Brown and Scambos* [2004], where strong katabatic wind accelerations cause drifting-snow erosion and high sublimation rates [*Frezzotti et al.*, 2005; *Scarchilli et al.*, 2010; *Lenaerts et al.*, 2012b]).

In this study we focus on Byrd Glacier (BG; 80–81 °S, 157–160 °E), where the latter type of BIA is found: wind-induced and on flowing ice. We combine ice-velocity SMB maps with a firm-densification model (FDM), to simulate the evolution of a firm column moving through the Byrd ablation area. The focus is mainly on determining which processes and firm-layer characteristics are important for BIA formation on fast-flowing ice, rather than to precisely quantify these effects. The different models and datasets are introduced first. Thereafter, the application to BG is discussed, including sensitivity experiments in which varying strengths of BIA feedback mechanisms are imposed.

4.2 Methods

4.2.1 Atmospheric forcing

Atmospheric forcing is provided by a simulation at 5.5 km horizontal resolution of the regional atmospheric climate model RACMO2 [*Van Meijgaard et al.*, 2008; *Lenaerts et al.*, 2012b]. In previous runs at 27 and 55 km resolution, RACMO2 realistically simulated the Antarctic near-surface climate and SMB [*Van de Berg et al.*, 2005; *Lenaerts et al.*, 2012a]. The model includes a module to calculate drifting-snow transport and sublimation, processes that significantly contribute to the SMB on both local and ice-sheet-wide scales [*Lenaerts and Van den Broeke*, 2012]. Drifting-snow processes in the model lead to an increased extent of ablation ($SMB < 0$) and glazed areas ($SMB \cong 0$) in interior East Antarctica, features that are shown to be realistic [*Stearns*, 2011; *Scambos et al.*, 2012; *Lenaerts and Van den Broeke*, 2012]. However, to resolve SMB gradients on smaller scales, which are mostly related to subtle variations in topography, subsequent wind field heterogeneity and snow erosion and deposition patterns, the model resolution was enhanced to 5.5 km resolution and run for a single year, 2009 [*Lenaerts et al.*, 2012b]. At this resolution, it is shown that these improvements are necessary to simulate the strong wind acceleration inside the Byrd glacial valley. Due to this acceleration, the cumulative amount of drifting-snow sublimation and erosion is

larger than precipitation, leading to ablation in the valley. These features are not resolved at 27 km resolution [Lenaerts *et al.*, 2012b].

In this study, we use daily output of RACMO2 for the year 2009 as climatic forcing for the FDM. We assume this forcing is representative of the long-term climate, a reasonable assumption since the 2009 SMB of this part of East Antarctica (Ice, Cloud and land Elevation Satellite (ICESat) basin 15 and 16; Shepherd *et al.* [2012]) is 49 Gt yr^{-1} , which is comparable to the 1979–2010 average of 47 Gt yr^{-1} .

4.2.2 Firn densification model

We use a one-dimensional, time-dependent FDM that calculates density, temperature and liquid water content in a vertical firn column [Ligtenberg *et al.*, 2011]. The FDM is forced at the surface with output from RACMO2; SMB components (precipitation, surface sublimation, surface melt and drifting-snow processes), surface temperature and 10-m wind speed. The climate forcing along the ice-flow trajectory is defined as the four-point inverse-distance weighted average of the nearest RACMO2 grid points. To keep the FDM computationally feasible, while taking into account the varying climate on locations along the flowline, a constant climate of 10 years is chosen before it is moved to the new trajectory point with its associated different climate. The trajectory extends far enough upstream of the BIA to build up and refresh a complete firn column, thereby spinning-up the FDM.

In previous studies, the FDM was used to simulate firn and surface height changes at a fixed position [Pritchard *et al.*, 2012; Ligtenberg *et al.*, 2012], whereas this study focuses on simulating the evolution of a firn layer that moves along an ice-flow trajectory. Also, the extreme conditions (ablation, high wind speeds) of the BG region are a rigorous test for the FDM compared with the accumulation zone of an ice sheet. For this purpose, some slight modifications to the FDM physics have been introduced, in comparison with the version of Ligtenberg *et al.* [2011].

Firstly, drifting-snow erosion/deposition is added as a mass removal/addition term, as it is one of the driving forces of BIA formation [Takahashi *et al.*, 1988]. Every model time-step, RACMO2-simulated SMB components (snowfall, rainfall, surface melt, surface sublimation, drifting-snow sublimation and drifting-snow erosion/deposition) are added to or removed from the top model layer with either the density of fresh snow (mass addition) or the density of the top model layer (mass removal). Secondly, the FDM must be able to accommodate a complete removal of the model firn layer. This is done by adding new layers with the density of ice at the bottom of the model firn layer when a minimum number of model layers is reached (50). Thirdly, the semi-empirical expression for the densification of firn used in the FDM depends on average accumulation (\dot{b}), and temperature [Herron and Langway, 1980; Arthern *et al.*, 2010; Ligtenberg *et al.*, 2011], and is therefore physically unusable in ablation areas. Therefore, we assume that \dot{b} is always at least equal to $15 \text{ kg m}^{-2} \text{ yr}^{-1}$, i.e. firn

densification is a continuous process. Even in a negative accumulation area, snowfall events occur that add mass and therefore increase pressure on the firn layers, thereby enhancing firn densification. When mass is removed from the surface, pressure on the firn layers is lowered, but this does not cause 'negative' firn densification, i.e. no air is added to the firn layer. The value of $\dot{b} = 15 \text{ kg m}^{-2} \text{ yr}^{-1}$ was chosen based on model experiments, and gives comparable densification rates at depth between ablation and accumulation regions. Firn models that use the overburden pressure as a measure for firn densification [e.g. *Barnola et al.*, 1991; *Spencer et al.*, 2001] are not affected by this, as they do not use the average accumulation rate in their equations. Like most firn models, our FDM is calibrated to density data from accumulation zones. In the absence of similar data from ablation areas, we currently have to rely on these models without being able to directly validate the modeled density profiles.

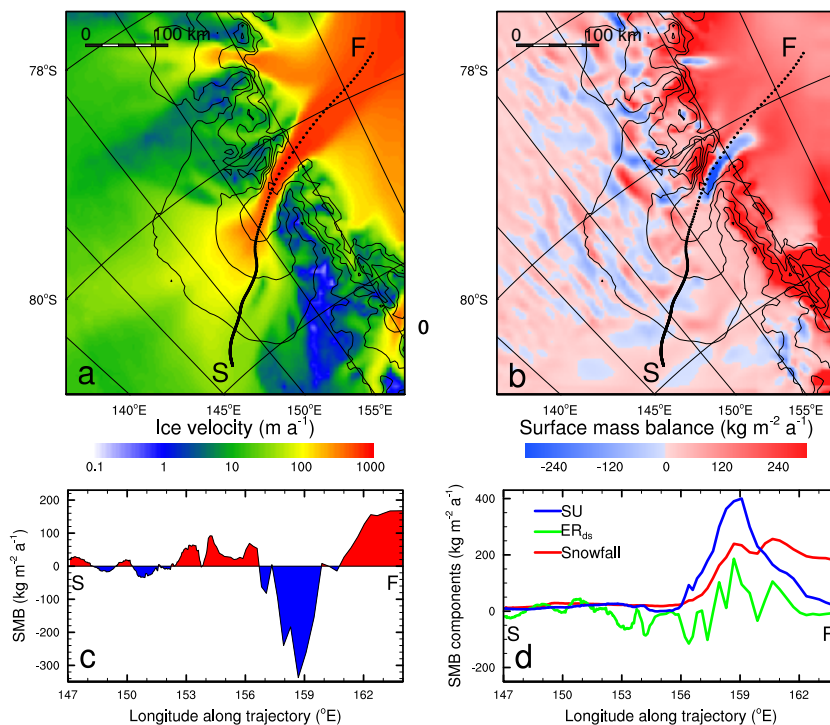


Figure 4.2: Ice-flow trajectory starting at 'S' on the East-Antarctic plateau and ending at 'F' on the Ross Ice Shelf. Colors indicate ice-flow velocity in (a), and modeled surface mass balance (SMB) in (b). Dots indicate a trajectory point every 10 years and the solid curves indicate topographic height contours with 500 m spacing. The SMB (c), and its components (d); snowfall, combined surface and drifting-snow sublimation (SU) and erosion/deposition by drifting snow (ER_{ds}), along the trajectory.

4.2.3 Ice velocity

To obtain a trajectory along an ice flowline, the AIS ice velocity field of *Rignot et al.* [2011a] is bilinearly interpolated onto the grid of RACMO2 (5.5 km). Firstly, a location downstream of the ablation area (i.e. negative SMB in RACMO2) is selected and the trajectory is calculated in a stepwise fashion in the upstream direction, using the average flow velocity and direction of the four neighboring points. A time-step of 10 years is used. These steps are repeated until the trajectory reaches the East-Antarctic plateau, where the climate is relatively stable and ice velocities are relatively low, conditions that are required to spin-up the model firn layer. Figure 4.2 shows the resulting ice-flow trajectory and SMB map and profile along the trajectory crossing BG. The trajectory starts at point 'S' on the East Antarctic plateau, at >2000 m a.s.l., where ice velocity is relatively low (~ 50 m yr $^{-1}$), and ends at point 'F' on the Ross Ice Shelf (RIS). The ice velocity in the first half of the trajectory is low; the more widely spaced trajectory dots indicate the increasing speed when the trajectory enters the narrow valley of BG, where the highest ice-flow velocities are reached (up to 1200 m yr $^{-1}$; Figure 4.2a). Ice-flow speed remains high when the trajectory leaves the narrow valley and enters the RIS.

At the start of the trajectory, the SMB is close to zero (Figures 4.2b–c), with small SMB components (Figure 4.2d). Alternating patterns of ablation and accumulation are caused by subtle differences in the RACMO2 topography that initiate acceleration and deceleration of the wind speed [*Lenaerts et al.*, 2012b]. In turn, this determines patterns of erosion or deposition of drifting snow (Figure 4.2d). This area of (near-)ablation agrees well with the 'wind-glaze' area found by *Das et al.* [2013], shaded green in Figure 4.3. The Transantarctic Mountain range represents a large gradient in elevation and precipitation, leading to higher SMB values on the RIS to the east (~ 150 kg m $^{-2}$ yr $^{-1}$) compared with the ice-sheet plateau to the west (-20 to $+20$ kg m $^{-2}$ yr $^{-1}$). In the valleys of BG and Darwin Glacier (79° S, 159° E) the SMB is dominated by large drifting-snow sublimation and erosion rates due to strong katabatic winds, leading to a locally negative SMB. Downstream at the RIS, the SMB turns positive due to more precipitation and lower wind speeds.

4.2.4 Blue ice area

Scambos et al. [2007] present a satellite image algorithm for mapping snow grain size, and use it to estimate BIA extent. Using two bands from the Moderate Resolution Imaging Spectroradiometer (MODIS) satellite sensor, specifically its two 250 m resolution bands (band 1: red visible light at 620–670 nm; band 2: near-infrared at 841–876 nm), grain size is determined by the increased absorption of infrared light as grain size increases. The MODIS band 1 and 2 data are corrected for sensor drift, satellite and solar geometry, and atmospheric absorption, and are converted to top-of-the-atmosphere reflectivity before using a look-up table of snow grain size and reflectivity in each band derived from a model [*Ricchiuzzi et al.*, 1998; *Painter et al.*, 2003]. A map of snow grain size produced from a MODIS mosaic of the

Antarctic continent was produced and described by *Scambos et al.* [2007], and data for this 2003–04 mosaic and a second mosaic produced from 2008–09 data [*Scambos et al.*, 2012] are available from NSIDC (nsidc.org).

An earlier Landsat-based study by *Brown and Scambos* [2004] used a supervised classification approach to map wind-induced BIAs near BG for seasonal and interannual variations in extent. Comparing the grain-size mapping results of the MODIS bands 1 and 2 approach with this earlier study indicates that an effective threshold for mapping BIA boundaries from optically determined snow grain-size data is $400\ \mu\text{m}$. Figure 4.3 shows the resulting BIA extent (in blue) when this threshold and the method described above are used. The two Mosaic of Antarctica grain-size datasets give results consistent with the BIAs considered by *Brown and Scambos* [2004], and other mapped Antarctic BIAs [e.g. *Van den Broeke et al.*, 2006a]. They indicate that the BIA in the central BG trunk extends from just east of 155°E to just west of 162°E . However, these boundaries can vary due to seasonal and interannual variations in snow cover. For example, the eastern extent boundary varies between 161.6°E and 161.9°E in the 2004 and 2009 mappings. The western boundary, and most other wind-induced BIAs in the region, are near identical in both mappings. The BG BIA is approximately 125–130 km along-flow and 20–30 km wide through the glacier trunk, extending quite close to the valley walls of the glacier. Along the ice-flow trajectory calculated in the previous subsection (Figure 4.2a), the BG BIA extends from 156.4°E to 161.8°E (Figure 4.3b). The trajectory also passes through a smaller BIA, upstream of BG, which extends from 150.8°E to 152.1°E .

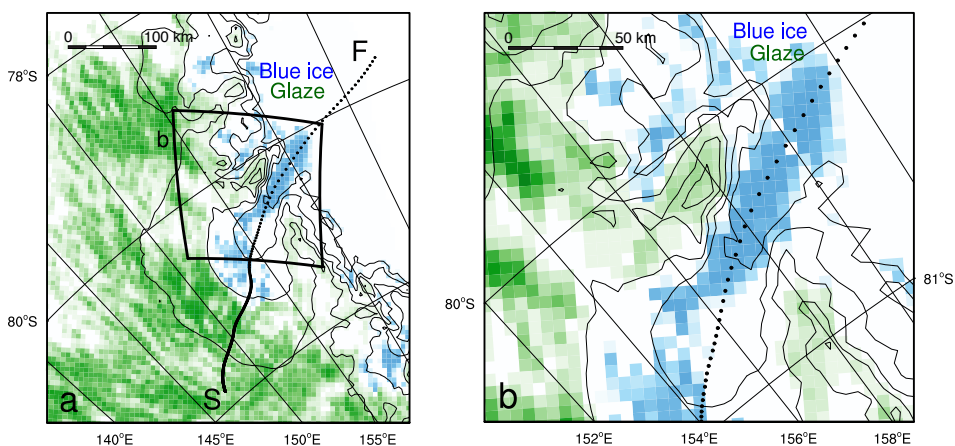


Figure 4.3: Ice-flow trajectory starting at 'S' on the East-Antarctic plateau and ending at 'F' on the Ross Ice Shelf. Shaded background colors are observed 'wind-glaze' surface (green, from *Das et al.* [2013]) and blue-ice areas (blue, after *Scambos et al.* [2012]). In (b) the Byrd Glacier region is enlarged.

4.3 Results

Figure 4.4a shows the modeled evolution of the firn mass along the ice-flow trajectory through BG with the control climate forcing (Figure 4.2c). Firn mass is defined as the vertically integrated mass of model layers with a density less than 830 kg m^{-3} , generally assumed to be the pore close-off depth and the boundary between firn and glacier ice [Herron and Langway, 1980; Ligtenberg *et al.*, 2011]. The upper x-axis indicates the elapsed time during the simulation, starting from the present day and assuming a steady-state climate throughout

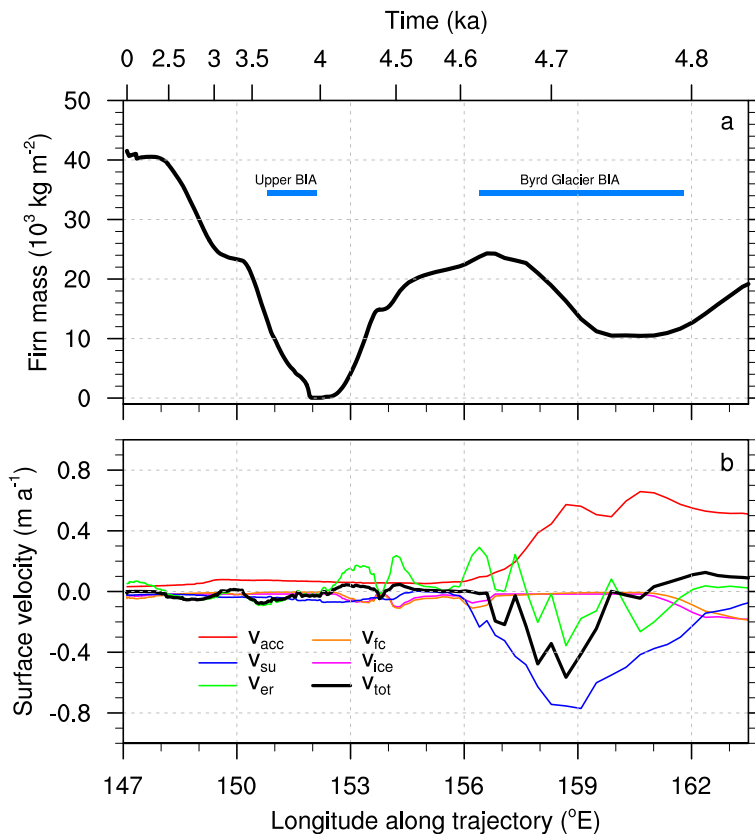


Figure 4.4: Evolution of firn mass (a) and corresponding vertical surface velocities (b) for the control simulation, along the trajectory shown in Figure 4.2b. Vertical surface velocity components due to snowfall (v_{acc}), sublimation (v_{su}), drifting-snow erosion/deposition (v_{er}), firn compaction (v_{fc}), firn-ice formation (v_{ice}) and the total vertical surface velocity (v_{tot}) are shown. The red, blue and green surface velocities correspond to the red, blue and green SMB components in Figure 4.2d. Both the longitude and elapsed time are shown. Blue bars in (a) indicate the locations of the 'Upper BIA' and the 'Byrd Glacier BIA'.

the period. Firm mass evolution follows that of the local SMB (Figure 4.2c): firm mass decreases/increases with a negative/positive SMB. To create a realistic firm layer at the start of the trajectory, the climate of the first trajectory point is used to spin-up the FDM until the firm mass reaches a steady state (~ 40 tons), indicating that the firm layer is in equilibrium with the local climate. For the next 2500 years, the trajectory moves slowly eastwards and SMB is small, but positive (Figure 4.2c), causing the firm mass to remain relatively constant. When the trajectory enters a negative SMB region ($148\text{--}152^\circ\text{E}$), the firm mass steadily drops and becomes zero around 152°E . Due to the low ice velocities on the East Antarctic plateau, the firm layer spends $\sim 80\%$ of the total time in the $147\text{--}152^\circ\text{E}$ sector. Because the firm column resides a long time in this near-zero SMB environment, the entire firm layer is removed. These conditions indicate that the $147\text{--}52^\circ\text{E}$ region is prone to BIA formation, as supported by Figure 4.3a. This BIA will be referred to as 'Upper BIA'. The strong nonlinear character of the trajectory timeline is indicated by the time axis in Figure 4.4a.

Figure 4.4b shows the components of the firm depth change rate due to the different firm and SMB processes [Ligtenberg *et al.*, 2011, 2012]. Around 153°E the ice velocity increases as it approaches the BG valley, and moves into a positive SMB region. Accumulation is mainly due to increased drifting-snow deposition (Figure 4.4b), and results in the build-up of a new firm layer and increasing firm mass (Figure 4.4a). The SMB remains positive until 157°E , because of low sublimation and periodically high drifting-snow deposition, further enhancing the firm mass. When the trajectory enters the BG valley, firm mass decreases rapidly, but not all the mass of the firm layer is removed (Figure 4.4a). The negative SMB is mainly caused by drifting-snow sublimation and erosion, but is counteracted by an increase in snowfall (Figure 4.4b). With ice velocities $> 1\text{ km yr}^{-1}$, it takes only ~ 70 years for the ice to move through the BG ablation area ($157\text{--}160^\circ\text{E}$), during which roughly half the existing firm mass is removed. When the trajectory enters the RIS ($\sim 162^\circ\text{E}$) the ice velocity remains high, and the annual SMB becomes significantly positive ($> 150\text{ kg m}^{-2}\text{ yr}^{-1}$), due to increasing snowfall and reduced snowdrift activity. As a consequence, firm mass increases rapidly to form a thicker firm layer, which is characteristic for most of the Antarctic ice sheet and ice shelves [Ligtenberg *et al.*, 2011].

The FDM does not simulate a BIA on BG, with a significant amount of firm mass still present at its minimum ($10,450\text{ kg}$ at 160.6°E). With an average annual SMB of $-200\text{ kg m}^{-2}\text{ yr}^{-1}$, it would take another ~ 70 years to remove the remainder of this firm layer. This can either mean that the ice velocity is overestimated, transporting the firm layer too quickly through the ablation region, or that SMB is not accurately simulated. The second option is more likely, since the ice velocity should be halved in order to create the BG BIA, while the uncertainty in local ice velocity is only $\sim 5\text{ m yr}^{-1}$ [Rignot *et al.*, 2011b]. SMB on BG is less certain, as RACMO2 simulations for the Antarctic ice sheet [Van de Berg *et al.*, 2006; Lenaerts *et al.*, 2012a; Ligtenberg *et al.*, 2013] are initialized with a homogeneous firm pack covering the entire ice sheet, which is a valid assumption for $\sim 98\%$ of the Antarctic ice sheet. However, at locations that experience significant snowmelt (e.g. the George VI Ice Shelf) or have a

negative SMB (e.g. BIAs), this assumption is not longer valid. Although RACMO2 has an interactive firn layer, and the 5.5 km RACMO2 simulation considered here is initialized with the 27 km RACMO2 simulation of *Lenaerts et al.* [2012a], the ~ 30 years of spin-up are not long enough to remove the entire model firn layer and form a BIA in RACMO2. Therefore, the feedback processes that play a major role in the formation and persistence of a BIA are not (fully) represented in RACMO2. In the next subsection, these feedback processes and their influence on the evolution of the firn layer around BG are discussed.

4.3.1 BIA feedback mechanisms

Positive feedback processes active at the BIA surface are related to i) the darker surface of a BIA compared to snow and ii) the smoother and harder surface of a BIA. The albedo of freshly fallen snow can be as high as 0.85, while the albedo of blue ice is in the range 0.5–0.6 [*Bintanja and Van den Broeke*, 1995], so blue ice absorbs three to four times more solar radiation than fresh snow. A part of this extra energy is transformed into heat, making the surface of BIAs warmer than the surrounding snow-covered areas. *Bintanja and Van den Broeke* [1995] found that, averaged over one summer, the surface temperature of a BIA was 6.4 K higher than over the surrounding snow-covered area. In the FDM, this effect was mimicked by adding a sine-like surface temperature correction, maximized at the summer solstice (+6 K) and zero when the sun is below the horizon at 80°S (Figure 4.5a). The associated increase in sublimation rate follows the correction for temperature, since the effects are coupled. At the summer solstice the sublimation correction is maximized at $+0.3 \text{ mm d}^{-1}$ (Figure 4.5b). This value is based on the difference in average summer latent heat flux above a BIA and snow (10 W m^{-2} ; *Bintanja and Van den Broeke* [1995]). The magnitude of both corrections (temperature and sublimation) is made a function of the density of the upper model layer: no correction is applied for a snow surface ($\rho < 400 \text{ kg m}^{-3}$) and the full correction

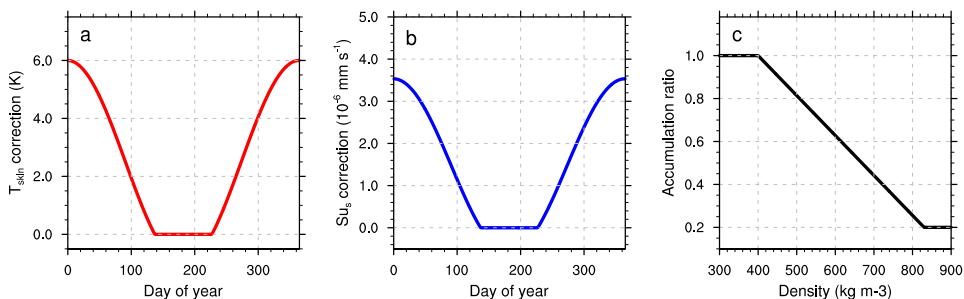


Figure 4.5: *Imposed idealized positive feedback mechanisms on a BIA, for (a) surface temperature (T_{skin}), (b) surface sublimation (SU_s) and (c) accumulation ratio (snowfall and deposition of drifting snow).*

is applied for blue ice ($\rho > 830 \text{ kg m}^{-3}$), with a linear dependency in between. The latter threshold is chosen as it represents the approximate pore close-off density, at which air bubbles get trapped in the ice, and firm characteristics no longer change appreciably.

The smoother and harder surface of a BIA makes it more difficult for precipitating snow particles to form a continuous snow layer at the surface [Van den Broeke and Bintanja, 1995a], especially during strong wind events. Therefore, less snow will accumulate at the surface of a BIA. To compensate for this effect, a fraction of the simulated snowfall and drifting-snow deposition is assumed to be removed from the surface, depending on the density of the surface. The threshold values for the surface density (400 and 830 kg m^{-3}) are similar to that for the temperature and sublimation feedback. For a snow surface, all accumulation remains at the surface (fraction = 1.0), whereas on a BIA the fraction decreases to 0.2, meaning that only 20 % of the accumulation is allowed to accumulate on the surface (Figure 4.5c).

To investigate the sensitivity of BIA formation to the above schematic adjustments, an ensemble of FDM simulations was performed with varying strengths. The feedback mechanisms as described in the previous paragraphs, were used as the maximized values (1.0, or 100 %): a 6 K temperature increase, a latent heat flux increase of 10 W m^{-2} (e.g. a sublimation increase of 0.3 mm d^{-1}) and an accumulation fraction of 20 %. In each consecutive run, numbered X10 to X1, the feedback strength was decreased by fractional increments of 0.1. For example, the 'T6-S4-A3' acronym refers to a simulation with a temperature increase of 3.6 K ($0.6 \times 6 \text{ K}$), a latent heat flux (or sublimation) correction of 0.12 mm d^{-1} ($0.4 \times 0.3 \text{ mm d}^{-1}$) and an accumulation fraction of 0.76 ($1.0 - (0.3 \times 0.8)$). The firm layer simulation without the feedback mechanisms ('control'), as shown in Figure 4.4a, is thus 'T0-S0-A0'.

4.3.2 Sensitivity experiments

Figure 4.6 shows the evolution of firm mass along the ice-flow trajectory with the three feedback mechanisms activated separately with varying strengths: (a) temperature, (b) sublimation and (c) accumulation. The temperature feedback appears to have a minor effect on the simulated firm mass; only in the low-velocity region of the trajectory ($151\text{--}152^\circ\text{E}$) does the increase in surface temperature result in a significant change from the control run. The higher temperatures lead to higher firm densification rates, causing a faster firm/ice transition than in the control run and therefore earlier BIA formation. On BG no change in firm mass evolution is simulated for increased temperatures; BIA feedback processes are only activated when the upper layer density becomes $>400 \text{ kg m}^{-3}$, and this threshold is not reached on BG. Apparently, snowfall and drifting-snow deposition are large and constant enough for the upper snow layer density to remain low.

In the sublimation (Figure 4.6b) and accumulation (Figure 4.6c) experiments, the impact on firm mass is much larger. Both have similar effects on the firm layer: an increase in sublimation or a decrease in snow accumulation both decrease the SMB at the surface. For moderate

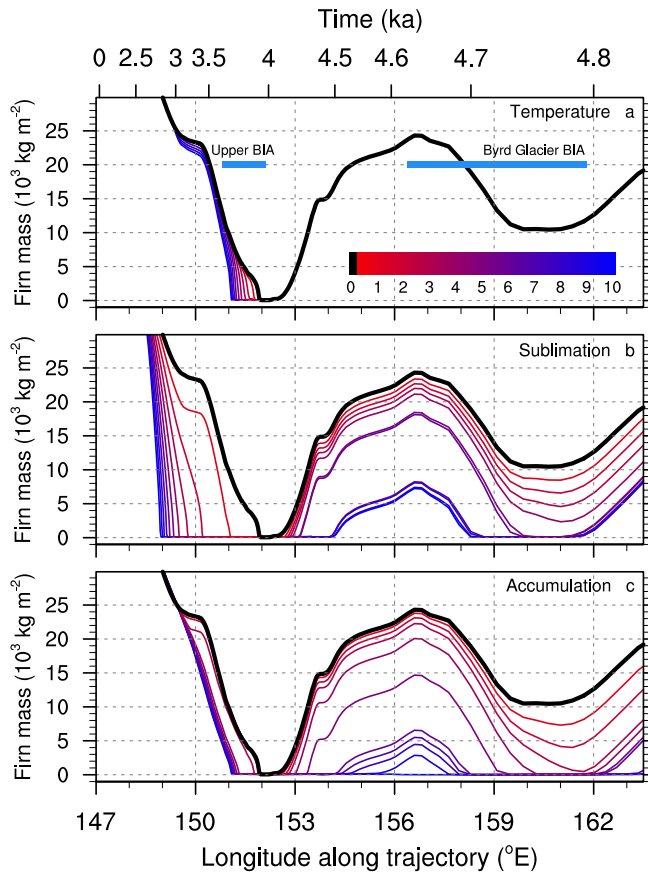


Figure 4.6: Evolution of firn mass along the trajectory for temperature (a), sublimation (b) and accumulation (c) experiments, along the trajectory shown in Figure 4.2b. The control simulation (thick black curve, same as Figure 4.4a), and light (red, 1) to strong (blue, 10) feedback experiments are shown. Both the longitude and elapsed time are shown. Blue bars in (a) indicate the locations of the 'Upper BIA' and the 'Byrd Glacier BIA'.

feedback strengths (1–4), firn mass is reduced fairly linearly over the fast-ice-flow region (153–162 °E). This is mainly caused by a lag effect that originates in the Upper BIA, where glacier ice is at the surface and the influence of the feedback processes therefore large. In both simulations, it takes more time for the new firn layer to re-establish itself and thereby deactivate the feedback mechanisms. When this happens (~153 °E), the SMB forcing is again equal to the control run and the evolution of firn mass is similar until 159 °E. Here BIA feedback processes again start to play a role as the upper layer density increases, causing the firn mass to reduce more rapidly. For relatively high feedback strengths (S5 and A4 and

higher), a BIA at BG is simulated (firm mass = 0 at 160 °E). These results suggest that the feedback mechanisms described here are essential to sustain the BG BIA. If no BIA were present, the feedback mechanisms would not be active and the climate would be comparable to the RACMO2 output, which does not lead to a BIA on BG (Figure 4.4).

Between simulations S6 and S7 (and also between A5 and A6), a rapid change in firm mass prior to BG (154–158 °E) occurs, which is also initiated by the previously discussed lag effect. The SMB around 153 °E (Figure 4.2c) is, in combination with the imposed increase in sublimation (or decrease in accumulation), too small to initiate fast firm layer growth. As the density of the upper layers remains high, the feedback processes remain active and no new firm layer is established. Only at ~154 °E the peak in SMB due to drifting-snow deposition is large enough to start the formation of a significant firm layer. Hereafter, the feedback mechanisms are switched off and firm mass increases regularly until 157 °E. Only for the strongest feedback simulation (A10, accumulation reduced by 80 %) no firm layer is simulated over the entire 152–164 °E section of the trajectory.

Although the sublimation and accumulation sensitivity simulations give quite similar results, there are also some notable differences. In the sublimation simulations, the onset of the Upper BIA occurs earlier with every experiment, whereas for the accumulation simulations an optimum is already reached in simulation A3. In this near-zero SMB environment, the individual SMB components are small (Figure 4.2d) and because the accumulation feedback mechanism is prescribed as a fraction of the absolute amount, the imposed accumulation effect is also rather small. The sublimation effect, however, is prescribed as an absolute value and therefore has a continuously increasing effect. In the faster-flowing sections of the trajectory (154–157 °E), the reverse effect is visible; here the sublimation simulations converge, with the strongest feedback simulations (S7–S10) showing the same firm mass. When individual SMB components are large, the absolute effect of the sublimation feedback is small and here the relative accumulation feedback has a much bigger impact. This is reflected in the reduction of firm mass in each subsequent simulation (A1–A10). When the trajectory enters the RIS (>162 °E), all sublimation experiments form a firm layer, whereas the firm mass in the high-impact accumulation experiments (>A8) remains zero.

4.3.3 Combination of feedbacks

A combination of the feedback mechanisms is more realistic; to that end 121 experiments with different combinations of the sublimation and accumulation effects were performed. The temperature effect, although of minor importance, is also included and is prescribed to have the same relative strength as the sublimation effect. Figure 4.7 shows the results of 25 moderate combination simulations (A1–A5, combined with S1–S5). Similar patterns to those in Figures 4.6b–c emerge; i) a faster formation of the Upper BIA, ii) the firm layer growth at the 153 or 154 °E accumulation event and iii) the varying presence and extent of the BG BIA.

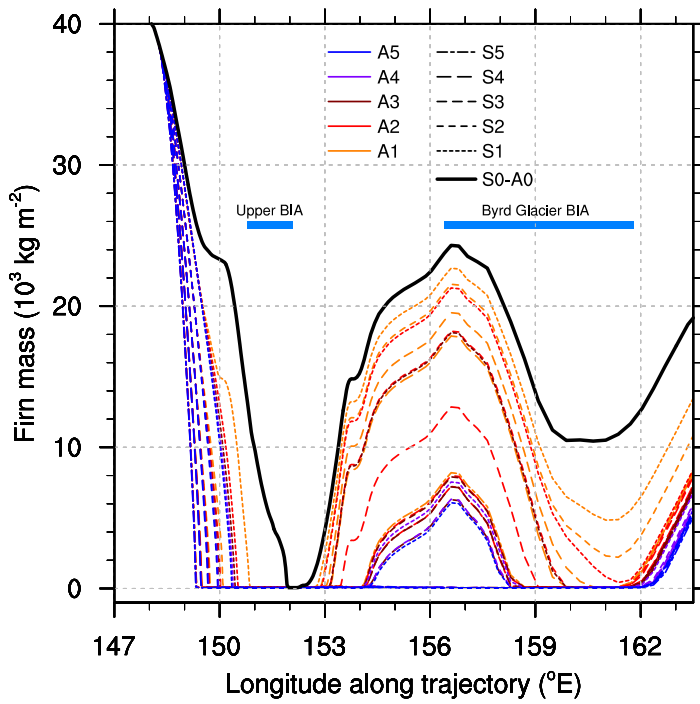


Figure 4.7: Evolution of firn mass along the trajectory shown in Figure 4.2b for simulations with a combination of accumulation (line color) and sublimation (line style) feedback processes. The control simulation is included (thick black curve, same as Figure 4.4a) and numbers indicate the strength of the feedback process, varying from light (1) to moderate (5). Blue bars indicate the locations of the 'Upper BIA' and the 'Byrd Glacier BIA'.

The formation of the Upper BIA is similar to Figure 4.6b, as sublimation is the main driver of the formation of this BIA. With each increase in sublimation feedback strength, the Upper BIA is formed earlier, while an increase in accumulation effect induces significantly less change. The difference in maximum firn mass prior to BG (at 156 °E) also shows the same pattern as for the separate sublimation and accumulation simulations (Figures 4.6b–c). For the control run it peaks at ~24 tons, and for moderate feedback simulations (~S2-A2) this reduces to 18–22 tons, due to the slight time lag in firn layer growth around 153 °E. From simulation S3-A3 onwards, the positive SMB event of 153 °E is not sufficient and the build-up of a firn layer is delayed until the positive SMB event at 154 °E, thereby generating significantly less firn mass (~7 tons). For stronger feedbacks, no firn layer is simulated and the BIA extends from 150 to 162 °E. The presence and/or length of the BG BIA depends mostly on this maximum firn layer mass prior to BG. If this firn mass is larger, more mass needs to be removed and the BIA forms later or not at all. The firn layer growth at the end of BG BIA is more robust, and is predicted to be ~162 °E in all experiments.

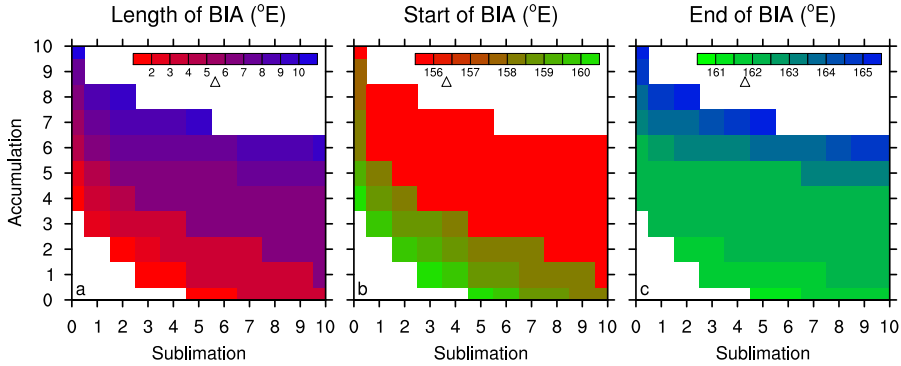


Figure 4.8: The length (a) and start position (b) and end position (c) of the simulated BG BIA, for simulations with a combination of accumulation and sublimation feedback processes. Axis labels indicate the strength of the feedback process, varying from light (1) to strong (10). The observed BIA characteristics are indicated by the triangles.

Figure 4.8 summarizes (a) the length, (b) the start position and (c) the end position of the BG BIA for the different model experiments, expressed in degrees longitude. The white area in the lower-left corner represents simulations in which no BIA develops. The white area in the upper-right corner represents simulations in which the BIA extends from at least 152°E to the end of the trajectory. The latter means that the feedback processes are so strong that no new firm layer forms between the Upper and BG BIAs. For increasing strength of the feedback processes, the length of the BIA increases, with the start and end of the BIA propagating westwards and eastwards, respectively. However, the transition is not gradual; the start of the BIA shows a distinct transition between simulations that do not simulate a firm layer prior to BG and simulations that do (start of BIA $>158^{\circ}\text{E}$ and $<158^{\circ}\text{E}$, respectively). Less distinct is the difference in start position above 158°E , which indicates simulated firm layer growth from either the 153 or 154°E accumulation event. The end position of the BIA is more evenly distributed, with the majority of the solutions predicting the BIA terminating around 162°E . The length of the BIA is simply the difference between the start and end position, and varies between 2 and 10°E .

An optimal combination of accumulation and sublimation feedback strengths is hard to provide, because no combination exists that best captures the start, end and length of the BG BIA. Figures 4.7 and 4.8 show that the end location of the BG BIA is positioned rather uniformly around 162°E , in agreement with observations. Based solely on the start position, the solutions along the line A5-S1 to A1-S9 (Figure 4.8b) contain the optimal combinations. Although the start of the observed BG BIA at 156.4°E is not well captured, they simulate a start location of $158\text{--}158.5^{\circ}\text{E}$. Experiments A4-S2, A3-S4 and A2-S5 seem the most realistic, assuming that the feedback mechanisms (accumulation and sublimation) are similar in strength.

4.4 Discussion

Validation of the firn mass evolution along the trajectory remains challenging, as few detailed firn profiles are available. According to MODIS imagery, the onset of the observed BIA on BG (156.4°E) is situated close to the start of the negative SMB region (from 156.6°E onwards; Figure 4.2c). In combination with the relatively high ice velocities in this region, this suggests that the upstream firn layer mass should at least be small. This is an indication that the moderate sensitivity simulations with a lower firn mass around 155–157°E could be more realistic than the control simulation. Moreover, most of the region of the East Antarctic plateau upstream of BG is observed to be 'wind-glaze' area, indicating that the firn mass is potentially low throughout the region.

The simulated firn mass is almost entirely determined by the SMB from RACMO2, which, in turn, is dominated by the variation in deposition and erosion of drifting snow in this region (Figure 4.2d). The simulation of this process is complex and depends on subtle differences in topography, which are probably not fully captured at this horizontal resolution (5.5 km). *Lenaerts et al.* [2012b] show large changes in the transition from 27 to 5.5 km horizontal resolution. It is highly likely that a further increase in resolution would enhance the drifting-snow details and further benefit the simulation of firn mass in the low-ice-velocity areas.

Location and extent of both the Upper BIA and the BG BIA are qualitatively correctly simulated by the FDM. For the Upper BIA, ice velocities are low to such a degree that even a slightly negative SMB can cause the complete removal of the firn layer. The simulated location of the BIA is mainly determined by the local drifting-snow erosion maximum, and is therefore sensitive to the resolved model topography, as described above. For the BG BIA to form, large ice velocities require significant negative SMB conditions, potentially in combination with a small firn mass upstream of the high-velocity region. Otherwise the complete firn layer could not be removed in the relatively short time it spends in the ablation zone.

4.5 Summary

In conclusion, the formation of a BIA is an interplay between i) ice velocity, ii) SMB and iii) the firn mass of the existing firn layer prior to the ablation area. If the ice velocity is low enough, the SMB negative enough or the firn mass prior to the ablation area small enough, a BIA is likely to form. Otherwise, these three variables need to occur in a favorable combination in order to remove the entire firn layer and form a BIA.

The FDM of *Ligtenberg et al.* [2011] has been adapted to simulate the formation and removal of a firn layer along an ice-flow trajectory that crosses BG in East Antarctica, where MODIS imagery shows the presence of an extensive BIA. The mass balance of the firn layer is mainly determined by the SMB. If the SMB is significantly positive, the firn layer grows towards

a steady state in which growth at the surface balances with ice formation at the bottom. A low or negative SMB (ablation) leads to a negative firn layer mass balance; if this process continues long enough, the firn layer is completely removed and a BIA forms.

When the RACMO2 simulated SMB is used directly as forcing for the FDM, no BIA on BG is formed. The possible causes are that the SMB is not negative enough to remove the complete firn layer, or that the simulated firn mass upstream of the BIA is too large. Because RACMO2 assumes the presence of a continuous snow surface across the entire Antarctic ice sheet, certain feedback processes that are characteristic of BIAs are underestimated. Three BIA feedback mechanisms were studied in more detail: i) increased surface temperature, ii) increased sublimation and iii) decreased accumulation. The increase of surface temperature alone has a minor effect, as it only affects the firn compaction speed, which is of secondary importance for firn mass removal and subsequent BIA formation. Decreasing the net SMB, by either increasing sublimation or decreasing accumulation, causes a more rapid decrease of firn layer mass. The formation and/or existence of the BG BIA represents the interplay between ice-flow velocity, SMB and firn mass upstream of the ablation area.

Once a BIA has formed, it can be self-sustaining, due to positive feedback mechanisms that remain active as long as the surface is not covered with a continuous layer of fresh snow. As a result, the BIA may persist longer before a new firn layer can establish itself. In our simulations this lag effect was especially important upstream of BG, which, in turn, has a distinct effect on the formation of the BG BIA. Using a moderate combination of the sublimation and accumulation feedback mechanisms, the extent of the observed BG BIA was reasonably well simulated. A robust result is that the sublimation and accumulation effects are of similar importance, while the effect of surface temperature is minor.

Case study: the Antarctic Peninsula firn layer

Summary

Firn layer characteristics, such as density, depth and thickness, are important for the production of surface runoff in the Antarctic Peninsula (AP). Meltwater produced at the surface can be stored locally in the firn pack, but will run off if there is not enough firn pore space available. Here, a steady-state firn layer, including the effect of surface melt, is calculated for the AP using a combination of a firn densification model (FDM), a regional atmospheric climate model (RACMO2) and firn air content (FAC) observations. Depending on the melt-accumulation (MA) ratio from RACMO2, the firn layer is simulated with either the steady-state or time-dependent version of the FDM. In some locations, an ice-only column is assigned as either the MA-ratio is too large (>0.7) or the observed FAC is too low (<0.5 m). In locations with low simulated FAC values (<5 m), little pore space is available to accommodate meltwater and it is likely that some meltwater will run off during the melt season. This is simulated on former Larsen B Ice Shelf and the northern part of George VI Ice Shelf, both in agreement with observations of meltwater ponding at the surface. In the near-future, surface melt will increase due to rising temperatures, making more firn layers susceptible to produce runoff. Locations with a moderate FAC (5–15 m), such as northern and eastern Larsen C Ice Shelf and Wilkins Ice Shelf, are likely to produce runoff during the next century.

This chapter is based on: Ligtenberg S. R. M., J. M. van Wessem, M. R. van den Broeke and P. R. Holland, *Constructing a high-resolution steady-state firn layer for the Antarctic Peninsula*. In preparation.

5.1 Introduction

The surface mass balance (SMB) of an ice sheet is composed of mass input by precipitation and mass output by sublimation, drifting snow erosion and runoff. On the Antarctic ice sheet, precipitation of snow is the major driver of variations in SMB, as sublimation is approximately an order of magnitude smaller and both drifting snow erosion and runoff are negligible averaged on a continental scale [Lenaerts *et al.*, 2012a]. The Antarctic Peninsula (AP) is the only part of the Antarctic ice sheet where significant annual surface melt leads to surface runoff. In a future warming climate, the extent and magnitude of surface runoff are likely to increase due to increasing melt [Ligtenberg *et al.*, 2013].

Next to the forcing climate, the presence and magnitude of surface melt and subsequent runoff depends greatly on the local firn layer conditions. At the start of the summer, a layer of winter snow/firn is often present at the surface that contains significant air space between its snow crystals. When surface melt occurs, the meltwater percolates down into the firn, where it either refreezes as ice or is stored as liquid water, depending on the local temperature of the firn. As more snow melts, this process continues until all pore space is filled and the firn layer cannot accommodate any more meltwater. The remaining meltwater will pond at the surface and eventually run off at the surface or base of the ice sheet.

Due to large spatial gradients in the AP climate, the firn layer conditions on the AP also vary greatly. Currently, a complete overview of the AP firn layer is absent as only parts are covered by observations, such as scarce firn core observations [Andy Shepherd (pers. com.), *Pasteur and Mulvaney*, 2000] or radar measurements [Holland *et al.*, 2011]. Using a combination of a climate model and a firn model, the complete range in climate conditions can be assessed [Ligtenberg *et al.*, 2011]. However, the horizontal resolution in that study (27 km) is too coarse to sufficiently resolve the complex topography of the AP. In this paper, we use a five times higher horizontal resolution (5.5 km) to obtain firn layer information for the entire AP.

This information can be used as a realistic initialization of climate models. For the correct simulation of temporal patterns in surface melt and runoff, it is important that the initial model firn layer is representative for the local climate. An incorrect firn initialization will lead to a bias in modeled melt and runoff. If the initial firn layer is too cold or has too much pore space, more meltwater can be refrozen, thereby underestimating runoff, and vice versa for a too warm initial firn layer. On a scale of the Antarctic ice sheet the effect of firn layer initialization is small, as the SMB is mainly determined by precipitation. However, this is not the case for the AP, where liquid water processes, such as surface melt, percolation, refreezing, surface ponding, hydrofracturing and runoff, are important and hence a correct estimate of the current firn layer is essential.

Knowledge of firn layer characteristics is also important for the calculation of ice sheet discharge. One way to determine ice discharge is to calculate the flux of solid ice over the grounding line, i.e. the ice velocity times the ice thickness [Rignot *et al.*, 2011a]. For the lat-

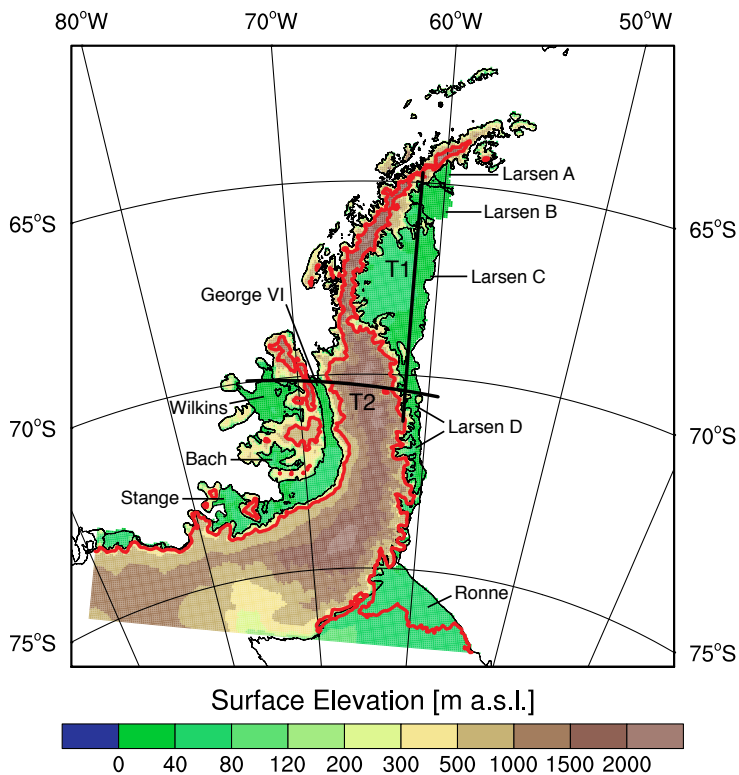


Figure 5.1: Map of the Antarctic Peninsula; shaded colors show the surface elevation of the ice sheet, in meters above sea level (m a.s.l.). Thin black lines show the ice-shelf ocean boundary and the grounding line, which marks the boundary between grounded and floating ice. Names indicate ice shelves (IS) used throughout the paper. The solid red line represents the upper boundary of the region where significant summer melt occurs ($>15 \text{ mm w.e. yr}^{-1}$ surface melt in 1988). Thick lines represent the two transects (T1 and T2) which are used in Figures 5.7 and 5.8. The sharp edges in the south and west mark the boundaries of the high-resolution (5.5 km) RACMO2 simulation domain.

ter, when a flotation criterion is used, remotely sensed surface elevation observations need a correction for the amount of air in the firn column. Until now, this quantity is either assumed constant for the complete ice sheet [e.g. *Rignot and Jacobs, 2002*] or calculated with a steady-state firn densification model [e.g. *Van den Broeke, 2008*]. Although the latter is a definite improvement over the first, as it takes spatial climate variability into account, the disadvantage of steady-state firn modeling is its inability to simulate melt processes. On the AP, this can have a large impact as surface melt occurs frequently, especially at lower altitudes where the grounding line is situated (Figure 5.1). Moreover, the AP grounding line is often located in complex topography making it useful to simulate it at higher horizontal resolution (5.5 km)

than currently available [27 km, *Ligtenberg et al.*, 2011]. Figure 5.1 shows the names of the ice shelves (IS) referred to in this manuscript.

In this study, an average firn layer for the AP region is calculated, using a combination of a firn densification model [*Ligtenberg et al.*, 2011], regional atmospheric climate model (RACMO2) [*Van Wesseem et al.*, 2014] and radar measurements of firn air content [*Holland et al.*, 2011]. First, the firn densification model and its atmospheric forcing will be discussed, as well as the different methods to calculate firn layers for different climate regimes. The result is a firn density map of the AP at high vertical and horizontal resolution (5.5 km), which is analyzed in Section 5.3 and discussed in Section 5.4.

5.2 Methods

5.2.1 Firn densification model

Observations of firn characteristics in the AP are scarce and therefore a firn densification model (FDM, *Ligtenberg et al.* [2011]) is used to simulate the AP firn characteristics. It is a one-column model that simulates both steady-state and time-dependent behavior of firn layer processes. It is equipped with a snowmelt module to simulate and calculate simple firn hydrology, i.e. percolation, retention, refreezing and runoff of meltwater. As a result, the FDM is able to simulate firn evolution across the complete range of Antarctic climate, instead of focussing solely on the dry-snow zone. Firn densification rates are calculated with the densification equations of *Arthern et al.* [2010], that were tuned to fit Antarctic firn depth-density observations [*Ligtenberg et al.*, 2011]. At the surface, the FDM is forced with realistic climate data: surface temperature, precipitation, sublimation, surface melt and 10-m wind speed.

5.2.2 Atmospheric forcing

Atmospheric forcing for the FDM is obtained from the regional atmospheric climate model RACMO2 [*Van Meijgaard et al.*, 2008; *Van Wesseem et al.*, 2014]. To simulate firn layer information at high horizontal resolution (5.5 km), also high resolution atmospheric forcing is required. No long period (>2 years) climate forcing at 5.5 km horizontal resolution is currently available, so the RACMO2 results at 27 km horizontal resolution [*Lenaerts et al.*, 2012a] are used to find a representative year in the period 1979–2012. Climate forcing for that particular year is generated on a 5.5 km horizontal grid by performing a dedicated run with RACMO2. This one-year climate forcing at 5.5 km resolution is assumed to be valid for the average climate and used iteratively to spin up the FDM [*Ligtenberg et al.*, 2011].

To find a representative 'average' year in the 27 km RACMO2 simulation, the differences in accumulation and surface melt between the annual average of each individual year and

the climate (1979–2012) average value are calculated for every land grid point. All absolute differences are squared and summed to gain a total combined deviation from the average for each year (Figure 5.2a). Differences in accumulation (precipitation minus sublimation minus drifting snow erosion) and melt are taken into account because both have a large impact on firn layer characteristics [Ligtenberg *et al.*, in review]. Differences in wind speed and temperature are second order effects. Figure 5.2a shows that four years (1988, 1991, 2002 and 2005) share the lowest total summed difference. After a qualitative assessment of the spatial difference in accumulation and melt (only 1988 shown in Figure 5.2b), 1988 was found to be the most suitable year. Especially above Larsen C IS, a region where firn characteristics are sensitive to differences in accumulation and melt, this year performed better than the other three.

Figures 5.3a–c show the annual averages for 1988 of three important climatic variables: surface temperature, accumulation and surface melt. The effect of the mountainous spine of the AP is clearly visible in all variables. At high altitudes, annual temperatures are relatively low (~ 250 K) and therefore no surface melt occurs. The west side of the mountain range is notably warmer and wetter than the east side, due to the predominately west-to-east transport of

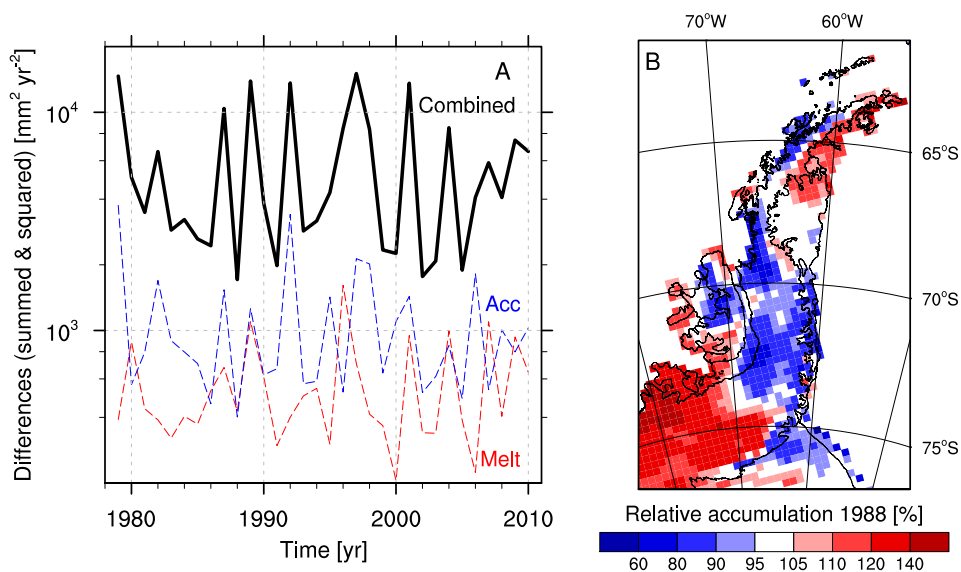


Figure 5.2: Time series of the least squares difference (A) in accumulation (blue dash), surface melt (red dash) and a combination of both (black solid) for every year compared to the 1979–2012 average from Lenaerts *et al.* [2012a]. To emphasize the variations, a logarithmic scale on the left axis was chosen and the accumulation and melt differences are multiplied by 10. Spatial variations in the relative difference of the average accumulation (precipitation minus sublimation minus drifting snow erosion) of 1988 (B) compared to the 1979–2012 average accumulation [Lenaerts *et al.*, 2012a].

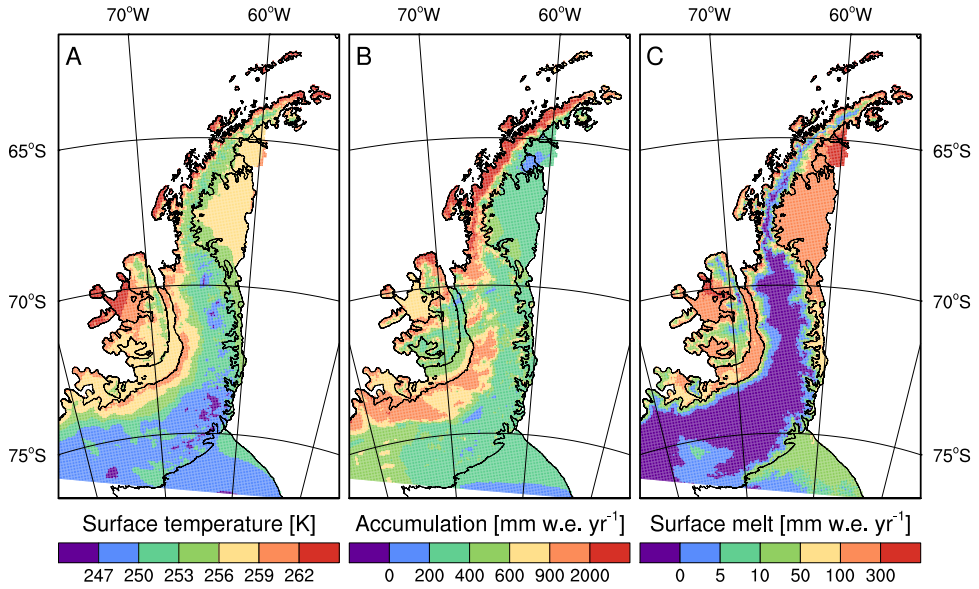


Figure 5.3: Annual average surface temperature in (A), accumulation (precipitation minus sublimation minus drifting snow erosion) in (B) and surface melt in (C) of 1988, from the high-resolution (5.5 km) RACMO2 simulation.

warm and moist ocean air over the mountains. At the north-western part of the AP some extremely high accumulation rates ($>10 \text{ m w.e. yr}^{-1}$) are simulated. Qualitatively, these results agree well with the 27 km RACMO2 simulation of the same year [Lenaerts *et al.*, 2012a].

Most ice shelves in the AP are located at the lee side of mountains (Larsen ABCD IS, George VI IS), causing relatively dry and warm conditions. The limit for ice shelf viability is found to be around -9°C annual near-surface temperature, with multiple ice shelves between -9°C and -5°C threshold have broken up during the last decades [Morris and Vaughan, 2003]. Due to the flat nature of ice shelves and their low surface altitude, they receive relatively little accumulation, and experience significant surface melt. The entire east side of the AP is fringed by ice shelves which show a distinct north-south gradient in melt; from $\sim 50 \text{ mm w.e. yr}^{-1}$ on the southern parts of Larsen D IS, melt increases towards the north to $\sim 400 \text{ mm w.e. yr}^{-1}$ on former Larsen A IS. Wilkins IS also experiences high melt rates, but receives significantly more accumulation due to its position on the west side of the AP. A distinct outlier is the Ronne IS, which is located so far south that it has a cold and dry climate with minor surface melt.

As accumulation and surface melt are the two main factors that determine firn density and depth variations in melt locations, their ratio is a measure for the type of firn layer present. The melt-accumulation ratio (MA) is therefore a useful measure for the ratio between the

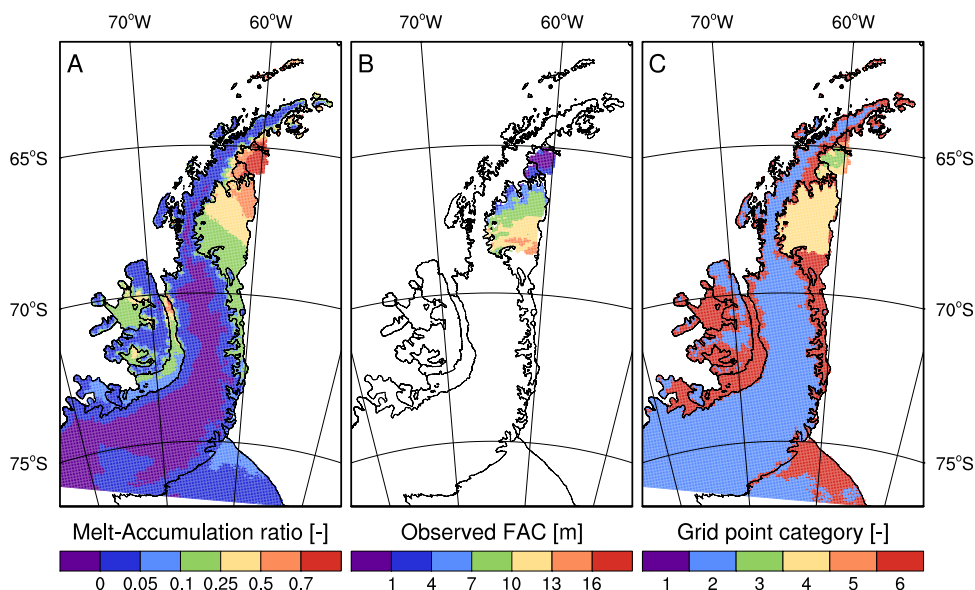


Figure 5.4: Spatial distribution of the Melt-Accumulation (MA) ratio from RACMO2 in (A), the firn air content (FAC) observation by radar measurements from Holland *et al.* [2011] in (B) and the category for the firn layer construction method (see Section 5.2.3) in (C).

annual accumulated firn air space and the amount of this pore space that is filled by refrozen meltwater. When MA exceeds ~ 0.7 , no permanent firn layer is present [Pfeffer *et al.*, 1991], indicating that $\sim 70\%$ of the annually accumulated snow can melt and refreeze in the remaining $\sim 30\%$ of accumulation. From Figure 5.4a it is clear that only the ice shelves have a MA ratio significantly > 0 . Most of the grounded ice sheet receives larger accumulation rates due to orographic uplift or does not experience substantial melt due to its high altitude, or a combination of both. On former Larsen B IS, MA is higher than 0.7 indicating that no long-term firn layer is present.

5.2.3 Firn layer construction

Due to the large variability in the AP climate, different methods to calculate the firn layer characteristics are used. At locations where annual melt is negligible, the firn layer is simulated with the steady-state FDM. This is computationally far less expensive and, at locations without melt the results from the steady-state and time-dependent simulations agree well [Ligtenberg *et al.*, in review]. Snowmelt has large seasonal and inter-annual variability, expressed by the highly variable firn density profiles with alternating layers of high and low density. Moreover, the firn temperature profile is influenced by the heat that is released when meltwater refreezes. For these locations, time-dependent FDM simulations are used. On

Larsen B and C IS, observations of the firn air content (FAC) from radar measurements [Holland *et al.*, 2011, , Figure 5.4b] are used as a guideline for the firn density profiles in this region. These FAC observations show a relatively good correlation with the MA ratio (Figure 5.5a), which will consequently be used to calculate firn density profiles on the remainder of the melt locations. Following the above, the grid points are subdivided into 6 categories:

- 1. annual accumulation < 0 : no firn layer
- 2. MA < 0.05 : steady-state FDM
- 3. present in Holland *et al.* [2011] and FAC < 0.5 m: ice-only layer
- 4. present in Holland *et al.* [2011] and FAC > 0.5 m: time-dependent FDM
- 5. not present in Holland *et al.* [2011] and MA > 0.7 : ice-only layer
- 6. not present in Holland *et al.* [2011] and MA < 0.7 : time-dependent FDM

Figure 5.4c indicates for every land grid point to what category it belongs. For example, along the spine of the major mountain range on the AP and in the southern part of the domain, no significant surface melt occurs and the firn layer is therefore simulated with the steady-state FDM. For the majority of Larsen C IS, observations of Holland *et al.* [2011] are available

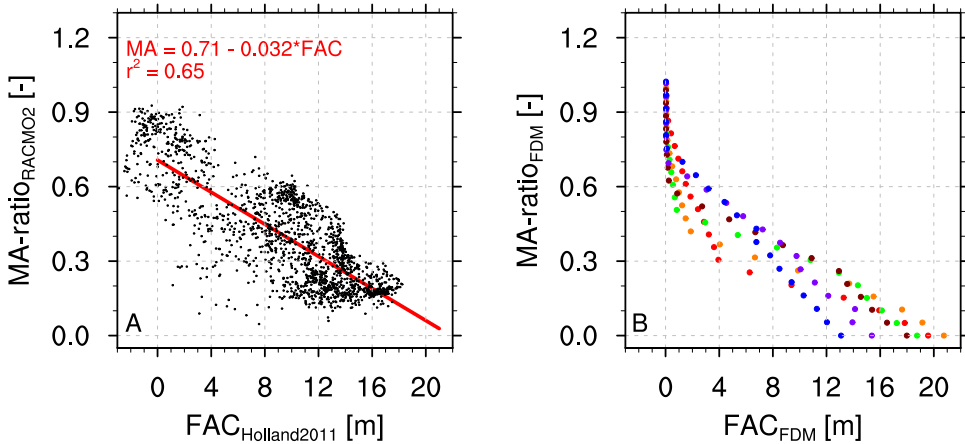


Figure 5.5: Observed firn air content (FAC) reported by Holland *et al.* [2011] ($FAC_{Holland2011}$) vs. Melting Accumulation (MA) ratio simulated by RACMO2 at high resolution ($MA-ratio_{RACMO2}$) in (A), including the linear regression line, equation and regression coefficient (red). FAC from the 120 FDM simulations (FAC_{FDM}) for different MA ratios in the atmospheric forcing ($MA-ratio_{FDM}$) with six different average accumulation rates (~ 200 (red), ~ 300 (orange), ~ 400 (green), ~ 600 (brown), ~ 750 (purple), ~ 900 (blue) mm w.e. yr⁻¹) in (B).

(Figure 5.4b) to constrain the firn density calculations. On former Larsen A and B IS, an ice-only layer is assumed, caused by either low FAC values from *Holland et al.* [2011] or high MA ratios in the RACMO2 climate (Figure 5.4a-b). On the remaining points, melt occurs annually and the time-dependent FDM is used to calculate the firn layer. In the 1988 climate forcing, no grid point with net annual ablation is simulated, so no category-1 point is present in Figure 5.4c. In the following sections, the different methods (2–6) for the firn layer construction will be discussed.

No surface melt (2)

On locations without melt, the density profile is calculated with the steady-state FDM solution of *Ligtenberg et al.* [2011]:

$$\frac{d\rho}{dz} = C dz \rho g (\rho_i - \rho) e^{\left(\frac{-E_c}{RT_s} + \frac{E_g}{RT_s}\right)} \quad (5.1)$$

$$\text{for } \rho < 550 \text{ kg m}^{-3} : C = 0.07 (1.435 - 0.151 \ln(\dot{b})) \quad (5.2)$$

$$\text{for } \rho > 550 \text{ kg m}^{-3} : C = 0.03 (2.366 - 0.293 \ln(\dot{b})) \quad (5.3)$$

where E_c and E_g are constants (see *Arthern et al.* [2010]), \dot{b} is the average annual accumulation, g the gravitational acceleration, ρ_i the ice density (917 kg m^{-3}), R the gas constant, dz the thickness of the layer and \bar{T}_s the average surface temperature. The density of the upper layer (i.e. the surface) is calculated following *Kaspers et al.* [2004], using the average accumulation, surface temperature and 10-m wind speed.

Firn air observations (3 & 4)

On the majority of Larsen B and C IS, FAC observations from radar measurements are available (Figure 5.4a). The FAC is defined as the firn layer thickness that results if the entire firn layer is compressed to the density of ice, and is therefore a useful indicator for the average density and depth of the firn layer. With the FDM, 120 sensitivity simulations with a combination of different accumulation rates (approximately 200, 300, 400, 600, 750 and $900 \text{ mm w.e. yr}^{-1}$) and MA values (0.02–1.0) are performed to simulate different climate conditions. The simulations are performed using realistic RACMO2 climate forcing, with adapted surface melt values to fulfill the prescribed MA value. These simulated density profiles encompass a large variety in FAC (Figure 5.5b). For every grid point that is assigned category 4, the resulting density profile from the sensitivity simulation with the best match in both local accumulation rate and observed FAC is chosen as the local density profile. The surface layer of the firn density profile is set to the local surface density, following *Kaspers et al.* [2004]. For a grid point where no firn air is observed (category 3), the entire firn column is initiated as ice ($\rho(z) = 917 \text{ kg m}^{-3}$).

Surface melt locations (5 & 6)

Locations that experience significant surface melt but have no spatial FAC observations (categories 5 and 6), cannot be treated by the above two methods. For these points, a relation between the FAC observations from *Holland et al.* [2011] and MA is used (Figure 5.5a). There is a significant linear correlation between increasing FAC and decreasing MA ($r^2 = 0.65$). For every grid point that is assigned category 6, a surrogate FAC value is calculated from the local MA using this linear relation (equation in Figure 5.5a). With this surrogate FAC and the local accumulation rate, the same procedure as for Larsen B and C IS is followed; the density profile from the sensitivity run with the best-match accumulation rate and FAC is chosen. Again, the upper layer for all points is calculated by the surface density equation of *Kaspers et al.* [2004]. For every grid point that has a $MA > 0.7$ (category 5), the complete firm layer is initialized as ice.

5.3 Results

Figures 5.6a–c show the resulting spatial distribution of the firm density at different depths (surface, 0–1 m and 20 m). The surface density is determined by the equation of *Kaspers et al.* [2004]. It shows high values on the western side of the mountain range spine and lower values on the eastern side, caused by the warmer and wetter conditions on the western side. On Larsen B IS, a small part of northern George VI IS and a few isolated grid points on the islands off the coast of the AP, the highest surface densities are calculated. On these locations no firm layer is calculated, either due to low FAC observations or too high MA (Figures 5.4a–b), and are initialized as ice-only.

At limited depth (0–1 m), the effect of melt on the firm density is clearly visible by the higher densities on ice shelves and across the coastal areas of the AP (Figure 5.6b). The FDM simulations start and end in January, i.e. austral summer, resulting in refrozen meltwater close to the surface. In surface melt locations, a highly variable pattern is found that can be attributed to the difference in accumulation rate and hence burial speed of ice layers. Since the depth of high density layers varies, an average over the depth interval 0–1 m is used in Figure 5.6b. In some locations (e.g. Wilkins IS, Bach IS and Stange IS), ice layers are simulated close to surface, resulting in a higher average density at limited depth. For the melt-free grounded ice sheet, Figure 5.6a and 5.6b are virtually similar, as firm density increases only slowly with depth.

At greater depth (20 m), a more uniform spatial pattern in firm density is visible, apart from some locations with substantial melt (Figure 5.6c). At these locations (e.g. the northern and western part of Larsen C IS and parts of Wilkins IS), the firm density at 20 m is high ($700\text{--}800 \text{ kg m}^{-3}$), indicating a thin firm layer. In part this is caused by the coarser vertical resolution at greater depths (below 15 m, the model layer thickness is 1 m), leading to smoother

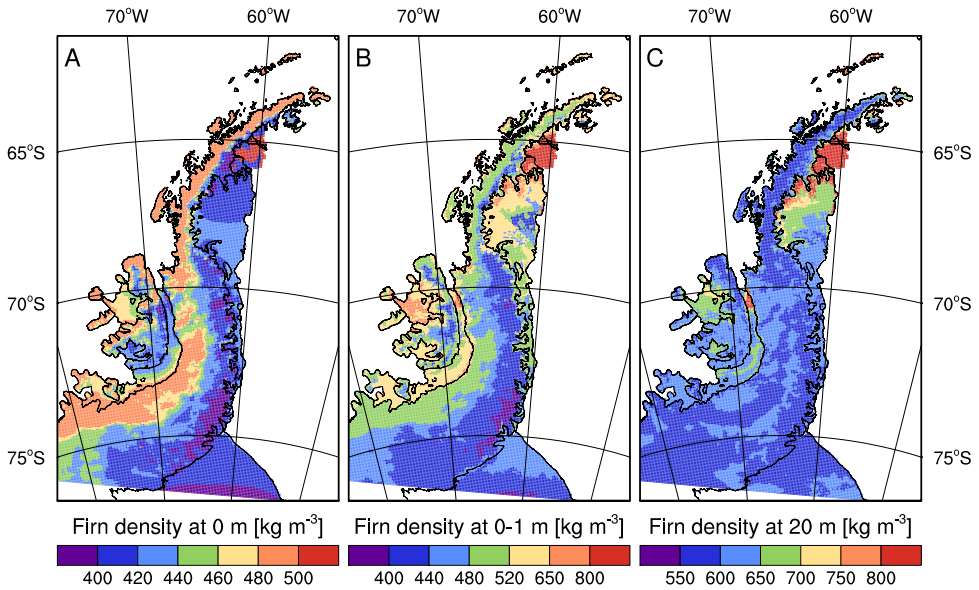


Figure 5.6: *Firn density at 0 m (A), averaged over the first meter, 0–1 m (B) and at 20 m (C) depth. Note the different, and non-linear color scales.*

horizontal and vertical patterns in firn density. On most of the other grid points, density ranges between $550\text{--}650\text{ kg m}^{-3}$, indicating the steady increase of density with depth. When the spatial pattern at depth (Figure 5.6c) is compared with that of the surface (Figure 5.6a), the suppressed densification rates in high accumulation regions is notable. On the western side of the mountains the density increases by $\sim 130\text{ kg m}^{-3}$ from the surface to 20 m, while on the eastern side this can be as much as 200 kg m^{-3} , resulting in a thicker firn layer on the western side of the mountains despite the higher surface densities.

In Figure 5.7, the spatial variability in density and depth of the firn layer along the north-south transect T1 (Figure 5.1) is shown. In the northern part of the transect, the ice-only column on Larsen B IS is distinctly visible between $65\text{--}66^\circ\text{S}$. Moving south, firn layers with high density are common due to the high melt rates on the northern section of Larsen C IS ($66.5\text{--}68^\circ\text{S}$). Further south, melt amounts are lower and FAC is higher. At the southern end (71.5°S), the transect moves off the ice shelf and to higher altitudes. As surface melt is negligible here (Figure 5.3c), a steady-state profile is calculated, characterized by a monotonous increase of density with depth. The north-south gradient in MA (Figure 5.4a) is resembled in the firn layer thickness along the transect, increasing from 60 m to >100 m moving southwards on Larsen C IS ($66.5\text{--}69.5^\circ\text{S}$).

Figure 5.8 shows the firn depth and density along the east-west transect T2 (Figure 5.1). At the western boundary, the transect starts on Wilkins IS ($73\text{--}71^\circ\text{W}$) where high density firn

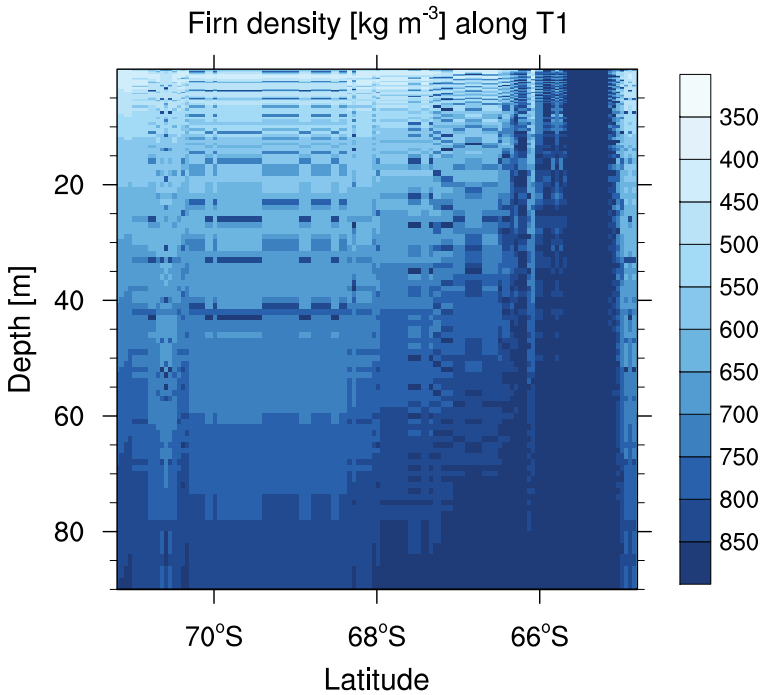


Figure 5.7: *Firn density cross-section along the north-south transect T1 (Figure 5.1).*

layers are simulated, caused by substantial melt. However, this area has a high accumulation rate, due to its location on the western side of the AP, and can therefore accommodate a large meltwater flux. Moving eastward, the transect passes over Alexander Island (70–69°W), which experiences high accumulation rates and little melt, resulting in a thick firn layer with low density. The firn density at 90 m depth (710 kg m⁻³) is one of the lowest values in the AP. Hereafter, the transect descends onto the northern part of George VI IS (~68°W), where high densities are simulated. This includes two grid points with an ice-only column, in qualitative agreement with observations of annual meltwater ponding at the surface [Reynolds, 1981; LaBarbera and MacAyeal, 2011], indicating there is no firn to accommodate summer melt. From 67–63°W, the transect ascends over the AP mountain range, where steady-state firn density profiles are calculated as this region experiences no melt. A gradual transition from the warmer and wetter western side to the colder and drier eastern side of the mountains is visible in the density profiles; at the surface, higher densities are present in the west, while at greater depths the highest densities are calculated in the east, showing the faster densification with depth in low accumulation regions. At the eastern end of the transect, high density layers are again simulated on the lower areas of the grounded ice and on Larsen D IS, where regular melt occurs.

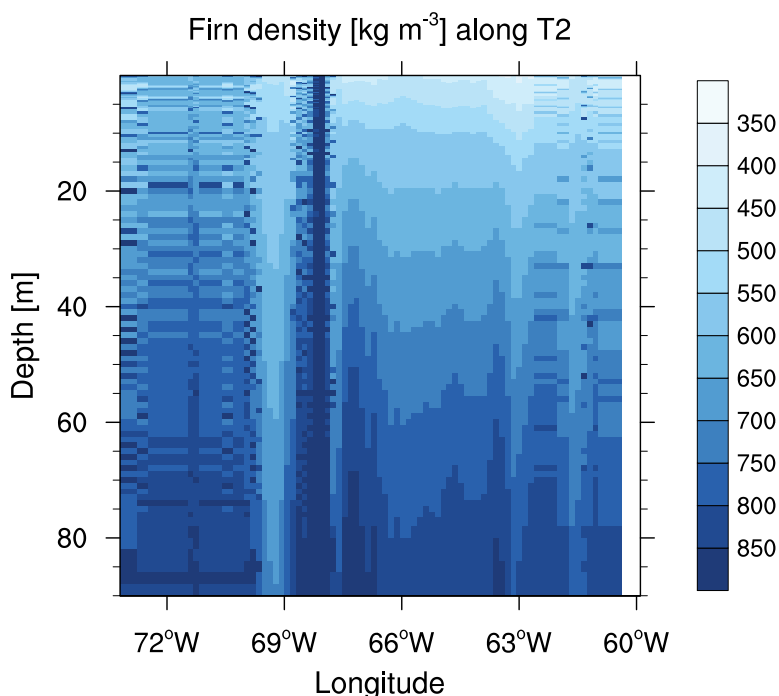


Figure 5.8: *Firn density cross-section along the east-west transect T2 (Figure 5.1).*

The density profiles along T2 show a wide spread in firn layer thickness, ranging between 40–70 m on the western ice shelves (Wilkins IS and George VI IS) to more than 150 m on the western side of the AP mountain range. Figure 5.9 shows the spatial distribution of FAC across the AP, which summarizes the conclusions from Figures 5.4, 5.6, 5.7 and 5.8. Former Larsen A and B IS, and the northern part of George VI IS are the only locations in the AP without a substantial firn layer. These, therefore, are regions where meltwater cannot be stored in the firn pack and will run off. In the future, more widespread runoff will occur due to the increase in surface melt and subsequent decrease in FAC. Regions with a currently low FAC, such as north(-west)ern Larsen C IS and northern Wilkins IS, are expected to become prone to firn air depletion and runoff production in the near-future. *Kuipers Munneke et al.* [2014] found that during the 21st century the largest FAC decrease is expected on the northern AP ice shelves. The other Antarctic ice shelves show the largest decreases during the 22nd century.

On Larsen C IS, the spatial pattern in FAC agrees well with that of *Holland et al.* [2011], indicating that the selection procedure, described in Section 5.2.3, works well. On the more southern located ice shelves (e.g. Stange IS, southern George VI IS, Larsen D IS and Ronne IS), a rather consistent pattern in FAC is found with FAC values ranging between 15–21 m.

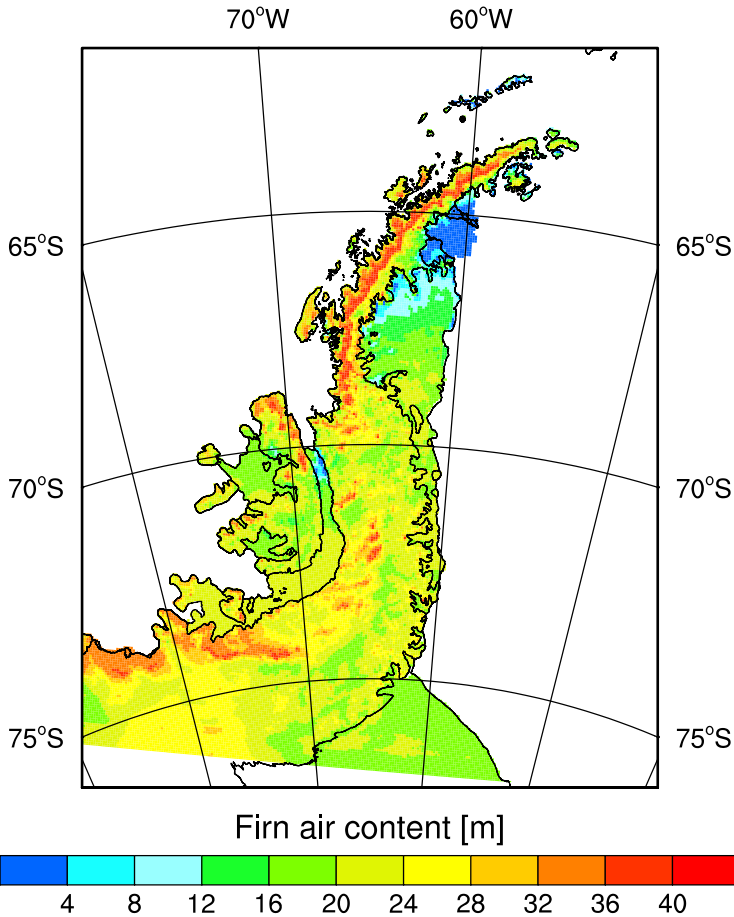


Figure 5.9: *Spatial distribution of the firn air content (FAC).*

Almost without exception, the FAC on the grounded ice sheet is higher than on the ice shelves, as a result of the higher accumulation rates and lack of substantial melt. Especially on the western side of the mountain range between 64–68°S, large FAC values (35–50 m) are simulated. Again, there is a distinct difference between the western and eastern side of the AP, where high/low accumulation causes high/low FAC values.

5.4 Discussion

The largest uncertainties in the results presented here are caused by the uncertain climate forcing from RACMO2 and the selection method to construct density profiles using multiple

FDM simulations. A firn layer consists of snow that has accumulated on the ice sheet over several decades to centuries, making knowledge of the long-term climate crucial for a correct calculation of the firn layer. Here, we use only one year (1988) of climate data and assume that it is representative for the long-term climate. Although this year is selected because it shows the smallest difference with the average 1979–2010 climate from *Lenaerts et al.* [2012a], a major part of the AP shows a significant ($>10\%$) deviation from this average (Figure 5.2b). Repeating the entire procedure using another year would provide insight in the uncertainty introduced by this assumption, which, however, is computationally expensive.

By using only a single year of climate forcing, no realistic inter-annual variability is introduced in the modeled firn layer. This is of minor importance on locations without melt, as long as the annual accumulation has the correct magnitude. However, for surface melt locations, the timing of melt and accumulation events has a major influence on the formation of high-density layers and hence the FAC. For instance, two subsequent strong melt summers followed by two summers without melt have a different effect on firn density than an alternating pattern of weak and strong melt summers. In addition to this lack of inter-annual variability, temporal variations in FAC are currently also not taken into account, while it has been shown that significant (as large as 2 m) year-to-year FAC variations can occur, especially in melt regions [*Ligtenberg et al.*, in review]. The above simplifications in the climate forcing introduces quite substantial uncertainties in firn characteristics. We claim, however, that both the spatial pattern and wide range in FAC are robust, as they depend on gradients in the climate forcing rather than on the absolute magnitude.

Additional uncertainty is introduced by the selection procedure for surface melt locations. In principle, every grid point has a unique climate, that generates a unique firn layer. Although the FDM sensitivity simulations cover a wide range of accumulation rates (6) and MA-ratios (20), only 120 different firn profiles are generated for ~ 9200 grid points that experience melt. Two neighboring grid points on a relatively large and homogeneous ice shelf are likely to have a similar climate (i.e. accumulation and melt), and therefore also a similar MA-ratio. As the annual accumulation and MA-ratio determine the selection procedure, it is also likely that the same density profile is assigned to both grid points. As a consequence, the grid-point-to-grid-point variability is underestimated. On Larsen C IS, a more variable FAC pattern is simulated, as a result of the availability of the observations of *Holland et al.* [2011]. These small-scale spatial variations are likely caused by the topography of the mountains to the east. The absence of similar variations in the RACMO2 climate indicates that the foehn effect over these mountains is not well represented in the RACMO2.

To conclude, a high-resolution firn-density map of the AP was obtained by a combination of steady-state and time-dependent firn modeling. In this way, we could assess the average firn characteristics and at the same time incorporate the effects of melt, while keeping the methods computationally feasible. The simulation of low FAC and ice-only columns on former Larsen B IS and northern George VI IS agrees well with visual observations of meltwater ponding and runoff. Elsewhere on the AP ice shelves, FAC varies between 6–20 m. The low values

represent ice shelves that are likely to produce future runoff (e.g. northern Larsen C IS and Wilkins IS), high values represent ice shelves with a much thicker firn layer that can easily accommodate future increasing melt fluxes (e.g. Stange IS and Ross IS). On the grounded ice sheet, a distinct difference between the western and eastern side of the mountain range is visible in the firn characteristics, mainly due to higher accumulation rates in the west.

Future climate and surface mass balance of Antarctica

Summary

A regional atmospheric climate model with multi-layer snow module (RACMO2) is forced at the lateral boundaries by global climate model (GCM) data to assess the future climate and surface mass balance (SMB) of the Antarctic ice sheet (AIS). Two different GCMs (ECHAM5 until 2100 and HadCM3 until 2200) and two different emission scenarios (A1B and E1) are used as forcing to capture a realistic range in future climate states. Simulated ice sheet averaged 2-meter air temperature (T_{2m}) increases (1.8–3.0 K in 2100 and 2.4–5.3 K in 2200), simultaneously and with the same magnitude as GCM simulated T_{2m} . The SMB and its components increase in magnitude, as they are directly influenced by the temperature increase. Changes in atmospheric circulation around Antarctica play a minor role in future SMB changes. During the next two centuries, the projected increase in liquid water flux from rainfall and snowmelt, together 60–200 Gt yr^{-1} , will mostly refreeze in the snow pack, so runoff remains small (10–40 Gt yr^{-1}). Sublimation increases by 25–50 %, but remains an order of magnitude smaller than snowfall. The increase in snowfall mainly determines future changes in SMB on the AIS: 6–16 % in 2100 and 8–25 % in 2200. Without any ice dynamical response, this would result in an eustatic sea level drop of 20–43 mm in 2100 and 73–163 mm in 2200, compared to the 20th century. Averaged over the AIS, a strong relation between ΔSMB and ΔT_{2m} of $98 \pm 5 \text{ Gt w.e. yr}^{-1} \text{ K}^{-1}$ is found.

This chapter is published as: Ligtenberg S. R. M., W. J. van de Berg, M. R. van den Broeke, J. G. L. Rae, and E. van Meijgaard (2013), Future surface mass balance of the Antarctic ice sheet and its influence on sea level change, simulated by a regional atmospheric climate model. *Climate Dynamics*, **41**, 867–884, doi:10.1007/s00382-013-1749-1.

6.1 Introduction

The fourth Assessment Report of the Intergovernmental Panel on Climate Change (IPCC AR4) projects global sea level to rise by 0.18–0.59 m at the end of the 21st century, relative to the end of the 20th century, excluding ice dynamical effects [IPCC, 2007]. Currently (1993–2009), the rate of global sea level rise (SLR) is $\sim 3.3 \text{ mm yr}^{-1}$ [Nicholls and Cazenave, 2010]. The largest contributors to SLR are the melting of ice sheets, ice caps and valley glaciers and thermal expansion of ocean water [Church *et al.*, 2011]. The two major ice sheets of Greenland and Antarctica lost mass at a combined rate of $402 \pm 201 \text{ Gt yr}^{-1}$ ($1.1 \pm 0.6 \text{ mm SLR yr}^{-1}$) over the 2003–2008 period [Van den Broeke *et al.*, 2011], hence contributing $\sim 30\%$ to ongoing SLR. In a warmer future climate, the relative contribution of these ice sheets to SLR is expected to increase further [Rignot *et al.*, 2011a].

Because of its size and remoteness, estimating the Antarctic ice sheet (AIS) mass balance and thereby its contribution to SLR is difficult. Three methods are currently used: i) the volumetric method, ii) the gravimetry method and iii) the mass budget method. The first converts remotely sensed surface elevation changes into mass changes [Davis *et al.*, 2005], the second deduces mass changes in time directly from satellite measured gravity changes [Velicogna, 2009] and the third differences mass in- and output, i.e. surface mass balance (SMB) and ice discharge [Rignot *et al.*, 2011a]. Over the last 30–50 years, the SMB of the AIS showed little change [Monaghan *et al.*, 2008; Lenaerts *et al.*, 2012a]. Combined with an increase in ice discharge, this currently leads to a positive contribution of the AIS to SLR: $0.2 \pm 0.15 \text{ mm SLR yr}^{-1}$ [Shepherd *et al.*, 2012]. Volumetric and/or gravimetric measurements suggest zero mass balance to a small mass gain in East Antarctica, and significant mass losses in West Antarctica and the Antarctic Peninsula [Davis *et al.*, 2005; Pritchard *et al.*, 2009; Velicogna, 2009]. The first and second method are fully based on observations and can therefore not be used to predict the future mass balance of Antarctica. For the third method however, future SMB and ice dynamics can be estimated with the use of climate and ice dynamical models.

The AIS is the largest reservoir of frozen fresh water on Earth; if melted completely, global sea level would rise by about 57 m [Lythe *et al.*, 2001]. With a mass turnover of $\sim 2500 \text{ Gt yr}^{-1}$ [Lenaerts *et al.*, 2012a], equivalent to $\sim 6.9 \text{ mm}$ eustatic sea level change, even a relatively minor change ($<10\%$) in the AIS mass balance has a significant effect on global sea level. With temperatures rising globally, the Antarctic climate is also expected to warm, probably resulting in more melting in low-lying regions, and more snowfall continent-wide because of the increased water vapor holding capacity of the Antarctic atmosphere [Krinner *et al.*, 2007]. The mass gain from enhanced snowfall is expected to be larger than the mass loss from enhanced runoff. Previous studies indicate that increasing temperatures cause a 5–9% K^{-1} mass input increase of the AIS [Wild *et al.*, 2003; Gregory and Huybrechts, 2006; IPCC, 2007]. For the coming century, the SMB of the AIS is therefore expected to cause a sea level drop of $\sim 50 \text{ mm}$ [Krinner *et al.*, 2007; Bengtsson *et al.*, 2011]. On the other hand, changes in

ocean circulation may have the potential to enhance melt rates at the bottom of ice shelves by directing warmer water underneath them [Hellmer *et al.*, 2012]. This could lead to thinning of these ice shelves from below and thereby reducing the buttressing effect on outlet glaciers, and increasing ice discharge [Rignot and Jacobs, 2002; Pritchard *et al.*, 2012]. How this will contribute to sea level change in the 21st century is currently uncertain.

Here, we present estimates of the future SMB of the AIS and its impact on SLR, as simulated by a regional atmospheric climate model. The horizontal model resolution of coupled atmosphere-ocean global climate models (GCMs) is currently insufficient to accurately resolve changes in the Antarctic coastal climate and SMB processes are often poorly parameterized in these models. Moreover, an accurate treatment of SMB requires a detailed description of processes in the snowpack. The regional atmospheric climate model RACMO2 has a higher resolution and includes a specially-developed multi-layer snow model [Ettema *et al.*, 2009; Kuipers Munneke *et al.*, 2011]. In this study, RACMO2 is forced at the boundaries by two different GCMs, each driven by two different greenhouse gas emission scenarios (A1B and E1), to obtain a range of possible future SMB scenarios. To check the reliability of the forcing fields, simulations for the period 1980–1999 are compared to a RACMO2 benchmark simulation forced by re-analysis data. Modelling of future ice-dynamics, to make an estimate of the AIS future mass balance, is outside the scope of this paper. In Section 6.2, RACMO2, the GCMs and the emission scenarios are discussed. In Section 6.3, we present a comparison of the GCM and re-analysis forced simulations for the 1980–1999 climate. Thereafter, the results of the future scenarios are discussed in Section 6.4, followed by conclusions and discussions in Section 6.5.

6.2 Methods

6.2.1 Surface mass balance

The surface mass balance (SMB) of an ice sheet is defined as the annual sum (in Gt yr^{-1}) of precipitation (P), surface sublimation (SU_s), runoff (RU), erosion by drifting snow (ER_{ds}) and sublimation due to drifting snow (SU_{ds}):

$$\text{SMB} = \int_{\text{year}} (P - SU_s - RU - ER_{ds} - SU_{ds}) dt \quad (6.1)$$

In Antarctica, runoff is currently small because nearly all liquid water from snowmelt and rainfall refreezes in the firn layer. Sublimation of surface and drifting snow is the most important ablation term for the AIS, yet it is an order of magnitude smaller than accumulation by snowfall. Erosion by blowing snow is small on a continental scale and only locally impor-

tant. Therefore, the current SMB of the AIS and its temporal and spatial variability is mainly determined by snowfall [Lenaerts and Van den Broeke, 2012].

6.2.2 Regional atmospheric climate model RACMO2

All simulations are performed with the regional atmospheric climate model RACMO2 [Van Meijgaard *et al.*, 2008]. At the lateral boundaries of the domain, RACMO2 is forced using fields of temperature, specific humidity, zonal and meridional wind components, and surface pressure from either GCM or re-analysis output. Relaxation of RACMO2 prognostic variables towards external forcings is restricted to the boundary relaxation zone (Figure 6.1). External forcings are updated every six hours and linearly interpolated in time to yield accurate values in between. Sea surface temperatures and sea-ice extent are also prescribed from the forcing model. The version of RACMO2 used for this study includes a snow model that calculates temperature, density and meltwater processes (percolation, retention, refreezing and runoff) in the snow [Ettema *et al.*, 2009], and an improved albedo scheme, where the snow albedo depends on snow grain size [Kuipers Munneke *et al.*, 2011]. For this study, contributions from drifting snow processes have not been included, because the module of Lenaerts and Van den Broeke [2012] was not yet fully implemented when we started the simulations.

For contemporary climate studies of the AIS (1–30 years), RACMO2 has been run on grids with 27 km and 5.5 km horizontal resolution [Lenaerts *et al.*, 2012a,b]. However, for the number of simulation years considered here (660 years in total), a horizontal resolution of 55 km is considered a good trade-off between computational expense and spatial detail; doubling the grid resolution would multiply the computational time by a factor 10. Moreover, the annual integrated SMB of the AIS at 55 km resolution [Van de Berg *et al.*, 2006] is similar to that at 27 km resolution [Lenaerts *et al.*, 2012a]. For the scenario runs, the largest uncertainty therefore derives not from the model resolution but from the chosen forcing model and scenario. Given this information, and the fact that a 27 km resolution run is ten times as expensive as a 5.5 km run, we chose 55 km as final resolution. The model topography, grid resolution and lateral relaxation boundary of the domain are shown in Figure 6.1.

For the period 1980–1999, a RACMO2 reference simulation, forced by ERA-40 re-analysis data from the European Centre for Medium-Range Weather Forecasts [Uppala *et al.*, 2005], was performed in order to check the reliability of the GCM-forced RACMO2 simulations. In this paper, ERA-40 has been used as forcing instead of its successor ERA-Interim [Dee and *et al.*, 2011], since the latter only covered the period 1989–2009 at the time the RACMO2 simulations were started. Other RACMO2 simulations forced by re-analysis data (ERA-40 or ERA-Interim) yielded realistic SMB results over Antarctica when compared to in-situ SMB measurements [Van de Berg *et al.*, 2006; Van den Broeke, 2008; Lenaerts *et al.*, 2012a]. For the purpose of this paper, we therefore consider the RACMO2 SMB field as a benchmark when assessing GCM-forced RACMO2 simulations.

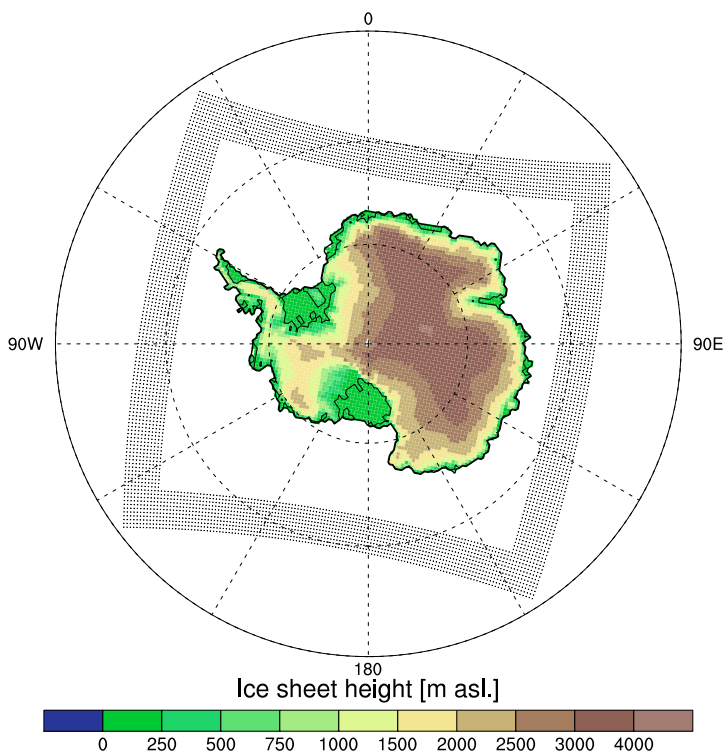


Figure 6.1: Map of Antarctica showing the model domain, the boundary relaxation zone (dotted area) and model topography in meters above sea level.

6.2.3 GCM forcing

Table 6.1 gives an overview of all simulations performed with RACMO2, their acronym, lateral forcing, emission scenario and time period. In the remainder of this paper, the full name of a GCM (HadCM3 or ECHAM5) is used to refer to direct GCM output, while acronyms starting with "R-" (left column in Table 6.1) refer to individual RACMO2 simulations.

For the six other simulations (Table 6.1, except R-ERA), RACMO2 is forced at the lateral boundaries with output from either ECHAM5 or HadCM3; two fully coupled GCMs from the Coupled Model Intercomparison Project (CMIP3, as used in IPCC [2007]). Data of these models have been made available through the ice2sea project. ECHAM5 contains the latest cycle of the European Centre/Hamburg model version 5 for the atmosphere and the Max Planck Institute Ocean Model (MPI-OM) for the ocean [Muller and Roeckner, 2007]. For HadCM3, that contains the atmospheric model HadAM3 [Pope et al., 2000] and the ocean model HadOM3 [Gordon et al., 2000], we use the model version that was used in the ENSEMBLES project; HadCM3C [Johns et al., 2011]. HadCM3 data are available for

Table 6.1: Overview of RACMO2 simulations (acronyms as used in this paper), their lateral forcings, emission scenarios and the time period covered.

Simulation acronym	Model forcing	Scenario	Time period
R-ERA	ERA-40	20c	1980–1999
R-H3	HadCM3	20c	1980–1999
R-E5	ECHAM5	20c	1980–1999
R-E5-A1B	ECHAM5	A1B	2000–2099
R-E5-E1	ECHAM5	E1	2000–2099
R-H3-A1B	HadCM3C	A1B	2000–2199
R-H3-E1	HadCM3C	E1	2000–2199

220 years (1980–2199) and ECHAM5 data for 120 years (1980–2099). Both ECHAM5 and HadCM3 have a reasonable horizontal resolution for GCM standards: $3.75^\circ \times 3.75^\circ$ and $2.5^\circ \times 3.75^\circ$ respectively, which translates to $\sim 400 \times 125$ km and $\sim 275 \times 125$ km in Antarctic coastal areas. ECHAM5 and HadCM3 are both preferred forcing models as they perform well in intercomparison and validation studies that focus on the polar regions [Connolley and Bracegirdle, 2007; Chapman and Walsh, 2007; Franco *et al.*, 2011; Maris *et al.*, 2012].

Two different greenhouse gas emission scenarios are considered: A1B and E1. In the IPCC SRES A1B scenario, fossil fuel emissions double in 2050, compared to 1990, and CO_2 concentrations rise to roughly 700 ppmv [Nakicenovic *et al.*, 2000]. As a consequence, the GCM ensemble in IPCC AR4 predict average global 2-m air temperature (T_{2m}) to rise by 2.8 K, with a likely range of 1.7–4.4 K, in the 21st century [IPCC, 2007]. A1B is a moderate emission scenario and represents the middle to high temperature rise as predicted by IPCC AR4. The A1B scenario is only defined until 2100; for post-2100 simulations CO_2 concentrations are considered to remain constant at their 2100-level (~ 900 ppmv). The European ENSEMBLES project E1 scenario is a strong mitigation scenario. It follows the European Union climate policy, stating that a 2 K rise in global T_{2m} compared to pre-industrial levels should be considered a maximum acceptable temperature rise. In the E1 scenario, CO_2 concentrations are therefore restricted to peak at 530 ppmv around 2050 and slowly decrease afterwards [Lowe *et al.*, 2009].

Figure 6.2 shows global (thick lines, left axis) and Antarctic (thin lines, right axis) average T_{2m} for the next two centuries as simulated by the HadCM3 model. In the E1 scenario, global T_{2m} reaches its maximum increase of 1.7 K in 2070, so it remains below the upper boundary imposed for this emission scenario. After 2070, temperatures remain rather constant, with even a slight negative trend in the late 22nd century. In the A1B scenario, global T_{2m} shows a more pronounced rise of 4.0 K in the 21st century, and the warming stabilizes around +5.4 K in 2130. The HadCM3 simulated temperature rise exceeds the average IPCC global temperature rise (+2.8 K in 2100). For both scenarios, the AIS averaged T_{2m} follows the same pattern of temperature increase and stabilization afterwards. The simulated temperature rise in ECHAM5 until 2100 is similar to that found in HadCM3 (not shown).

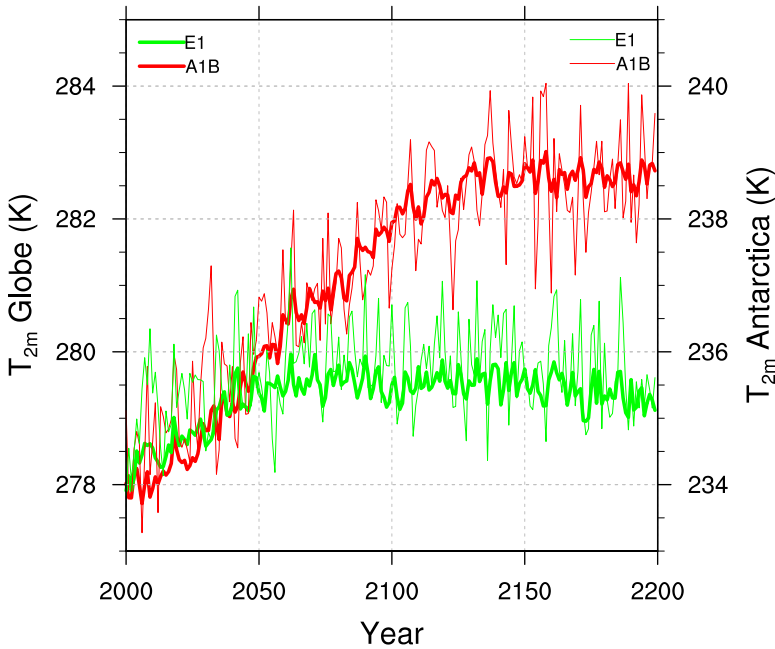


Figure 6.2: Time series (2000–2199) of globally averaged (thick lines, left axis) and Antarctic averaged (thin lines, right axis) 2-m air temperature (T_{2m}) as simulated by HadCM3 for the A1B (red) and E1 (green) emission scenarios.

6.3 Results: current climate

6.3.1 Temperature

For the period 1980–1999, Table 6.2 lists the simulated Antarctic climate of the GCM-forced RACMO2 simulations R-H3, R-E5, the RACMO2 benchmark simulations R-ERA and the direct GCM output of HadCM3 and ECHAM5. Annual ice sheet average T_{2m} in both R-H3 (-1.5 K) and R-E5 (-2.0 K) is lower than in R-ERA (Figure 6.3 and Table 6.2). The inter-annual variability in the reference period, given as the standard deviation in Table 6.2, is similar for the three historical RACMO2 simulations (R-ERA, R-H3 and R-E5). The average temperature in the vertical atmospheric column (T_{atm}) is also lower, with R-H3 (-2.6 K) yielding smaller differences than R-E5 (-3.0 K). In both GCM forced simulations (R-H3 and R-E5), T_{2m} shows a spatially uniform negative temperature deviation over the AIS (Figure 6.3). R-E5 shows more spatial variation in the difference than R-H3, with differences up to -4 K on the Ross and Filchner-Ronne ice shelves and in West-Antarctica, and the smallest differences in coastal Dronning Maud Land (DML, 75°S, 10°S). A likely cause for the lower T_{2m} in the GCM forced simulations is the lower sea surface temperatures (south of

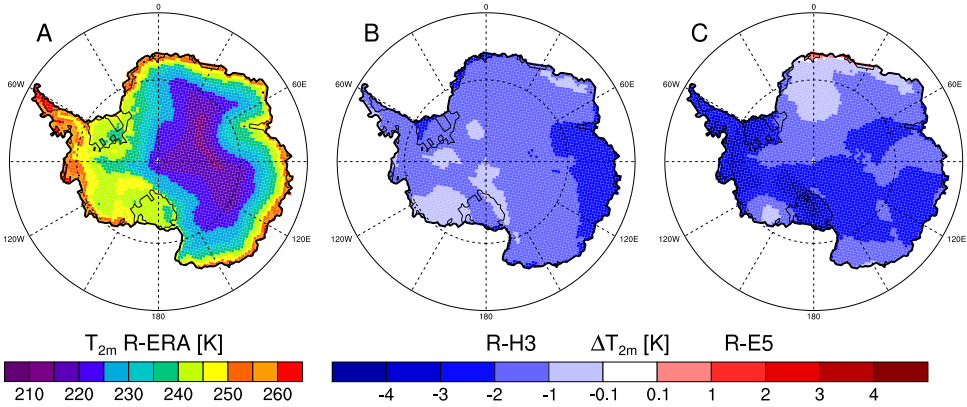


Figure 6.3: Spatial distribution (1980–1999 average) of 2-m temperature (T_{2m}) for R-ERA (A) and the difference in T_{2m} between R-H3 and R-ERA (B) and R-E5 and R-ERA (C).

60°S, -0.2 K in HadCM3 and -0.6 K in ECHAM5), and associated higher sea ice concentrations. This reduces the transport of heat towards the atmosphere over the AIS. The reduced strength of low pressure systems over the Southern Ocean further weakens this meridional heat transport, as will be discussed later in in this section.

6.3.2 Surface mass balance (SMB)

All SMB components are underestimated by R-E5 and R-H3, compared to R-ERA (Table 6.2), due to the lower simulated temperatures in the GCM-forced simulations, as colder air has less water vapor holding capacity than warmer air. Snowfall amounts are therefore lower in the GCM-forced simulations (R-H3 -14 % and R-E5 -19 %). The larger temperature deviation in R-E5 is reflected in a larger snowfall difference. Also rainfall, sublimation, and snowmelt are underestimated due to the cold biases in R-E5 and R-H3 (Table 6.2). The reduction of available liquid water from rainfall and snowmelt leads to lower refreezing and runoff amounts in R-E5 and R-H3. Runoff is a small SMB component in R-ERA ($\sim 10 \text{ Gt yr}^{-1}$) and almost absent in R-H3 and R-E5. It should be noted that the average runoff values in all historical RACMO2 simulations (R-E5, R-H3 and R-ERA) are lower due to model spin-up: the snow pack in RACMO2 is initialized without liquid or refrozen meltwater and the model takes ~ 10 years to adjust [Ettema, 2010], especially in areas where liquid water processes are important (e.g. the Antarctic Peninsula). However, as runoff on Antarctica is small, the impact on the SMB is minor. All in all, we find lower SMB values in R-H3 (-14 %) and R-E5 (-19 %) compared to R-ERA. These values again show that differences in snowfall almost fully determine differences in SMB.

Figure 6.4a shows the spatial distribution of the AIS SMB in R-ERA, which is similar to the spatial pattern found by *Van de Berg et al.* [2006] and *Lenaerts et al.* [2012a]. It also resembles the range of simulated SMB values ($<20 \text{ mm yr}^{-1}$ in a large part of East Antarctica and up to 2000 mm yr^{-1} on the Antarctic Peninsula). Figures 6.4b–c show the spatial differences in SMB between the GCM-forced simulations (R-H3 and R-E5) and R-ERA. The differences are generally within 10 % of the total SMB; large increases are found on the Ross Ice Shelf and its vicinity and in parts of coastal DML, while the largest negative deviations are found in Wilkes Land and West Antarctica. These patterns are caused by differences in the surface pressure (p_{surf}) distribution around Antarctica (Figure 6.4d–f). There are typically three climatological low pressure centers located around Antarctica; i) in the Amundsen Sea, ii) off the coast of DML and iii) off the coast of Wilkes Land (Figure 6.4d), as described by *Van den Broeke and Van Lipzig* [2004]. These low pressure centers determine the location and strength of the meridional transport of heat and moisture onto the AIS. In both R-H3 and R-E5, the low pressure systems are less pronounced than in R-ERA, regionally resulting in less transport of moisture towards the AIS. For example, lower snow accumulation/SMB in West Antarctica can be attributed to a weaker Amundsen Sea low pressure system: 980.8 hPa in R-ERA, 981.5 hPa in R-H3 and ~ 985 hPa in R-E5 (in the latter model, there is no distinct low pressure center in the Amundsen Sea). Simultaneously, the flow off the ice sheet around the Ross Ice Shelf is also weakened and as a result moist air from the ocean will more often flow onto the ice sheet, leading to more precipitation in this region. For R-E5, p_{surf} differences are larger, compared to R-H3, resulting in larger SMB differences, however the spatial patterns are similar to R-H3.

Table 6.2: RACMO2 output, forced by ERA-40 (R-ERA), ECHAM5 (R-E5) and HadCM3 (R-H3) and direct GCM output (ECHAM5 and HadCM3). Listed are 20-year (1980–1999) ice sheet averages and corresponding standard deviations for $T_{2\text{m}}$, T_{atm} , snowfall, rainfall, total precipitation, sublimation, snowmelt, refreezing, runoff and SMB. *HadCM3 output represents 1.5-m temperature.

Variable	R-ERA	R-E5	ECHAM5	R-H3	HadCM3
$T_{2\text{m}}$	235.0 ± 0.6	233.0 ± 0.7	233.1 ± 0.5	233.5 ± 0.7	$234.3^* \pm 0.5$
T_{atm}	228.5 ± 0.5	225.5 ± 0.4		225.9 ± 0.7	
Snowfall	2421 ± 97	1957 ± 57		2083 ± 89	
Rainfall	27.5 ± 6.7	12.8 ± 4.5		18.2 ± 5.9	
Precipitation	2448 ± 97	1970 ± 58	2428 ± 81	2101 ± 90	2381 ± 118
Sublimation	75.8 ± 7.2	64.3 ± 8.6	7.6 ± 3.5	61.5 ± 7.7	175 ± 8.7
Snowmelt	100.3 ± 23.4	55.5 ± 28.5		46.0 ± 15.6	
Refreezing	123.5 ± 25.1	68.1 ± 32.6		64.0 ± 19.7	
Runoff	4.3 ± 4.3	0.3 ± 0.4	0.0 ± 0.0	0.2 ± 0.3	171 ± 37
SMB	2353 ± 97	1896 ± 57	2421 ± 81	2029 ± 88	1988 ± 132

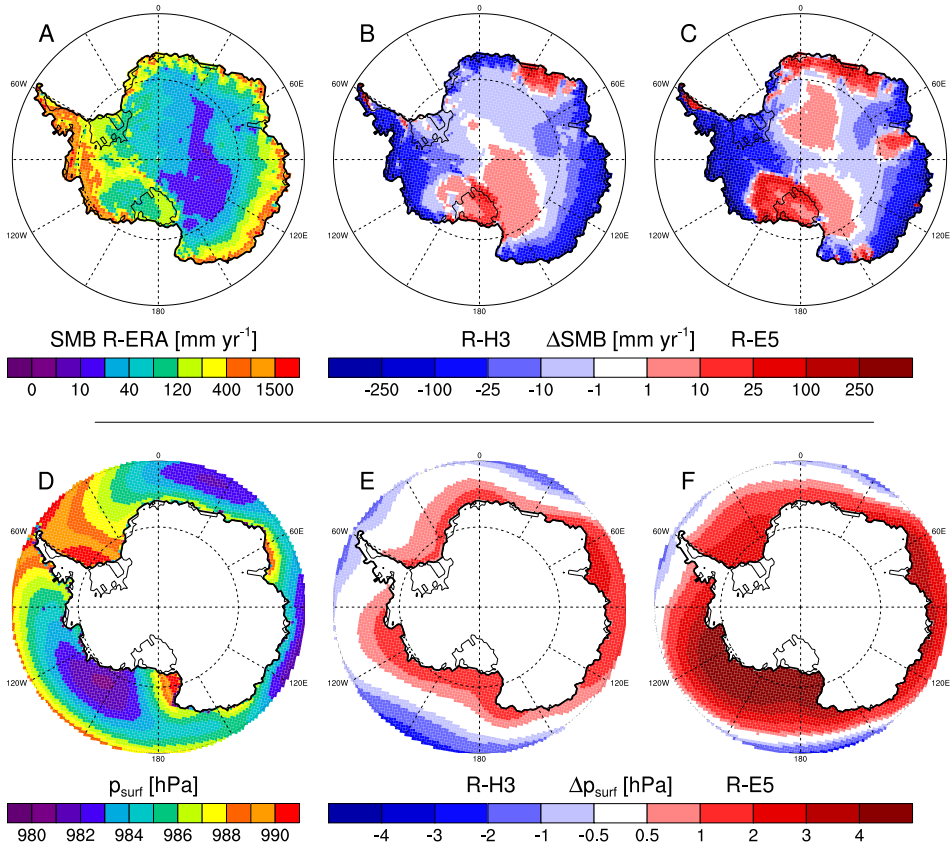


Figure 6.4: Spatial distribution (1980–1999 average) of SMB (A) and surface pressure (p_{surf}) (D) for R-ERA and the difference between R-H3 and R-ERA (B and E) and R-E5 and R-ERA (C and F) for SMB and p_{surf} , respectively.

6.3.3 RACMO2 - GCM comparison

Direct GCM output lacks the resolution and realistic snow physics to accurately capture the individual SMB components (Table 6.2). In ECHAM5, precipitation and SMB are virtually the same as no runoff is simulated and sublimation is an order of magnitude smaller than in RACMO2 (8 Gt yr^{-1} vs 76 Gt yr^{-1}). The latter is mainly caused by ECHAM5’s coarse meridional resolution ($\sim 400 \text{ km}$) in the steep coastal area (Figure 6.5b), where most sublimation takes place. In HadCM3, precipitation is higher than in R-ERA, however this is compensated by an overestimation of sublimation (165 Gt yr^{-1} vs 76 Gt yr^{-1}) and runoff (165 Gt yr^{-1} vs 10 Gt yr^{-1}). Especially the latter is unrealistically high, as in reality runoff hardly occurs in Antarctica [Lenaerts *et al.*, 2012a].

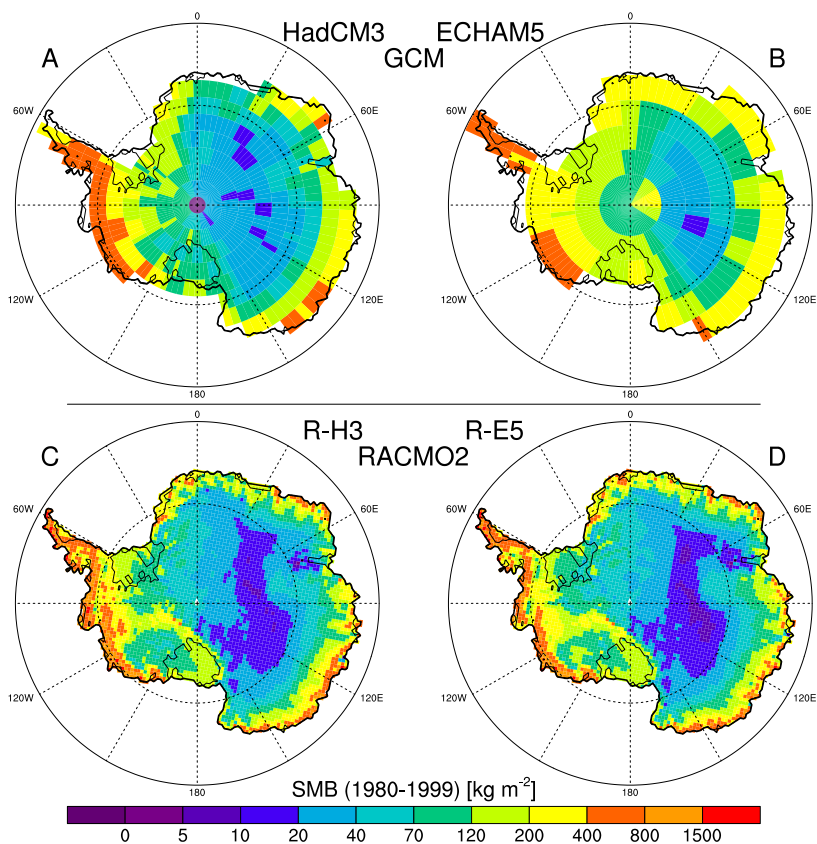


Figure 6.5: Spatial distribution (1980–1999 average) of SMB for GCM simulations HadCM3 (A) and ECHAM5 (B) and RACMO2 simulations R-H3 (C) and R-E5 (D). RACMO2 grounding line and land contours are used in all figures.

In Figure 6.5 the impact of the difference in grid resolution between GCM and RACMO2 output is clearly visible. R-E5 and R-H3 show more spatial detail in the SMB patterns, but qualitatively the overall spatial distribution in HadCM3 is quite good; with the highest SMB values occurring along the West-Antarctic coast and the western Antarctic Peninsula, and lower values in DML and Victoria Land (80°S , 150°E). ECHAM5's coarser meridional resolution precludes resolving these spatial details. Both GCMs overestimate the SMB in the AIS interior. Also note that both GCMs have problems near the geographical South Pole. HadCM3 simulates hardly any precipitation in these grid boxes, leading to a negative SMB, while ECHAM5 on the other hand simulates more precipitation on the eastern side than in the surrounding grid boxes, which also leads to an unrealistic spatial SMB pattern.

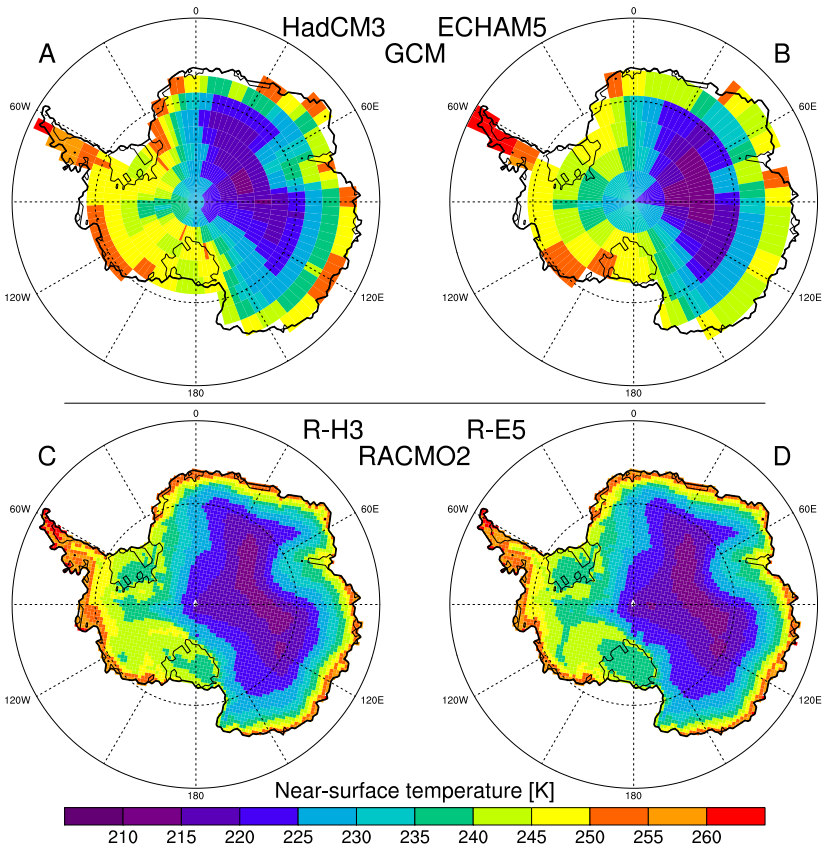


Figure 6.6: Spatial distribution (1980–1999 average) of near-surface temperature for GCM simulations HadCM3 (A) and ECHAM5 (B) and RACMO2 simulations R-H3 (C) and R-E5 (D). RACMO2 grounding line and land contours in all figures. Near-surface temperature is 2-m temperature (T_{2m}) in ECHAM5, R-H3 and R-E5, and 1.5-m temperature in HadCM3.

Figure 6.6 shows that the GCMs simulate a realistic spatial pattern for near-surface temperature and the AIS average value is in the same range as the three RACMO2 simulations (R-ERA, R-E5 and R-H3). Both GCMs simulate the correct T_{2m} -range between the East-Antarctic plateau and coastal areas (215–250 K). In areas with more topographic detail, GCMs overestimate temperature; for example, ECHAM5 overestimates T_{2m} in the northern Antarctic Peninsula and both GCMs overestimate T_{2m} over the large ice shelves (Ross and Filchner-Ronne), an indication that topography is smoothed and on average lower.

In summary, both GCM-driven RACMO2 simulations (R-H3 and R-E5) are colder and drier than R-ERA. Reasons for these deficiencies are underestimated SST, overestimated sea ice cover and less pronounced low pressure systems along the Antarctic coast, the latter being the

main source of meridional heat and moisture transport onto the ice sheet. In both R-H3 and R-E5, relative inter-annual variability of the SMB components is in the same range as R-ERA (Table 6.2). For snowfall, the most important SMB component, the R-H3 simulation is closer to R-ERA than the R-E5 simulation, as well in absolute amounts as in inter-annual variability. Moreover, HadCM3 provides forcing data until 2200 compared to 2100 for ECHAM5; in the next section, we will therefore mainly discuss the results of RACMO2 simulations forced with HadCM3. The absolute differences (Table 6.2) between the three RACMO2 simulations are smaller than the RACMO2-GCM and inter-GCM differences [Maris *et al.*, 2012]. Although both GCMs predict quite similar AIS average SMB values compared to RACMO2 historical simulations (R-ERA, R-H3 and R-E5), there are compensating errors: both ECHAM5 and HadCM3 simulate sublimation and runoff amounts that are one to two orders of magnitude different from R-ERA. Therefore, no future SMB projections from direct GCM output are discussed in this paper.

6.4 Results: future climate

6.4.1 Evolution of T_{2m}

Table 6.3 shows T_{2m} and SMB-component anomalies for 2080–2099 and 2180–2199 averages of the future RACMO2 simulations (R-H3-A1B, R-H3-E1, R-E5-A1B and R-E5-E1), relative to the 1980–1999 average of R-H3 or R-E5. Temperature increases of 3.0 K (R-H3-A1B) and 2.0 K (R-H3-E1) in 2100 and 5.3 K and 2.4 K in 2200 are simulated (Figure 6.7a), similar to the GCM simulated warming (Figure 6.8a). However, Figure 6.7a shows that R-H3-A1B reaches the stabilization temperature later in the 22nd century than HadCM3 in Figure 6.2. Still, the final value of the temperature rise is similar: +5.3 K and +5.4 K in 2200. Also the variability in T_{2m} is similar in HadCM3 and R-H3-A1B (Figures 6.2 and 6.7a). A possible explanation for the warming lag between a GCM and RACMO2 could be found in differences in model physics and parameterizations. For example, the use of more vertical layers to resolve the snowpack and the application of a more realistic albedo parameterization in RACMO2 makes the albedo more sensitive to snowfall events. With future increasing snowfall, this mechanism could slow down the temperature increase near the surface [Picard *et al.*, 2012]. Also, the difference in horizontal grid size between GCM and RACMO2 could act as a temperature buffer along the coastal margins of the AIS. Rising temperatures in these regions can affect a greater area in GCMs, due to the larger grid cells, and thereby trigger temperature-snowmelt-albedo feedbacks. These feedbacks are also present in RACMO2, only on much smaller scales.

For the E1 scenario, HadCM3 (Figure 6.2) follows the T_{2m} increase of the A1B simulation until 2050, as is the case in R-H3-E1 (Figure 6.7a and 6.8a). After this, HadCM3 T_{2m} remains rather constant for the remainder of the simulation period, and the warming remains below

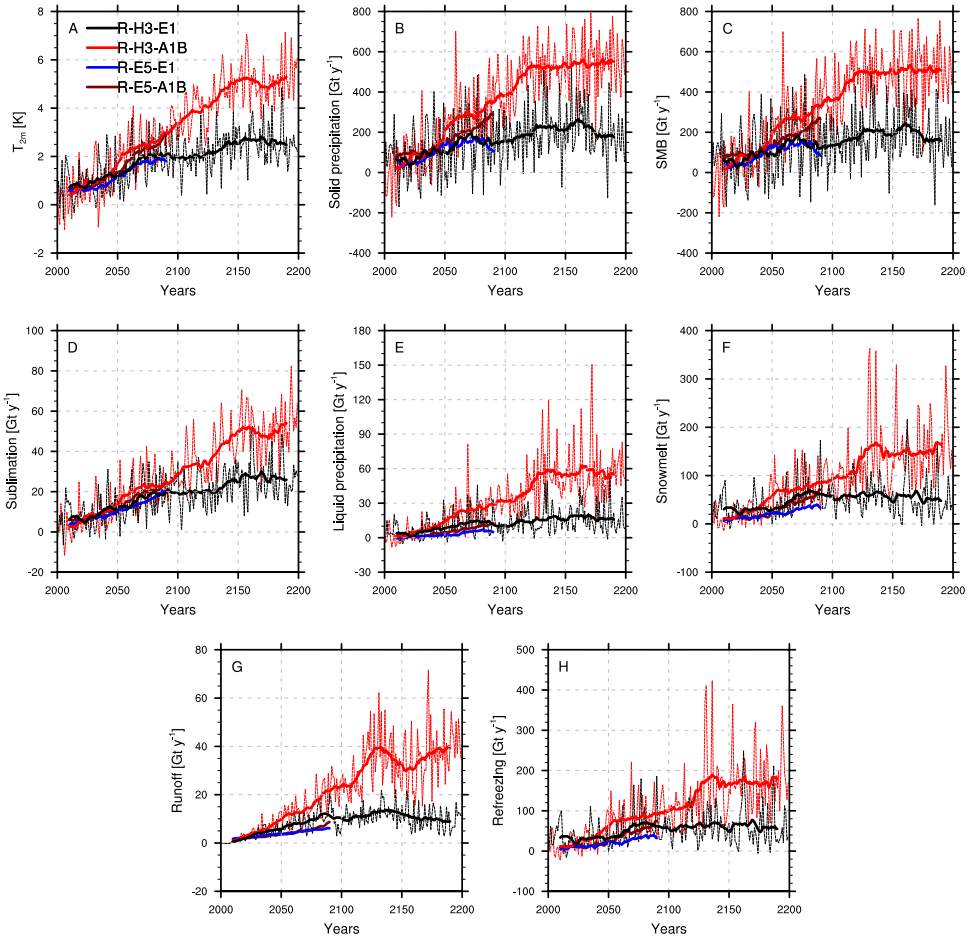


Figure 6.7: Time series (2000–2199) of annual and ice sheet averaged T_{2m} (A), solid precipitation (B), SMB (C), sublimation (D), liquid precipitation (E), snowmelt (F), runoff (G) and refreezing (H), for four RACMO2 simulations; R-E5-A1B (brown), R-E5-E1 (blue), R-H3-A1B (red) and R-H3-E1 (black), relative to the 1980–1999 average values of R-E5 and R-H3 respectively. For all four simulation 20-year running averages (solid) and for both H3 simulations also annual averages (dashed) are shown.

the +2 K threshold (Figure 6.2). In R-H3-E1 however, there is a second warming episode at the end of the 22nd century, increasing T_{2m} above the +2 K threshold. This is likely caused by the same time lag effect as in the A1B simulations, however less pronounced due to a smaller amplitude in temperature change. For both future R-E5 simulations, the T_{2m} increase in 2100 is similar (+1.8 K (E1) and +2.9 K (A1B)) to the future R-H3 simulations. In none of the future simulations is relative inter-annual variability found to change significantly with time.

Table 6.3: Difference in absolute (Gt yr^{-1}) and relative (%) amounts between RACMO2 future simulations (R-E5-A1B, R-E5-E1, R-H3-A1B, R-H3-E1) and 1980–1999 simulations (R-E5 and R-H3, respectively). Listed are differences between 2080–2099 and 1980–1999 20-year ice sheet averages for T_{2m} , snowfall, SMB, sublimation, rainfall, snowmelt, runoff and refreezing. The second row in the H3 results shows the differences between 2180–2199 and 1980–1999 averages. For runoff no relative differences are shown as the 1980–1999 averages are close to zero.

Variable	R-E5-A1B	R-E5-E1	R-H3-A1B	R-H3-E1
T_{2m}	+2.9	+1.8	+3.0 +5.3	+2.0 +2.4
Snowfall	+287 (15 %)	+105 (5.4 %)	+353 (17 %) +551 (26 %)	+144 (6.9 %) +176 (8.4 %)
SMB	+265 (14 %)	+ 84 (4.4 %)	+334 (16 %) +508 (25 %)	+124 (6.1 %) +157 (7.7 %)
Sublimation	+24.6 (38 %)	+19.6 (30 %)	+24.6 (40 %) +54.0 (88 %)	+19.7 (32 %) +25.9 (42 %)
Rainfall	+12.7 (99 %)	+4.8 (38 %)	+28.9 (159 %) +54.8 (301 %)	+11.6 (64 %) +16.0 (88 %)
Snowmelt	+70.6 (127 %)	+33.3 (60 %)	+84.1 (183 %) +164 (356 %)	+61.8 (134 %) +47.8 (104 %)
Runoff	+8.7	+6.3	+21.5 +39.4	+11.4 +8.9
Refreezing	+74.5 (109 %)	+32.0 (47 %)	+92.0 (144 %) +179 (280 %)	+62.0 (97 %) +54.9 (86 %)

Figures 6.9b–c show that the temperature rise in the 21st century is uniform across the entire AIS for both emission scenarios. In both cases the temperature increase varies by 0.5 K from the average increase; 2.5–3.5 K (A1B) and 1.5–2.5 K (E1). In general, the temperature increase along the coastal margins is slightly larger than in the interior. On the East-Antarctic plateau (80°S, 90°E) a numerical artifact is visible. At this location, which receives very low accumulation, the snow in the upper RACMO2 model layer is refreshed too slowly, causing unrealistically large snow grain sizes and therefore a too low albedo. However, the effect on AIS average T_{2m} is minor (~ 0.02 K).

6.4.2 Evolution of the SMB

Figures 6.7b–h show the evolution of the SMB components for the four GCM forced RACMO2 simulations. In general, the hydrological cycle of the AIS intensifies in a warmer Antarctic climate. Snowfall increases by 26 % in R-H3-A1B, from $\sim 2100 \text{ Gt yr}^{-1}$ in R-H3 to $\sim 2650 \text{ Gt yr}^{-1}$ in 2200, while R-H3-E1 shows a more moderate increase of 8 % by 2200 (Figure 6.7b and Table 6.3). In both scenarios, snowfall and T_{2m} appear linked: periods with increasing and stabilizing T_{2m} coincide with periods of increasing and stabilizing snowfall

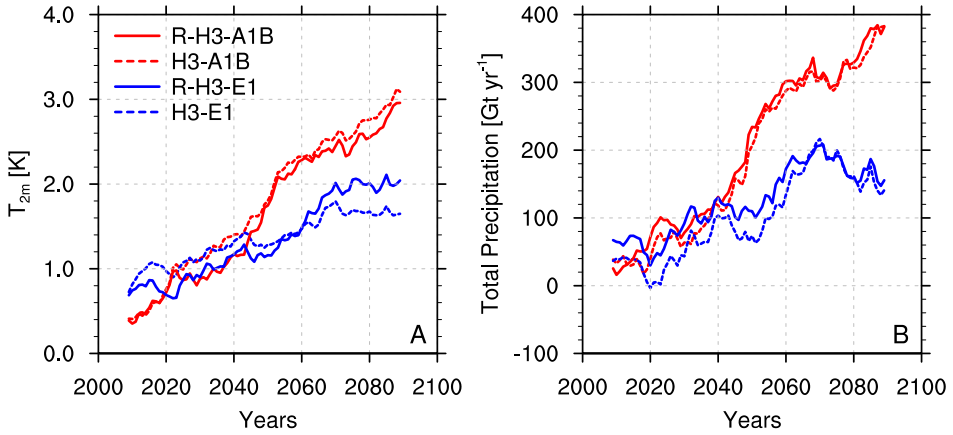


Figure 6.8: Time series (2000–2099) of 20-year, ice sheet averaged T_{2m} (A) and total precipitation (B) for RACMO2 simulations; R-H3-A1B (red, solid) and R-H3-E1 (blue, solid) and GCM simulations; H3-A1B (red, dashed) and H3-E1 (blue, dashed), relative to the 1980–1999 average values of R-H3 and HadCM3 respectively.

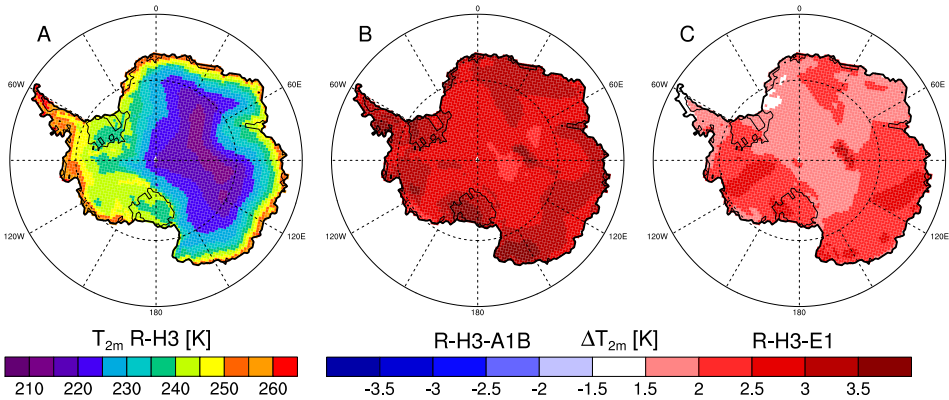


Figure 6.9: Spatial distribution of R-H3 1980–1999 T_{2m} -average (A), the difference between R-H3-A1B 2080–2099 T_{2m} -average and Figure A (B) and R-H3-E1 2080–2099 T_{2m} -average and Figure A (C), respectively.

(Figures 6.7a–b). Figures 6.8a–b emphasize the casual relation between rising temperatures and increasing precipitation in both GCM and RACMO2 simulations. A strong increase in T_{2m} (e.g. around 2050 in the A1B simulations) is accompanied by a rapid precipitation increase. Also, a reduction in T_{2m} increase (e.g. around 2070 in the A1B simulations) translates into a reduced precipitation increase. For the E1-simulations, the relation between rising tem-

peratures and increasing precipitation is also evident, however, due to the smaller increase in T_{2m} the signal is more variable.

The spatial pattern of snowfall (or SMB) increase over the 21st century shows the same relation between temperature and precipitation (Figures 6.10b–c). The increase is rather uniform over the continent, with the largest increases in West-Antarctica and along the coastal margins, which are both locations with high annual snowfall totals. The uniformity of the increase in both temperature and snowfall suggests that future snowfall changes are mainly caused by increased atmospheric water vapor holding capacity and less by atmospheric circulation changes. For R-H3-E1, a smaller increase in SMB is found (Table 6.3), which is probably due to the smaller temperature increase (+2.0 K) than in R-H3-A1B (+3.0 K). The future increase in SMB, especially in the strong mitigation scenario simulations (R-E5-E1 and R-H3-E1), is smaller than or similar to the difference in the historical simulations (R-E5/R-H3 vs R-ERA). This could simply imply that the simulated increase falls within the uncertainty margin. However, it is more likely that the cold and dry bias from the historical runs is also present in the future simulations. As will be shown in Section 6.4.3, there is a strong linear relation between temperature and snowfall/SMB in Antarctica, indicating that SMB will rise with temperature independent of the starting conditions (as long as these fall within a realistic range).

In Figures 6.10e–f, the relative differences in p_{surf} over the 21st century show no large deviations from the average R-H3 pattern, as was the case for SMB (Figures 6.10b–c). In both simulations, the differences in p_{surf} between R-H3-A1B/R-H3-E1 and R-H3 (Figure 6.10e–f) are smaller than between R-ERA and R-H3 (Figure 6.4e). This confirms that the differences in SMB (Figure 6.10b–c) are mainly influenced by temperature changes and less by circulation changes.

In the present climate, rainfall only occurs along the coastal margins of the AIS, roughly below 1000 m a.s.l., and on the ice shelves. In R-H3-A1B, rainfall increases by more than 50 Gt yr⁻¹ in the next two centuries, a threefold increase from R-H3 simulated rainfall (Figure 6.7e and Table 6.3). Our results show only minor changes in the spatial rainfall distribution, most likely because the ice sheet is rather steep in the coastal regions, preventing the penetration of warmer near surface temperatures inland. In R-H3-E1, the increase is less pronounced and stabilizes around 16 Gt yr⁻¹ (~80%). The relative inter-annual variability in rainfall, taken as the ratio of the standard deviation and the mean absolute value, is strongly influenced by a few peak years, but shows no significant trend.

In R-H3-E1, snowmelt evolution shows the same increase and stabilization as rainfall; amounts roughly double during the 21st century and remain constant afterwards. In the A1B simulation, snowmelt increases more strongly, with an increase of 80–85 Gt yr⁻¹ in both the 21st and 22nd century (Figure 6.7f and Table 6.3). As with rainfall, inter-annual variability is strongly influenced by a few peak years, but there is no significant trend. The peak years around 2130, in which annual snowmelt exceeds 400 Gt yr⁻¹, are remarkable.

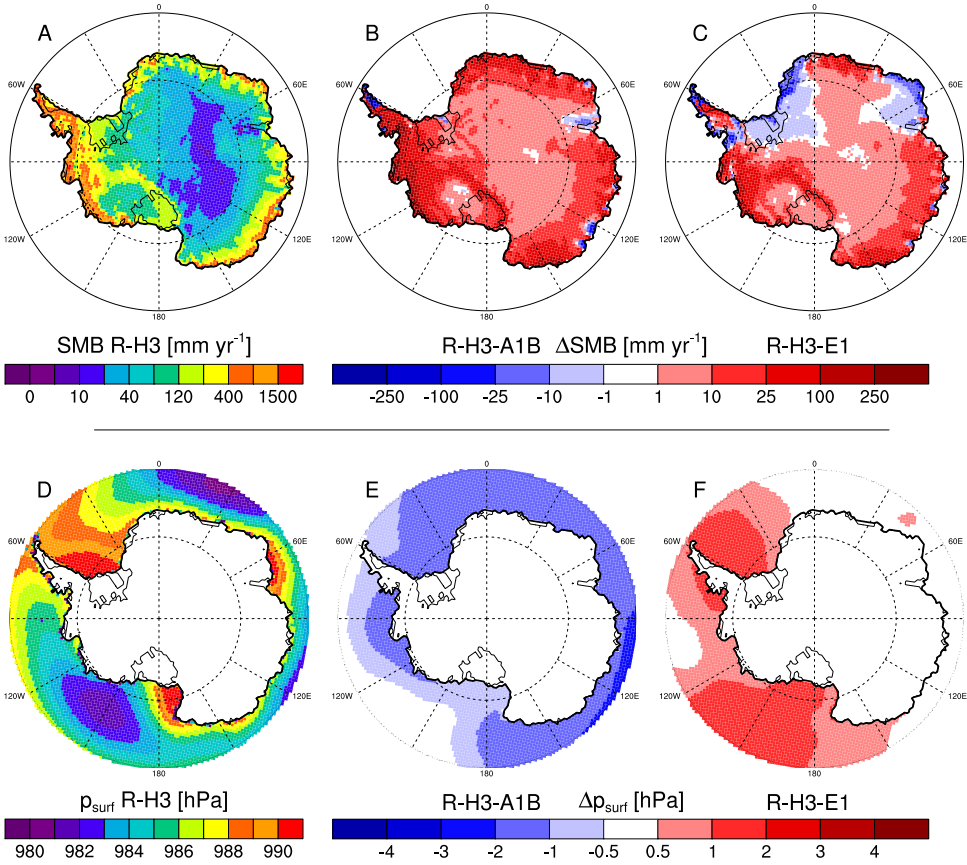


Figure 6.10: Spatial distribution of SMB (A) and surface pressure (p_{surf}) (D) for R-H3 (1980–1999 average), the difference between R-H3-A1B 2080–2099 SMB-average and Figure A (B), R-H3-E1 2080–2099 SMB-average and Figure A (C), R-H3-E1 2080–2099 p_{surf} -average and Figure D (E) and R-H3-E1 2080–2099 p_{surf} -average and Figure D (F), respectively.

The increase in liquid water flux from enhanced rainfall and snowmelt is not reflected in high runoff rates (Figure 6.7g), as most liquid water refreezes in the snow pack (Figure 6.7h). In R-H3-A1B, the liquid water flux increases with more than 200 Gt yr⁻¹ in 2180–2199 (Table 6.3). Runoff only increases by 40 Gt yr⁻¹, so most of the additional rainfall is a positive contribution to the SMB of the AIS. In R-H3-E1, runoff follows the same temporal pattern as snowmelt, i.e. an increase until 2100 and stabilization afterwards. Values remain low. In both emission scenarios, future runoff occurs only on ice shelves in the Antarctic Peninsula (Larsen C, Wilkins and George VI), which is also reflected in decreasing SMB values in these regions (Figure 6.10b). As snowmelt is underestimated by ~50% in R-E5 and R-H3, compared to R-ERA (see Table 6.2), snowmelt and related runoff estimates in the future

RACMO2 simulations are also likely to be underestimated. For runoff, this will probably have a minor effect, because of the large available refreezing capacity on the AIS and the linear relation between T_{2m} and SMB, as will be discussed later.

As T_{2m} increases, sublimation of surface snow also increases due to the greater snow-to-atmosphere moisture gradient (Figure 6.7d). Higher temperatures in the A1B scenarios lead to larger sublimation increases (+88 %) than in the E1 scenario (+42 %). During 2000–2099, the increase in sublimation is rather uniform in all four RACMO2 simulations. Thereafter, sublimation increases in R-H3-A1B at the same rate until 2150, while in R-H3-E1 sublimation only shows a minor increase during the 22nd century. Surface sublimation is a relatively constant process, and relative inter-annual variability remains constant during the full simulation period: $\sim 10\%$ of the total sublimation.

In summary, the T_{2m} increase strengthens the AIS hydrological cycle, however the increase in surface mass loss components is by far outweighed by the increase in mass influx from precipitation. Sublimation increases by 25–50 Gt yr^{-1} in the next 200 years, and while rainfall and snowmelt occasionally exceed 200 Gt yr^{-1} and 400 Gt yr^{-1} , almost all of this liquid water refreezes in the snowpack. As a result, runoff values remain low and hardly influence the SMB. Therefore, the temporal and spatial patterns of SMB changes are very similar to that of snowfall: +26 % in A1B and +8 % in E1 in 2180–2199 (Figure 6.7c) compared to the 1980–1999 averages in R-H3. No significant trend in relative inter-annual variability is found. The R-E5-A1B and R-E5-E1 simulations (not shown) show results and trends similar to the respective H3 future simulations.

6.4.3 Influence on future sea level

Figure 6.11 shows sea level change resulting from the cumulative SMB anomaly (Figure 6.7c) relative to the 1980–1999 average SMB of the corresponding simulation. To estimate sea level change from SMB, only grounded ice-sheet totals are used. For the R-H3-A1B scenario, a total cumulative SMB anomaly of $+59 \cdot 10^3 \text{ Gt}$ in 200 years is found, corresponding to a sea level drop of 163 mm in 2200 (using 360 Gt w.e. to equal 1 mm eustatic sea level change). For the 21st century, a sea level drop of 43 mm is found. In the R-E5-A1B scenario, a potential sea level drop of 32 mm is simulated for the 21st century, slightly lower than the value found in R-H3-A1B. This difference represents part of the uncertainty that is introduced by the choice of forcing models. For E1, the strong mitigation scenario, a potential sea level drop of 20 mm (R-E5-E1) and 27 mm (R-H3-E1) is found for the 21st century (Figure 6.11). Uncertainties in the simulated Antarctic SMB are estimated at $\sim 10\%$ [Rignot *et al.*, 2008], so error bars in Figure 6.11 are calculated by using 90 % and 110 % of the SMB anomalies.

Models without explicit SMB calculation, such as ice-dynamical models or simplified global climate models, often make use of a relation between the change in T_{2m} (ΔT_{2m}) and the change in SMB (ΔSMB). For R-H3-A1B, this SMB sensitivity (given in $\text{Gt w.e. yr}^{-1} \text{ K}^{-1}$,

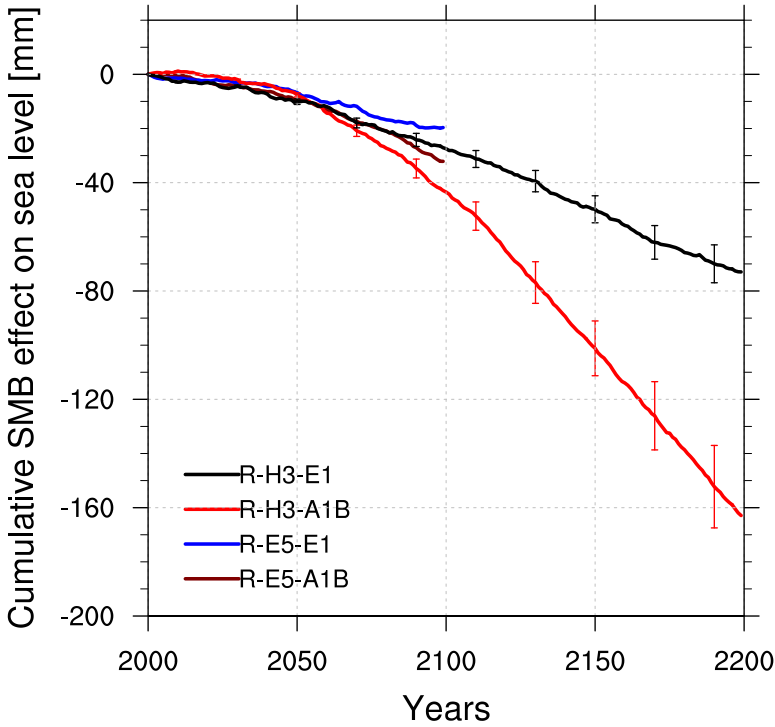


Figure 6.11: Cumulative sea level change from grounded AIS SMB anomalies in four RACMO2 simulations; R-E5-A1B (brown), R-E5-E1 (EC-E1, blue), R-H3-A1B (red) and R-H3-E1 (black). Error bars (only shown for both H3 simulations) indicate the cumulative uncertainty based on Van de Berg [2008].

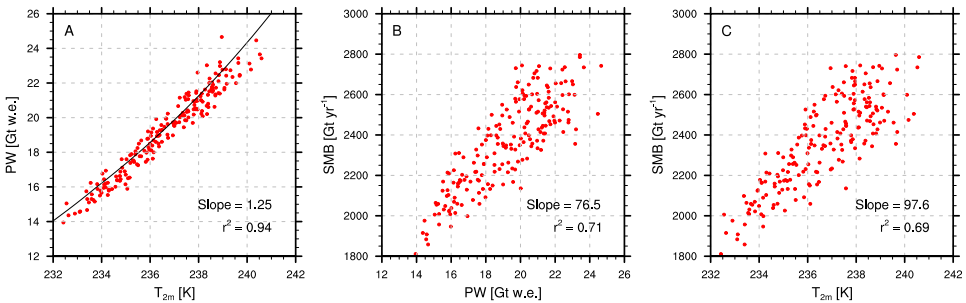


Figure 6.12: Relation between total precipitable water (PW) and T_{2m} (A), SMB and PW (B) and SMB and T_{2m} (C), including their slopes and correlation (r^2) for R-H3-A1B. All are annual ice sheet averages and a schematic Clausius-Clapeyron relation (black) is shown in A, that was obtained with $7\% K^{-1}$ [Held and Soden, 2006], crossing 16 Gt w.e. at 233.8 K.

Table 6.4: SMB sensitivity and sea level drop during the 21st century for selected studies. These results were obtained using: i) present day data from a regional atmospheric climate model simulation [Van Lipzig et al., 2002], ii) high resolution GCM simulations [Wild et al., 2003; Krinner et al., 2007; Bengtsson et al., 2011] or iii) statistical SMB perturbations in GCMs [Gregory and Huybrechts, 2006].

Reference	SMB sensitivity	Sea level drop in 21 st century
IPCC [2007] AR4	6–9 % K ⁻¹	20–120 mm
Van Lipzig et al. [2002] ⁱ⁾	8.9 % K ⁻¹	70 mm
Wild et al. [2003] ⁱⁱ⁾	7.3 % K ⁻¹	45 mm
Gregory and Huybrechts [2006] ⁱⁱⁱ⁾	~5 % K ⁻¹	50 mm
Krinner et al. [2007] ⁱⁱ⁾	7.1 % K ⁻¹	60 mm
Bengtsson et al. [2011] ⁱⁱ⁾	3.7 % K ⁻¹	40 mm
This study	4.8 % K ⁻¹	32–43 ± 4 mm

as in Van Lipzig et al. [2002] among others) is shown in Figures 6.12a–c, and is based on the strong linear relations between annual ice sheet averaged T_{2m} , SMB and the total precipitable water (PW) in the atmosphere above the ice sheet (in Gt w.e.). The strong linear relation between T_{2m} and PW with a positive slope of 1.25 Gt w.e. K⁻¹ indicates an 6–8 % increase of water vapor in the atmosphere per degree warming (Figure 6.12a). This is in line with the Clausius-Clapeyron relation (black line in Figure 6.12a) that gives an increase of 7 % K⁻¹ [Held and Soden, 2006]. As snowfall is the dominant component of the SMB, a strong PW-SMB relation is expected (Figure 6.12b) and combining these two relations, a T_{2m} -SMB relation is derived (Figure 6.12c). Owing to the variability of other SMB components (sublimation and runoff), the correlation ($r^2 = 0.69$) in Figure 6.12c is lower than found for the relations shown in Figure 6.12a–b. The ΔT_{2m} - Δ SMB relation has a positive linear slope of $+97.6 \pm 4.7$ Gt w.e. yr⁻¹ K⁻¹ (or -0.27 ± 0.01 mm SLR yr⁻¹ K⁻¹). This again confirms that the future increase in Antarctic SMB is mainly driven by an increase in near-surface temperatures and to a lesser degree by changes in atmospheric circulation patterns.

In Table 6.4, SMB sensitivity and sea level change for the AIS in the 21st century from this study are compared to results from previous work. All results show a clear increase of SMB with increasing temperature; values vary from 4–9 % K⁻¹. Van Lipzig et al. [2002] reduced the sea ice fraction in their experiment, thereby causing atmospheric circulation to change and generating higher SMB sensitivities. From Figure 6.12c we find that the SMB increases with 97.6 Gt K⁻¹, which corresponds to a SMB sensitivity of 4.8 % K⁻¹ relative to the 1980–1999 average. The results presented in this study are among the lower estimates of sea level change induced by SMB changes compared to previous studies (Table 6.4). It should be noted that only sea level change due to SMB changes is considered and it is likely that a part of this change will be counteracted by ice-dynamical effects [IPCC, 2007; Rignot et al., 2011a; Levermann et al., 2012].

Figure 6.13a shows that the SMB sensitivity remains partially valid when applied on grid cell scale; roughly half the AIS shows an SMB increase of 15–35 %, which is similar to the

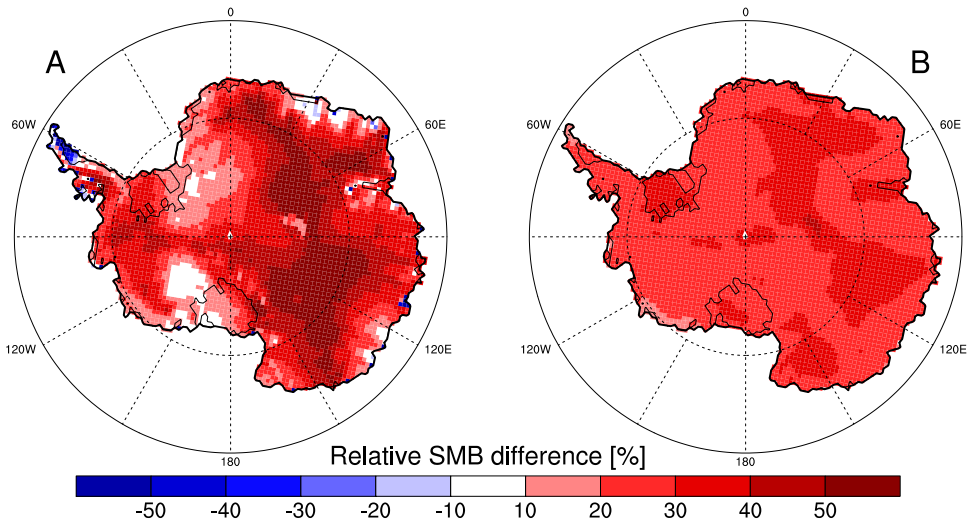


Figure 6.13: Relative SMB differences between R-H3-A1B 2180–2199 average SMB and R-H3 1980–1999 average SMB (A) and between 2180–2199 average SMB derived using the ΔT_{2m} - Δ SMB relation (Section 4.3) and R-H3 1980–1999 average (B). For the B, ΔT_{2m} was taken as the difference between R-H3-A1B 2180–2199 average T_{2m} and R-H3 1980–1999 T_{2m} .

AIS averaged SMB sensitivity (Figure 6.13b). Using the SMB sensitivity of $4.8\% \text{ K}^{-1}$, the increase in SMB is uniform over the AIS, because it is linearly related to the uniform increase in T_{2m} (Figure 6.9b). The average increase in SMB is $\sim 25\%$, which agrees with the $\sim 5 \text{ K}$ temperature rise in R-H3-A1B (Table 6.3). When the SMB difference between R-H3 and R-H3-A1B is calculated directly (Figure 6.13a), more variability is introduced, owing to the temporal and spatial variability in the three SMB components. Apart from a decrease in SMB on the Antarctic Peninsula ice shelves, due to increased runoff, precipitation/SMB increases on the rest of the AIS. Along the coastal margins, sublimation increases more rapidly than in the interior of the AIS, leading to larger ($>50\%$) SMB increases in the interior and smaller (10 – 20%) SMB increases along the coastal margins (Figure 6.13a). The minor increases near the Filchner-Ronne and Ross ice shelf are caused by a locally lower than average snowfall increase, likely due to atmospheric circulation changes. These results again show that the increase in SMB is in first order determined by temperature increase, and to a lesser extent by atmospheric circulation changes.

6.5 Conclusion

The RACMO2 simulations, forced with output from two different GCMs with two different emission scenarios, provide new insights into the future climate and SMB of the AIS.

Both GCMs (HadCM3 and ECHAM5) simulate a global T_{2m} rise of ~ 4 K, larger than the average of the IPCC models ($+2.8$ K), using emission scenario A1B. In the stronger mitigation emission scenario (E1), both GCMs predict a temperature rise close to 2 K, which is the target of this emission scenario. The simulation of the SMB with RACMO2 provides more detail compared to GCM output. In neither GCM, simulation of the SMB was very realistic; ECHAM5 underestimates sublimation and runoff, while HadCM3 overestimates both these components. However, due to these compensating errors, total SMB values from RACMO2 and GCM output are in the same range.

For the 1980–1999 period, RACMO2 forced with HadCM3 and ECHAM5 output results in a colder and drier Antarctic climate compared to RACMO2 forced with ERA-40 re-analysis. This difference is explained by the lower sea surface temperature and higher sea ice concentrations prescribed from the GCM output, reducing transport of heat and moisture onto the ice sheet.

In most RACMO2 future simulations, the increase in T_{2m} lags that of the GCMs by ~ 20 years, but reaches the same final value as simulated by the GCMs in 2200. In both emission scenarios, the greenhouse gas emissions and associated atmospheric warming level off in the late 22nd century. The hydrological cycle of the AIS responds strongly to the simulated temperature increase. By 2200, snowfall increases by 550 Gt yr^{-1} (26 %) in R-H3-A1B and by 176 Gt yr^{-1} (8 %) in R-H3-E1 compared to the R-H3 average. By comparing spatial patterns of 21st century changes in T_{2m} , SMB and p_{surf} , it is clear that the future SMB changes are mainly caused by the increase in temperature and to a lesser extent by atmospheric circulation changes. Sublimation increases by $25\text{--}50 \text{ Gt yr}^{-1}$, thereby compensating ~ 15 % of the increase in snowfall. By 2200, rainfall and snowmelt have strongly increased in low-lying regions of the AIS, by 301 % and 356 % (R-H3-A1B) and 88 % and 104 % (R-H3-E1), respectively. Most of this additional liquid water refreezes in the snowpack and does not run off; runoff increases to only $\sim 40 \text{ Gt yr}^{-1}$ in R-H3-A1B and to $\sim 10 \text{ Gt yr}^{-1}$ in R-H3-E1. So even in a significantly warmer climate, rainfall remains a positive contribution to the SMB of the AIS.

The future SMB change of the AIS is dominated by the increase in snowfall and contributes negatively to global SLR. A significant relation is found between ice sheet averaged ΔT_{2m} and ΔSMB : $+97.6 \text{ Gt w.e. yr}^{-1} \text{ K}^{-1}$ or $-0.27 \text{ mm SLR yr}^{-1} \text{ K}^{-1}$. Changes in mass loss due to ice-dynamical effects will most probably counteract this surface mass gain. When these ice dynamical effects are neglected, our results represent a sea level fall of $32\text{--}43 \pm 4 \text{ mm}$ and $20\text{--}27 \pm 3 \text{ mm}$ in 2100, compared to 1980–1999. For the 22nd century, an additional sea level drop of 46 mm (R-H3-E1) or 120 mm (R-H3-A1B) is predicted.

It is likely that the cold and dry biases in the 1980–1999 simulations persist in the future GCM-forced RACMO2 simulations, as the future simulations are continuations of the historical simulations. However, the impact of this bias can be interpreted relatively easily because of the strong first-order relations in the Antarctic climate: T_{2m} , snowfall and SMB are all

closely coupled. Combining that, i) the SMB of the AIS is determined for 90 % by snowfall and ii) the good agreement in T_{2m} and snowfall increase (following the Clausius Clapeyron relation), results in a ΔT_{2m} - Δ SMB relation with good spatial and temporal agreement. In R-H3-A1B, these relations are valid for a temperature range of at least ~ 6 K, which is three times larger than the differences between the historical simulations (R-ERA, R-H3 and R-E5). Therefore it is reasonable to assume that the results presented here are representative for a future temperature rise of at least 4 K. Also beyond this temperature increase it is likely that the T_{2m} -SMB relation remains valid, because runoff remains only locally important during our simulations and the other mass removing SMB-component, sublimation, is rather constant and not expected to strongly increase in a warming climate.

Present and future variations in Antarctic firn air content

Summary

A firn densification model (FDM) is used to assess spatial and temporal (1979–2200) variations in the depth, density and temperature of the firn layer covering the Antarctic ice sheet (AIS). Results from a time-dependent version of the FDM are compared to more commonly used steady-state FDM results. Although the average AIS firn air content (FAC) between both models is similar (22.5 m), large spatial differences are found: in the ice-sheet interior, the steady-state model underestimates the FAC by up to 2 m, while the FAC is overestimated by 5–15 m along the ice-sheet margins, due to significant surface melt. Applying the steady-state FAC values to convert surface elevation to ice thickness (i.e. assuming flotation at the grounding line) potentially results in an underestimation of ice discharge at the grounding line, and hence an underestimation of current AIS mass loss by 23.5 %, or 16.7 Gt yr⁻¹ [with regard to the reconciled estimate over 1992–2011, *Shepherd et al.*, 2012]. The timing of the measurement is also important as temporal FAC variations of 1–2 m are simulated within the 33-year period. Until 2200, the Antarctic FAC is projected to change due to a combination of increasing accumulation, temperature and surface melt. The latter two result in a decrease of FAC, due to i) more refrozen meltwater, ii) a higher densification rate and iii) a faster firn-to-ice transition at the bottom of the firn layer. These effects are however more than compensated by increasing snowfall, leading to a 4–14 % increase in FAC. Only in melt-affected regions, future FAC is simulated to decrease, with the largest changes (-50 to -80 %) on the ice shelves in the Antarctic Peninsula and Dronning Maud Land. Integrated over the AIS, increased precipitation results in a combined ice and air volume increase of $\sim 300 \text{ km}^3 \text{ yr}^{-1}$ until 2100, equivalent to an elevation change of +2.1 cm yr⁻¹. This shows that variations in firn depth remain important to consider in future mass balance studies using (satellite) altimetry.

This chapter is based on: Ligtenberg S.R.M., P. Kuipers Munneke, and M.R. van den Broeke (2014), Present and future variations in Antarctic firn air content. *The Cryosphere Discussions*, **8**, 421-451, doi:10.5194/tcd-8-421-2014

7.1 Introduction

The most common method to determine the effect of climate change on the ice sheets of Greenland and Antarctica is to calculate the change in their mass over time. Due to their remoteness, adverse climate conditions, and sheer size, it is difficult to measure the mass balance of these two ice sheets directly. Over the last few decades, the introduction of satellite and airborne remote sensing techniques has increased the understanding of ice sheet processes and led to more accurate mass balance estimates. Three methods involving satellite remote sensing are generally used for ice sheet mass balance calculations: i) the mass-budget method [e.g. *Rignot et al.*, 2008], ii) the gravimetric method [e.g. *Velicogna*, 2009] and iii) the volumetric method [e.g. *Davis et al.*, 2005]. The first method calculates the mass in- and output of the ice sheet directly, by subtracting the ice discharge over the grounding line from the surface mass balance (SMB) of the grounded ice sheet. The second method directly measures mass variations in the Earth's gravity field, from which ice mass changes can be deduced if a correction is applied for all other mass-varying processes (e.g. ocean tides and bedrock movement). The third method measures the change in ice volume from surface elevation changes. These variations can be converted into ice mass change if the density of the material at which the volume change takes place is known.

To obtain meaningful mass balance estimates, all three remote sensing techniques require corrections for surface processes, such as precipitation anomalies [*Horwath et al.*, 2012], firn pack changes [*Zwally and Li*, 2002; *Helsen et al.*, 2008] or bedrock movement by glacial isostatic adjustment [*Peltier*, 2004; *Whitehouse et al.*, 2012]. These corrections are often provided by models that simulate the aforementioned processes. While the three methods are based on different principles and measure different quantities, they give reasonably consistent results for the mass balance of the Greenland and Antarctic ice sheets over the past two decades [*Shepherd et al.*, 2012].

This paper focuses on firn layer variations and their influence on mass balance measurements. Knowledge of variations in firn volume and mass is a necessity for the mass-budget method and the volumetric method and aids in the interpretation of gravity measurements. Firn-induced surface elevation changes, as simulated by a firn densification model, are used to correct remotely sensed surface elevation changes in order to obtain the mass loss/gain of the glacier ice underneath [e.g. *Pritchard et al.*, 2012]. Firn pack variations also need to be considered for the mass budget method. Ice thickness measurements that are used to calculate ice discharge over the grounding line [e.g. *Rignot et al.*, 2011a], must be corrected for the amount of air in the firn column to prevent an overestimation of the mass flux [*Van den Broeke*, 2008].

Firn air content (FAC) is a measure for the pore space fraction of the firn layer and is defined as the change in thickness (in m) that occurs when the firn column is compressed to the density of glacier ice:

$$FAC = \int_{z_s}^{z_{\rho_i}} (\rho_i - \rho(z)) dz \quad (7.1)$$

where ρ_i is the ice density, here assumed to be 910 kg m^{-3} , and z_s and z_{ρ_i} indicate the surface and the depth at which the ice density is reached, respectively. The FAC depends both on the shape of the firn density profile and the firn layer depth; these in turn are governed by the local surface climate conditions [Ligtenberg *et al.*, 2011]. Due to the large spatial heterogeneity in climate conditions over the Antarctic ice sheet (AIS), the FAC also exhibits a large variability. In locations with net ablation, no firn layer is present, while favorable local climate conditions can lead to a FAC of more than 40 m [Van den Broeke, 2008; Ligtenberg *et al.*, 2011]. These values are usually obtained from a steady-state firn density profile that is calculated with the long-term average temperature and accumulation [Herron and Langway, 1980; Barnola *et al.*, 1991; Zwally and Li, 2002]. Until now, ice thickness observations have been corrected with either a constant FAC value [e.g. Rignot and Jacobs, 2002] or with a spatially varying pattern, based on steady-state density profiles [e.g. Fretwell *et al.*, 2013]. Either way, temporal variations in firn layer density and thickness are neglected.

Due to large seasonal and inter-annual variations in the Antarctic climate, temporal variations in firn pack characteristics can be significant [Ligtenberg *et al.*, 2012]. At higher temperatures, the densification rate of firn increases, i.e. near-surface firn densifies quicker in summer than in winter [Herron and Langway, 1980]. This also implies that a snowfall event in winter/summer deposits a firn layer with lower/higher density. When surface melt occurs in summer, the local refreezing of meltwater in the firn pore space is a very efficient densification process. Steady-state firn solutions are based on dry-firn compaction and do not take melt into account [Herron and Langway, 1980; Ligtenberg *et al.*, 2011]. On higher parts of the AIS, constituting $\sim 90\%$ of its area, this is a valid assumption as surface melt does not occur [Lenaerts *et al.*, 2012a]. However, along the coasts and on the fringing ice shelves, annual surface melt can be significant and cause large seasonal variations in firn characteristics. Furthermore, the grounding line of the AIS is often located in these low-elevation areas, making it sensitive to these variations.

This study presents and explains temporal variations in FAC on the AIS, as well as their climatic cause. We do this for the present-day (1979–2012), as well as for future variations over the next two centuries. First, the firn densification model and its different atmospheric forcing fields will be introduced.

7.2 Methods

7.2.1 Firn densification model

The present-day and future evolution of the Antarctic firn layer are simulated with a one-dimensional, time-dependent firn densification model (FDM). The full details of the FDM are described in *Ligtenberg et al.* [2011] and will only be summarized briefly here. The current model version is based on *Herron and Langway* [1980], and subsequent modifications by *Zwally and Li* [2002] and *Helsen et al.* [2008]. It uses the adapted densification equations of *Arthern et al.* [2010], that were tuned to fit Antarctic firn depth-density observations [*Ligtenberg et al.*, 2011]. A snowmelt module is included to simulate and calculate simple firn hydrology, i.e. the amount of percolation, retention, refreezing and runoff of meltwater. With this latter improvement, the FDM is capable to simulate firn evolution in both the dry-snow zone and melt-affected regions.

One of the basic principles of the FDM is its 'steady-state assumption', i.e. the firn layer is in equilibrium with the local long-term climate forcing. To fulfill this criterion, the available climate forcing time series needs to be long enough to represent the long-term average climate. This has been previously done by assuming that the past 33 years (1979–2012) are a good representation of the Antarctic climate over the last centuries [*Ligtenberg et al.*, 2011, 2012]. Indeed, the AIS climate shows no significant trends in the recent past [*Monaghan et al.*, 2006; *Bromwich et al.*, 2011; *Lenaerts et al.*, 2012a], making this assumption valid. However, this steady-state assumption is not valid for future simulations (which will be introduced in the next section), and therefore requires small adaptations to the FDM. First, the climate of 1960–1979 is assumed to equal the long-term average climate and serve as spin-up climate for the FDM. Thereafter, the modeled firn layer is allowed to evolve over the period 1980–2199. Secondly, the annual average surface temperature and accumulation, that are used in the densification equations, are taken as the running average over the last 40 simulation years. This is done to include the effect of the changing climate on firn densification. For example, in 2120 the annual average temperature and accumulation are calculated over the period 2080–2119. Thirdly, the deep-layer temperature (>15 m depth) is allowed to rise with future rising surface temperatures, while the present-day simulation uses a fixed annual average temperature at depth, consistent with the above-described steady-state assumption.

7.2.2 Atmospheric forcing

Output of the regional atmospheric climate model RACMO2 is used as atmospheric forcing of the FDM. At the surface, it is forced with SMB components (precipitation, surface sublimation, surface melt and drifting snow processes), surface temperature and 10-m wind speed.

Present-day climate

For the present-day simulation (August 1979 to August 2012), 6-hourly RACMO2 output of *Lenaerts et al.* [2012a] is used. The same forcing was previously used for present-day FDM simulations [*Ligtenberg et al.*, 2011, 2012]. To obey the steady-state assumption and create a realistic initial firn profile, the FDM is run iteratively until the complete firn layer is refreshed, after which the final simulation starts. The spatial resolution of the FDM is 27 km, equal to that of the forcing model, RACMO2. The temporal resolution of present-day FDM output is 2 days for surface properties and every week for depth-density profiles.

Future climate

For the future simulation, we used the same approach and data as *Kuipers Munneke et al.* [2014]. This approach is based on a future climate simulation with RACMO2, forced by global climate model data (HadCM3) using the A1B emission scenario [*Ligtenberg et al.*, 2013]. To extend the climate forcing prior (1960–1979) to the RACMO2 simulation, the Antarctic climate is reconstructed using an 'analogue method', based on historical observational temperatures and accumulation fields from *Monaghan et al.* [2008]. In short, one starts with finding the nearest monthly average temperature in the 1980–1999 period compared to January 1960 and copies the daily climate values (e.g. temperature, precipitation and surface melt) from this month into January 1960. This is subsequently done for every month in the 1960–1979 period and for every RACMO2 grid point. In this way, a synthetic daily climate is reconstructed, while spatial variations are preserved and sub-monthly variability is introduced. Afterwards, the daily values of 1960–1979 are bias-corrected for the introduced difference between the 1960–1979 and 1980–1999 average climates. Finally, a 40-year average climate without trend is obtained. A more detailed description and discussion of this procedure is found in the Appendix of *Kuipers Munneke et al.* [2014].

The period 1960–1979 is used as spin-up period and the FDM is run iteratively as often as needed to refresh the complete firn layer, after which the final 240-year simulation starts (1960–2200). For computational efficiency, the RACMO2 climate simulation was performed on 55 km horizontal resolution, which is therefore also the spatial resolution of the FDM future simulation. The temporal resolution of future FDM output is 2 days for surface properties and 1 month for depth-density profiles.

7.3 Results

7.3.1 Present day variations

Figure 7.1a shows the average FAC for 1979–2012, as simulated by the present-day FDM simulation. High values are found on the East-Antarctic plateau, where firn densification is a slow process due to the low temperatures. High values are also found at isolated spots in mountainous regions and along the coast, particularly in West-Antarctica, where the highest accumulation rates of the AIS are recorded [Van den Broeke *et al.*, 2006b; Lenaerts *et al.*, 2012a]. Due to these high accumulation rates, the firn is buried quickly and has less time to densify, leading to a thick firn layer with a significant amount of pore space. Low FAC values are found in regions with a relatively warm and dry climate. Here, fresh snow is buried more slowly and the high temperatures enhance firn densification. Siple Coast (82°S and 140°W) and the Lambert Glacier catchment (73°S and 70°E) are examples of regions with this type of climate. Surface melt has a significant effect on producing low FAC (<15 m) in coastal areas and on the ice shelves. On the two largest Antarctic ice shelves (IS), the Ross IS and Filchner-Ronne IS, higher FAC values are found due to their southerly locations, associated with lower temperatures and weaker melt. The West-Antarctic ice shelves receive high annual accumulation rates that partly mask the melt signal. The white areas indicate locations where

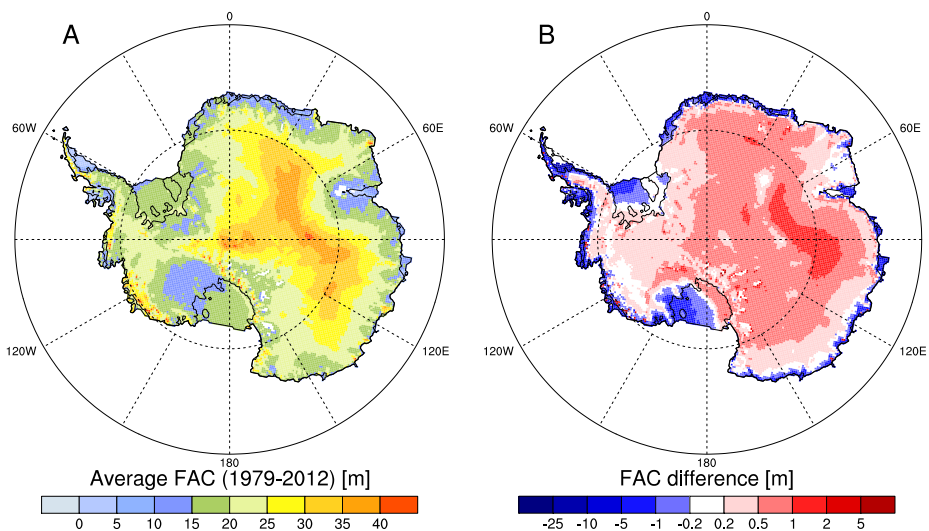


Figure 7.1: Average firm air content (FAC) for 1979–2012 (a), simulated by the time-dependent model, and the difference between (a) and the steady-state model (b), from Ligtenberg *et al.* [2011] (Figure 8a). The FAC represents the height difference of the column (in m) that remains when the firn layer is compressed to ice density (here assumed to be 910 kg m^{-3}).

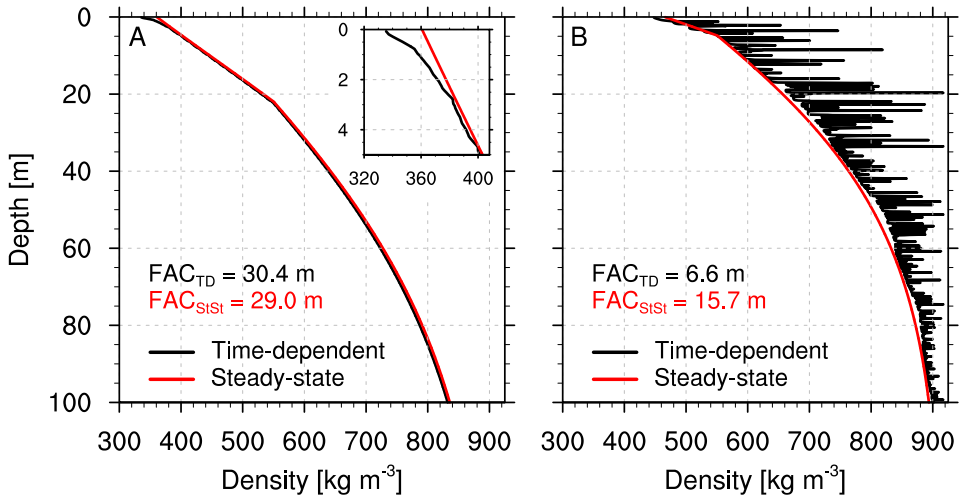


Figure 7.2: Typical firn density profiles for two locations in Antarctica; one without snowmelt (a) on the East-Antarctic plateau (85°S , 84°E) and one with significant summer snowmelt (b) near George VI ice shelf (73°S , 67°W). For both locations, the steady-state ("StSt", red) and time-dependent ("TD", black) solutions of the FDM are shown, with in (a) an inset showing the first 5 m, as well as the firn air content (FAC) for both profiles.

no firn layer is simulated as a consequence of annual sublimation and/or melt exceeding annual accumulation in the RACMO2 forcing. These locations coincide reasonably well with observed blue ice areas, i.e. locations where no firn layer is present [Scambos *et al.*, 2012; Das *et al.*, 2013].

The general spatial pattern of the average FAC from the time-dependent FDM (Figure 7.1a) is similar to that of the steady-state FDM (Figure 8a in Ligtenberg *et al.* [2011]) and the ice-sheet average is identical for both models at 22.5 m. However, Figure 7.1b shows that substantial spatial differences exist between the two. In the AIS interior, the time-dependent FDM simulates slightly more firn air, with the largest positive differences (as large as 2 m), occurring near the domes of the East-Antarctic plateau. The positive differences are simulated in the part of Antarctica where no surface melt occurs and are caused by a bias correction in the surface density used in the steady-state FDM [Ligtenberg *et al.*, 2011], introduced to simulate the majority of the depth-density profile (i.e. the depth at which the 550 kg m^{-3} and 830 kg m^{-3} density levels are reached) similarly in both models (Figure 7.2a). A disadvantage of this bias correction is that the density in the top $\sim 2\text{ m}$ of the firn layer is overestimated in the steady-state solution, causing a lower total air content for the firn column. In this part of the firn column, the seasonal temperature variations are large and especially the higher firn temperatures in summer and autumn cause a quicker density increase with depth than

is simulated by the steady-state solution. In the remainder of the firn column, both density profiles are virtually indistinguishable (Figure 7.2a).

Along the margins of the AIS, the time-dependent FDM simulates significantly less FAC than the steady-state FDM (Figure 7.1b). These negative differences are an order of magnitude larger than the positive differences in the ice-sheet interior (note the skewed color bar in Figure 7.1b) and are mainly caused by significant melt. Refreezing of meltwater in the firn is a very effective densification process which rapidly reduces the FAC (Figure 7.2b). Surface melt is not taken into account in the steady-state FDM because of its large seasonal and inter-annual variability. Figure 7.2b shows the difficulty of defining a steady-state firn density profile for locations with substantial melt, due to the uneven distribution of high and low density layers that move downward with time. In locations with occasional melt, such as the Filchner-Ronne IS and Ross IS regions, the difference between the models is relatively small; 1–2 m. In contrast; differences in the Antarctic Peninsula can be as large as 20 m, caused by large summer melt rates.

When calculating the total mass of the AIS from surface elevation observations [e.g. *Fretwell et al.*, 2013], the difference between the steady-state and time-dependent FAC is negligible, as both ice-sheet averages are similar. However, for individual locations, the difference in firn air correction can be as large as 80 %. Coincidentally, the largest FAC deviations are found in locations where ice thicknesses are relatively small (coastal regions and ice shelves). This is even more relevant, because ice thickness at the grounding line is an important quantity in mass balance studies of both the grounded ice sheet [e.g. *Rignot et al.*, 2011a] and ice shelves [e.g. *Depoorter et al.*, 2013; *Rignot et al.*, 2013]. Combined with the local ice velocity, it determines the ice discharge over the grounding line. A systematic error in the FAC at the grounding line directly affects the ice thickness and therewith the ice discharge estimate. Figures 7.3a–b show the difference in FAC between both models along a part of the grounding line in East Antarctica (80–120 °E). The average time-dependent FAC (13.6 m) is lower than the steady-state FAC (17.2 m), with the largest differences simulated where ice shelves are formed; 82–87 °E (West IS), 94–102 °E (Shackleton IS), 110–112 °E (Vincennes IS) and 115–120 °E (Totten IS and Moscow University IS). These locations are often situated lower than the neighboring parts of the grounding line and are therefore more susceptible to surface melt; the time-dependent FAC is often lower than 8 m, while the steady-state models simulates values greater than 12 m. The relative FAC difference is especially large on the eastern parts of Shackleton IS (100–102 °E), where the time-dependent model simulates FAC less than 3 m on average.

Averaged over the entire AIS grounding line, the FAC simulated by the time-dependent FDM is 2.70 m higher than simulated by the steady-state FDM, which is only 0.7 % of the total ice thickness at the grounding line [371 m, from *Fretwell et al.*, 2013]. But since the ice thickness, ice discharge and ice-sheet mass balance are linearly related to one another, a FAC difference directly affects the current mass balance estimate [$-71 \pm 53 \text{ Gt yr}^{-1}$, by *Shepherd et al.*, 2012]. This ice-sheet mass balance is only a fraction (3.1 %) of the total ice discharge

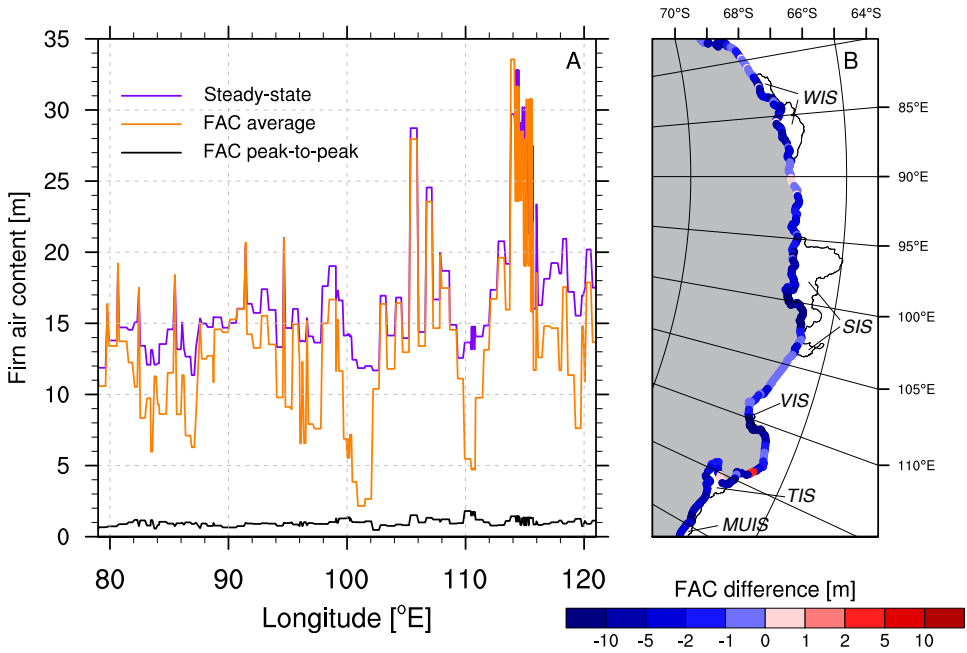


Figure 7.3: Firn air content (FAC) along part of the grounding line in East Antarctica (78–122°E, projected as a function of longitude (°E) (a) and as a map (b). In (a), the FAC from the steady-state (purple) and time-dependent (orange) FDMs, as well as the peak-to-peak difference (black) in the time-dependent model, are shown. In (b) the average difference between both models is shown. Names of ice shelves: West ice shelf (WIS), Shackleton ice shelf (SIS), Vincennes ice shelf (VIS), Totten ice shelf (TIS) and Moscow University ice shelf (MUIS).

[$\sim 2300 \text{ Gt yr}^{-1}$, by *Rignot et al.*, 2011a], as it is the residual of two large, and almost equal, values; the ice discharge and the SMB. This implies that the 0.7% increase in ice discharge due to the average FAC difference, leads to a 23.5% increase (or 16.7 Gt yr^{-1}) in the current mass loss estimate of the AIS.

In Figure 7.3a, also the peak-to-peak FAC difference (i.e. difference between maximum and minimum FAC in the 1979–2012 period) as simulated by the time-dependent FDM is shown. Large differences indicate that seasonal and inter-annual climate variations cause large temporal variations in FAC. This means that, depending on the timing of the observation, the firn layer thickness and its air content could differ from the average value. Along the East-Antarctic part of the grounding line (Figure 7.3a), this difference is rather constant, between 0.5–1.5 m. Depending on the timing of the observation, this introduces additional uncertainty in FAC along the grounding line.

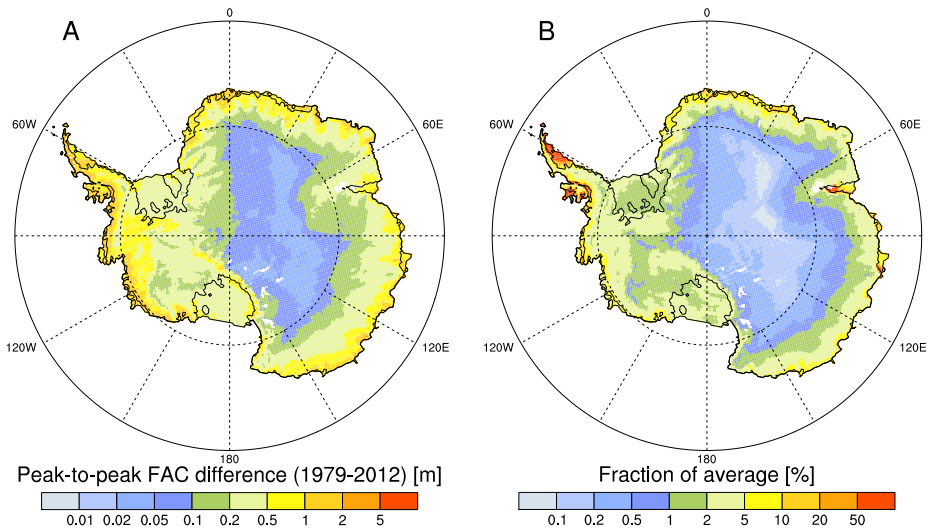


Figure 7.4: The absolute (a) and relative (b) peak-to-peak variations in firm air content (FAC) in the time-dependent FDM simulation over the 1979–2012 period. The relative difference is compared to the average FAC from Figure 7.1a.

Figure 7.4 shows the spatial distribution of the absolute (a) and relative (b) peak-to-peak difference in FAC (Figure 7.1a). On the East-Antarctic plateau, the peak-to-peak differences are small (<0.2 m), due to a combination of low accumulation rates, low temperatures and a lack of surface melt. Since the average FAC is large (Figure 7.1a), the relative variations are small (<1 %). In coastal areas, temporal variations are much larger due to both the occurrence of melt and higher accumulation rates. A coastal band of ~ 150 km wide experiences peak-to-peak differences of 1–3 m, with the highest values (~ 3 m) on the western side of the Antarctic Peninsula, due to a favorable combination of extremely high accumulation rates and substantial surface melt. In the Antarctic Peninsula, this leads to relative differences as large as 50 %, while other ice shelves mostly show relative differences in the order of 10–20 %. In the remaining coastal areas, the relative magnitude of the peak-to-peak difference is mostly 5–10 % of the average FAC.

The causes of temporal variations in FAC are threefold; variability in rates of i) accumulation, ii) firm densification and iii) melt processes. Figure 7.5 shows the spatial distribution of the relative importance of these three effects. It is clear that accumulation (Figure 7.5a) is the main driver of FAC variations, which was already found in earlier studies [Davis *et al.*, 2005; Helsen *et al.*, 2008; Ligtenberg *et al.*, 2012], but never quantified. In most parts of the AIS, more than 99 % of the FAC variations are explained by accumulation variability. In the steeper regions of the ice sheet (~ 250 km inland of the coast), where accumulation rates are relatively high, this increases to more than 99.9 %. At locations without snowmelt, the remainder of

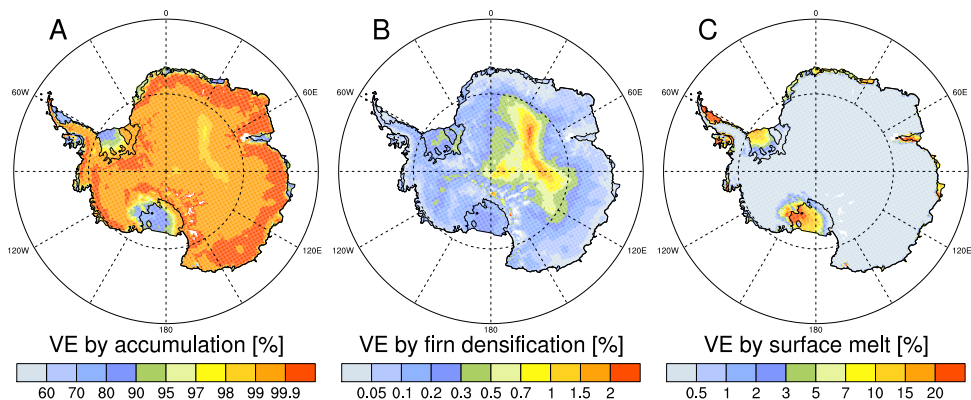


Figure 7.5: Fraction of firn air content variations (Figure 7.4a) explained (VE) by accumulation (a), firn densification (b) and surface melt (c). Note the different scales in (a), (b) and (c).

the signal is explained by variations in firn densification. At the highest elevations, where accumulation rates are among the lowest in Antarctica, the highest variance explained by firn densification is found: $\sim 2\%$ (Figure 7.5b). This reflects the fact that firn densification is a relatively constant process; variations are minor due to the near-constant temperature in most of the firn layer. Obviously, the variance explained by surface melt is only present at locations where melt occurs; i.e. the coastal areas and ice shelves (Figure 7.5c). The largest values ($>30\%$) are found on the Antarctic Peninsula ice shelves (Larsen C IS and Wilkins IS), where the largest annual surface melt rates are found. Interestingly, at locations with little melt, but also low accumulation rates (e.g. Siple Coast and Amery IS), the influence of melt on FAC variations is also large. A by-product of melt is that refreezing meltwater increases the firn temperature and therefore increases the firn densification rate. In Dronning Maud Land, for example, the variance explained by firn densification is slightly larger on the ice shelves than on the inland ice sheet due to this effect.

7.3.2 Future variations

The future evolution of the AIS firn layer is simulated with the time-dependent FDM, using RACMO2 climate forcing over the 1960–2200 period at 55 km horizontal resolution. Figure 7.6a shows the average FAC at the start of this period (1960–1999), which should be in agreement with the FAC as presented in Figure 7.1a. The spatial pattern is roughly the same, with the highest values (>35 m) at the domes of the East-Antarctic plateau and lower values (<15 m) along the coast. Obviously, spatial detail is reduced due to the coarser horizontal resolution, especially in regions with complex topography, such as the Transantarctic Mountains and the Antarctic Peninsula.

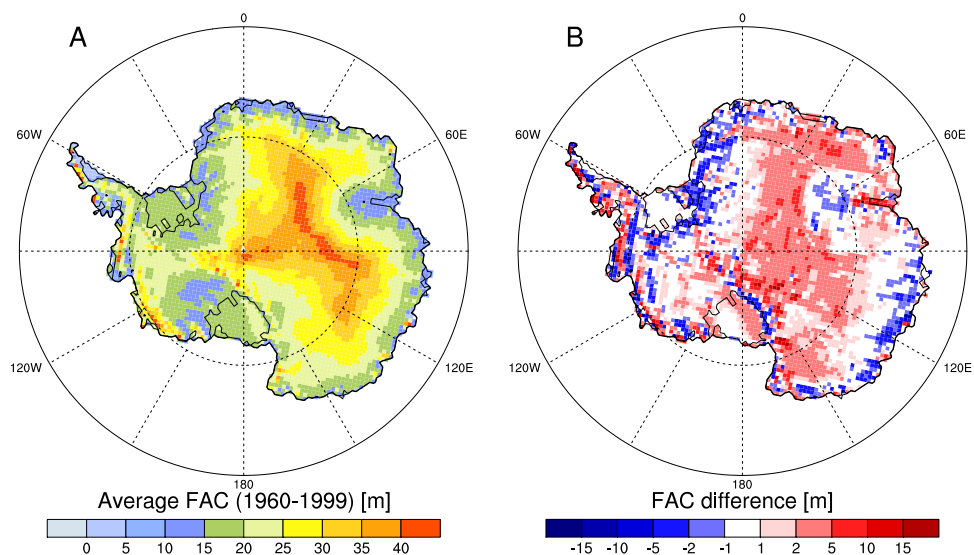


Figure 7.6: Average firn air content (FAC) for 1960–1999 (a) from the future FDM simulation, and the difference between (a) and average FAC from the contemporary climate simulation (b), interpolated from Figure 7.1a to the same grid as in (a).

Figure 7.6b indicates that most of the FAC differences can be attributed to climate differences caused by the varying topographic detail between the two. Basically, the patterns of high and low accumulation are slightly shifted, leading to subsequent differences in FAC. For example, the Transantarctic Mountains are less pronounced in the coarser resolution of the future simulation, leading to lower accumulation rates and hence smaller FAC. As a consequence, their shielding effect on the East-Antarctic interior is also less distinct, resulting in higher accumulation rates and larger FAC values. No negative SMB is simulated in this region, while this is present in the 27 km simulation (Figure 7.1a). Another notable difference is the higher FAC on Amery IS; apparently, the 55 km grid is too coarse to resolve the complex local topography and its effects on surface melt, that leads to low FAC values in the 27 km simulation. Looking at the large-scale spatial patterns, the difference is mostly positive in the East-Antarctic interior and negative along the coastal margins (Figure 7.6b), likely caused by the less steep topography in the coastal areas of the 55 km grid, resulting in less orographically forced precipitation. On the other hand, more water vapor reaches the interior of the ice sheet and enhances precipitation in this region. Averaged over the entire ice sheet, the average FAC is 23.57 m (Figure 7.6a), compared to 22.50 m in the 27 km simulation (Figure 7.1a).

When studying the future FAC evolution, the anomalies with regards to the 1960–1999 average are more important than the absolute differences outlined above. For example, two firn layers with a different FAC that are in equilibrium with their local climate will react similarly

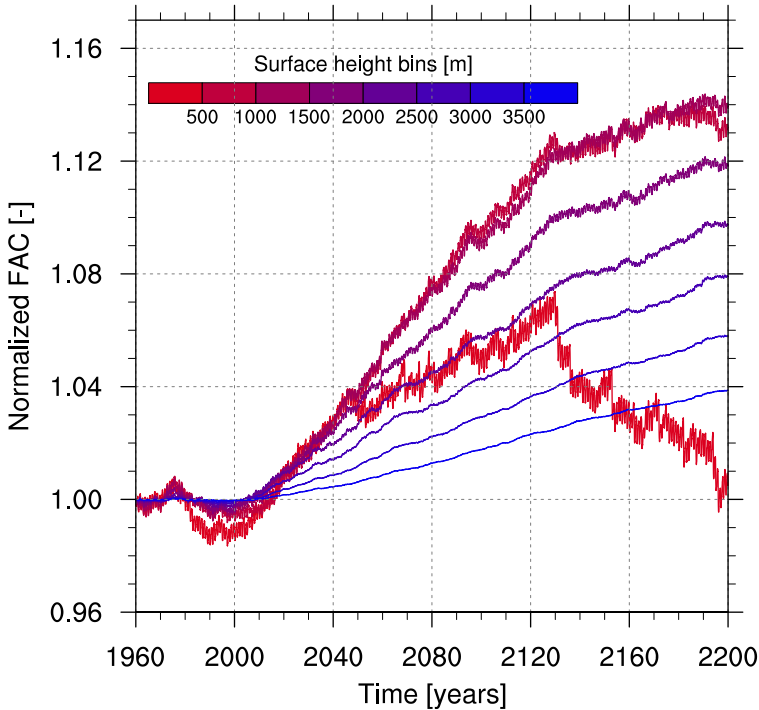


Figure 7.7: Temporal evolution of firn air content (FAC) in different surface height bins (line color) of the grounded ice sheet. The FAC is normalized using the value of 1 January 1960.

to an increase in precipitation (increase in FAC) or an increase in melt (decrease in FAC). In the next paragraphs, the main focus will therefore be on anomalies in FAC, rather than the absolute values of the change.

Figures 7.7 and 7.8 show the spatiotemporal FAC changes in Antarctica over the next two centuries. Averaged over the AIS, there is no trend in FAC over 1960–1979 (Figure 7.7), which is consistent with the set-up of the FDM: the firn characteristics in 1960 and 1980 are virtually similar, as the model is spun-up iteratively until it is in equilibrium with the 1960–1979 climate. As the average climate of 1980–1999 is used to scale the average climate of 1960–1979, no large changes are expected during this period. However, especially at lower altitudes, a deviation of a few percent is simulated for 1980–1999, likely caused by the non-linear response of FAC on inter-annual variability in the climatic forcing. The temporal evolution of FAC depends on the timing of inter-annual variations in accumulation (dry or wet), temperature (warm or cold) and surface melt (evenly spread or large pulses). For instance, when starting with a same initial firn layer, the resulting FAC is different when a wet period is followed by a dry period, than vice versa [Helsen *et al.*, 2008]. The same

accounts for multiple years with large melt rates followed by multiple non-melt years, and vice versa. Averaged over the entire AIS, the relative decrease in FAC in these 20 years is 0.5 % (Figure 7.7b).

Much larger changes in FAC are simulated for the 21st and 22nd centuries in response to increased snowfall and melt. Over the 21st century, the average FAC increases by 4.4 % (~1.0 m), with the spatial pattern shown in Figure 7.8a. Most of the ice-sheet interior shows a uniform increase in FAC. In general, the increase is lower further from the coast; the largest increases are simulated in a wide band along the Wilkes Land and West Antarctic coasts. This pattern is similar to the accumulation increase in the climate forcing (Figure 10b in *Ligtenberg et al.* [2013]). The largest FAC increases are simulated in the vicinity of Mertz Glacier (68 °S, 145 °E), where it increases by 29.6 % (7.7 m) in 100 years. The FAC increase due to fresh snow is partly counteracted by the faster firn-to-ice transition at the bottom of the firn layer and a faster firn densification rate. In the FDM, both these processes are parameterized using the average annual accumulation, and therefore both are projected to increase in the future.

In the coastal areas of West Antarctica and the Antarctic Peninsula, a significant FAC decrease is simulated, caused by the increase in surface melt in these lower-lying regions. The eastern part of the Ross IS is also expected to experience significantly more melt, resulting in a lower FAC. When the FAC approaches zero, ice shelves can become susceptible to meltwater ponding and hydrofracturing [*Kuipers Munneke et al.*, 2014].

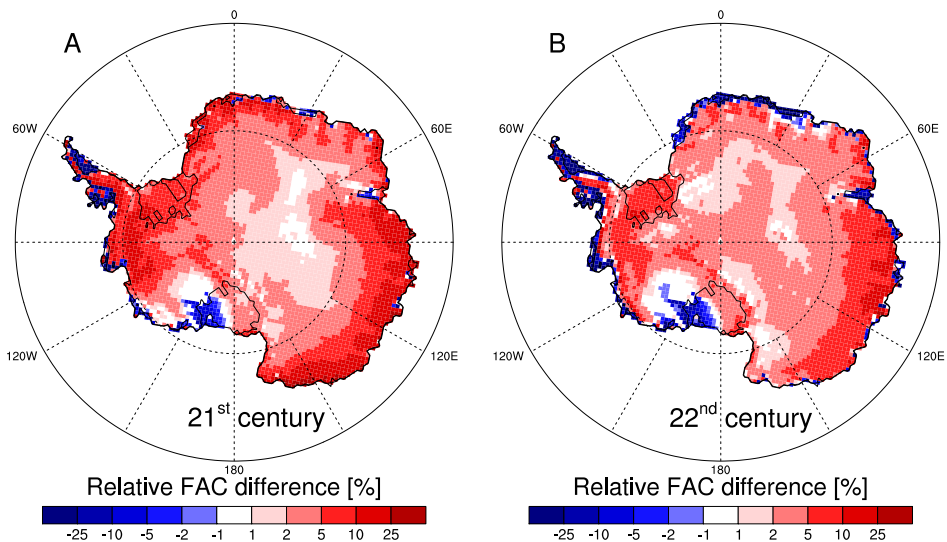


Figure 7.8: Relative firm air content (FAC) difference over the 21st (a) and 22nd (b) century. The relative differences are calculated as the difference between the 20-year averages of 1980–1999 and 2080–2099, and 2080–2099 and 2180–2199, respectively.

During the 22nd century, the spatial pattern of FAC change (Figure 7.8b) is roughly similar to that of the 21st century (Figure 7.8a). Again, there is a distinct and uniform FAC increase in the interior of the ice sheet and a decrease along the margins. However, there are two notable differences. First, the increase over most of the ice sheet is slightly smaller than the 21st century increase, owing to a less distinct increase in precipitation in the 22nd century. In the second half of the 22nd century, the Antarctic climate stabilizes as the greenhouse forcing of the climate model is set constant at the 2100-level [Ligtenberg *et al.*, 2013]. In part, this also explains the flattening of the FAC increase towards the end of the simulation (Figure 7.7). Second, along the East-Antarctic coast, the decrease in FAC is more pronounced. Especially the ice shelves in Dronning Maud Land show a significant reduction in FAC (25–40 % or 4–7 m). Also the other East-Antarctic ice shelves (e.g. Amery IS, West IS, Shackleton IS) show decreasing firn air values. The relative FAC changes along the West-Antarctic coast and in the Antarctic Peninsula are also large, but do not lead to large absolute differences as many of these ice shelves already approach zero FAC by 2100 [Kuipers Munneke *et al.*, 2014].

The future, melt-driven FAC reduction in lower-lying regions is illustrated by the FAC evolution of the <500 m height bin in Figure 7.7. From 2000 until 2050, the simulated FAC increase is equal to or slightly larger than the increase in other height bins, indicating that the increase in precipitation during this interval is largest at lower altitudes. Over the next 80 years (2050–2130), the slope decreases: precipitation is still increasing, but this effect is partly counteracted by a simultaneous increase in surface melt. Around 2135, a couple of strong melt years occur [Ligtenberg *et al.*, 2013] that initiate an abrupt decrease in FAC. Hereafter, a negative trend persists that reduces FAC by 6 % over the last 60 years of the simulation, and result in a similar FAC amount as in 1960–1979. In all other altitudes bins, the FAC increases significantly. The largest relative increases ($\sim 14\%$) are found at lower altitudes (500–1500 m), in agreement with the largest simulated precipitation increase. Higher up on the AIS, the increase in precipitation becomes smaller, leading to smaller FAC increases. In the highest altitude bin (> 3500 m), FAC is simulated to increase by $\sim 4\%$ over the next two centuries.

These FAC increases can be put in perspective by converting them into volume changes for the entire ice-sheet. Over the 21st century, the simulated volume increase is $\sim 150 \text{ km}^3 \text{ yr}^{-1}$, representing the sum of contributions from positive ($+158 \text{ km}^3 \text{ yr}^{-1}$) and negative difference grid points ($-8 \text{ km}^3 \text{ yr}^{-1}$). During the 22nd century, the increase summed over the positive grid points is similar ($+147 \text{ km}^3 \text{ yr}^{-1}$), but mainly due to a larger volume change over the negative grid points ($-25 \text{ km}^3 \text{ yr}^{-1}$), the total volume change is significantly smaller than during 2000–2100. Next to this increase in firn air due to enhanced precipitation, the mass increase by snowfall itself [$\sim 150 \text{ Gt yr}^{-1}$, from Ligtenberg *et al.*, 2013] also causes a volume increase; $\sim 150 \text{ km}^3 \text{ yr}^{-1}$. The ratio between the simulated volume increase due to ice crystals and air (more or less 1:1) is lower than expected (1:2) when solely considering the density of fresh snow ($\sim 350 \text{ kg m}^{-3}$). This indicates that half of the additional FAC by enhanced

snowfall is removed by either snowmelt, increased firn densification or a faster firn-to-ice transition at the bottom of the firn layer. The combined volume increase from ice crystals and air ($\sim 300 \text{ km}^3 \text{ yr}^{-1}$) causes the surface of the AIS to rise with $\sim 2.1 \text{ cm yr}^{-1}$ until 2100. Therefore, these surface and firn layer effects must be taken into account for future ice-sheet mass balance studies based on volumetric changes. Moreover, this illustrates that knowledge of firn layer behavior and its response to climate variations remains invaluable for a correct interpretation of current and future observations of ice-sheet volume balance.

7.4 Discussion

The results presented here depend strongly on the climate output of the forcing climate model RACMO2. Based on previous work, RACMO2 produces a realistic Antarctic climate. For example, the simulated SMB corresponds well with ~ 750 in-situ SMB observations [Lenaerts *et al.*, 2012a]. Forced with 27 km RACMO2 climate (1979–2011), the steady-state FDM agrees well with firn-core observations [Ligtenberg *et al.*, 2011] and simulates firn densities similar to earlier steady-state solutions [e.g. Zwally and Li, 2002; Van den Broeke, 2008]. Seasonal and inter-annual variations in RACMO2 accumulation and subsequent variations in FDM-simulated firn depth compare well with satellite observations [e.g. Pritchard *et al.*, 2012; Ligtenberg *et al.*, 2012; Horwath *et al.*, 2012; Medley *et al.*, 2013]).

In the future RACMO2 climate forcing, more uncertainties are present. The 1980–1999 climate of the global climate model used to force RACMO2 shows a cold and dry bias, when compared to the re-analysis forced RACMO2 simulation [Ligtenberg *et al.*, 2013]. This bias is removed from both the present-day period (1980–1999) and the future period (2000–2199) in order to obtain realistic average precipitation and snowmelt values [Kuipers Munneke *et al.*, 2014]. The resulting difference in FAC between both present-day simulations is quite small, but spatially more significant differences occur, which can for a large part be explained by the difference in horizontal resolution between both forcings. In Ligtenberg *et al.* [2013], an assessment of the future climate results shows that the Antarctic snowfall sensitivity (in $\text{Gt yr}^{-1} \text{ K}^{-1}$) is in the same range as in other studies. Moreover, Antarctic precipitation scales more or less linearly with temperature and since the simulated change is more than three times larger than the bias in the 1980–1999 climate, at least two-thirds of the simulated accumulation change in RACMO2 is expected to be realistic.

Also, the possible range in future temperature change can produce uncertainty that is not included. It was computationally not feasible to perform more than one FDM future simulation for the complete AIS, so a mid-range emission scenario (A1B) was selected. Due to the relatively linear response of precipitation and SMB to a temperature increase, the results from this manuscript in combination with those from Ligtenberg *et al.* [2013] can be used to scale the firn layer response for different climate scenarios.

Another uncertainty derives from the FDM itself and its ability to simulate temporal evolution of firn temperature and density. The used FDM is based on semi-empirical equations and errors in the measurements therefore introduce errors in the FDM results. In the Supplementary Online Material of *Depoorter et al.* [2013], the uncertainty in FAC is assessed as a combination of the three fixed points in a steady-state firn profile: 1) surface density, 2) depth at which the density reaches $\rho = 550 \text{ kg m}^{-3}$ and 3) depth at which the density reaches $\rho = 830 \text{ kg m}^{-3}$. From FDM sensitivity experiments, a FAC uncertainty of $\sim 10\%$ was obtained.

7.5 Conclusion

The amount of air in the Antarctic firn layer greatly varies in time and space. Knowledge of these variations is critical for a correct interpretation of satellite measurements. FAC has often been estimated using a steady-state solution, thereby assuming that the firn layer density is constant in time. This approach does not consider temporal variations in FAC due to climate variability, nor the effect of meltwater refreezing on firn density and air content. Here, we examined the temporal variations in Antarctic FAC and assessed the differences with an earlier-published steady-state solution. Also, a transient simulation of the firn layer until 2200 is performed to estimate the effect of a warmer and wetter Antarctic climate on the FAC.

Averaged over the ice sheet, there is virtually no difference in average FAC between the steady-state and the time-dependent solution. However, regional differences are quite large. In the part of the AIS where no surface melt occurs ($\sim 90\%$), the FAC is slightly underestimated ($\sim 3\%$) by the steady-state solution. For coastal locations, where summer melt is significant, the steady-state solution overestimates the FAC, because refrozen meltwater that occupies firn pore space is not taken into account. A major application of simulated FAC is to correct ice thickness measurements at the grounding line, in order to determine ice discharge of the ice sheet. Most of the grounding line is located in the low-elevation region where melt occurs, indicating that the discharge of grounded ice is underestimated when steady-state FAC values are used. Between the steady-state and time-dependent models, the average FAC difference at the grounding line is 2.7 m, which is 0.7 % of the local ice thickness. Differences in ice thickness are however directly translated into difference in ice discharge and ice-sheet mass balance. Since the latter is a relatively small number, the influence of the FAC difference is quite significant (23.5 % or 16.7 Gt yr^{-1}) when estimating the sea-level contribution of the AIS.

Seasonal and inter-annual variations in accumulation and temperature introduce short-term variability in FAC. In the East Antarctic interior, these variations are small ($< 1\%$), due to low accumulation rates and low temperatures. Along the warmer and wetter coastal margins however, variations are larger ($\sim 5\%$). At locations with significant summer melt (e.g. coastal ice shelves), temporal FAC variations in the contemporary climate simulation can be as large

as 50 %. Elsewhere, the FAC variations are predominantly caused by variability in accumulation.

In the future, the largest part of the AIS will remain melt-free, resulting in a FAC increase due to an accumulation increase. This increase is partly counteracted by an increase in firn compaction and the faster transition from firn to ice at the bottom of the firn layer. At the highest altitudes, the smallest relative increase (2200 minus 2000) is simulated (4 %), while at moderate altitudes (1000–2000 m) a FAC increase of 12–14 % is simulated. At the lowest altitudes (generally below 500 m), this effect is partly or fully compensated by the increase in surface melt. The ice shelves in West Antarctica, the Antarctic Peninsula and Dronning Maud Land lose most of their FAC due to this process and therewith their buffer capacity to refreeze meltwater, making them susceptible to hydrofracturing [Kuipers Munneke *et al.*, 2014].

The simulated future increase in FAC indicates that, next to a mass increase due to increased accumulation [Ligtenberg *et al.*, 2013], the volume of the AIS will likely increase at a rate of $\sim 300 \text{ km}^3 \text{ yr}^{-1}$. Interpreting this as a change in ice mass would lead to an underestimation of the contribution of the AIS to sea-level rise. Corrections for variations in the firn layer are therefore crucial for a correct interpretation of future AIS volume changes and their conversion to mass changes.

8

Summary and outlook

In this final chapter, the main results and conclusions from this thesis are highlighted, together with an outlook towards future research in firn modeling. First, the firn densification model and the results for the contemporary Antarctic firn layer from Chapters 2–5 are recapitulated. Next, the future Antarctic climate and the response of the firn layer to these changes (Chapters 6 and 7) is summarized and discussed. The future outlook contains suggestions for improvements in the field of firn modeling. Although this thesis is a step forward in our knowledge of the Antarctic firn layer and the processes that drive its spatiotemporal variations, a number of possible improvements can be made, which are discussed first. Hereafter, possible firn modeling on the Greenland ice sheet and other land-ice regions on Earth are reviewed.

8.1 Summary and conclusions

The main goal of the research presented in this thesis is to determine the present state of the Antarctic firn layer, and its response to a future warming climate. The Antarctic ice sheet is for more than 98 % covered by firn, a 50–150 m thick layer of compressed snow that slowly transforms to glacier ice. The thickness, temperature and density of this layer vary in both space and time. The underlying ice is what has been attracting more and more interest over the last few decades, due to its (potential future) contribution to sea level change. To correctly assess the changes in Antarctic ice mass, knowledge of spatial and temporal changes in the ice sheet firn layer is a necessity.

8.1.1 Firn densification model

As a consequence of the remoteness, size and harsh climate conditions of the Antarctic ice sheet, it is difficult to obtain sufficient observations of the Antarctic firn layer. To overcome this problem, a firn densification model (FDM) that simulates firn layer evolution in space and time is used throughout this thesis. The FDM is based on principles of previous firn models that were used for similar purposes [*Herron and Langway*, 1980; *Zwally and Li*, 2002; *Helsen et al.*, 2008]. Improvements include the implementation of a snowmelt module to allow for the simulation of simple firn hydrology, and the inclusion of updated densification equations from *Arthern et al.* [2010]. At the surface, the FDM is forced with realistic climate variables (e.g. surface mass balance (SMB), temperature, wind speed) from a regional atmospheric climate model (RACMO2). In Chapter 2, the capability of the FDM is verified against 48 firn core observations, which reveals an underestimation of the firn densification rate in low-accumulation regions (i.e. the simulated firn layer is too thick), and vice versa for high-accumulation regions. An extra accumulation dependence is introduced in the densification equation to compensate for this bias.

8.1.2 Current state of the Antarctic firn layer

Using FDM simulations, the present state of the Antarctic firn layer is discussed in Chapters 2–5 and 7. The FDM can simulate firn layer behavior in two modes: steady-state and time-dependent. The first calculates the average firn profiles using the local average climate conditions and is computationally four to five orders of magnitude faster than the latter. A disadvantage of this mode is the inability to simulate temporal variations in the firn layer. Moreover, it does not take the effect of surface melt on firn density and temperature into account. Both these processes are included in the time-dependent mode.

The steady-state solution provides a good first guess of the spatial differences in firn properties; a thick firn layer (100–150 m) in the cold interior of the ice sheet and a thinner firn

layer (40–60 m) along the coasts (Chapter 2). An exception is found in coastal locations that receive large accumulation rates. Here, fresh snow has less time to densify as it is quickly buried by new accumulation, hence leading to a thick firn layer. In general, the thickest firn layers are found at cold and/or wet locations, while the thinnest firn layers are simulated on dry and/or warm locations, or when surface melt is present. In the latter case, meltwater refreezes in the air pores of the firn layer, thereby quickly increasing the firn density and subsequently thinning the firn layer. Melt is not incorporated in the steady-state FDM, so in this mode the firn layer thickness is overestimated at these locations.

With the time-dependent FDM, temporal variations in firn characteristics are examined (Chapters 3 and 7). As a result of large spatiotemporal variations in the Antarctic climate, the thickness, density and air content of the firn layer also vary. The firn air content (FAC) is defined as the layer of air that remains when the firn layer is compressed to the density of ice. In Chapter 7, it is shown that substantial surface melt can result in a FAC difference of 5–10 m (or $\sim 50\%$) between both FDM modes. Among other things, this has implications for ice thickness and ice discharge observations that rely on firn air corrections. Along the grounding line of the Antarctic ice sheet, an important location for the determination of ice sheet discharge, the average FAC difference is 2.7 m, or 0.7% of the average ice thickness at the grounding line. This difference is directly translated into the derived ice sheet mass imbalance, a much smaller quantity, where it leads to a significant (23.5% or 16.7 Gt yr^{-1}) underestimation of the current estimate [Rignot *et al.*, 2011a; Shepherd *et al.*, 2012].

The temporal changes in firn layer characteristics (thickness, density, temperature) also have an effect on the surface elevation; when snow compacts over time, or melt removes mass from the surface, the surface elevation will drop. The opposite occurs when fresh snow accumulates on the surface. As a consequence of the seasonal cycle in Antarctic accumulation and air temperature (i.e. warm and dry in summer, cold and wet in winter), the surface elevation of the firn layer follows this seasonal cycle (Chapter 3). During autumn, winter and spring, the surface slowly rises due to relatively low temperatures and high accumulation, while in summer the surface rapidly drops due to a combination of higher temperatures, lower accumulation and (in some locations) surface melt. These seasonal oscillations are also represented in the air content of the firn layer, and the resulting process is therefore also referred to as 'the seasonal breathing of the Antarctic ice sheet'. This 'breathing' effect explains roughly one-third of the seasonal oscillations found in ENVISAT satellite radar altimetry measurements.

Chapters 4 and 5 describe two case studies that were conducted to examine the robustness of the FDM, while simultaneously studying two interesting regions of the Antarctic ice sheet. First, the influence of firn layer properties on the formation and extent of blue ice areas (BIA) is investigated. At BIAs, glacier ice is exposed at the surface as a consequence of long-term ablation, i.e. more snow/firn is removed from the surface than is accumulated. BIA formation appears to be an interplay between; 1) ice velocity, 2) SMB and 3) firn layer mass. These three conditions need to occur in a favorable combination in order for a BIA to form: low ice velocity, negative SMB and a firn layer with relatively little firn mass upstream of the

ablation area. The surface of a BIA is generally harder, smoother and darker than a snow surface, which leads to more absorption of solar radiation and less fresh snow that remains on the surface. Due to these feedback mechanisms, a BIA is in part self-sustaining and a significantly positive SMB is required to cover a BIA with fresh snow and thereby terminate the feedback effects.

Next, the firn layer of the Antarctic Peninsula (AP) is modeled at high horizontal resolution in Chapter 5. The AP is the only part of the more or less circular Antarctic ice sheet that extends northwards into the Southern Ocean. It therefore has a wetter and milder climate than the rest of the ice sheet. Also, the topography of the AP is complex with a variety of high, steep mountains, relatively small, confined ice streams and flat ice shelves. A couple of these ice shelves are the only locations in Antarctica where surface runoff occurs. Knowledge of the AP firn layer is important for both ice thickness measurements and to provide locations that are prone to produce runoff at present or in the near-future. With the help of relations between surface melt, accumulation and FAC (modeled and observed), a steady-state firn map of the AP is constructed that also includes the effect of melt. On the northern part of George VI Ice Shelf and the former Larsen B Ice Shelf, no firn layer is simulated, indicating that these regions are likely to produce regular runoff due to a lack of firn refreezing capacity. For both locations, this is verified by observations of meltwater ponding in summer. Elsewhere in the AP, a firn layer is simulated that varies in thickness between a few meters on the northern Larsen C Ice Shelf and almost 50 m on the spine of the mountain range, due to large accumulation rates.

In conclusion, the FDM is capable of realistically simulating the behavior of the present Antarctic firn layer. Two large improvements compared to earlier studies are, 1) the inclusion of melt processes, as a result of which the entire ice sheet can be examined instead of only the dry-snow zone, and 2) the quantification of seasonal and inter-annual variability in FAC and surface elevation, which accentuates their necessity for the correct interpretation of satellite observations. Another robust result is that the FDM is able to simulate firn layer behavior under extreme climate conditions, i.e. net annual ablation by sublimation and/or melt, leading to bare ice at the surface.

8.1.3 Future state of the Antarctic firn layer

In order to correctly simulate the future evolution of the Antarctic firn layer, a realistic climate forcing over the same period is required. Four simulations of the future Antarctic climate and SMB are therefore discussed in Chapter 6. By forcing RACMO2 with two different global circulation model datasets (HadCM3 and ECHAM5) and two different greenhouse gas emission scenarios (A1B and E1), the spread in possible climate change scenarios is mimicked. Averaged over the entire Antarctic ice sheet, the 2-m air temperature is expected to rise at a similar pace as the global mean temperature rise: 1.8–3.0 K in the 21st century and 2.4–5.3 K in the 22nd century. The hydrological cycle on Antarctica is coupled to temperature, meaning

that a temperature increase also leads to a change in the individual SMB components. The larger water vapor holding capacity of warmer air increases the precipitation on the Antarctic ice sheet. Both rainfall and surface melt increase, but most of this excess liquid water refreezes in the firn pack, hence surface runoff remains small during the next two centuries. The increase in surface sublimation is minor compared to the other components, meaning that the future SMB increase is dominated by the increase in snowfall: $+98 \text{ Gt w.e. yr}^{-1} \text{ K}^{-1}$. Without any ice dynamical response, this would result in a significant negative sea level contribution (-73 to -163 mm SLR by 2200).

When this 220-year climate (1980–2200) is used as forcing for the FDM, the response of the current firn layer to a significant temperature, precipitation and surface melt increase is obtained. The increase in precipitation adds more fresh snow, and consequently more air, to the Antarctic firn layer, resulting in a thicker firn layer. This effect is partly counteracted by the increase in firn densification rate, due to higher temperatures and an enhanced firn-to-ice transition at the bottom of the firn layer, due to increased firn loading. In melt-free regions, the FAC increase (4–14 %) depends on the absolute amount of accumulation increase, with higher absolute accumulation increases leading to larger FAC increases. In the coastal areas of the ice sheet, summer melt will increase, leading to additional refrozen meltwater in the firn layer, thereby occupying air pore space and diminishing FAC over the coming centuries. On many ice shelves the FAC is expected to reduce by 50–70 % by 2200. Averaged over the entire ice sheet, the increase in the ice-sheet interior has the upper hand over the decrease along the margins, leading to an extra volume change due to firn air of $120\text{--}150 \text{ km}^3 \text{ yr}^{-1}$ over the next two centuries.

8.2 Outlook

8.2.1 Firn modeling in Antarctica

The research in this thesis describes variations in firn layer processes on the Antarctic ice sheet. Although this thesis increases our understanding of these processes, Antarctic firn modeling can make an additional step forward in three ways; i) a more realistic, physical FDM, ii) improved climate forcing and iii) more observations. The latter is rather obvious, as Antarctic firn core observations are scarce. The ice sheet is spatially poorly sampled, while large climate gradients exist. Also, most observations are limited to a point measurement in time, making it difficult to verify temporal differences as simulated by the FDM. A satellite remote sensing method to observe changes inside the firn layer up to a few meters depth has the potential to produce very useful verification data.

The current FDM uses a couple of equations that rely on long-term average climate quantities, while temporal variations in firn conditions are being targeted. For example, the density of fresh snow is determined using the average surface temperature, accumulation and wind

speed, and is taken constant in time. In reality, the density of fresh snow is not constant in time (i.e. every snow flake is unique) and is in fact determined by upper-air climate variables, such as temperature and humidity. Also, the firn densification equations are parameterized to capture different processes into one equation, such as grain settling and sublimation and deformation of ice crystals. Currently, our knowledge of these individual processes is restricted to laboratory experiments and it will take time to model them satisfactorily. When a more physical densification model is available, the different processes that lead to variations in firn layer density and thickness can be better distinguished.

The previous paragraph suggests that progress can be obtained by using a more physically-based FDM, however, it is expected to have a relatively small influence on its results. Most of the inter-annual and seasonal variations that are simulated by the FDM originate from climate variations in its forcing. Although RACMO2 is considered the state-of-the-art SMB product for Antarctica and has shown to agree well with in-situ observations [Lenaerts *et al.*, 2012a], it remains a model with a relative coarse horizontal resolution (27 km). Many of the interesting features in Antarctica (e.g. mountainous regions, ice streams, BIAs and ice shelves) are only partly resolved at this resolution, while some satellites observe changes at km scale. Focussing on specific regions, and thereby increasing the horizontal resolution of RACMO2, is a method to obtain FDM data that have the ability to better interpret these observed local changes.

Another critical aspect of the current FDM set-up is the relatively short time period (1979–2012) of the climate forcing. The initial firn profile at the start of a FDM simulation greatly influences the result, an improvement could therefore be obtained by better constraining the initial conditions. A firn layer contains snow that is 100–1,000 years old, indicating that a climate forcing over this entire period would be desirable to correctly simulate the present firn layer. This time span can only be obtained from ice core records, which provide an indication about the past climate but contain no information about spatial or seasonal variability.

Another interesting addition to the field is to simulate firn layer evolution along ice flowlines for the entire Antarctic ice sheet. When an ice column moves along an ice flowline, the firn layer on top is carried through different climates. From the chapter on BIA formation (Chapter 4), it is clear that the firn layer at a certain point is not necessarily in equilibrium with the local climate. Especially at fast-flowing ice ($>500 \text{ m yr}^{-1}$), this effect can be substantial when climate gradients are large. For example, a random glacier in the AP experiences a large difference in forcing climate between the high accumulation rates in the mountainous region and the low accumulation rates, including summer surface melt, on the flat ice shelf in which it terminates. Locally, the influence on the FAC and surface elevation is expected to be quite significant. The differences in FAC will likely be positive, as on average the thicker firn layers from the interior are advected towards the coast.

8.2.2 Firn modeling in Greenland

Similar to the Antarctic ice sheet, the Greenland ice sheet is also covered with a layer of firn, making it equally difficult to interpret satellite/airborne observed changes in ice thickness and surface elevation. In the near-future, a similar research as in this thesis is necessary for the Greenland ice sheet. Its climate and firn layer are, however, more complicated than its Antarctic counterparts. In Antarctica, surface melt does not occur on the majority of the ice sheet (>90%), while more than half of the Greenland ice sheet experiences significant surface melt every summer. Along the margins of the ice sheet, the annual melt exceeds the annual accumulation, resulting in exposed bare ice at the surface and run off of the excess meltwater.

The Greenland surface melt climate leads to some firn layer behavior that is specific for the Greenland ice sheet; such as heterogenous meltwater percolation, perennial firn aquifers and meltwater lakes. All these features are not included in the current FDM, as they are not observed in Antarctica. Surface melt research in Greenland indicates that persistent melt can lead to preferential flow paths in the firn layer [Benson, 1962; Marsh and Woo, 1984]. In other words, vertical channels and tubes are formed which transport meltwater quickly down into the firn layer, where it refreezes at depth. In the FDM, this is not modeled and meltwater refreezes immediately when it enters an underlying layer that is below freezing temperature. Perennial firn aquifers are another characteristic that is not specifically included in the FDM. When both surface melt and accumulation occur in large enough amounts, summer-produced meltwater can survive inside the firn pack during the following winter [Kuipers Munneke *et al.*, in press]. As a result, some kind of sub-surface lakes form on top of the underlying ice column. This feature was only recently discovered [Forster *et al.*, 2013], and its formation and possible lateral transport of liquid water is not yet fully understood. A third complicating factor for firn modeling on Greenland is the presence and draining of meltwater lakes, especially at the western side of Greenland. Here, the excess meltwater runs off over the ice-sheet surface into lakes that form in surface depressions. These lakes steadily expand until they quickly drain through moulins and sub-glacial cavities. In the FDM, only downward flow of meltwater is allowed, so an adaptation would be necessary to accommodate for meltwater-lake formation. Also, there is currently no lateral exchange of mass between neighboring firn columns, making it difficult to account for any kind of lateral transport of meltwater.

To set up a robust FDM for the Greenland ice sheet, research mainly has to focus on meltwater processes. For the large majority of the Antarctic ice sheet, it is sufficient to rely on relatively simple firn hydrology, but a Greenland FDM version requires a more sophisticated module to encompass the above described processes.

8.2.3 Firn modeling on glaciers and ice caps

Outside of the two large ice sheets, firn layers are also present on the remainder of the Earth's land ice. In the accumulation zones of mountain glaciers (e.g. the Alps and the Himalaya) and smaller ice caps (e.g. Patagonia, Alaska and the Canadian Archipelago), more snow accumulates than is removed on an annual basis, thereby building up a firn layer. Recently, multiple studies [e.g. *Moholdt et al.*, 2010; *Berthier et al.*, 2010; *Gardner et al.*, 2011, 2013] have tried to assess the mass change of some of these ice bodies using the altimetry method (Chapter 1). When the surface consists of glacier ice (i.e. in the ablation zone), this method works well and the measured volume changes can be easily converted into a mass change using the density of glacier ice. However, in the accumulation zone, these measured surface elevation changes can also be caused by changes in firn layer thickness. The uncertainty in the current mass balance estimates of these regions can be significantly reduced when the temporal evolution of these firn layers is modeled. The greatest difficulty in doing so, is to obtain a realistic climate forcing. As described in this thesis, a realistic forcing climate is of major importance for the correct simulation of firn layer behavior. Most of the smaller ice caps and glaciers are located in regions with complex topography, implying large climate gradients over small distances. The resolution of global re-analysis data is too coarse to resolve these details and high-resolution dedicated climate model simulations for these regions are currently not available.

Bibliography

- Arthern, R. J., D. J. Wingham, and A. L. Ridout (2001), Controls on ERS altimeter measurements over ice sheets: Footprint-scale topography, backscatter fluctuations, and the dependence of microwave penetration depth on satellite orientation, *Journal of Geophysical Research*, *106*(D24), 33,471–33,484, doi:10.1029/2001JD000498.
- Arthern, R. J., D. P. Winebrenner, and D. G. Vaughan (2006), Antarctic snow accumulation mapped using polarization of 4.3-cm wavelength microwave emission, *Journal of Geophysical Research*, *111*(D06107), doi:10.1029/2004JD005667.
- Arthern, R. J., D. G. Vaughan, A. M. Rankin, R. Mulvaney, and E. R. Thomas (2010), In situ measurements of Antarctic snow compaction compared with predictions of models, *Journal of Geophysical Research*, *115*(F03011), doi:10.1029/2009JF001306.
- Bamber, J. L., D. G. Vaughan, and I. Joughin (2000), Widespread complex flow in the interior of the Antarctic ice sheet, *Science*, *287*(5456), 1248–1250, doi:10.1126/science.287.5456.1248.
- Bamber, J. L., et al. (2013), A new bed elevation dataset for Greenland, *The Cryosphere*, *7*, 499–510, doi:10.5194/tc-7-499-2013.
- Barnola, J.-M., P. Pimienta, D. Raynaud, and Y. S. Korotkevich (1991), CO₂-climate relationship as deduced from the Vostok ice core: a re-examination based on new measurements and on a re-evaluation of the air dating, *Tellus*, *43B*, 83–90, doi:10.1034/j.1600-0889.1991.t01-1-00002.x.
- Bengtsson, L., S. Koumoutsaris, and K. Hodges (2011), Large-scale surface mass balance of ice sheets from a comprehensive atmospheric model, *Surveys in Geophysics*, *32*, 459–474, doi:10.1007/s10712-011-9120-8.
- Benson, C. S. (1962), Stratigraphic studies in the snow and firn of the Greenland ice sheet, *SIPRE Research Report 70*, pp. 1–182.
- Berthier, E., E. Schiefer, G. K. C. Clarke, B. Menounos, and F. Rémy (2010), Contribution of Alaskan glaciers to sea-level rise derived from satellite imagery, *Nature Geoscience*, *3*, 92–95, doi:10.1038/NCEO737.
- Bintanja, R. (1999), On the glaciological, meteorological, and climatological significance of Antarctic blue ice areas, *Reviews in Geophysics*, *37*(3), 337–359, doi:10.1029/1999RG900007.
- Bintanja, R., and M. R. van den Broeke (1995), The surface energy balance of Antarctic snow and blue ice, *Journal of Applied Meteorology*, *34*, 902–926, doi:10.1175/1520-0450(1995)034<0902:TSEBOA>2.0.CO;2.
- Braithwaite, R. J., M. Laternser, and W. T. Pfeffer (1994), Variations of near-surface firn density in the lower accumulation area of the Greenland ice sheet, Pakitsoq, West Greenland, *Journal of Glaciology*, *40*(136), 477–485.
- Bromwich, D. H., J. P. Nicolas, and A. J. Monaghan (2011), An assessment of precipitation changes over Antarctica and the Southern Ocean since 1989 in contemporary global reanalyses, *Journal of Climate*, *24*(16), 4189–4209, doi:10.1175/2011JCLI4074.1.
- Brown, I. C., and T. A. Scambos (2004), Satellite monitoring of blue-ice extent near Byrd Glacier, Antarctica, *Annals of Glaciology*, *39*(1), 223–230, doi:10.3189/172756404781813871.
- Cassidy, W., R. Harvey, J. Schutt, G. Delisle, and K. Yanai (1992), The meteorite collection sites of Antarctica, *Meteoritics*, *27*(5), 490–525, doi:10.1111/j.1945-5100.1992.tb01073.x.
- Chambers, D. P., J. Wahr, and R. S. Nerem (2004), Preliminary observations of global ocean mass variations with GRACE, *Geophysical Research Letters*, *31*(L13310), doi:10.1029/2004GL020461.
- Chapman, W. L., and J. E. Walsh (2007), Simulations of Arctic temperature and pressure by Global Coupled Models, *Journal of Climate*, *20*, 609–632, doi:10.1175/JCLI4026.1.
- Church, J. A., et al. (2011), Revisiting the Earth's sea-level and energy budgets from 1961 to 2008, *Geophysical Research Letters*, *38*(L18601), doi:10.1029/2011GL048794.
- Coléou, C., and B. Lesaffre (1998), Irreducible water saturation in snow: experimental results in a cold laboratory, *Annals of Glaciology*, *26*, 64–68.
- Conolley, W. M., and T. J. Bracegirdle (2007), An Antarctic assessment of IPCC AR4 coupled models, *Geophysical Research Letters*, *34*(L22505), doi:10.1029/2007GL031648.
- Cook, A. J., and D. G. Vaughan (2010), Overview of areal changes of the ice shelves on the Antarctic Peninsula over the past 50 years, *The Cryosphere*, *4*, 77–98, doi:10.5194/tc-4-77-2010.
- Das, I., et al. (2013), Influence of persistent wind-scour on surface mass balance of Antarctica, *Nature Geoscience*, *6*, 367–371, doi:10.1038/ngeo1766.

- Davis, C. H., Y. Li, J. R. McConnell, M. M. Frey, and E. Hanna (2005), Snowfall-driven growth in East Antarctic ice sheet mitigates recent sea-level rise, *Science*, *308*, 1898–1901, doi:10.1126/science.1110662.
- Dee, D. P., and et al. (2011), The ERA-Interim reanalysis: configuration and performance of the data assimilation system, *Quarterly Journal of the Royal Meteorological Society*, *137*(656), 553–597, doi:10.1002/qj.828.
- Depoorter, M. A., J. L. Bamber, J. A. Griggs, J. T. M. Lenaerts, S. R. M. Ligtenberg, M. R. van den Broeke, and G. Moholdt (2013), Calving fluxes and melt rates of Antarctic ice shelves, *Nature*, *502*, 89–92, doi:10.1038/nature12567.
- Doake, C. S. M., and D. G. Vaughan (1991), Rapid disintegration of the Wordie Ice Shelf in response to atmospheric warming, *Nature*, *350*, 328–330, doi:10.1038/350328a0.
- Doake, C. S. M., H. F. J. Corr, H. Rott, R. Skvarca, and N. W. Young (1998), Breakup and conditions for stability of the northern Larsen Ice Shelf, Antarctica, *Nature*, *391*, 778–780, doi:10.1038/35832.
- Dong, D., T. Yunck, and M. Hefflin (2003), Origin of the International Terrestrial Reference Frame, *Journal of Geophysical Research*, *108*(B4), 2200, doi:10.1029/2002JB002035.
- Ettema, J. (2010), The present-day climate of Greenland: A study with a regional climate model. PhD thesis, Utrecht University, pp 123, (<http://igitur-archive.library.uu.nl/dissertations/2010-0408-200308/uuindex.html>).
- Ettema, J., M. R. van den Broeke, E. van Meijgaard, W. J. van de Berg, J. Bamber, J. E. Box, and R. C. Bales (2009), Higher surface mass balance of the Greenland ice sheet revealed by high-resolution climate modeling, *Geophysical Research Letters*, *36*(L12501), doi:10.1029/2009GL038110.
- Fettweis, X., M. Tedesco, M. R. van den Broeke, and J. Ettema (2011), Melting trends over the Greenland ice sheet (1958–2009) from spaceborne microwave data and regional climate models, *The Cryosphere*, *5*, 359–375, doi:10.5194/tc-5-359-2011.
- Forster, R. R., et al. (2013), Perennial liquid water discovered in Greenland firn layer, *Nature Geoscience*, *7*, 95–98, doi:10.1038/ngeo2043.
- Franco, B., X. Fettweis, M. Erpicum, and S. Nicolay (2011), Present and future climates of the Greenland ice sheet according to the IPCC AR4 models, *Climate Dynamics*, *36*, 1897–1918, doi:10.1007/s00382-010-0779-1.
- Fretwell, P., et al. (2013), Bedmap2: improved ice bed, surface and thickness datasets for Antarctica, *The Cryosphere*, *7*, 375–393, doi:10.5194/tc-7-375-2013.
- Frezzotti, M., et al. (2005), Spatial and temporal variability of snow accumulation in East Antarctica from traverse data, *Journal of Glaciology*, *51*(172), 113–124, doi:10.3189/172756505781829502.
- Gardner, A. S., G. Moholdt, B. Wouters, G. J. Wolken, D. O. Burgess, M. J. Sharp, J. G. Cogley, C. Braun, and C. Labine (2011), Sharply increased mass loss from glaciers and ice caps in the Canadian Arctic Archipelago, *Nature*, *473*, 357–360, doi:10.1038/nature10089.
- Gardner, A. S., et al. (2013), A reconciled estimate of glacier contributions to sea level rise: 2003 to 2009, *Science*, *340*, 852–857, doi:10.1126/science.1234532.
- Gordon, C., C. Cooper, C. A. Senior, H. Banks, J. M. Gregory, T. C. Johns, J. F. B. Mitchell, and R. A. Wood (2000), The simulation of SST, sea ice extents and ocean heat transports in a version of the Hadley Centre coupled model without flux adjustments, *Climate Dynamics*, *16*, 147–168, doi:10.1007/s003820050010.
- Gregory, J. M., and P. Huybrechts (2006), Ice-sheet contributions to future sea-level change, *Philosophical transactions of the Royal Society A*, *364*, 1709–1731, doi:10.1098/rsta.2006.1796.
- Grinsted, A. (2013), An estimate of global glacier volume, *The Cryosphere*, *7*, 141–151, doi:10.5194/tc-7-141-2013.
- Gunter, B., T. Urban, R. Riva, M. Helsen, R. Harpold, S. Poole, P. Nagel, B. Schutz, and B. Tapley (2009), A comparison of coincident GRACE and ICESat data over Antarctica, *Journal of Geodesy*, *83*(1051-1060), doi:10.1007/s00190-009-0323-4.
- Held, I. M., and B. J. Soden (2006), Robust response of the hydrological cycle to global warming, *Journal of Climate*, *19*, 5686–5699, doi:10.1175/JCLI3990.1.
- Hellmer, H. H., F. Kauker, R. Timmermann, J. Determann, and J. Rae (2012), Twenty-first-century warming of a large Antarctic ice-shelf cavity by a redirected coastal current, *Nature*, *485*, 225–228, doi:10.1038/nature11064.
- Helsen, M. M., M. R. van den Broeke, R. S. W. van de Wal, W. J. van de Berg, E. van Meijgaard, C. H. Davis, Y. Li, and I. Goodwin (2008), Elevation changes in Antarctica mainly determined by accumulation variability, *Science*, *320*, 1626–1628, doi:10.1126/science.1153894.
- Herron, M., and C. Langway (1980), Firn densification: an empirical model, *Journal of Glaciology*, *25*(93), 373–385.
- Holland, P. R., H. F. J. Corr, H. D. Pritchard, D. G. Vaughan, R. J. Arthern, A. Jenkins, and M. Tedesco (2011), The air content of Larsen C ice shelf, *Geophysical Research Letters*, *38*(L10503), doi:10.1029/2011GL047245.
- Horwath, M., B. Legresy, F. Remy, F. Blarel, and J.-M. Lemoine (2012), Consistent patterns of Antarctic ice sheet interannual variations from ENVISAT radar altimetry and GRACE satellite gravimetry, *Geophysical Journal International*, *189*, 863–876, doi:10.1111/j.1365-246X.2012.05401.x.
- Huss, M., and D. Farinotti (2012), Distributed ice thickness and volume of all glaciers around the globe, *Journal of Geophysical Research*, *117*(F04010), doi:10.1029/2012JF002523.

- Illangasekare, T. H., R. J. Walter Jr., M. F. Meier, and W. T. Pfeffer (1990), Modeling of meltwater infiltration in sub-freezing snow, *Water Resource Research*, 26(5), 1001–1012, doi:10.1029/WR026i005p01001.
- IPCC (2007), *Climate Change 2007: The Physical Science Basis. Contribution of Working Group I to the Fourth Assessment Report of the Intergovernmental Panel on Climate Change*, 996 pp., Cambridge University Press, Cambridge, United Kingdom and New York, NY, USA.
- IPCC (2013), *Working Group I contribution to the IPCC 5th Assessment Report "Climate Change 2013: The Physical Science Basis"*, Cambridge University Press, Cambridge, United Kingdom and New York, NY, USA.
- Johns, T. C., et al. (2011), Climate change under aggressive mitigation: the ENSEMBLES multi-model experiment, *Climate Dynamics*, 37, 1975–2003, doi:10.1007/s00382-011-1005-5.
- Joughin, I., S. B. Das, M. A. King, B. E. Smith, I. M. Howat, and T. Moon (2008), Seasonal speedup along the western flank of the Greenland ice sheet, *Science*, 320(5877), 781–783, doi:10.1126/science.1153288.
- Kaspers, K. A., R. S. W. van der Wal, M. R. van den Broeke, J. Schwander, N. P. M. van Lipzig, and C. A. M. Brenninkmeijer (2004), Model calculations of the age of firn air across the Antarctic continent, *Atmospheric Chemistry and Physics*, 4, 1817–1853, doi:10.5194/acp-4-1365-2004.
- Khazendar, A., M. P. Schodlok, I. Fenty, S. R. M. Ligtenberg, E. Rignot, and M. R. van den Broeke (2013), Observed thinning of Totten Glacier is linked to coastal polynya variability, *Nature Communications*, 4:2857, doi:10.1038/ncomms3857.
- Krinner, G., O. Magand, I. Simmonds, C. Genthon, and J.-L. Dufresne (2007), Simulated Antarctic precipitation and surface mass balance at the end of the twentieth and twenty-first centuries, *Climate Dynamics*, 28, 215–230, doi:10.1007/s00382-006-0177-x.
- Kuipers Munneke, P., M. R. van den Broeke, J. T. M. Lenaerts, M. G. Flanner, A. S. Gardner, and W. J. van de Berg (2011), A new albedo parameterization for use in climate models over the Antarctic ice sheet, *Journal of Geophysical Research*, 116(D05114), doi:10.1029/2010JD015113.
- Kuipers Munneke, P., S. R. M. Ligtenberg, M. R. van den Broeke, and D. G. Vaughan (2014), Firn air depletion as a precursor for Antarctic ice-shelf collapse, *Journal of Glaciology*, 60(220), 205–214, doi:10.3189/2014JoG13J183.
- Kuipers Munneke, P., S. R. M. Ligtenberg, M. R. van den Broeke, J. H. van Angelen, and R. R. Forster (in press), Explaining the presence of perennial liquid water bodies in the firn of the Greenland Ice Sheet, *Geophysical Research Letters*, doi:10.1002/2013GL058389.
- LaBarbera, C. H., and D. R. MacAyeal (2011), Traveling supraglacial lakes on George VI Ice Shelf, Antarctica, *Geophysical Research Letters*, 38(L24501), doi:10.1029/2011GL049970.
- Lacroix, P., M. Dechambre, B. Legrésy, F. Blarel, and F. Remy (2008), On the use of the dual-frequency ENVISAT altimeter to determine snowpack properties of the Antarctic ice sheet., *Remote Sensing of the Environment*, 112(4), 1712–1729, doi:10.1016/j.rse.2007.08.022.
- Lacroix, P., B. Legrésy, F. Rémy, F. Blarel, G. Picard, and L. Brucker (2009), Rapid change of the snow surface properties at Vostok, East Antarctica, revealed by altimetry, *Remote Sensing of the Environment*, 113, 2633–2641, doi:10.1016/j.rse.2009.07.019.
- Lee, H., C. K. Shum, I. M. Howat, A. Monaghan, Y. Ahn, J. Duan, J.-Y. Guo, C.-Y. Kuo, and L. Wang (2012), Continuously accelerating ice loss over Amundsen Sea catchment, West Antarctica, revealed by integrating altimetry and GRACE data, *Earth and Planetary Science Letters*, 321-322, 74–80, doi:10.1016/j.epsl.2011.12.040.
- Legrésy, B., and F. Rémy (1998), Using the temporal variability of satellite radar altimetry observations to map surface properties of the Antarctic ice sheet, *Journal of Glaciology*, 44(147), 197–206.
- Legrésy, B., F. Rémy, and F. Blarel (2006), Along track repeat altimetry for ice sheets and continental surface studies, in *Proceedings of Symposium on 15 Years of Progress in Radar Altimetry, Venice, Italy, 13–18 March 2006*, vol. 614, edited by ESA-SP, p. 181, European Space Agency Publication Division, Noordwijk, The Netherlands.
- Lenaerts, J. T. M. (2013), Drifting snow climate of the Antarctic and Greenland ice sheets. PhD thesis, Utrecht University, 147 pp, (<http://www.staff.science.uu.nl/~lenae101/pubs.php>).
- Lenaerts, J. T. M., and M. R. van den Broeke (2012), Modeling drifting snow in Antarctica with a regional climate model, part II: Results, *Journal of Geophysical Research*, 117(D05109), doi:10.1029/2010JD015419.
- Lenaerts, J. T. M., M. R. van den Broeke, W. J. van de Berg, E. van Meijgaard, and P. Kuipers Munneke (2012a), A new, high-resolution surface mass balance map of Antarctica (1979–2010) based on regional atmospheric climate modeling, *Geophysical Research Letters*, 39(L04501), doi:10.1029/2011GL050713.
- Lenaerts, J. T. M., M. R. van den Broeke, C. Scarchilli, and C. Agosta (2012b), Impact of model resolution on simulated wind, drifting snow and surface mass balance in Terre Adélie, East Antarctica, *Journal of Glaciology*, 58(211), 821–829, doi:10.3189/2012JoG12J020.
- Lenaerts, J. T. M., M. R. van den Broeke, S. J. Déry, E. van Meijgaard, W. J. van de Berg, S. P. Palm, and J. Sanz Rodrigo (2012c), Modeling drifting snow in Antarctica with a regional climate model, part I: Methods and model evaluation, *Journal of Geophysical Research*, 117(D05108), doi:10.1029/2011JD016145.

- Levermann, A., et al. (2012), Projecting Antarctic ice discharge using response functions from SeaRISE ice-sheet models, *The Cryosphere Discussions*, 6, 3447–3489, doi:10.5194/tcd-6-3447-2012.
- Li, J., J. Paden, C. Leuschen, F. Rodriguez-Morales, R. D. Hale, E. J. Arnold, R. Crowe, D. Gomez-Garcia, and P. Gogineni (2013), High-altitude radar measurements of ice thickness over the Antarctic and Greenland ice sheets as a part of Operation IceBridge, *IEEE Transactions on Geoscience and Remote Sensing*, 51(2), 742–754, doi:10.1109/TGRS.2012.2203822.
- Ligtenberg, S. R. M., M. M. Helsen, and M. R. van den Broeke (2011), An improved semi-empirical model for the densification of Antarctic firn, *The Cryosphere*, 5, 809–819, doi:10.5194/tc-5-809-2011.
- Ligtenberg, S. R. M., M. Horwath, M. R. van den Broeke, and B. Legrésy (2012), Quantifying the seasonal 'breathing' of the Antarctic ice sheet, *Geophysical Research Letters*, 39(L23501), doi:10.1029/2012GL053628.
- Ligtenberg, S. R. M., W. J. van de Berg, M. R. van den Broeke, J. G. L. Rae, and E. van Meijgaard (2013), Future surface mass balance of the Antarctic ice sheet and its influence on sea level change, simulated by a regional atmospheric climate model, *Climate Dynamics*, 41, 867–884, doi:10.1007/s00382-013-1749-1.
- Ligtenberg, S. R. M., P. Kuipers Munneke, and M. R. van den Broeke (in review), Present and future variations in Antarctic firn air content, *The Cryosphere*.
- Lowe, J. A., C. D. Hewitt, D. P. van Vuuren, T. C. Jones, E. Stehfest, J.-F. Royer, and P. J. van der Linden (2009), New study for climate modeling, analyses, and scenarios, *EOS Trans. AGU*, 90(21), 181, doi:10.1029/2009EO210001.
- Lundin, J., W. Leahy, and F. participants (in preparation), Firn model inter-comparison experiment (FirnMICE), *Journal of Glaciology*.
- Lythe, M. B., D. G. Vaughan, and the BEDMAP Consortium (2001), BEDMAP: A new ice thickness and subglacial topographic model of Antarctica, *Journal of Geophysical Research*, 106(B6), 11,335–11,352, doi:10.1029/2000JB900449.
- Maris, M. N. A., B. de Boer, and J. Oerlemans (2012), A model comparison study for the Antarctic region: present and past, *Climate of the Past*, 8, 803–814, doi:10.5194/cp-8-803-2012.
- Marsh, P., and M.-K. Woo (1984), Wetting front advance and freezing of meltwater within a snow cover I. observation in the Canadian Arctic, *Water Resource Research*, 20(12), 1853–1864, doi:10.1029/WR020i012p01853.
- Mawson, D. (1915), *The home of the blizzard*, 438 pp, Heinemann, London.
- McConnell, J. R., R. J. Arthern, E. Mosley-Thompson, C. H. Davis, R. C. Bales, R. Thomas, J. F. Burkhart, and J. D. Kyne (2000), Changes in Greenland ice sheet elevation attributed primarily to snow accumulation variability, *Nature*, 406, 877–879, doi:10.1038/35022555.
- Medley, B., et al. (2013), Airborne-radar and ice-core observations of annual snow accumulation over Thwaites Glacier, West Antarctica confirm the spatiotemporal variability of global and regional atmospheric models, *Geophysical Research Letters*, 40, 1–6, doi:10.1002/grl.50706.
- Moholdt, G., C. Nuth, J. O. Hagen, and J. Kohler (2010), Recent elevation changes of Svalbard glaciers derived from ICESat laser altimetry, *Remote Sensing of the Environment*, 114, 2756–2767, doi:10.1016/j.rse.2010.06.008.
- Monaghan, A. J., et al. (2006), Insignificant change in Antarctic snowfall since the International Geophysical Year, *Science*, 313(5788), 827–831, doi:10.1126/science.1128243.
- Monaghan, A. J., D. H. Bromwich, W. Chapman, and J. C. Comiso (2008), Recent variability and trends of Antarctic near-surface temperature, *Journal of Geophysical Research*, 113(D04105), doi:10.1029/2007JD009094.
- Morris, E. M., and D. G. Vaughan (2003), Glaciological climate relationships spatial and temporal variation of surface temperature on the Antarctic Peninsula and the limit of viability of ice shelves, in *Antarctic Peninsula climate variability: historical and paleoenvironmental perspectives*, Antarctic Research Series, vol. 79, edited by E. Domack et al., pp. 61–68, AGU, Washington D. C., doi:10.1029/AR079p0061.
- Muller, W. A., and E. Roeckner (2007), ENSO teleconnections in projections of future climate in ECHAM5/MPI-OM, *Climate Dynamics*, 31, 533–549, doi:10.1007/s00382-007-0357-3.
- Nakicenovic, N., et al. (2000), *IPCC Special Report on Emissions Scenarios (SRES)*, Cambridge University Press.
- Nghiem, S. V., D. K. Hall, T. L. Mote, M. Tedesco, M. R. Albert, K. Keegan, C. A. Shuman, N. E. DiGirolamo, and G. Neumann (2012), The extreme melt across the Greenland ice sheet in 2012, *Geophysical Research Letters*, 39(L20502), doi:10.1029/2012GL053611.
- Nicholls, R. J., and A. Cazenave (2010), Sea-level rise and its impact on coastal zones, *Science*, 328(1517), doi:10.1126/science.1185782.
- Painter, T. H., J. Dozier, D. A. Roberts, R. E. Davis, and R. O. Green (2003), Retrieval of subpixel snow-covered area and grain size from imaging spectrometer data, *Remote Sensing of the Environment*, 85(1), 64–77, doi:10.1016/S0034-4257(02)00187-6.
- Pasteur, E. C., and R. Mulvaney (2000), Migration of methane sulphonate in Antarctic firn and ice, *Journal of Geophysical Research*, 105(D9), 11,525–11,534, doi:10.1029/2000JD900006.
- Paterson, W. S. B. (1994), *The physics of glaciers*, 3rd ed., Pergamon.
- Peltier, W. R. (2004), Global glacial isostasy and the surface of the ice-age Earth: The ICE-5G (VM2) model and GRACE, *Annual Review of Earth and Planetary Science*, 32, 111–149, doi:10.1146/annurev.earth.32.082503.144359.

- Pfeffer, W. T., T. H. Illangasekare, and M. F. Meier (1990), Analysis and modeling of melt-water refreezing in dry snow, *Journal of Glaciology*, *36*(123), 238–246.
- Pfeffer, W. T., M. F. Meier, and T. H. Illangasekare (1991), Retention of Greenland runoff by refreezing: Implications for projected future sea level change, *Journal of Geophysical Research*, *96*(C12), 22.117–22.124, doi:10.1029/91JC02502.
- Picard, G., F. Domine, G. Krinner, L. Arnaud, and E. Lefebvre (2012), Inhibition of the positive snow-albedo feedback by precipitation in interior Antarctica, *Nature Climate Change*, *2*, 795–798, doi:10.1038/nclimate1590.
- Pimienta, M., and P. Duval (1987), Rate controlling processes in the creep of polar glacier ice, *Journal de Physique*, *48*, 243–248, doi:10.1051/jphyscol:1987134.
- Pope, V. D., J. A. Pamment, D. R. Jackson, and A. Slingo (2000), The representation of water vapor and its dependence on vertical resolution in the Hadley Centre climate model, *Journal of Climate*, *14*, 3065–3085, doi:10.1175/1520-0442(2001)014<3065:TROWVA>2.0.CO;2.
- Pritchard, H. D., R. J. Arthern, D. G. Vaughan, and L. A. Edwards (2009), Extensive dynamic thinning on the margins of the Greenland and Antarctic ice sheets, *Nature*, *461*, 971–975, doi:10.1038/nature08471.
- Pritchard, H. D., S. R. M. Ligtenberg, H. A. Fricker, D. G. Vaughan, M. R. van den Broeke, and L. Padman (2012), Antarctic ice-sheet loss driven by basal melting of ice shelves, *Nature*, *484*, 502–505, doi:10.1038/nature10968.
- Rack, W., and H. Rott (2004), Pattern of retreat and disintegration of the Larsen B ice shelf, Antarctic Peninsula, *Annals of Glaciology*, *39*, 505–510, doi:10.3189/172756404781814005.
- Radić, V., A. Bliss, A. C. Beedlow, R. Hock, E. Milles, and J. G. Cogley (2014), Regional and global projections of twenty-first century glacier mass changes in response to climate scenarios from global climate models, *Climate Dynamics*, *42*(1–2), 37–58, doi:10.1007/s00382-013-1719-7.
- Ramilien, G., A. Lombard, A. Cazenave, E. R. Ivins, M. Llubes, F. Rémy, and R. Biancale (2006), Interannual variations of the mass balance of the Antarctica and Greenland ice sheets from GRACE, *Global and Planetary Change*, *53*(3), 198–208, doi:10.1016/j.gloplacha.2006.06.003.
- Reynolds, J. M. (1981), Lakes on George VI ice shelf, Antarctica, *Polar Record*, *20*(128), 425–432, doi:10.1017/S0032247400003636.
- Ricchiazzi, P., S. Yang, C. Gautier, and D. Soble (1998), SBDART: A research and teaching software tool for plane-parallel radiative transfer in the Earth's atmosphere, *Bulletin of the American Meteorological Society*, *79*(10), 2101–2114, doi:10.1175/1520-0477(1998)079<2101:SARATS>2.0.CO;2.
- Rignot, E., and S. S. Jacobs (2002), Rapid bottom melting widespread near Antarctic ice sheet grounding lines, *Science*, *296*(2020), doi:10.1126/science.1070942.
- Rignot, E., G. Casassa, P. Gogineni, W. Krabill, A. Rivera, and R. Thomas (2004), Accelerated ice discharge from the Antarctic Peninsula following the collapse of Larsen B ice shelf, *Geophysical Research Letters*, *31*(L18401), doi:10.1029/2004GL020697.
- Rignot, E., J. L. Bamber, M. R. van den Broeke, C. Davis, Y. Li, W. J. van de Berg, and E. van Meijgaard (2008), Recent Antarctic ice mass loss from radar interferometry and regional climate modelling, *Nature Geoscience*, *1*, 106–110, doi:10.1038/ngeo102.
- Rignot, E., I. Velicogna, M. R. van den Broeke, A. Monaghan, and J. T. M. Lenaerts (2011a), Acceleration of the contribution of the Greenland and Antarctic ice sheets to sea level rise, *Geophysical Research Letters*, *38*(L05503), doi:10.1029/2011GL046583.
- Rignot, E., J. Mouginot, and B. Scheuchl (2011b), Ice flow of the Antarctic ice sheet, *Science*, *333*(6048), 1427–1430, doi:10.1126/science.1208336.
- Rignot, E., J. Mouginot, and B. Scheuchl (2011c), Antarctic grounding line mapping from differential satellite radar interferometry, *Geophysical Research Letters*, *38*(L10504), doi:10.1029/2011GL047109.
- Rignot, E., S. Jacobs, J. Mouginot, and B. Scheuchl (2013), Ice shelf melting around Antarctica, *Science*, *341*(6143), 266–270, doi:10.1126/science.1235798.
- Riva, R. E. M., et al. (2009), Glacial isostatic adjustment over Antarctica from combined ICESat and GRACE satellite data, *Earth and Planetary Science Letters*, *288*, 516–523, doi:10.1016/j.epsl.2009.10.013.
- Rosenau, R., R. Dietrich, and M. Baessler (2012), Temporal flow variations of major outlet glaciers in Greenland using LANDSAT data., *Proceedings IEEE International Geosci. and Rem. Sensing. Symp., Munich, 22-27 July 2012*.
- Scambos, T. A., J. A. Bohlander, C. A. Shuman, and P. Skvarca (2004), Glacier acceleration and thinning after ice shelf collapse in the Larsen B embayment, Antarctica, *Geophysical Research Letters*, *31*(L18402), doi:10.1029/2004GL020670.
- Scambos, T. A., T. M. Haran, M. A. Fahnestock, T. H. Painter, and J. Bohlander (2007), MODIS-based Mosaic of Antarctica (MOA) data sets: Continent-wide surface morphology and snow grain size, *Remote Sensing of the Environment*, *111*(2), 242–257, doi:10.1016/j.rse.2006.12.020.
- Scambos, T. A., et al. (2012), Extent of low-accumulation 'wind glaze' areas on the East Antarctic plateau: implications for continental ice mass balance, *Journal of Glaciology*, *58*(210), 633–647, doi:10.3189/2012JoG11J232.

- Scarchilli, C., M. Frezzotti, P. Grigioni, L. De Silvestri, L. Agnoletto, and S. Dolci (2010), Extraordinary blowing snow transport events in East Antarctica, *Climate Dynamics*, *34*(7–8), 1195–1206, doi:10.1007/s00382-009-0601-0.
- Schytt, V. (1961), Blue-ice fields, moraine features and glacier fluctuations, *Norwegian-British-Swedish Antarctic Expedition 1949-1952 Scientific Results, IV(E)*, 182–204.
- Shepherd, A., E. R. Ivins, A. Geruo, and IMBIE project group (2012), A reconciled estimate of ice-sheet mass balance, *Science*, *338*, 1183–1189, doi:10.1126/science.1228102.
- Sinisalo, A., and J. C. Moore (2010), Antarctic blue ice areas - towards extracting palaeoclimate information, *Antarctic Science*, *22*(2), 99–115, doi:10.1017/S0954102009990691.
- Spada, G., et al. (2011), A benchmark study for glacial isostatic adjustment codes, *Geophysical Journal International*, *185*, 106–132, doi:10.1111/j.1365-246X.2011.04952.x.
- Spencer, M. K., R. B. Alley, and T. T. Creyts (2001), Preliminary firn-densification model with 38-site dataset, *Journal of Glaciology*, *47*(159), 671–676, doi:10.3189/172756501781831765.
- Stearns, L. A. (2011), Dynamics and mass balance of four large East Antarctic outlet glaciers, *Annals of Glaciology*, *52*(59), 116–126, doi:10.3189/172756411799096187.
- Swithinbank, C. (1991), Potential airfield sites in Antarctica for wheeled aircraft, *CRREL Special Report 91-24*.
- Takahashi, S., R. Naruse, M. Nakawo, and S. Mae (1988), A bare ice field in east Queen Maud Land, Antarctica, caused by horizontal divergence of drifting snow, *Annals of Glaciology*, *11*, 156–160.
- Takahashi, S., T. Endoh, N. Azuma, and S. Meshida (1992), Bare ice fields developed in the inland part of Antarctica, *Proceedings NIPR Symp. Polar Meteorol. Glaciol.*, *5*, 128–139.
- Tapley, B. D., S. Bettadpur, J. C. Ries, P. F. Thompson, and M. M. Watkins (2004), GRACE measurements of mass variability in the Earth system, *Science*, *305*, 503–505, doi:10.1126/science.1099192.
- Tedesco, M., X. Fettweis, T. Mote, J. Wahr, P. Alexander, J. E. Box, and B. Wouters (2013), Evidence and analysis of 2012 Greenland records from spaceborne observations, a regional climate model and reanalysis data, *The Cryosphere*, *7*, 615–630, doi:10.5194/tc-7-615-2013.
- Thomas, R., C. Davis, E. Frederick, W. Krabill, Y. Li, S. Manizade, and C. Martin (2008), A comparison of Greenland ice-sheet volume changes derived from altimetry measurements, *Journal of Glaciology*, *54*(185), 203–212, doi:10.3189/002214308784886225.
- Uppala, S. M., et al. (2005), The ERA-40 re-analysis, *Quarterly Journal of the Royal Meteorological Society*, *131*(612), 2961–3012, doi:10.1256/qj.04.176.
- Van Angelen, J. H., J. T. M. Lenaerts, M. R. van den Broeke, X. Fettweis, and E. van Meijgaard (2013), Rapid loss of firn pore space accelerates 21st century Greenland mass loss, *Geophysical Research Letters*, *40*, 1–5, doi:10.1002/grl.50490.
- Van de Berg, W. J. (2008), Present-day climate of Antarctica: A study with a regional climate model. PhD thesis, Utrecht University, pp 138, (<http://www.staff.science.uu.nl/~berg0138/publications.php>).
- Van de Berg, W. J., M. R. van den Broeke, C. H. Reijmer, and E. van Meijgaard (2005), Characteristics of the Antarctic surface mass balance (1958-2002) using a regional atmospheric climate model, *Annals of Glaciology*, *41*, 97–104, doi:10.3189/172756405781813302.
- Van de Berg, W. J., M. R. van den Broeke, C. H. Reijmer, and E. van Meijgaard (2006), Reassessment of the Antarctic surface mass balance using calibrated output of a regional atmospheric climate model, *Journal of Geophysical Research*, *111*(D11104), doi:10.1029/2005JD006495.
- Van den Broeke, M. R. (1997), Spatial and temporal variation of sublimation on Antarctica: Results of a high-resolution general circulation model, *Journal of Geophysical Research*, *102*(D25), 29,765–29,777, doi:10.1029/97JD01862.
- Van den Broeke, M. R. (2008), Depth and density of the Antarctic firn layer, *Arctic, Antarctic and Alpine Research*, *40*(2), 432–438, doi:10.1657/1523-0430(07-021)[BROEKE]2.0.CO:2.
- Van den Broeke, M. R., and R. Bintanja (1995a), Summertime atmospheric circulation in the vicinity of a blue ice area in Queen Maud Land, Antarctica, *Boundary-Layer Meteorology*, *72*(4), 411–438, doi:10.1007/BF00709002.
- Van den Broeke, M. R., and R. Bintanja (1995b), The interaction of katabatic winds and the formation of blue-ice areas in East Antarctica, *Journal of Glaciology*, *41*(138), 395–407.
- Van den Broeke, M. R., and N. P. M. van Lipzig (2004), Changes in Antarctic temperature, wind and precipitation in response to the Antarctic Oscillation, *Annals of Glaciology*, *39*, 119–126, doi:10.3189/172756404781814654.
- Van den Broeke, M. R., W. J. van de Berg, E. van Meijgaard, and C. H. Reijmer (2006a), Identification of Antarctic ablation areas using a regional atmospheric climate model, *Journal of Geophysical Research*, *111*(D18110), doi:10.1029/2006JD007127.
- Van den Broeke, M. R., W. J. van de Berg, and E. van Meijgaard (2006b), Snowfall in coastal West Antarctica much greater than previously assumed, *Geophysical Research Letters*, *33*(L02505), doi:10.1029/2005GL025239.
- Van den Broeke, M. R., W. J. van de Berg, and E. van Meijgaard (2008), Firn depth correction along the Antarctic grounding line, *Antarctic Science*, *20*, 513–517, doi:10.1017/S095410200800148X.

- Van den Broeke, M. R., J. L. Bamber, J. Ettema, E. Rignot, E. Schrama, W. J. van de Berg, E. van Meijgaard, I. Velicogna, and B. Wouters (2009), Partitioning recent Greenland mass loss, *Science*, 326, 984–986, doi:10.1126/science.1178176.
- Van den Broeke, M. R., J. Bamber, J. Lenaerts, and E. Rignot (2011), Ice sheets and sea level: thinking outside the box, *Surveys in Geophysics*, doi:10.1007/s10712-011-9137-z.
- Van Lipzig, N. P. M., E. van Meijgaard, and J. Oerlemans (2002), Temperature sensitivity of the Antarctic surface mass balance in a regional atmospheric climate model, *Journal of Climate*, 15, 2758–2774, doi:10.1175/1520-0442(2002)015<2758:TSOTAS>2.0.CO;2.
- Van Meijgaard, E., L. H. van Ulft, W. J. van de Berg, F. C. Bosveld, B. J. J. M. van den Hurk, G. Lenderink, and A. P. Siebesma (2008), *The KNMI regional atmospheric climate model RACMO version 2.1*, Royal Netherlands Meteorological Institute, De Bilt, The Netherlands.
- Van Wessem, J. M., C. H. Reijmer, J. T. M. Lenaerts, W. J. van de Berg, M. R. van den Broeke, and E. van Meijgaard (2014), Updated cloud physics improve the modelled near surface climate of Antarctica of a regional atmospheric climate model, *The Cryosphere*, 8, 125–135, doi:10.5194/tc-8-125-2014.
- Vaughan, D. G., J. L. Bamber, M. Giovinetto, J. Russell, and A. P. R. Cooper (1999), Reassessment of net surface mass balance in Antarctica, *Journal of Climate*, 12, 933–946, doi:10.1175/1520-0442(1999)012<0933:RONSMB>2.0.CO;2.
- Vaughan, D. G., G. J. Marshall, W. M. Connolley, C. Parkinson, R. Mulvaney, D. A. Hodgson, J. C. King, C. J. Pudsey, and J. Turner (2003), Recent rapid regional climate warming on the Antarctic Peninsula, *Climate Change*, 60(3), 243–274, doi:10.1023/A:1026021217991.
- Velicogna, I. (2009), Increasing rates of ice mass loss from the Greenland and Antarctic ice sheets revealed by GRACE, *Geophysical Research Letters*, 36(L19503), doi:10.1029/2009GL040222.
- Velicogna, I., and J. Wahr (2006), Measurements of time-variable gravity show mass loss in Antarctica, *Science*, 311(5768), 1754–1756, doi:10.1126/science.1123785.
- Wendler, G., C. Stearns, G. Weidner, G. Dargaud, and T. Parish (1997), On the extraordinary katabatic winds of Adélie Land, *Journal of Geophysical Research*, 102(D4), 4463–4474, doi:10.1029/96JD03438.
- Whitehouse, P. L., M. J. Bentley, and A. M. L. Brocq (2012), A deglacial model for Antarctica: geological constraints and glaciological modelling as a basis for a new model of Antarctic glacial isostatic adjustment, *Quaternary Science Reviews*, 32, 1–24, doi:10.1016/j.quascirev.2011.11.016.
- Wild, M., P. Calanca, S. C. Scherrer, and A. Ohmura (2003), Effects of polar ice sheets on global sea level in high-resolution greenhouse scenarios, *Journal of Geophysical Research*, 108(D5), 4165, doi:10.1029/2002JD002451.
- Wilkinson, D. S. (1988), A pressure-sintering model for the densification of polar firn and glacier ice, *Journal of Glaciology*, 34(116), 40–45.
- Willis, J. K., D. P. Chambers, and R. S. Nerem (2008), Assessing the globally averaged sea level budget on seasonal to interannual timescales, *Journal of Geophysical Research*, 113(C06015), doi:10.1029/2007JC004517.
- Wingham, D. J., A. Shepherd, A. Muir, and G. J. Marshall (2006), Mass balance of the Antarctic ice sheet, *Philosophical transactions of the Royal Society A*, 364, 1627–1635, doi:10.1098/rsta.2006.1792.
- Wingham, D. J., D. W. Wallis, and A. Shepherd (2009), Spatial and temporal evolution of Pine Island Glacier thinning, *Geophysical Research Letters*, 36(L17501), doi:10.1029/2009GL039126.
- Winther, J.-G., M. N. Jaspersen, and G. E. Liston (2001), Blue-ice areas in Antarctica derived from NOAA AVHRR satellite data, *Journal of Glaciology*, 47(157), 325–334.
- Yi, D., C. R. Bentley, and M. D. Stenoien (1997), Seasonal variation in the apparent height of the East Antarctic ice sheet, *Annals of Glaciology*, 24, 191–198.
- Yoshida, M., H. Ando, K. Omoto, R. Naruse, and Y. Ageta (1971), Discovery of meteorites near Yamato Mountains, East Antarctica, *Japanese Antarctic Record*, 39, 62–65.
- Yu, J., H. Liu, L. Wang, K. C. Jezek, and J. Heo (2012), Blue ice areas and their topographical properties in the Lambert Glacier, Amery Ice Shelf system using Landsat ETM+, ICESat laser altimetry and ASTER GDEM data, *Antarctic Science*, 24(1), 95–110, doi:10.1017/S0954102011000630.
- Zwally, H. J., and J. Li (2002), Seasonal and interannual variations of firn densification and ice-sheet surface elevation at the Greenland Summit, *Journal of Glaciology*, 48(161), 199–207, doi:10.3189/172756502781831403.
- Zwally, H. J., W. Abdalati, T. Herring, K. Larson, J. Saba, and K. Steffen (2002), Surface melt-induced acceleration of Greenland ice-sheet flow, *Science*, 297(5579), 218–222, doi:10.1126/science.1072708.
- Zwally, H. J., M. B. Giovinetto, J. Li, H. G. Cornejo, M. A. Beckley, A. C. Brenner, J. L. Saba, and D. Yi (2005), Mass changes of the Greenland and Antarctic ice sheets and shelves and contributions to sea-level rise: 1992–2002, *Journal of Glaciology*, 51(175), 509–527, doi:10.3189/172756505781829007.

Bedankt! / Thanks!

Ondanks dat er maar één naam op de voorkant van dit boekje staat, zijn er een hoop mensen die mij hebben geholpen of gesteund gedurende de afgelopen vier jaar. Tijdens mijn promotie zat ik vaak alleen achter mijn computer, maar juist de stimulerende samenwerking met (buitenlandse) collega's, de prettige werkomgeving en de afleiding naast het werk, hebben dit boekje gemaakt tot wat het is. Daarom maak ik graag van deze gelegenheid gebruik om een aantal van deze mensen te bedanken.

Allereerst wil ik mijn promotor en dagelijks begeleider Michiel van den Broeke bedanken. Na mijn stage op het IMAU, waarin je mij kennis liet maken met polaire meteorologie en het begrip 'firn', bood je mij de mogelijkheid om over hetzelfde onderwerp een PhD te starten. Allereerst bedankt voor deze kans, maar ook voor het scheppen van de juiste omstandigheden om deze te doen slagen. Jouw kennis en enthousiasme over alles wat met ijs en klimaat te maken heeft werkt erg motiverend, evenals het actief meedenken over wat nu wel –of juist niet– interessant is om verder te onderzoeken. Ik heb jouw open-deur policy en informele manier van begeleiden als erg prettig ervaren en mijn academische schrijfstijl is de afgelopen vier jaar sterk verbeterd, vooral dankzij jouw grondige commentaar op de manuscripten die keer op keer jouw kant op kwamen. Daarnaast heb je mij laten ervaren dat wetenschap niet neerkomt op eenzaam ploeteren, maar dat de sleutel tot succes juist schuilt in (internationale) samenwerking. De mate waarin de resultaten van ons firnmodel momenteel door anderen worden gebruikt overtreft al mijn verwachtingen.

Ondanks dat ik officieel geen co-promotor of tweede begeleider had zijn er wel een aantal mensen op het IMAU die mij inhoudelijk nogal eens hebben geholpen. Michiel Helsen, in mijn eerste jaren op het IMAU heb jij mij kennis laten maken met firn, iets waar ik tot dan toe nog nooit van had gehoord. Ik mocht destijds jouw firnmodel gebruiken en later zelfs uitbreiden, zodat het uiteindelijk ons firnmodel is geworden. Bedankt voor de prettige samenwerking en begeleiding, het huidige succes van het firnmodel is een gezamenlijke verdienste.

Willem Jan, jij hebt mij wegwijs gemaakt in de black box die RACMO2 heet. Dit model is soms onnavolgbaar en we hebben samen heel wat uren achter mijn computer doorgebracht met grote vraagtekens boven ons hoofd. Maar of Jamie nu de noord- en zuidpool had omgedraaid, ons werd gevraagd om de ijskap 'eventjes' 100 meter op te hogen of ik een scriptje zocht om het firnmodel parallel te laten draaien op het ECMWF; jij had altijd een oplossing paraat. Heel erg bedankt voor de tijd en energie die je daarin hebt gestopt. Ook kijk ik met veel plezier terug op onze samenwerking bij het vak Hydrodynamica en Turbulentie.

Peter, inmiddels ben ook jij door het firnvirus geïnfecteerd, waardoor ik al mijn goede en minder goede ideeën met jou kan bespreken. En dan blijkt het vaak erg nuttig om je eigen model eens door de ogen van een ander te bezien. De laatste maanden waren erg productief en ik denk dat wij als firm-tandem ook de komende tijd nog een hoop artikelen zullen schrijven. Samen met Paul vormden wij ook ruim 3 jaar kamer 666 en ik had mij geen leukere en gezelligere kamergenoten kunnen wensen. Behalve de vele nuttige discussies over werkgerelateerde onderwerpen, variërend van gletsjerlengtes tot MA-ratio's en NCL-code, was er gelukkig ook altijd meer dan genoeg tijd voor andere zaken. Of het nu over (toer)skiën, (on)mogelijke reisbestemmingen, wielerpoules, onze pæperplant of het weer ging, het was altijd een fijne en interessante afleiding naast het werk. Het gezamenlijk kijken van een willekeurige Giro-, Tour- of Vuelta-finish op één van onze beeldschermen was altijd een waardige afsluiting van een goede werkdag, of juist een extra motivatie om toch nog een paar uurtjes door te werken.

Jan, als vriend en collega hebben we de afgelopen jaren voor- en (gelukkig wat minder) tegenspoed gedeeld. Ik denk dat onze beider promotietrajecten voordeel hebben gehad van deze samenwerking en ben vooral trots dat ons initiële hobby-projectje over blauw ijs is uitgegroeid tot een volwaardig en goed paper. Bedankt voor al je hulp bij RACMO-probleempjes, NCL-vraagstukken en promotieperikelen. Daarnaast zijn er natuurlijk de fameuze gezamenlijke conferentiebezoeken, waarbij ik er nog steeds niet uit ben of de AGU nou écht één van de beste conferenties is, of dat de culinaire hoogstandjes en aangeplakte skitripjes een groot deel van dit beeld bepalen. Laten we de huidige trend de komende jaren voortzetten! Samen met Aimée ben je ook mijn paranimf; beide bedankt voor het verbeteren van mijn talloze typfouten en alvast bedankt voor de morele steun op 23 april. Aimée, ik vind het erg leuk en speciaal dat jij mijn paranimf *from down under* wilt zijn en hoop van harte dat we ons frequente (e-mail)contact voortzetten de komende jaren.

Daarnaast wil ik graag ook alle andere collega's bedanken voor de fijne werksfeer op het IMAU, welke zeker heeft bijgedragen aan het succesvol afronden van deze PhD. De dagelijkse koffiepauzes en lunchwandelingen (wanneer mogelijk) zijn een welkome afwisseling van het computerwerk. Verder bewaar ik goede herinneringen aan onze HOEMBA-vergaderingen, badmintonsessies, klaverjas- en jeu-de-boules potjes of gewoon een lekker biertje op vrijdagmiddag. Tijdens de afgelopen jaren zijn er genoeg mensen geweest om de ervaringen mee te delen; Paul, Bas, Jan, Jan, Ward, Aimée, Irene, Malou, Melchior, Matthijs, Brice, Christian, Werner, Carina, Dewi, Lisa, Wim en vele anderen, allemaal bedankt voor de gezellige tijd! Als laatste wil ik ook Marcel bedanken voor het stug volhouden om telkens de broodnodige updates te installeren op mijn Mac, en Yvonne, Wanda en Sandra; bedankt voor het draaiend houden van ons mooie instituut.

I would also like to acknowledge our collaborators outside the IMAU, without whom my PhD would have been less successful and definitely less interesting. Our different research backgrounds led to a lot of interesting discussions and broadened my view on ice sheets in general and their interaction with the atmosphere and ocean. First of all, I want to thank

Hamish Pritchard for his early interest in our firm modeling results and his patience when the model results were (again) delayed. You also provided an invaluable experience by showing me the art of writing a paper for a high-impact journal, at a time when I was just discovering how to write a decent scientific paper at all. Martin Horwath and Benoit Legrésy, thanks for your help with the 'breathing' paper, your knowledge about satellite altimetry was invaluable to satisfy the requests of a certain editor. Ted Scambos, your help and critical opinion on the blue-ice paper is really appreciated. Early in my career, Helen Fricker and Laurie Padman provided me with an excellent introduction to floating ice shelves. Later work together with Mathieu Depoorter, Fernando Paolo and Ala Khazendar (although separately) increased my understanding of this phenomenon, thanks! Also, I really enjoyed the frequent discussions and meetings with Olga Didova and Brian Gunter about glacial isostatic adjustment in Antarctica. Nick Barrand and Laura Davies, thanks for introducing me to modeling of past and future ice sheet dynamics on the Antarctic Peninsula. Brooke Medley, your enthusiasm is contagious and I am sure our collaboration will be fruitful over the coming year(s). Last, but not least, I want to thank all people involved in the ice2sea project; the open-forum meetings were useful and enjoyable at the same time. In particular, I want to acknowledge David Vaughan and Elaina Ford for their excellent project management, without which it would not have been such a successful project.

Tot slot wil ik graag mijn familie; papa, mama, Astrid en Max, schoonfamilie; Henny en Wim, en mijn vrienden bedanken voor de interesse in mijn onderzoek, maar vooral ook voor alle dingen die de aandacht daar juist plezierig vanaf hebben geleid. Bedankt voor de lekkere dinertjes (Lineke & Jan), gezellige spelletjesavonden (Tamar & Maarten), of beide (Lai & Maarten), uitgaansavonden in Den Bosch of Utrecht (o.a. Ina, Jannie en Sjoerd), het ontdekken van nieuwe bandjes (Lenny, John, Thijs en Ard), de vele skivakanties (o.a. Bas, Henk en Jan) of gewoon een lekker speciaal biertje op z'n tijd (iedereen)! Ook wil ik graag iedereen uit Heren-1 en de wedstrijdcommissie van Golfclub Anderstein bedanken voor alle fijne uren op onze prachtige golfbaan, een mooie plek om aan niks anders te denken dan een klein wit balletje.

Lieve papa en mama, dank jullie wel voor de steun over de afgelopen jaren en voor het vertrouwen dat mijn keuzes de juiste keuzes zouden zijn. Het is enorm fijn om te weten dat jullie er altijd voor mij zijn. En natuurlijk mijn lieve Cathy, wat zou ik moeten zonder jou. Dank je wel voor al je liefde en steun, dat er nog vele jaren mogen volgen, want samen met jou is het leven gewoon veel leuker!

Publications

First author

Ligtenberg S. R. M., M. M. Helsen, and M. R. van den Broeke (2011), An improved semi-empirical model for the densification of Antarctic firn. *The Cryosphere*, **5**, 809–819, doi:10.5194/tc-5-809-2011

Ligtenberg S. R. M., M. Horwath, M. R. van den Broeke, and B. Legrésy (2012), Quantifying the seasonal 'breathing' of the Antarctic ice sheet. *Geophysical Research Letters*, **39**, L23501, doi:10.1029/2012GL053628

Ligtenberg S. R. M., W. J. van de Berg, M. R. van den Broeke, J. G. L. Rae, and E. van Meijgaard (2013), Future surface mass balance of the Antarctic ice sheet and its influence on sea level change, simulated by a regional atmospheric climate model. *Climate Dynamics*, **41**, 867–884, doi:10.1007/s00382-013-1749-1

Ligtenberg S. R. M., J. T. M. Lenaerts, M. R. van den Broeke, and T. A. Scambos (2014), On the formation of blue ice on Byrd Glacier, Antarctica. *Journal of Glaciology*, **60**, 219, 41–50, doi:10.3189/2014JG13J116

Ligtenberg S. R. M., P. Kuipers Munneke, and M. R. van den Broeke (2014), Present and future variations in Antarctic firn air content. *The Cryosphere Discussions*, **8**, 421-451, doi:10.5194/tcd-8-421-2014

Co-author

Padman, L., D. P. Costa, M. S. Dinniman, H. A. Fricker, M. E. Goebel, L. A. Huckstadt, A. Humbert, I. Joughin, J. T. M. Lenaerts, S. R. M. Ligtenberg, T. A. Scambos, and M. R. van den Broeke (2012), Oceanic controls on the mass balance of Wilkins Ice Shelf, Antarctica. *Journal of Geophysical Research*, **117**, C01010, doi:10.1029/2011JC007301

Pritchard, H. D., S. R. M. Ligtenberg, H. A. Fricker, D. G. Vaughan, M. R. van den Broeke, and L. Padman (2012), Antarctic ice sheet loss driven by basal melting of ice shelves. *Nature*, **484**, 502–505, doi:10.1038/nature10968

Shepherd, A., E. R. Ivins, A. Geruo, and the IMBIE project group (2012), A reconciled estimate of ice sheet mass balance. *Science*, **338**, 6111, 1183–1189, doi:10.1126/science.1228102

- Gardner, A. S., G. Moholdt, J. G. Cogley, B. Wouters, A. A. Arendt, J. Wahr, E. Berthier, R. Hock, W. T. Pfeffer, G. Kaser, S. R. M. Ligtenberg, T. Bolch, M. J. Sharp, J.-O. Hagen, M. R. van den Broeke, and F. Paul (2013), A reconciled estimate of glacier contributions to sea level rise: 2003 to 2009, *Science*, **340**, 6134, 852–857, doi:10.1126/science.1234532
- Lenaerts, J. T. M., E. van Meijgaard, M. R. van den Broeke, S. R. M. Ligtenberg, M. Horwath, and E. Isaksson (2013), Recent snowfall anomalies in Dronning Maud Land, East Antarctica, in a historical and future climate perspective, *Geophysical Research Letters*, **40**, 1–5, doi:10.1002/grl.50559
- Barrand, N. E., R. C. A. Hindmarsh, R. J. Arthern, C. R. Williams, J. Mouginit, B. Scheuchl, E. Rignot, S. R. M. Ligtenberg, M. R. van den Broeke, T. L. Edwards, A. J. Cook, and S. B. Simonsen (2013), Computing the volume response of the Antarctic Peninsula ice sheet to warming scenarios to 2200. *Journal of Glaciology*, **59**, 215, 397–409, doi:10.3189/2013JG12J139
- Depoorter, M. A., J. L. Bamber, J. A. Griggs, J. T. M. Lenaerts, S. R. M. Ligtenberg, M. R. van den Broeke, and G. Moholdt (2013), Calving fluxes and basal melt rates of Antarctic ice shelves. *Nature*, **502**, 89–92, doi:10.1038/nature12567
- Khazendar A., M. P. Schodlok, I. Fenty, S. R. M. Ligtenberg, E. Rignot, and M. R. van den Broeke (2013), Observed thinning of Totten Glacier is linked to coastal polynya variability. *Nature Communications*, **4**, 2857, doi:10.1038/ncomms3857
- Kuipers Munneke P., S. R. M. Ligtenberg, M. R. van den Broeke, and D. G. Vaughan (2014), Firn air depletion as a precursor for Antarctic ice-shelf collapse. *Journal of Glaciology*, **60**, 220, 205–214, doi:10.3189/2014JG13J183
- Maris M. N. A., S. R. M. Ligtenberg, M. Crucifix, B. de Boer, and J. Oerlemans (2014), Modelling the evolution of the Antarctic Ice Sheet since the last interglacial. *The Cryosphere Discussions*, **8**, 85-120, doi:10.5194/tcd-8-85-2014
- Kuipers Munneke P., S. R. M. Ligtenberg, M. R. van den Broeke, J. H. van Angelen, and R. R. Forster (2014), Explaining the presence of perennial liquid water bodies in the firn of the Greenland Ice Sheet. *Geophysical Research Letters*, in press, doi:10.1002/2013GL058389
- Gunter B. C., O. Didova, R. E. M. Riva, S. R. M. Ligtenberg, J. T. M. Lenaerts, M. King, M. R. van den Broeke, and T. Urban (2014), Empirical estimation of present-day Antarctic glacial isostatic adjustment and ice mass change. *The Cryosphere*, in press

Curriculum vitae

Stefan Roderick Martijn Ligtenberg

20-09-1986 born in Apeldoorn

1998 – 2004 VWO, Het Nieuwe Eemland College, Amersfoort

2004 – 2007 BSc Bodem, Water en Atmosfeer, Wageningen University
Bachelor thesis: *A sensitivity analysis of changes in surrounding parameters on the Iberian Peninsula thermal low.*

2007 – 2009 MSc Meteorology and Air Quality, Wageningen University
Master thesis: *Integrating large-scale atmospheric circulation patterns above Europe ('Grosswetterlagen') into a statistical weather forecast for The Netherlands.*
Internship: *The influence of melt on surface height changes in Antarctica using a firn densification model.*

2010 – 2014 PhD research at IMAU, Utrecht University
Title: *The present and future state of the Antarctic firn layer.*
Promotor: prof. dr. M.R. van den Broeke

2014 – Postdoctoral research at IMAU, Utrecht University